Dissertation

Multipath Propagation, Mitigation and Monitoring in the Light of Galileo and the Modernized GPS

eingereicht von

Dipl.-Ing. Markus Irsigler

Vollständiger Abdruck der an der Fakultät für Luft- und Raumfahrttechnik der Universität der Bundeswehr München zur Erlangung des akademischen Grades eines Doktors der Ingenieurwissenschaften (Dr.-Ing.) eingereichten Dissertation.

Vorsitzender: (Chairman)	**Prof. Dr. rer. nat. Bernd Häusler,** Institute of Space Technology, Bundeswehr University Munich
1. Berichterstatter: (1st reviewer)	**Univ.-Prof. Dr.-Ing. Günter W. Hein**, Institute of Geodesy and Navigation, Bundeswehr University Munich
2. Berichterstatter: (2nd reviewer)	**Univ.-Prof. Dr.-Ing. Bernd Eissfeller**, Institute of Geodesy and Navigation, Bundeswehr University Munich
3. Berichterstatter: (3rd reviewer)	**Prof. Dr. Per K. Enge**, Dept. of Aeronautics and Astronautics, Stanford University

Die Dissertation wurde am 4. April 2008 bei der Universität der Bundeswehr München, Werner-Heisenberg-Weg 39, 85577 Neubiberg eingereicht und durch die Fakultät für Luft- und Raumfahrttechnik am 23. April 2008 angenommen. Tag der mündlichen Prüfung: 18. Juli 2008.

Abstract

Content of Thesis

Among the numerous potential sources of GNSS signal degradation, multipath takes on a prominent position. Unlike other errors like ionospheric or tropospheric path delays which can be modeled or significantly reduced by differential techniques, multipath influences cannot be mitigated by such approaches. Although a lot of multipath mitigation techniques have been proposed and developed in the past – among them many receiver internal approaches using special signal processing algorithms – multipath (especially multipath with small geometric path delays) still remains a major error source. This is why multipath has been a major design driver for the definition of the Galileo signal structure carried out in the past years and the subsequent signal optimization activities.

This thesis tries to provide a broad and comprehensive insight into various aspects of multipath propagation, mitigation and monitoring (without claiming to be exhaustive). It contains an overview of the most important aspects of ***multipath propagation****, including the discussion of different types of multipath signals (e.g. specular vs. diffuse multipath, satellite vs. receiver multipath or hardware-induced multipath), typical characteristics such as periodic signal variations whose frequency depends on the satellite-antenna-reflector geometry and the impact on the signal tracking process within a GNSS receiver.*

A large part of this thesis is dedicated to aspects of ***multipath mitigation****, first providing a summary of the most common multipath mitigation techniques with a special focus on receiver-internal approaches such as the narrow correlation technique, double-delta correlator implementations, the Early-Late Slope (ELS) technique or Early/Early tracking implementations. However, other mitigation approaches such as using arrays of closely spaced antennas or multipath-limiting antennas are discussed as well. Some of these techniques are used for subsequent multipath performance analyses considering signals of the (modernized) GPS and Galileo. These analyses base on a new methodology to estimate typical and meaningful multipath errors making use of multipath error envelopes that are scaled in a suitable way to account for different multipath environments. It will be shown that typical (mean) multipath errors can be derived from these scaled envelopes by computation of the envelope's running average and that these mean multipath errors are of the same order as multipath errors obtained from complex statistical channel models.*

Another part of this thesis covers various aspects of ***multipath detection and monitoring****. First, current techniques for multipath detection and monitoring are described and discussed with respect to their benefits and drawbacks or their real-time capability. Among the considered approaches are techniques like "code minus carrier" monitoring, SNR monitoring, the use of differenced observations or spectral and wavelet analysis. Following this introductory overview, a completely new approach for real-time multipath monitoring by processing multi-correlator observations will be introduced. Previously being used primarily for the detection of Evil Waveforms (signal failures that originate from a malfunction of the satellite's signal generation and transmission hardware), the same basic observations (linear combinations of correlator outputs) can be used for the development of a multi-correlator-based real-time multipath monitoring system. The objective is to provide the user with instant information whether or not a signal is affected by multipath. The proposed monitoring scheme has been implemented in the form of a Matlab-based software called RTMM (Real-Time Multipath Monitor) which has been used to verify the monitoring approach and to determine its sensitivity.*

Major Scientific Contributions and Achievements

The major scientific contributions and achievements provided through this thesis can be summarized as follows:

***General achievements**. The majority of the multipath-related knowledge is spread in conference papers, theses and journal articles. There is almost no textbook that covers this topic in a comprehensive and exhaustive way. This thesis combines a multitude of important aspects of multipath propagation, mitigation and monitoring in one coherent piece of work.*

***Scientific Contributions**. Besides the general achievement of carrying together all important multipath-related work, the thesis contains the following significant scientific contributions:*

- *Detailed analysis of occurring frequencies of multipath oscillations for different geometric conditions. Expected frequencies are computed and visualized for ground multipath scenarios and for varying reflector locations (see section 3.1.4, "The Frequency of Multipath Variations", p. 37 - 44).*

- *Analysis of the suitability of the carrier smoothing approach for the purpose of multipath mitigation and elaboration of limitations and shortcomings of this approach. It is shown that carrier smoothing does not ensure efficient multipath mitigation in any situation (see section 4.1.7, "Carrier Smoothing", p. 66 - 72).*

- *Development of a new and very efficient methodology to obtain typical and meaningful multipath errors from common multipath error envelopes. The proposed methodology makes use of the concept of scaling the envelopes in a suitable way to account for different multipath environments. The typical (mean) multipath errors that can be derived from these scaled envelopes are of the same order as multipath errors obtained from complex statistical channel models (see section 5.1, "Criteria for Multipath Performance Assessment", p. 81 - 97). This methodology was used to compute expected multipath errors for the future Galileo signals and the signals of the modernized GPS (see sections 5.2 and 5.3, "Expected Code Multipath Errors"," Expected Carrier Multipath Errors", p. 97 - 104).*

- *Development of a real time multipath monitor based on multi-correlator observations. The proposed monitoring approach allows instant detection of multipath signals and can either be used to detect multipath-affected observations and exclude them from the subsequent positioning process or to de-weigh the affected observations. By determining the optimum metric (i.e. a suitable combination of correlator peak observations), the monitor can be made very sensitive, so that even weak multipath signals can be detected (see section 7, "Development of a Real-Time Multipath Monitor (RTMM)", p. 122 - 195). The development of this method is the principal topic of this thesis.*

Zusammenfassung

Inhalt der Arbeit

Die Qualität eines Satellitensignals wird durch eine Vielzahl potenzieller Fehlerquellen negativ beeinflusst. Neben atmosphärischen Einflüssen wie ionosphärischen oder troposphärischen Laufzeitfehlern tragen Mehrwegeeinflüsse einen wesentlichen Anteil zum Gesamtfehlerbudget der Satellitennavigation bei. Während eine ganze Reihe von Fehlereinflüssen (z.B. die bereits erwähnten atmosphärischen Fehler) durch geeignete Modellierung oder differenzielle Verfahren deutlich reduziert werden können, ist dies durch die räumliche Dekorrelation der Mehrwegeeffekte nicht möglich. Obwohl in der Vergangenheit eine Vielzahl von Verfahren zur Mehrwegereduzierung vorgeschlagen und entwickelt wurden – darunter eine Reihe spezieller empfängerinterner Signalprozessierungsalgorithmen – stellen Mehrwegesignale noch immer eine wesentliche, stets zu berücksichtigende Fehlerquelle dar. Aus diesem Grund spielten die zu erwartenden Mehrwegefehler auch eine sehr wichtige Rolle im Zuge der Definition sowie der Optimierung der Galileo-Signalstruktur und können somit als wesentliches Design-Kriterium angesehen werden.

Die vorliegende Arbeit gibt einen umfassenden Einblick in verschiedene Aspekte der Mehrwegeausbreitung, -reduzierung sowie der Detektion und der Überwachung (Monitoring) auftretender Mehrwegeeffekte, ohne dabei allerdings Anspruch auf Vollständigkeit zu erheben. Die Arbeit beschreibt zunächst die wichtigsten Aspekte der ***Mehrwegeausbreitung****, wobei beispielsweise unterschiedliche Arten von Reflexionen (gerichtete vs. diffuse Reflexion) oder unterschiedliche Entstehungsarten (Reflexionen am Satelliten vs. Reflexionen in der Empfängerumgebung sowie Reflexionen an Hardwarekomponenten) ebenso diskutiert werden wie typische Auswirkungen von Mehrwegesignalen wie die Entstehung periodischer Signalvariationen. Solche Signalvariationen sind in starkem Maße abhängig von der durch die Satellitenposition, dem Antennenstandpunkt und der Lage des Reflexionspunktes definierten Geometrie. Die Frequenz dieser Signalvariationen wird für unterschiedliche geometrische Verhältnisse berechnet. Zudem werden der Einfluss bzw. die Auswirkungen einer Mehrwegeausbreitung auf den Signalverarbeitungsprozess in einem GNSS Empfänger aufgezeigt.*

Einen weiteren Schwerpunkt dieser Arbeit bilden die derzeit gebräuchlichen Methoden zur ***Reduzierung von Mehrwegeeinflüssen****. Dabei werden zunächst die wichtigsten empfängerinternen Ansätze wie die Verwendung enger Korrelatoren (Narrow Correlator), Double-Delta-Implementierungen, Early-Late-Slope-Techniken (ELS) oder die Verwendung mehrerer früher Korrelatoren (Early/Early Tracking) vorgestellt. Aber auch Methoden wie die Verwendung von Antennenarrays oder spezieller Antennen wie Multipath-Limiting Antennas (MLA) bleiben nicht unberücksichtigt. Einige dieser Methoden bilden im Folgenden die Grundlage für die Bestimmung von typischen, unter bestimmten Bedingungen zu erwartenden Mehrwegefehlern. Dazu wird eine neuartige Methodik vorgestellt, um aus Hüllkurven des Mehrwegefehlers, welche üblicherweise zur Darstellung der maximal auftretenden Fehler als Funktion des geometrischen Umwegs verwendet werden, aussagekräftige mittlere Mehrwegefehler zu bestimmen. Dazu werden die Hüllkurven mit Hilfe einiger aus statistischen Kanalmodellen abgeleiteter Parameter in geeigneter Weise skaliert, um unterschiedlichen Mehrwegeumgebungen (z.B. ländliche oder städtische Umgebungen) Rechnung zu tragen. Es wird gezeigt, dass die mit Hilfe dieser relativ einfachen und effizienten Methode ermittelten Mehrwegefehler in derselben Größenordnung liegen wie die aus komplexen statistischen Kanalmodellen ermittelten Fehler.*

Einen weiteren Themenkomplex stellen Methoden zur ***Detektion und*** *zum* ***Monitoring von Mehrwegeeinflüssen*** *dar. Dabei werden zunächst die derzeit verwendeten Ansätze vorgestellt und hinsichtlich ihrer Vor- und Nachteile sowie hinsichtlich ihrer Echtzeitfähigkeit*

diskutiert. Unter den vorgestellten Methoden finden sich die Überwachung von „Code minus Carrier"-Beobachtungen, die Auswertung des Signal-zu-Rausch-Verhältnisses, die Verwendung differenzierter Beobachtungen oder der Einsatz komplexer Methoden wie der Spektral- oder Wavelet-Analyse. In Anschluss an diesen einführenden Überblick wird ein neuartiger Ansatz zur Detektion und zum Monitoring von Mehrwegesignalen in Echtzeit vorgestellt. Der vorgeschlagene Ansatz basiert auf der Auswertung von Multikorrelatorbeobachtungen, welche bisher vorwiegend zur Detektion so genannter „Evil Waveforms" – Satellitensignalfehler, welche durch fehlerhafte Hardware in der Signalgenerierungseinheit des Satelliten hervorgerufen werden – verwendet werden. Dabei können prinzipiell dieselben grundlegenden Beobachtungen wie zur Detektion von „Evil Waveforms" zum Einsatz kommen (nämlich Kombinationen unterschiedlicher Korrelationswerte) und zur Mehrwegedetektion genutzt werden. Ziel dieser Entwicklung ist es, einen potenziellen Nutzer sofort darüber informieren zu können, wenn ein Signal mit Mehrwegefehlern behaftet ist. Der vorgeschlagene Ansatz wurde in Form einer Matlab-basierten Auswertesoftware (RTMM – Real Time Multipath Monitor) implementiert, welche im Folgenden zur Verifizierung und zur Bestimmung der Empfindlichkeit des Verfahrens verwendet wird.

Wesentliche wissenschaftliche Beiträge

Wesentliches Ziel dieser Arbeit war es, das in den vergangenen Jahren und Jahrzehnten erarbeitete und veröffentlichte umfangreiche Know-How bezüglich Mehrwegeausbreitung, deren Detektion sowie deren Reduzierung umfassend und strukturiert zusammenzufassen und zudem neue wissenschaftliche Beiträge in diesen Kontext einzuordnen.

Das über den Themenkomplex „Mehrwegeausbreitung" veröffentlichte Know-How existiert zum großen Teil lediglich in Form von Konferenzbeiträgen, Dissertationen oder Fachzeitschriftenartikeln. Eine umfassende Behandlung der Thematik (z.B. in Form von Lehrbüchern), welche alle in der vorliegenden Arbeit behandelten Aspekte abdeckt, findet sich praktisch überhaupt nicht. Aus einer Vielzahl von Einzelveröffentlichungen, welche jede für sich lediglich einen kleinen Teil dieses umfangreichen Themengebietes behandeln, konnte – angefangen von den theoretischen Grundlagen der Mehrwegeausbreitung - eine in sich zusammenhängende Abhandlung dieses Themas erarbeitet werden, welche zusätzlich um eigene wissenschaftliche Beiträge ergänzt werden konnte. Diese sind in nachfolgender Auflistung zusammengefasst:

- *Detaillierte Analyse der Frequenzen der typischerweise auftretenden periodischen Mehrwegevariationen unter unterschiedlichen geometrischen Bedingungen. Die Frequenzen werden sowohl für den Fall von Bodenreflexionen als auch für unterschiedliche Reflektorpositionen in Bezug zur Empfangsantenne berechnet und visualisiert (siehe Abschnitt 3.1.4, "The Frequency of Multipath Variations", S. 37 - 44).*

- *Analyse der Eignung des „Carrier Smoothing" zur Reduzierung von Mehrwegeeffekten. In diesem Zusammenhang werden insbesondere die Einschränkungen bzw. die Nachteile dieses Verfahrens erarbeitet und aufgezeigt, dass damit in vielen Fällen keine wirksame Fehlerreduzierung erreicht werden kann (siehe Abschnitt 4.1.7, "Carrier Smoothing", S. 66 - 72).*

- *Entwicklung einer neuartigen und effizienten Methode, typische und aussagekräftige Mehrwegefehler aus Hüllkurven (welche eigentlich nur Informationen über die maximal zu erwartenden Fehlereinflüsse liefern) zu extrahieren. Es wird gezeigt, dass die damit ermittelten mittleren Mehrwegefehler in derselben Größenordnung liegen wie die durch aufwändige Analyse statistischer Kanalmodelle ermittelten Fehler (siehe Abschnitt 5.1, "Criteria for Multipath Performance Assessment", S. 81 - 97). Der vorgeschlagene Ansatz wird im Folgenden für die Berechnung von Mehrwegefehlern verwen-*

det, wie sie für zukünftige Galileo- oder GPS-Signale zu erwarten sein werden (siehe Abschnitte 5.2 und 5.3, “Expected Code Multipath Errors”, “Expected Carrier Multipath Errors, p. 97 - 104).

- *Entwicklung einer echtzeitfähigen Methode zur Detektion und zum Monitoring von Mehrwegesignalen. Der vorgeschlagene Ansatz basiert auf einer Überwachung der Korrelationsfunktion mittels mehrerer Korrelatoren (Multikorrelatorbeobachtungen) und erlaubt die sofortige Detektion von Mehrwegesignalen; diese können dann aus dem weiteren Verarbeitungsprozess ausgeschlossen oder zumindest entsprechend gewichtet werden. Mittels einer geeigneten Kombination einzelner Korrelatorbeobachtungen kann die Sensitivität des vorgeschlagenen Monitors derart gesteigert werden, dass auch extrem schwache Mehrwegesignale detektiert werden können. Die Entwicklung dieses Ansatzes bildet den Hauptteil der vorliegenden Arbeit (siehe Abschnitt 7, “Development of a Real-Time Multipath Monitor (RTMM)”, p. 122 - 195).*

Table of Contents

1. Introduction

Today's operational GNSS (GPS and GLONASS) are radio navigation systems that use radio frequency (RF) signals at dedicated center frequencies. Suitable ranging codes and navigation data are modulated onto the carrier waves allowing a receiver to estimate the distance between the user antenna and the satellite based on the current satellite position and the time difference between signal transmission and reception. However, the satellite signals received anywhere on or near the earth are very weak and well below the natural background noise level of any antenna environment. The weakness of these signals make the systems vulnerable and susceptible to RF interference and jamming. These types of signal degradation typically increase the noise level and might prevent the receiver from detecting the signal. But even if interference or jamming does not occur, there are still many other influences which have the potential to degrade the navigation performance. Such influences are discussed in the following sections.

1.1 Sources of Satellite Signal Degradation

Figure 1-1 summarizes some important sources of signal degradation. They can be classified into three categories:

- **Signal degradation that is inherent to the system.** This category contains all sources of degradation caused by the satellites or the system architecture itself. Among them are "Evil Waveforms", anomalous signals transmitted from a satellite.
- **Signal degradation along the signal path.** This category contains all atmospheric influences the signal experiences as it travels through the Earth's different atmospheric layers as well as the Doppler shift of a satellite signal caused by the relative movement of the satellite with respect to the user.
- **Signal degradation due to user environment characteristics.** This category contains signal-masking effects caused by trees or buildings, sources of jamming/interference and multipath.

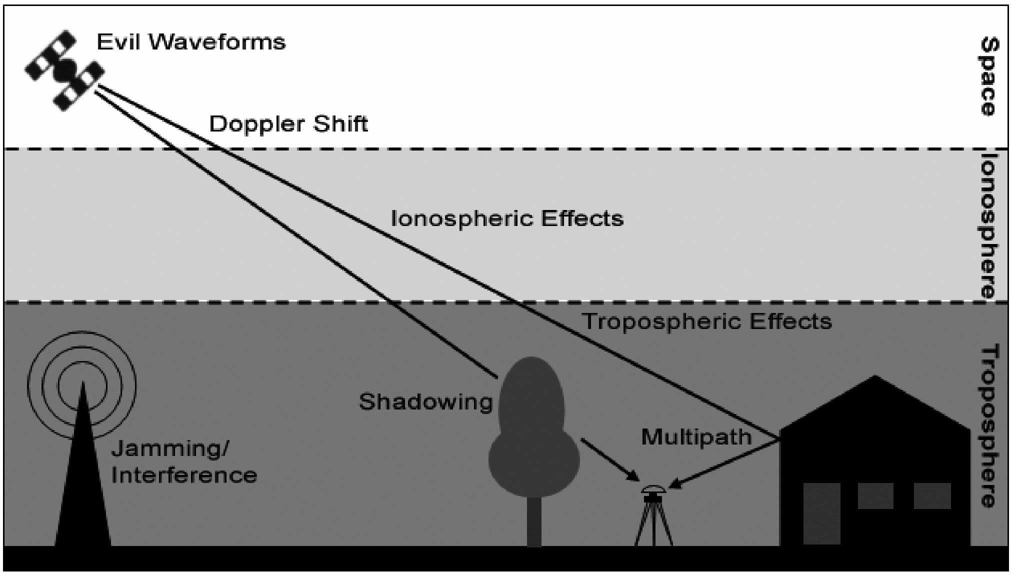

Figure 1-1: Possible sources of GNSS signal degradation.

The next section provides a more detailed overview of these sources of signal degradation. A similar overview can be found in [MacGougan et al. 2001].

1.1.1 Signal Generation

Failures in the satellite's signal generation and transmission hardware are commonly referred to as "Evil Waveforms". In 1993, such a failure was detected for the first time. It resulted in a severe degradation of the differential positioning performance (accuracy of 2-8m instead of 50cm without consideration of the affected satellite SV19). Instead of showing a normal *sinc* function shape, the power spectrum of the anomalous signal showed a large spike at the center frequency. This event led to the development of several candidate threat models to explain the anomalous behavior. One such model is the "2nd Order Step" Threat Model (TM). It can explain the distorted spectrum as well as the observed position errors ([PHELTS 2001]). Three classes of signal failures can be expected, namely digital and analog failures as well as a combination of both. They are named TM A, B and C and affect the signal's code sequence and correlation function (see Table 1-1).

TM	Characteristics	Code Sequence	Correlation Functions
A	Advance (lead) or delay (lag) in the falling edge of a code chip. Can also occur in the rising edge of a code chip. Creates flattened and shifted correlation peaks.	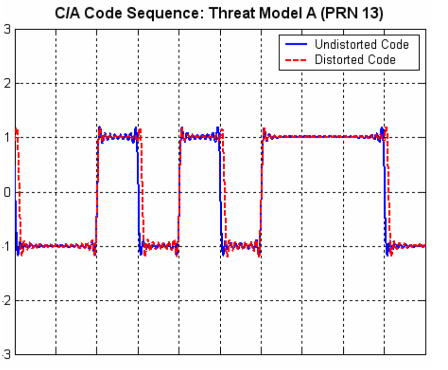	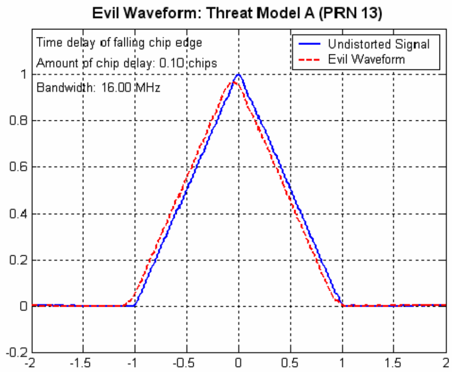
B	Modeled by applying an amplitude modulation or "ringing" to the code sequence. Creates distorted and asymmetric correlation peaks.	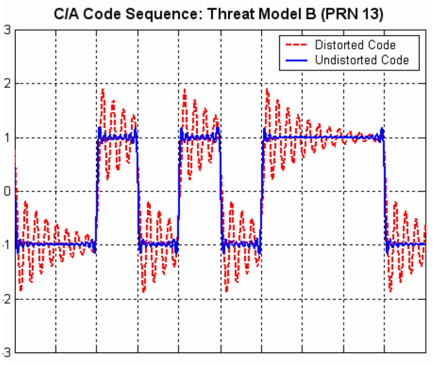	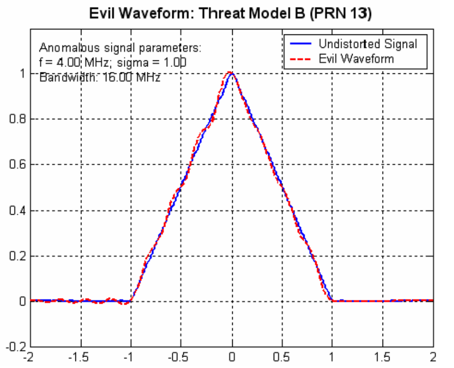
C	Combines lead/lag effects in the code chip transitions (TM A) with the oscillations of TM B. Can create flattened peaks, distorted peaks and additional (false) peaks at the same time.	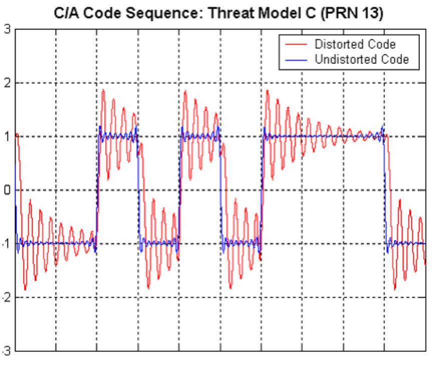	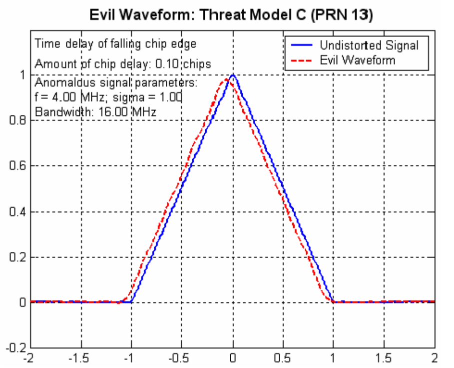

Table 1-1: Modeling of "Evil Waveforms".

"Evil Waveforms" can pose an integrity threat to any GNSS user, especially when safety-of-life applications are considered. As a result, satellite or ground based augmentation systems like LAAS or WAAS require some Signal Quality Monitoring (SQM) concepts to protect airborne users against such threats. Further aspects of this topic are discussed in section 7.1 in more detail.

1.1.2 Signal Propagation

1.1.2.1 Ionospheric Influences

The ionosphere is the atmospheric layer between altitudes of approximately 50 and 1000km and primarily consists of ionized gas molecules and electrons. The ionization of gas molecules and the concurrent formation of mobile electrons is a result of intensive solar radiation (ultraviolet radiation and x-rays) in the ionosphere. For frequencies commonly used for satellite navigation, only the mobile electrons are of importance, whereas the ions only play a significant role for frequencies of around 100MHz and below ([HARTL 1988]). As the solar radiation is absorbed by different gas molecules in different altitudes, the ionization process takes place in different altitudes as well so that different ionospheric layers are formed. These ionospheric layers are characterized by their electron densities which vary with time and location. The variations of electron density can be subdivided into

- **Diurnal variations**. The electron density varies with the day/night cycle; due to reduced solar radiation, the ionospheric ionization at night decreases significantly. Ionization reaches its maximum at 2 p.m. local time and a minimum between midnight and 6 a.m.
- **Seasonal variations**. The electron density is subject to seasonal variations.
- **Variations due to solar activity**. Solar activity varies with an 11-year-cycle. A solar maximum results in increased solar radiation penetrating the atmosphere and in increased ionospheric ionization. During these periods, the number of coronal mass ejections increases as well. Such ejections can cause short-period variations of ionospheric ionization that can be very intense (ionospheric storm).
- **Location-dependent variations**. Large values for the electron density can be observed approximately between latitudes from 20° to 30° north and south of the geomagnetic equator which approximately coincides with the geographical equator. In these regions, the observed values are larger than at mid-latitudes by a factor of two ([BAUER 1997]).
- **Traveling Ionospheric Disturbances (TID).** For this type of electron density variation, typical periods of a few minutes up to one hour can be observed. According to [WANNINGER 1993], they frequently occur around a solar maximum, typically at daytime during winter months.

Moreover, due to the interaction between the radio waves and mobile electrons, the refractive index of the ionosphere is frequency-dependent. Thus, the ionosphere is a “dispersive” medium. With respect to satellite navigation, the following effects must be expected (see also [KLOBUCHAR 1996]):

- **Group delay and carrier phase advance**. For a dispersive medium like the ionosphere, two velocities have to be considered, namely phase and group velocity. The first term describes the phase propagation of an electromagnetic wave with uniform wavelength (no transmission of information). The latter one assumes the propagation of a wave group that can be formed by superimposition of waves of different frequencies. The velocity of propagation of these wave groups is called group velocity (to be considered for transmission of information). According to the theory of relativity, information cannot be transmitted with velocities that exceed the speed of light. The group velocity is therefore always smaller than or equal to the speed of light in vacuum. The phase velocity, however, can exceed the speed of light. Therefore, different refractive indices (n_p and n_g) for phase and group velocity have to be considered in a dispersive medium like the ionosphere. The resulting ionospheric ranging errors Δs_p and Δs_G are obtained by integrating (1-n) along the entire signal path. They depend on the carrier frequency f and have identical absolute values but opposite signs:

$$\Delta s_P = -\frac{40.31}{f^2} \cdot TEC \qquad \Delta s_G = \frac{40.31}{f^2} \cdot TEC \tag{1}$$

The unit of the constant term in equation (1) (C=40.31) is [m^3/s^2]. *TEC* is the integrated electron density along the signal path, is expressed in [$1/m^2$] and quantifies the number of electrons inside a column with a footprint of $1m^2$ ranging from the observer to the satellite. *TEC* represents the degree of ionospheric ionization and is, as already mentioned above, to a great extent time- and location-dependent. In case of “normal” ionospheric conditions (typical day/night variations), ionospheric path delays are ~1-8m for L1 and ~1-13m for L2, respectively ([IRSIGLER et al. 2002]). In case of an ionospheric storm, however, they can exceed 100m. Ionospheric ranging errors can be reduced by either modeling the ionospheric conditions (e.g. Klobuchar model), by means of differential GNSS or by processing dual-frequency observations.

- **Ionospheric refraction**. The refractive index of the Earth’s ionosphere is responsible for bending the radio waves from a straight geometric path between the satellite and the ground. This angular refraction produces an apparently higher elevation angle than the geometric elevation. Maximum values for the ionospheric refraction occur for low elevation angles and are ~4” for L1 and ~7” for L2, respectively ([KLOBUCHAR 1996]). Although depending on the actual ionospheric ranging error, ionospheric refraction itself does not affect the positioning/navigation performance.

- **Ionospheric Doppler shift**. According to equation (1), the carrier phase advance depends on the electron density along the signal path. As a satellite constantly moves along its orbit, the satellite signal will traverse different ionospheric layers during a certain observation period resulting in temporal variations of *TEC* leading to temporal variations of the carrier phase advance (1). Therefore, in addition to geometrical Doppler shifts, ionospheric Doppler shifts have to be expected as well. They can be expressed as follows ([KLOBUCHAR 1996]):

$$\Delta f = \frac{40.31}{cf} \cdot \frac{dTEC}{dt} \text{ [Hz]} \tag{2}$$

The ionospheric Doppler shift is proportional to 1/f and depends on the temporal rate of change of *TEC*. An upper limit for this rate of change is given by approximately $0.1 \cdot 10^{16}$ [$1/m^2s$] in [KLOBUCHAR 1996]. Based on this value, ionospheric Doppler shifts of 0.085 Hz for L1 and 0.11 Hz for L2 can be expected. Compared to the typical geometrical Doppler shifts, these values are too small to have any negative impact on signal acquisition or tracking.

- **Faraday rotation**. When a linearly polarized radio wave traverses the ionosphere, the wave undergoes rotation of the plane of this linear polarization. Since current satellite navigation system use circular polarization instead of linear polarization, Faraday rotation has no effect on these signals.

- **Distortion of pulsed waveforms**. A navigation signal consists of spread spectrum pseudorandom noise codes transmitted at a certain bandwidth. The ionosphere can produce dispersion of the spread spectrum signals resulting in a difference Δt in pulse arrival time that is proportional to the *TEC* value. However, even in case of a severe ionospheric storm, Δt does not exceed ~1.4E-8s for the current GNSS signals ([IRSIGLER 2001]).

- **Scintillation**. Ionospheric scintillation is caused by temporary electron density irregularities within the different ionospheric layers. It causes rapid amplitude and/or phase variation of an RF signal traversing these irregularities. Both effects may present a tracking problem for a GNSS receiver. Amplitude scintillation may lead to rapid power fluctuations of the received signal and can cause the signal power to drop below the tracking threshold. Phase scintillation may cause rapid random phase rate variation inducing additional stress to the carrier tracking loop. As a result, both effects (amplitude and phase scintillation) may result in loss of lock.

1.1.2.2 Tropospheric Influences

The atmospheric layers below the ionosphere (at altitudes between 0 and 50km) consist of dry gases and water vapor. Strictly speaking, only the atmospheric layer up to an altitude of approximately 12km is referred to as the troposphere, because this is where most of the weather processes take place. The troposphere is characterized by a linear decrease of temperature with increasing altitude. The atmospheric layer above the troposphere is called stratosphere and is separated from the troposphere by the so-called tropopause. The stratosphere reaches an altitude of approximately 50km.

The dry atmosphere can be considered non-dispersive for frequencies below approximately 30 GHz, i.e. the refractive index does not depend on the carrier frequency. As a result, code and carrier phase are delayed by the same amount. In the presence of rainfall, however, the refractive index of the troposphere becomes frequency-dependent resulting in slightly different path delays for code and carrier phase. The following tropospheric effects might occur:

- **Tropospheric path delay**. When the signal traverses atmospheric layers of different density, the corresponding refractive index will not be constant along the signal path. As it is the case with ionospheric influences, this changing refractive index results in path delays and signal bending. Tropospheric path delay can be divided into a dry and a wet component. While the dry component accounts for ~90% of the entire path delay and can be easily modeled (slow temporal variations), the wet component is much smaller but harder to model because it is subject to more rapid temporal variations ([SPILKER 1996b or MISRA and ENGE 2001]). Tropospheric ranging errors strongly depend on the elevation angle and typically vary between 2.5m near zenith and up to 25m at low elevation angles. They can be effectively reduced by suitable tropospheric models (e.g. Hopfield, Saastamoinen, Black and Eisner) or by differential GNSS techniques. In the presence of rainfall, the troposphere becomes a dispersive medium. This leads to additional ranging errors that depend – to a small extent – on the carrier frequency and – to a much larger extent – on the amount of rainfall. However, the resulting additional ranging errors are rather small (up to 9mm/km signal path in case of heavy rain).

- **Tropospheric attenuation**. There are two major sources of tropospheric attenuation, namely attenuation by water vapor and oxygen and rainfall attenuation. Both sources of attenuation are frequency-dependent (larger frequencies result in more severe signal attenuation). Attenuation by water vapor and oxygen mainly depends on the water vapor content in the atmosphere (attenuation caused by oxygen is relatively constant and only depends on the carrier frequency). Rainfall attenuation mainly depends on the actual amount of rainfall and the length of the signal path within the rainfall region. Worst case analyses by using appropriate tropospheric models (e.g. ITU-R rainfall model) lead to overall tropospheric attenuation values of ~0.31dB for L1 and ~0.25dB for L2. Clouds and fog also attenuate the GNSS signal. However, their influence is usually smaller than 1dB. Details on tropospheric attenuation can be found in [MARAL and BOUSQUET 1998] or [SPILKER 1996b].

- **Tropospheric scintillation**. Tropospheric scintillation is caused by irregularities and turbulences of the atmospheric refractive index, primarily in the lower part of the atmosphere (first few kilometers above the ground). The effect varies with time and depends on carrier frequency, elevation angle and weather conditions. Especially dense clouds are a major source of scintillation which can cause signal amplitude degradations. For the L1 frequency band, amplitude attenuation of up to a few dB can occur for very small fractions of time and low signal elevations. For larger elevations and for most of the time, though, tropospheric scintillation is quite small ([SPILKER 1996b]).

1.1.2.3 Doppler Shift

Doppler shift is the difference between the nominal frequency of a signal (frequency at which the transmitter generates the signal) and the apparent frequency (actual frequency the receiver observes). This difference is caused by the motion of the transmitter relative to the receiver or vice versa. Satellite based navigation systems like GPS produce Doppler shifted signals due to the satellite motion relative to a ground-based receiver. Assuming a stationary receiver on the ground, Doppler shifts can be of the order of ±6kHz for current GNSS and even larger for dynamic applications with moving receivers ([SPILKER 1996d]).

Doppler shift affects GNSS receiver performance in several ways. First, the higher the occurring Doppler frequencies are, the larger is the frequency search region during the signal acquisition process. As a result, larger Doppler shifts can lead to larger acquisition times. Modern receivers, however, are able to predict the expected Doppler shift for each satellite so that frequency search is not really an issue anymore. Second, high dynamics negatively affect the accuracy of the velocity estimation ([MACGOUGAN et al. 2001]). And third, high Doppler frequencies due to high velocity or acceleration can induce stress on the tracking loops. Especially the carrier tracking loop is very sensitive to dynamic stress. Dynamic stress contributes to the overall PLL phase jitter, which also consists of the influence of thermal noise, oscillator frequency jitter, and vibration induced phase noise. If the total jitter exceeds a certain threshold, the PLL loses lock. The effect of dynamic stress depends on the bandwidth of the carrier tracking loop. It can be reduced by increasing the PLL bandwidth at the cost of increasing the influence of thermal noise.

1.1.3 User Environment

1.1.3.1 Shadowing Effects

Depending on the user environment, GNSS signals may be obstructed partially or even completely from time to time. Sources of obstructions can be buildings, mountains or dense foliage. Such signal masking effects may result in signal attenuation or even complete signal blockage. Foliage attenuation is commonly expressed in dB/m and depends on various parameters such as foliage type, size and density. Previous work on this subject indicates that typical foliage attenuation at L1 is between 0.7dB/m and 1.7dB/m ([SPILKER 1996a, KAJIWARA 2000, GOLDHIRSCH 1998]). Any kind of partial signal obstruction results in decreased signal power (decreased C/N_0) and thus in increased noise influences which in turn negatively affect the positioning performance. The same holds true for the case of complete signal blockage, which may severely affect the geometry of the satellite constellation and leads to increased DOP values.

1.1.3.2 Interference and Jamming

Because GNSS signals are rather weak, they are vulnerable to RF interference. This can result either in degraded navigation performance or even in a complete loss of receiver tracking. RF interference can be friendly or intentional. Intentional (in-band) jamming must be anticipated for military receivers whereas unintentional (out-of-band) jamming is expected for all types of satellite receivers. According to [WARD 1996], the following types and sources of RF interference may occur:

Type of RF Interference	Typical Source
Wideband-Gaussian	Intentional noise jammers
Wideband phase/frequency modulation	Television transmitters' harmonics or near band microwave link transmitters overcoming the front-end filter of GNSS receivers
Wideband-spread spectrum	Intentional spread spectrum jammers or near-field of pseudolites
Wideband-pulse	Radar transmitters
Narrowband phase/frequency modulation	AM station transmitters' harmonics or CB transmitters' harmonics
Narrowband-swept continuous wave	Intentional CW jammers or FM stations transmitters' harmonics
Narrowband-continuous wave	Intentional CW jammers or near-band unmodulated transmitter's carrier

Table 1-2: Types of RF interference and typical sources (adopted from [WARD 1996]).

RF interference typically results in a degradation of the signal's C/N_0 by increasing the noise level. This may result in loss of signal tracking or even prevent the receiver from acquiring GNSS signals. Some types of interference, namely continuous wave interference, may cause code measurement errors resulting in a false positioning solution. A more comprehensive view on RF interference and jamming can be found in [MACGOUGAN 2001], [WARD 1996] or [SPILKER 1996c].

A special type of intentional interference is spoofing, the intentional transmission of a false but strong version of the GPS signal. In case the receiver locks onto this strong signal, the positioning process most probably provides a false and useless solution. To avoid this problem with GPS, the public P-Code has been encrypted and the resulting P(Y)-Code is accessible only via a cryptographic key that is available for authorized users only (Anti-Spoofing, AS). For the future Galileo system, signal authentication schemes are planned to ensure that the desired signal and not a false version of the signal is received.

1.1.3.3 Multipath

Multipath is a phenomenon where the satellite signal is reflected by objects in the vicinity of a receiver, so that not only the direct signal (line-of-sight (LOS) component) enters the receiver but rather a composite signal consisting of the LOS signal plus one or several multipath signals. It is also possible that the LOS signal is completely obstructed so that the receiver processes only the multipath components. Multipath typically distorts the correlation function and leads to pseudorange and carrier phase errors that degrade the navigation performance. Unlike other error sources, multipath errors are generally uncorrelated between two vicinal receivers (even if they are separated by only a few meters) and will thus not cancel out by differencing observations. Therefore, code and carrier multipath is still a major issue for high-precision applications, because it is one of the largest error sources.

1.2 The Multipath Problem

Signal degradation due to multipath may originate from different "types of reflections". The signal may be reflected by obstacles such as buildings or by the ground. Based on the geometrical conditions in the vicinity of the antenna, one satellite signal can be reflected several times. A signal may also undergo edge diffraction, i.e. the signal deviates from its original path and the diffracted signal is finally received by the antenna. All these propagation scenarios are illustrated in Figure 1-2.

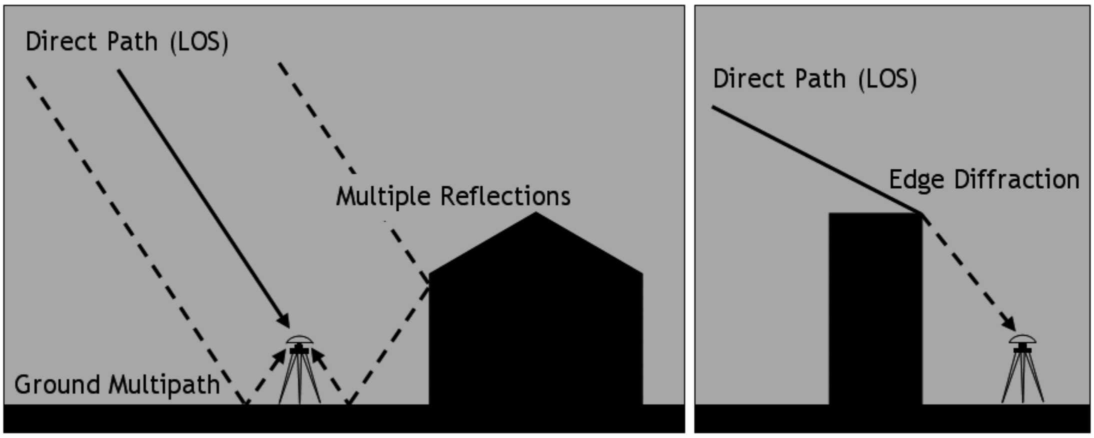

Figure 1-2: Different scenarios for multipath propagation.

The actual amount of received multipath signals strongly depends on the geometrical conditions. In the context of most existing multipath propagation models, these geometrical conditions are commonly characterized by the amount (or density) and structure of buildings (e.g. building heights) and natural multipath sources like trees and forests. Accordingly, these environments are named "open", "rural", "suburban" or "urban". In urban areas, for example, a mean number of approximately five multipath signals has to be expected most of the time ([IRSIGLER et al. 2005]).

The power of a multipath signal relative to the LOS component is determined mainly by the electromagnetic properties of the reflecting surface. Most reflections cause signal attenuation, so that multipath signals are typically weaker than the LOS component. The degree of attenuation can be expressed in terms of "multipath relative amplitude" α (typical range: $0 \leq \alpha \leq 1$) or in terms of "multipath relative power" (expressed in [dB]). Due to one or several reflections, the path length of the reflected signal is extended with respect to the length of the LOS path. This path extension is referred to as "multipath delay" or "geometric path delay". It can be expressed in [m] or [s]. Due to this path delay, the phase of the LOS component and the multipath signal may not match anymore. The difference between the phase of the LOS component and the multipath signal is referred to as "multipath relative phase" (expressed in [rad] or [°]).

In case of multipath, the antenna does not only receive the LOS component but the sum of the LOS plus all existing multipath components with dedicated multipath relative amplitudes, path delays and relative phases. The way this compound signal affects the tracking and navigation performance of the receiver depends on a variety of signal and receiver parameters:

- Signal type/modulation scheme
- Pre-correlation bandwidth and filter characteristics
- Chipping rate of code
- Chip spacing(s) d between correlators used for tracking
- Type of discriminator (tracking technique)
- Loop architecture (loop noise bandwidth)
- Carrier frequency f_{RF}
- User dynamics (static vs. dynamic applications)
- Actual number of multipath signals
- Geometric path delay(s) of multipath signal(s)

The signal type (i.e. modulation scheme), the pre-correlation bandwidth and the type of filter used for band-limiting the incoming signal determine the actual shape of the signal's correlation function which is then used to set up the code discriminator (by using two or several shifted copies of the correlation function). The type of discriminator and the chip spacing(s) used to set up the discriminator function determine the shape of the code discriminator that strongly influences the resulting multipath performance. The chipping rate of code determines the code chip length T_C which finally determines the resulting ranging error caused by code multipath (expressed in [m]). Carrier frequency and user dynamics influence the multipath phase rate, the difference in carrier frequency between the desired LOS and the undesired multipath signal(s). This difference is also referred to as "fading frequency" or "fading bandwidth" ([VAN NEE 1992]). The fading frequency and the DLL loop noise bandwidth influence the temporal characteristics and the amplitude of the resulting multipath errors. The remaining parameters listed above depend on the multipath environment (multipath relative power levels or amplitudes, geometric path delays, number of multipath signals). All these aspects will be discussed within the scope of this thesis.

1.3 Previous Multipath-Related Work

The first studies on multipath propagation have been carried out in the early 1970s. In this context, the work of [HAGERMAN 1973] is often cited as a cornerstone for all subsequent work on this subject. Soon after multipath has been realized to be a major error source, many efforts have been made to exactly describe the characteristics and effects of multipath propagation, to model the multipath propagation channel or to provide methods and approaches for multipath mitigation. Interestingly, most of the existing multipath-related literature comprise conference papers, journal articles or theses. There is hardly any comprehensive treatment of this subject that can be found in GPS/GNSS-related textbooks. One exception may be the work of [BRAASCH 1996], providing more than just a few pages on multipath propagation. The following sections try to categorize previous work on different aspects of multipath propagation. Note that this listing of multipath-related work may not be exhaustive.

Multipath Characteristics and Effects on Receiver Performance. Among the most important contributions to this category is the work of Van Nee ([VAN NEE 1992] or [VAN NEE 1993]), describing multipath effects on code phase measurements. The work of [BRAASCH 1996] that was already referred to in the previous paragraph extends the view on occurring multipath effects, additionally considering the effects of carrier multipath. Papers focusing on the effects of carrier multipath are [GEORGIADOU and KLEUSBERG 1988] or [RAY and CANNON 1999]. General aspects of GNSS signal propagation including the effects of multipath can be found in [HANNAH et al. 2000] or [KLUKAS et al. 2004]. The latter work examines the influence of different materials on signal propagation. Other papers focus on the effects of multipath under special conditions or are related to special applications. Ground multipath, for example, is treated in [ALOI and VAN GRAAS 1999], multipath effects for dynamic users are discussed in [EISSFELLER and WINKEL 1996] and multipath effects for GNSS-based landing systems can be found in [BRAASCH 1992] or [BRENNER et al. 1998]. The effects of fast-fading multipath are treated extensively in [KELLY and BRAASCH, 1999, 2000, 2001] and [KELLY et al. 2003].

Modeling of Multipath Propagation Channel. The German Aerospace Center (DLR) has carried out extensive work in the field of modeling the multipath channel. In the mid 1990s, a first statistical channel model based on extensive field measurements has been derived ([JAHN and BISCHL 1996] or [LUTZ et al. 2000]). During the last years, a revised statistical channel model was being developed ([STEINGASS and LEHNER 2004]). Multipath propagation models for urban environments as derived from simulations can be found in [FISHER et al. 2002] and [SUH et al. 2004]. Other approaches for modeling the effects of multipath propagation are discussed in [BRENNER at al. 1998] (discussion of diffuse multipath) and [VAN NEE 1992] (use of power-delay multipath profiles).

Multipath Mitigation (Special Tracking Techniques). During the past years, many innovative tracking techniques have been developed with the aim of mitigating multipath effects by means of suitable signal processing approaches. Overviews on these activities can be found in [Weill 1997a] or [Van Dierendonck and Braasch 1997]. Important receiver-internal mitigation approaches are the Narrow Correlator™ which has been introduced by NovAtel Inc. during the early 1990s. Information on this technique can be found in [Van Dierendonck et al. 1992] or [Cannon et al. 1994]. Further enhancement can be achieved by implementing Double Delta (ΔΔ) or gating tracking concepts. A ΔΔ tracking scheme has been first implemented as “Strobe Correlator” into some Ashtech receivers ([Garin et al. 1996], [Garin and Rousseau 1997]). Other work that should be mentioned is [McGraw and Braasch 1999] discussing gated correlator concepts or [Weill 1997b] treating suitable correlator reference waveforms for multipath mitigation. Another class of multipath mitigation techniques uses multi-correlator observations. Among them are NovAtel’s Multipath Elimination Technology (MET) based on slope measurements ([Townsend and Fenton 1994]), the Multipath Estimating Delay Lock Loop (MEDLL) based on several correlators that are distributed along the correlation peak ([Van Nee et al. 1994], [Townsend et al. 1995a] and [Townsend et al. 1995b]) or NovAtel’s latest development, the Vision Correlator [Fenton and Jones 2005]. An estimation to what extent multipath can be reduced can be found in [Weill 1995] where a lower bound for the remaining multipath errors has been derived for the GPS L1 signal. Lower bounds for the proposed signals of the modernized GPS are presented in [Weill 2002] and [Weill 2003a] and for Galileo in [Avila-Rodriguez et al. 2006].

Multipath Mitigation (Other Approaches). Other mitigation approaches make use of special antennas, antenna arrays or try to process SNR measurements to reduce the negative impact of multipath. One possible attempt to reduce the influence of ground multipath is the use of ground planes or choke ring antennas. Choke ring antennas optimized for GPS L1 and L2 are discussed in [Filippov at al. 1998] or [Filippov at al. 1999]. A three-dimensional choke ring antenna has been introduced in [Kunysz 2003]. Other antenna-based multipath mitigation techniques include the use of special multipath-limiting antennas (MLA) which are mainly used for GNSS-based augmentation systems like LAAS (e.g. [Thornberg et al. 2003]) or make use of phased-array antennas providing digital beam forming capabilities (e.g. [Fu et al. 2003]). Several papers addressed the potential of using more than just one antenna or even an array of several closely spaced antennas for multipath mitigation. The latter approach seems to be suitable for reducing carrier multipath. Further information on this subject can be found in [Ray et al. 1998], [Ray et al. 1999] or [Ray 1999]. Several receivers/antennas have also been used to detect and reduce reference station multipath ([Raquet and Lachapelle 1996]) or to determine the direction of incoming multipath signals ([Becker et al. 1994] or [Moelker 1997]). Another way to mitigate multipath is to process the SNR observations as reported by the receiver. Such approaches can be found in [Axelrad et al. 1994], [Comp and Axelrad 1996], [Reichert and Axelrad 1999] or [Sleewaegen 1997]. Furthermore, adaptive filter approaches can also be useful for multipath mitigation purposes (e.g. [Ge et al. 2000]).

Multipath Monitoring and Estimation of Multipath Parameters. Several publications deal with the detection of multipath influences at GPS reference stations (e.g. [Wanninger and Wildt 1997],[Wanninger and May 2001] or [Höper et al. 2001]). Most of the detection algorithms used in this context base on the formation of differences (single/double differences), linear combinations or the use of SNR data. [Höper et al. 2001] propose a frequency analysis approach for multipath detection. The development of a real-time multipath monitor based on code minus carrier observations is described in [Itani et al. 1996] or [Lee et al. 2004]. A method for the detection of code and multipath delays based on an adaptive filtering process has been proposed in [Nelson et al. 1997]. A method for the estimation of the ratio of LOS to multipath signal power by using statistical signal processing techniques has been discussed in [Schmid and Neubauer 2004]. The so-called SAGE algorithm provides another method of multipath detection and multipath parameter estimation. A detailed introduction of this approach can be found in [LOGOTHETIS and CARLEMALM 2000] or [FLEURY et al. 1999]. Estimation of all relevant multipath parameters (delay, relative phase and amplitude) can also be achieved by using the MEDLL approach (see references listed in the section “Multipath Mitigation (Special Tracking Techniques)”).

Multipath Performance Analysis for Future GNSS Signals. During the past years, the performance of new GNSS signals, e.g. as they will appear in Galileo or the modernized GPS, has been evaluated in several papers. The author of this thesis also contributed to this topic by determining the multipath performance of the proposed Galileo signals for different multipath mitigation techniques ([IRSIGLER and EISSFELLER 2003] and [IRSIGLER et al. 2004]). Multipath performance also played a significant role during the efforts to find an optimized signal for the Galileo L1 Open Service. In this context, extensive multipath performance analyses have been carried out, especially at the Institute of Geodesy and Navigation at the University FAF Munich. The results of these analyses have been published in several papers (e.g. [HEIN et al. 2004], [AVILA-RODRIGUEZ et al. 2004] or [AVILA-RODRIGUEZ et al. 2005]). Other work on this subject contains more general investigations on the BOC modulation scheme and its multipath performance (e.g. [BETZ 2002], [BETZ and GOLDSTEIN 2002] or [RIES et al. 2002]), some considerations on the future GPS civil signal on L2 ([VAN DIERENDONCK et al. 1998], the synergy of GPS L2/L5 observations for multipath mitigation ([WEILL 2003b]) or the development of suitable tracking techniques for BOC signals ([JULIEN at al. 2004] or [GARIN 2005]). In order to optimize the multipath performance for all types of signals, a method to determine the optimum discriminator function has been proposed in [PANY et al. 2005] and – as already mentioned above - lower multipath bounds for the proposed modernized GPS signals are presented in [WEILL 2002] and [WEILL 2003].

1.4 Objectives and Structure of Thesis

Since most of the knowledge about multipath can be found in conference papers, theses and journal articles only, one objective of this thesis is to summarize these multipath-related activities and to provide a self-contained work on this subject. The thesis can be divided into two major parts, covering aspects of multipath propagation, multipath mitigation, multipath performance analysis (part 1, chapters 2-5) and multipath monitoring (part 2, chapters 6 and 7).

Part I. After some introductory notes on current and future GNSS systems, regional systems and augmentation systems in chapter 2 (covering not only Galileo and the Modernized GPS but also the modernization efforts for GLONASS or the development of the Japanese QZSS), the most important aspects and effects related to multipath propagation are summarized in chapter 3. It deals with different “types” of multipath propagation (e.g. specular multipath vs. diffuse multipath) and discusses the most important characteristics of multipath signals such as path delay, relative phase and relative amplitude (referred to as multipath parameters) or polarization. Depending on the multipath parameters, multipath commonly causes periodic signal variations. The frequency of these variations can be expressed as a function of the signal’s and reflector’s azimuth and elevation angles. Such aspects are also discussed in chapter 3. A summary of the most important and common multipath mitigation techniques is given in chapter 4. Although this chapter focuses on receiver-internal approaches, other approaches such as the use of an array of closely spaced antennas or special multipath-limiting antennas (MLAs) are discussed as well.

Chapter 5 contains detailed multipath performance analyses for signals of the (modernized) GPS and Galileo. These analyses consider some of the multipath mitigation techniques discussed in chapter 4. The analyses are not restricted to the pure computation of multipath error envelopes - a common approach to characterize the multipath performance of a given signal/receiver combination - but rather base on a new methodology to estimate typical and meaningful multipath errors. This methodology makes use of multipath error envelopes that are scaled in a suitable way to account for different multipath environments. It will be shown that typical (mean) multipath errors can be derived from these scaled envelopes by computation of the envelope's running average. The objective is to provide an efficient way to compute typical multipath errors that can serve as an input for GNSS error budgets.

Part II. The second part of this document is dedicated to the field of multipath monitoring. After an overview of current multipath monitoring approaches in chapter 6, a completely new approach for real-time multipath monitoring by processing multi-correlator observations will be introduced. So far, multi-correlator observations have primarily been used for the detection of satellite signal failures ("Evil Waveforms") and for some special multipath mitigation techniques. The proposed multipath monitoring scheme makes use of the same basic observations as used for the detection of Evil Waveforms and utilizes them for the purposes of real-time multipath monitoring. The objective is to provide the user with instant information whether or not a signal is affected by multipath. The basic monitoring concept is presented in chapter 7. Moreover, the proposed monitoring scheme has been implemented in the form of a Matlab-based software called RTMM (Real-Time Multipath Monitor) which has been used to verify the monitoring approach and to determine its sensitivity. Further topics are discussions on how the monitoring approach can be further optimized or a detailed discussion on the benefits and the shortcomings of this approach.

Part III. The final part of this thesis contains further information on special topics of this thesis in the form of several appendices. Appendix A provides the necessary formulas to determine the theoretical noise variances of different types of test metrics that are used for the implementation of the real-time multipath monitor introduced in chapter 7 (based on the shape of the underlying correlation function). Appendix B contains the derivation of an empirical function to determine the monitoring sensitivity of the proposed real-time multipath monitor and appendix C provides some basics on wavelet analysis, which can be used for multipath detection and mitigation. The remaining appendices contain lists of references, figures, tables and acronyms.

Part I.

Multipath Propagation, Mitigation and Error Analyses

The first part of this thesis commences with a brief overview on current and future satellite-based navigation systems, not only including global systems such as GPS, GLONASS and Galileo but also regional systems and satellite-based augmentation systems (chapter 2). Chapter 3 covers the most important aspects of multipath propagation, discussing different types of multipath signals and its typical characteristics such as periodic signal variations whose frequency depends on the actual satellite-antenna-reflector geometry. Chapter 4 provides a summary of the most common multipath mitigation techniques with a special focus on receiver-internal approaches. Moreover, multipath mitigation approaches such as using arrays of closely spaced antennas or multipath-limiting antennas are discussed as well. Chapter 5 contains multipath performance analyses for signals of the (modernized) GPS and Galileo considering some of the multipath mitigation techniques discussed in chapter 4. The analyses are based on a new methodology to determine typical and meaningful multipath errors making use of multipath error envelopes which are scaled in a suitable way to account for different multipath environments. It will be shown that typical (mean) multipath errors can be derived from these scaled envelopes by computation of the envelope's running average.

2. Satellite-Based Navigation Systems

Prior to the development of GPS, the Navy Navigation Satellite System (NNSS, better known as TRANSIT) became the first GNSS ever. It was developed by the U.S. Navy in the late 1950s, became operational in 1964 and accessible to civil users in 1967. TRANSIT was a hyperbolic positioning system and based on the computation of range differences between the user and two satellites. These range differences were derived from Doppler observations, or – to be more specific – from integrated Doppler counts. TRANSIT was being operational until the mid 1990s. Today's operational GNSS, the GPS and the Russian GLONASS can be deemed as successors of the TRANSIT system.

This chapter provides a brief overview on the current operational status of GPS and GLONASS, the modernization plans for these systems and the development status of the other satellite navigation systems which are currently being developed (especially the European Galileo system). Additionally, current and planned regional satellite navigation systems as well as satellite-based augmentation systems are also discussed. Since many of the discussed systems are currently under development, the information (especially the dates) provided in the following sections may not be entirely valid by the time this thesis is published. The related information has been collected in January 2008.

2.1 Global Systems

2.1.1 Galileo

After GPS and GLONASS, the European satellite navigation system Galileo which is currently being developed will be the third operational GNSS. Galileo provides a highly accurate global positioning service and is – according to the current SIS ICD – interoperable with GPS and GLONASS. After having completed the definition phase of Galileo in 2003, the development and in-orbit validation phase has been initiated consisting of the two Galileo System Test Bed programs (GSTB-V1 and GSTB-V2) and the in-orbit validation phase (IOV). As part of the GSTB-V2 program whose main objectives are to secure the Galileo frequency filings, to validate key technologies (e.g. related to the operation of atomic clocks) and to carry out experiments using new navigation signals, the first Galileo test satellite Giove-A was launched successfully on December 28th 2005. The launch of Giove-B, the second Galileo test satellite, is planned for 2008. During the so-called IOV phase, a reduced constellation of four satellites will be available before the constellation will be completed during the full deployment phase. The full Galileo constellation is scheduled to be available approximately by 2013.

After the full deployment phase, the Galileo system will consist of 30 satellites (27 operational satellites and 3 spares) evenly distributed in three orbital planes. The Galileo satellites will be launched into MEO orbits with an altitude of approximately 23.000 km and an inclination of 56°. One plane contains 9 evenly spaced satellites (plus one spare satellite). This type of constellation is called a Walker 27/3/1 constellation and ensures a good global coverage between latitudes up to ±75°.

Galileo provides four navigation services and one service to support search and rescue operations. These services cover a wide range of user needs and are provided worldwide and independently from other systems. They can be characterized as follows (see also [EUROPEAN SPACE AGENCY 2007a]):

- The Open Service (OS) is based on open signals which are accessible free of user charges. It provides position and timing performance that is competitive with other GNSS systems.
- The Safety of Life Service (SoL) improves the Open Service performance by providing timely warnings to the user when it fails to meet certain margins of accuracy (provision of integrity information).
- The Commercial Service (CS) provides access to additional signals with higher data rates for accuracy improvement. The service will be charged but most probably a service guarantee will be provided.
- The Public Regulated Service (PRS) provides position and timing information only to specific users requiring a high continuity of service. Two PRS navigation signals will be available.
- The Search and Rescue Service (SAR) globally broadcasts alert messages received from distress emitting beacons. It will contribute to enhance the performance of the international COSPAS-SARSAT search and rescue system with which it will be interoperable.

Galileo signals are transmitted on four frequency bands, namely on E5a, E5b, E6 and E1 (which is in fact identical to L1). The corresponding carrier frequencies are 1176.450 MHz (E5a), 1207.140 MHz (E5b), 1191.795 MHz (E5=E5a+E5b), 1278.750 MHz (E6) and 1575.420 MHz (E1), respectively. The transmitted signals have the following characteristics (adopted from [EUROPEAN SPACE AGENCY 2006]):

- **E1 signal**. E1 is an open access signal transmitted in the L1 band comprising a data channel E1-B and a pilot (or data-less) channel E1-C. It has unencrypted ranging codes and navigation data accessible to all users. The E1-B data stream also contains unencrypted integrity messages and encrypted commercial data. Current baseline (as of July 2007) for the OS signal on E1 is the use of an MBOC(6,1,1/11) modulation (Multiplexed Binary Offset Carrier). The E1 frequency band also contains a PRS signal (E1-A) for which the $BOC_{cos}(15,2.5)$ is foreseen.

- **E6 signal**. E6 is a commercial access signal transmitted in the E6 band including a data channel E6-B and a pilot (or data-less) channel E6-C. BPSK(5) will presumably be used as modulation scheme. The signal's ranging codes and data are encrypted. As it is the case for E1, the E6 frequency band also contains a PRS signal component (E6-A) for which a $BOC_{cos}(10,5)$ is foreseen.

- **E5a signal**. E5a is an open access signal transmitted in the E5 band including a data channel and a pilot (or data-less) channel. The E5a signal has unencrypted ranging codes and navigation data, which are accessible by all users. It transmits the basic data to support navigation and timing functions using a relatively low data rate that enables more robust data demodulation.

- **E5b signal**. E5b is an open access signal transmitted in the E5 band also including a data channel and a pilot (or data-less) channel. It has unencrypted ranging codes and navigation data accessible to all users. The E5b data stream also contains unencrypted integrity messages and encrypted commercial data.

- **E5 (composite) signal**. The E5a and E5b signals which both make use of the BPSK(10) modulation scheme are modulated onto a single E5 carrier using a technique known as AltBOC (Alternative BOC, the transmitted signal will be an AltBOC(15,10)). The composite of the E5a and E5b signals is denoted as E5 signal and can be processed as a single large bandwidth signal with a suitable user receiver implementation.

2.1.2 Current and Modernized GPS

The successor of TRANSIT, the *Global Positioning System* (GPS) has been developed from 1973 on. Originally designed to serve military needs, the system has been made available for civilian use during the 1980s and has hence turned into a dual-use system. Important milestones were the deployment of the first experimental satellites in 1978 and the full operational capability that was reached in 1995.

The baseline satellite constellation consists of 24 operational and 3 spare space vehicles positioned in six nearly circular orbital planes with a radius of approximately 26.560km (MEO constellation). Each orbital plane contains 4 satellites (without considering the spare satellites). The orbits are inclined by ~55° relative to the equatorial plane. The constellation repeats every half sidereal day (~11h 58m) so that after one sidereal day (~23h 56m) a stationary user on the ground would see the same spatial distribution of the satellites.

Until the end of 2005, the GPS provided two navigation services, the standard positioning service (SPS) and the precise positioning service (PPS). The SPS is provided by a BPSK(1) modulation on L1, also known as the coarse/acquisition (C/A) code modulated onto a carrier with a frequency of 1575.42 MHz. The PPS is implemented in the form of the (encrypted) P(Y) code (BPSK(10) modulation) on L1 and L2 (f_2=1227.6 MHz). With the launch of the first operational Block IIR-M satellite in December 2005, the modernization of GPS has begun. The GPS modernization plans are related to new generations of navigation satellites. They can be categorized as follows (see also overview provided in [Hein et al. 2007]):

- **Block IIR-M satellites**. These satellites provide a second civil signal on L2 (called L2C). The signal uses the same BPSK(1) modulation as the C/A code on L1. The current GPS satellites will have been replaced by the IIR-Ms by approximately 2012. For military purposes, a BOC(10,5) will be added on L1 and L2. This signal is called M-Code.
- **Block IIF satellites**. These satellites provide a third civil signal on L5, where a QPSK(10) is modulated on the L5 carrier (f_{L5}=1176.45 MHz, the L5 frequency band corresponds with Galileo E5a). This modernization step is expected to be finished approximately 2015.
- **Block III satellites**. These satellites offer increased anti-jam power, security, accuracy and availability. They will transmit a fourth civil signal on L1 (called L1C). Current baseline is an MBOC(6,1,1/11) to ensure full compatibility and interoperability with the Galileo E1 OS signal (see previous section). The fourth civil signal will be fully available by approximately 2020.

2.1.3 Current and Modernized GLONASS

As from the early 1980s, the former Soviet Union began to deploy the first GLONASS satellites. Designed primarily for military purposes, the Russian counterpart to GPS became fully operational in 1995. Only at this time, the nominal number of 24 operational satellites was reached. Due to a lack of funding and relatively short satellite lifetimes of only 3-4.5 years, the GLONASS constellation could not be maintained and the number of operational satellites decreased to only 7 in 2001. Forced by a GLONASS modernization program, the number of operational satellites could be increased to 13 in early 2006. Full global operational capabilities are expected to be provided by 2009 when the nominal number of 24 operational satellites will presumably be available ([Revnivykh 2006]). By that time, the GLONASS performance is expected to be comparable to that of GPS and Galileo. To achieve this, the GLONASS modernization plan includes modernized satellites transmitting new navigation signals, modernization and extension of the existing ground segment architecture as well as the use of optimized methods and algorithms for time synchronization or orbit determination ([Revnivykh 2006]). Core of the space segment modernization will be a new generation of GLONASS satellites, named GLONASS-M and GLONASS-K.

The GLONASS-M satellites have an expected lifetime of 7 years and provide two civil signals at the frequency bands L1 and L2. Furthermore, the stability of the cesium clocks onboard the satellites could be increased significantly and additional information was added to the navigation message (e.g. difference between GPS and GLONASS time scale or navigation data age). According to [Polischuk et al. 2002], the navigation accuracy can be doubled by these measures. The first GLONASS-M satellite was launched in 2003. In contrast to the GLONASS-M satellite, the GLONASS-K satellites have an expected lifetime of ca. 10 years but only 50% of the mass of their GLONASS-M counterparts. As from 2008, GLONASS-K satellites will provide a third civil signal. Due to their decreased size and weight, up to 6 satellites can be launched simultaneously ([Polischuk et al. 2002]).

As already mentioned, the nominal GLONASS constellation consists of 24 satellites which are distributed in three orbital planes. 8 space vehicles are evenly distributed within one orbital plane resulting in a nominal spacing of 45° between adjacent satellites. The orbital planes are inclined by 64.8° with respect to the equatorial plane. With an orbital altitude of about 19.100 km and a circular orbit (e=0), the period of revolution is ~11h 15m 44s or 8/17 of a sidereal day. For an observer on the ground, the GLONASS constellation repeats after 17 orbital periods or 7d 23h 27m 28s ([Coordination Scientific Information Center 2002]). Despite the GLONASS modernization plans, the current constellation status (15 operational satellites by the beginning of 2008) is significantly poorer than intended.

2.1.4 COMPASS

The People’s Republic of China is also developing its own global satellite navigation system. The COMPASS constellation will use both geostationary and non-geostationary satellites. The five geostationary satellites are planned to be located at longitudes of 58.75°E, 80°E, 110.5°E, 140°E and 160°E. Besides the 5 GEO satellites, 27 MEO and 3 IGSO satellites will be put into orbit resulting in an overall number of 35 satellites. The non-geostationary orbits will have an inclination of 55° and a semi-major axis of about 27.840 km.

Between 2000 and 2003, three geostationary COMPASS test satellites (called Beidou 1A, 1B and 1C) were launched. A fourth geostationary satellite (Beidou 1D) was launched early in 2007. Since these satellites use a geostationary orbit, they virtually form a straight line in the sky (as seen from a user’s perspective on the ground). Although it is possible to use such a constellation for positioning purposes within a limited service region (the system covers China, parts of Russia, India, Japan, Indonesia, Australia and the Antarctica so far), the obtained latitude estimate is rather inaccurate. On the other hand, the longitudinal estimate is much more accurate. This system of geostationary satellites was called “Beidou”. It can be seen as predecessor of the COMPASS system and was thought to serve mainly military purposes (some assumptions on Beidou’s military capabilities can be found in [Forden 2004]).

In 2007, China began to expand the “Beidou” system into a GNSS by launching the first non-geostationary satellite Compass-M1 (MEO). In a similar way as GPS, GLONASS and Galileo, COMPASS will provide different navigation services. They are currently called “Open Service” (for commercial applications) and “Authorized Service”. To implement these services, China has filed navigation signals on E5, E6 and E1/L1.

2.2 Regional Systems

2.2.1 QZSS

The Japanese *Quasi-Zenith Satellite System* (QZSS) is currently being developed mainly to increase the availability of navigation and communication services in urban areas where signal masking due to high buildings may be an issue. It can be deemed as an augmentation system to GPS (and Galileo), providing signals from satellites that achieve high elevation angles for most of their passes.

The space segment of QZSS will consist of three satellites located in three geosynchronous orbits. The three orbital planes are inclined by 45°, separated by 120°and have an eccentricity of 0.099 ([SAWABE 2006]). These orbital parameters result in an asymmetric 8-shaped ground track covering the service area. They ensure that at least one satellite with a very high elevation is available over Japan (one satellite typically operates more than 12 hours a day with an elevation of >70°). This characteristic explains the term “quasi-zenith” ([PETROVSKI 2003]). Although designed to provide the highest elevations for Japan, QZSS will also cover large parts of Eastern Asia and the Oceania region.

Once operational, QZSS will transmit navigation signals on three frequency bands (L1, L2 and L5). The signals are designed to be compatible and interoperable to those of GPS and Galileo. During the test phase of QZSS, an experimental signal on E6 is foreseen. Similar to the current and future satellite-based augmentation systems which will be introduced in section 2.3, QZSS will transmit correction data and integrity information for the GPS. The launch of the first QZSS satellite is planned for 2008 ([SAWABE 2006]).

2.2.2 IRNSS

The constellation of the *Indian Radio Navigation Satellite System* (IRNSS) consists of 7 satellites. Three satellites are geostationary, located at 34°E, 83°E and 132°E and form the Indian satellite augmentation system known as GAGAN (see next section). The remaining 4 satellites are geosynchronous with equatorial crossings at 55°E and 112°E, respectively. Their inclination is 29°. The IRNSS is planned to be compatible with other GNSS as well as with other satellite-based augmentation systems in that region. It could reach its operational status in 2009 ([HEIN et al. 2007]).

2.3 Satellite-Based Augmentation Systems (SBAS)

Since the current operational GNSS neither provide sufficient accuracy nor the required degree of integrity for some critical applications (e.g. airborne applications), additional (geostationary) satellites can be used for augmentation purposes. Especially integrity is an important issue for airborne applications due to the short time-to-alarm requirement of six seconds. SBAS is an implementation of the differential GNSS concept which can provide the user with differential corrections which in turn improves the positioning accuracy.

The basic principle is the same for all SBAS currently under development. The GPS satellites are constantly monitored by a large number of monitoring stations distributed across the service area. All collected information is then transferred to one (or more) control and processing facilities that derive integrity information, compute pseudo-range differential corrections for each satellite, determine ionospheric delays and generate the ephemeris data for the geostationary satellites. Based on this information, an SBAS navigation message can be generated that is then up-linked to the SBAS satellites together with a corresponding ranging signal. The geostationary satellites downlink the signal at the L1 frequency band using a modulation and coding scheme similar to GPS ([EUROPEAN SPACE AGENCY 2007b],[TORAN-MARTI and VENTURA-TRAVESET 2005]). The SBAS signal can be processed by any receiver that supports the demodulation of the SBAS navigation message.

2.3.1 EGNOS

The *European Geostationary Navigation Overlay Service* (EGNOS) augments the two operational satellite navigation systems GPS and GLONASS. The ground segment consists of 34 Ranging and Integrity Monitoring Stations (RIMS) and four Mission Control Centers (MCCs). Several up-link stations (so called Navigation Land Earth Stations, NLES) are available to forward the SBAS signals to three geostationary satellites that form the space segment of EGNOS. The system uses two INMARSAT-3 satellites - one over the eastern part of the Atlantic (INMARSAT-3 AOR-E), the other over the Indian Ocean (IOR-W) - and ARTEMIS which is located over the central part of Africa. In contrast to the GPS and GLONASS satellites, the EGNOS satellites do not use signal generators but transponders to down-link the signal back to the ground ([EUROPEAN SPACE AGENCY 2007b]).

2.3.2 WAAS

The *Wide Area Augmentation System* (WAAS) has been developed by the U.S Federal Aviation Administration (FAA) and the U.S. Department of Transportation (DOT). It became operational for general aviation in 2003 and has the same general structure as the European EGNOS. It consists of 25 Ground Reference Stations (GRS), a Wide Area Master Station (WMS) and a Ground Uplink System (GUS). At present, the ground segment consists of two geostationary INMARSAT-3 satellites (POR, located over the Pacific Ocean and AOR-W), located over the western Atlantic Ocean. In late 2005, two additional geostationary satellites with WAAS payloads were launched (PanAmSat Galaxy XV and Telesat Anik F1R) increasing the number of WAAS satellites to four ([FEDERAL AVIATION ADMINISTRATION 2007]). The satellites are located in slots at longitudes of 54°W, 107°W, 133°W and 178°E.

2.3.3 MSAS

MSAS (*Multifunction Transport Satellite Space-based Augmentation System*) is the Japanese counterpart of WAAS and EGNOS. It has been developed by the Japanese Meteorological Agency and the Japanese Ministry of Transport. The MSAS satellites are a combination of weather and communication satellites and will be located in a geostationary orbit centered around a longitude of 140°E covering Japan and Australia. In late 1999, the launch of the first MSAS satellite (MTSAT-1) failed. In February 2005, MTSAT-1R was launched successfully and is currently operational. In February 2006, MTSAT-1R was followed by MTSAT-2 which is not operational yet ([AUSTRALIAN GOVERNMENT 2007]).

2.3.4 GAGAN

The Airports Authority of India (AAI) and the Indian Space Research Organization (ISRO) are jointly developing the Indian *GPS And Geo Augmented Navigation* (GAGAN). The GAGAN system will have the same basic architecture as the other SBAS systems mentioned so far and will also use geostationary satellites to provide ranging and correction data ([KIBE 2006]). The system is still under development and will be further expanded to form the future IRNSS. Full operation is expected for the year 2009.

The listing of current and future satellite-based navigation aids provided in this chapter gives an impression how many of such systems will be available in the near future. Whatever system is used by a specific user, the corresponding navigation signals are always susceptible to the sources of signal degradation introduced in chapter 1. In this context, multipath is one possible error source that cannot be excluded from the outset, that cannot be eliminated completely and, as far as the overall error budget is concerned, can become the largest contribution to the overall ranging error. For this reason, multipath performance was a major design driver for the past and present signal definition activities for Galileo. Against this background, it is important to understand the characteristics of multipath signals and to understand how multipath affects the process of signal tracking within a receiver. Such aspects are discussed in the following chapter.

3. Aspects of Multipath Propagation

3.1 Multipath Propagation Basics

3.1.1 Signal Model and Multipath Parameters

To characterize the basic influence of multipath, a rather simple signal model can be used. In the presence of multipath, the LOS signal component is superimposed by N multipath signals. In general, the actual number of multipath signals is unknown. In case that A denotes the amplitude, τ_0 the propagation time of the direct path, θ_0 the carrier phase and $\omega_0=2\pi f$ the angular frequency including the Doppler shift $\Delta\omega_0$ for the direct signal component (f is the carrier frequency, ranging and data codes are denoted by p), the compound signal $s(t)$ can be expressed as follows:

$$s(t) = \underbrace{Ap(t-\tau_0)\cos(\omega_0 t+\theta_0)}_{\text{Direct Signal (LOS)}} + \underbrace{A\sum_{k=1}^{N}\alpha_k p(t-\tau_0-\tau_k)\cos[\omega_0 t+\theta_0+\Delta\Phi_{M,k}+(\Delta\omega_k-\Delta\omega_0)t]}_{\text{N Multipath Signals}} \tag{3}$$

Equation (3) represents the signal that reaches the antenna and is then processed by the receiver. The signal contains four **multipath parameters**:

- Multipath relative amplitude $A\alpha_k$ (α_k is the coefficient of reflection characterizing the signal attenuation due to the reflection process and the antenna gain pattern)
- Multipath delay τ_k [s] (time shift between the direct signal component and the k^{th} multipath signal; when expressed in [m], τ_k is called “geometric path delay”)
- Multipath relative phase $\Delta\Phi_{M,k}$ (phase shift between the direct signal and the k^{th} multipath component)
- Doppler difference $\Delta\omega_k$-$\Delta\omega_0$ between direct and k^{th} multipath signal (determines the multipath phase rate, also called “fading frequency” or “fading bandwidth” ([VAN NEE 1992])

Together with a variety of other signal and receiver parameters (see section 1.2), these multipath parameters determine how code and phase observations are influenced by multipath propagation. A detailed analysis of how multipath signals affect the tracking loops of a GNSS receiver can be found in section 3.2. More general effects are discussed in the following sections.

3.1.2 Superimposition of Direct and Multipath Signal

The superimposition of the direct signal component and one or several multipath signals can be visualized by means of vector diagrams. In such illustrations, the compound signal is the sum of two or more vectors representing the distinct signal components. The length of each vector is a measure for the amplitude of the corresponding signal component.

Figure 3-1 illustrates a vector diagram for the superimposition of a direct signal with one single multipath component. The amplitudes for the direct signal, the multipath signal and the compound signal are denoted by A, αA and C, respectively. The phase difference between the direct signal and the multipath signal (multipath relative phase) is represented by the angle $\Delta\Phi_M$. The angle between the direct signal and the compound signal can be interpreted as a phase error ϕ_C due to the influence of multipath.

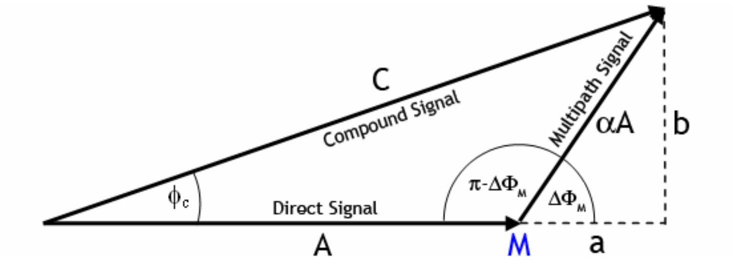

Figure 3-1: Amplitudes of signal components, multipath relative phase and resulting phase error in the presence of one multipath signal.

Due to the constant motion of the satellites, the multipath relative phase $\Delta\Phi_M$ changes with time (in fact, the multipath relative phase can be expressed as a function of the satellite's azimuth and elevation angle, see section 3.1.4 for details). As a result, the vector representing the multipath signal undergoes a circular motion around *M*, causing the phase error ϕ_C to show periodic variations as well. Figure 3-1 allows the derivation of the **phase error** ϕ_C as a function of the multipath relative phase $\Delta\Phi_M$ and the amplitude *C* of the compound signal that is processed by the receiver. The resulting phase error ϕ_C can be expressed as a function of the triangle elements *A*, *a* and *b* :

$$\tan\phi_C = \frac{b}{A+a} \tag{4}$$

The multipath relative phase $\Delta\Phi_M$ can be expressed as

$$\sin\Delta\Phi_M = \frac{b}{\alpha A} \quad \text{or} \quad \cos\Delta\Phi_M = \frac{a}{\alpha A}, \tag{5}$$

so that the distances *a* and *b* can be calculated as

$$b = \alpha A \sin\Delta\Phi_M \quad \text{and} \quad a = \alpha A \cos\Delta\Phi_M . \tag{6}$$

Inserting equation (6) into equation (4) leads to the desired phase error ϕ_C:

$$\begin{gathered}\tan\phi_C = \frac{b}{A+a} = \frac{\alpha A \sin\Delta\Phi_M}{A+\alpha A\cos\Delta\Phi_M} = \frac{\alpha A\sin\Delta\Phi_M}{A(1+\alpha\cos\Delta\Phi_M)} = \frac{\alpha\sin\Delta\Phi_M}{1+\alpha\cos\Delta\Phi_M} \\ \phi_C = \arctan\left(\frac{\alpha\sin\Delta\Phi_M}{1+\alpha\cos\Delta\Phi_M}\right)\end{gathered} \tag{7}$$

Equation (7) can be extended to the case where more than one multipath signal is present. Assuming *k* multipath components, the resulting phase error can be expressed as follows:

$$\phi_C = \arctan\left(\frac{\sum_k \alpha_k \sin\Delta\Phi_{M,k}}{1+\sum_k \alpha_k \cos\Delta\Phi_{M,k}}\right) \tag{8}$$

The **amplitude of the compound signal** *C* can be derived by applying Pythagoras' theorem:

$$C^2 = (A+a)^2 + b^2 \tag{9}$$

Inserting equation (6) leads directly to the amplitude of the compound signal *C*, which can be expressed as follows:

$$
\begin{aligned}
C^2 &= (A + \alpha A \cos\Delta\Phi_M)^2 + \alpha^2 A^2 \sin^2 \Delta\Phi_M \\
&= A^2 + 2\alpha A^2 \cos\Delta\Phi_M + \alpha^2 A^2 \cos^2 \Delta\Phi_M{}^2 + \alpha^2 A^2 \sin^2 \Delta\Phi_M \\
&= A^2 + 2\alpha A^2 \cos\Delta\Phi_M + \alpha^2 A^2 \\
&= A^2 (1 + 2\alpha \cos\Delta\Phi_M + \alpha^2) \\
C &= A\sqrt{1 + 2\alpha \cos\Delta\Phi_M + \alpha^2}
\end{aligned}
\tag{10}
$$

Equation (10) can be also extended to the case where more than one multipath signal is present. Assuming *k* multipath components, the resulting phase error can be expressed as

$$
C = A\sqrt{\left(1 + \sum_k \alpha_k \cos\Delta\Phi_{M,k}\right)^2 + \left(\sum_k \alpha_k \sin\Delta\Phi_{M,k}\right)^2}
\tag{11}
$$

Figure 3-2 illustrates equations (7) and (10) as a function of the multipath relative phase $\Delta\Phi_M$. Four different values of α have been assumed in order to examine the dependency of the phase error and the resulting amplitude on the coefficient of reflection.

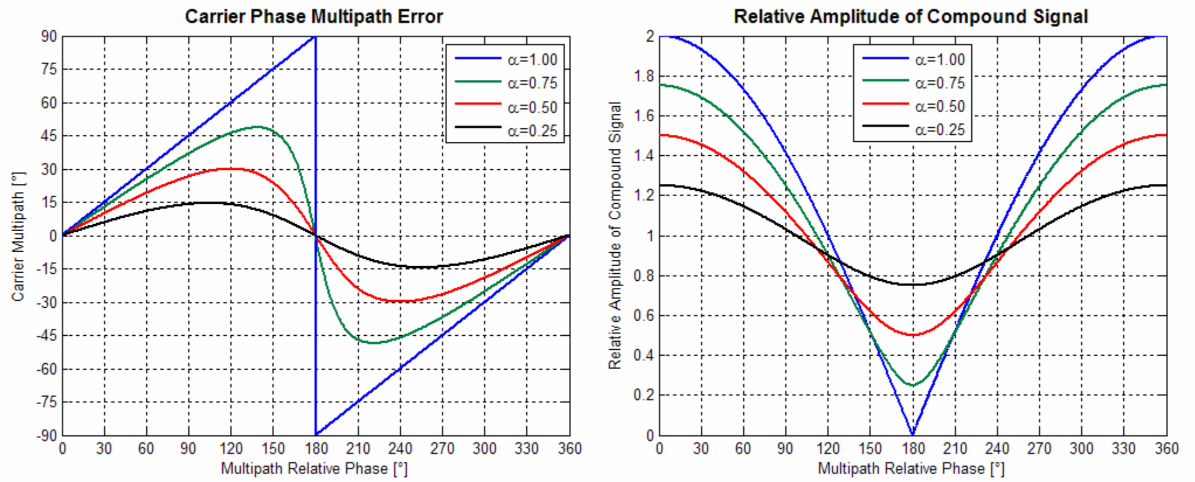

Figure 3-2: Carrier phase multipath error and relative amplitude of compound signal in the presence of one single multipath signal as a function of the multipath relative phase.

The multipath induced carrier phase error and the relative amplitude of the compound signal strongly depend on the multipath relative phase. The largest phase errors occur for a relative phase of 180° if the multipath signal is not attenuated at all (α=1.0). For these values, the multipath error reaches 90°, corresponding to one fourth of the underlying carrier wavelength ($\lambda/4$). This leads to a maximum carrier multipath error of ~4.8cm for the L1 carrier, a value that is often cited in various publications. It should be noted, however, that this maximum multipath error is only valid in the presence of one single multipath signal. For lower values of α (high signal attenuation), the multipath error does not vary as strong as in case of low signal attenuation. The amplitude of the compound signal has a maximum at $\Delta\Phi_M$=0° and a minimum at $\Delta\Phi_M$=180°. The absolute value of the amplitude at these points depends on the coefficient of reflection α. Depending on the actual multipath relative phase, the amplitude of the compound signal can be either larger or smaller than that of the direct signal component - an effect that some statistical channel models describing multipath propagation under realistic conditions are also accounting for (e.g. [JAHN 1996]). The variation of the relative amplitude of the compound signal diminishes with larger signal attenuation (smaller values for α).

3.1.3 Types of Multipath Signals

3.1.3.1 Satellite vs. Receiver Multipath

Signal reflections do not necessarily occur only in the vicinity of the receiver, they may also occur near the transmit unit. In this context, the terms “satellite multipath” (due to reflections at parts of the satellite) and “receiver multipath” (due to reflecting surfaces near the receiving antenna) can be found in the literature ([GEORGIADOU and KLEUSBERG 1988]). In contrast to receiver multipath, the effect of satellite multipath is expected to be the same for two receivers when using short baselines. Therefore, it can be eliminated by means of differential techniques ([GEORGIADOU and KLEUSBERG 1988]).

In general, the effects of satellite multipath are limited due to the limited size of the space vehicle. However, the situation is different and more complex if pseudolites instead of orbiting satellites are considered. Depending on the local environment where the pseudolite is located, “satellite (or pseudolite) multipath” can be caused by any reflector in the vicinity of the pseudolite. Furthermore, if the signal is transmitted with high power, the multipath signals are expected to be rather strong. Another characteristic of “pseudolite multipath” is that since the pseudolites do not move, there is no varying multipath relative phase between the direct signal and the multipath component(s). This type of multipath is called “Fixed-Offset” multipath.

3.1.3.2 Time-Varying vs. Fixed-Offset Multipath

In equation (3), the term $\Delta\Phi_{M,k}+(\Delta\omega_k-\Delta\omega_0)t$ can be interpreted as an initial phase difference between the direct signal and the k^{th} multipath component plus a time-varying phase contribution due to the multipath relative Doppler shift. This term leads to the circular motion of the multipath vector around M as illustrated in Figure 3-1. The angular velocity of this motion is determined by the Doppler difference $\Delta\omega_k-\Delta\omega_0$ which in turn determines the frequency of the occurring multipath variations. Such variations can be observed in various GNSS observables such as differenced code or carrier observations, code minus carrier residuals or SNR recordings. Figure 3-3 illustrates an example of time-varying multipath on code minus carrier residuals as obtained from a GPS hardware simulator. As soon as the multipath signal was activated, a sinusoidal behavior became visible in the CMC residuals.

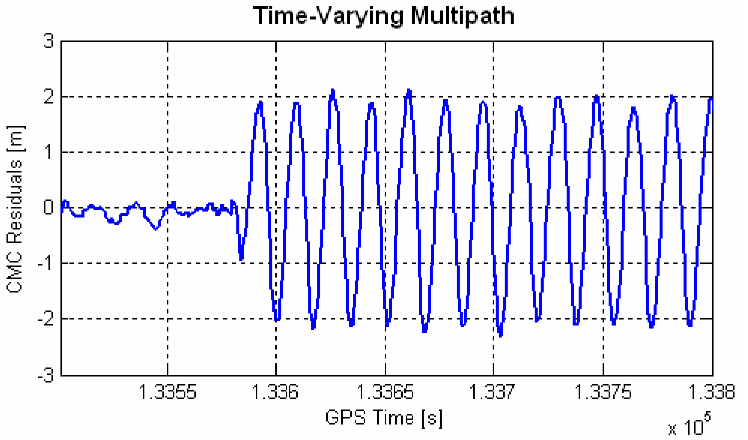

Figure 3-3: Effects of time-varying multipath on code minus carrier residuals.

In contrast to time-varying multipath, fixed-offset multipath is characterized by a time-invariant multipath relative phase, i.e. the multipath relative phase has a constant value of $\Delta\Phi_{M,k}$ and the term $\Delta\omega_k-\Delta\omega_0$ becomes zero (or constant as well). Due to the static behavior of the multipath relative phase, GNSS observations will not show periodic signal variations but they are biased instead. The actual bias only depends on the term $\Delta\Phi_{M,k}$ that can be related to the geometric path delay. Figure 3-4 illustrates the effects of fixed-offset multipath on code minus carrier residuals as obtained from a GPS hardware simulator. The simulated path delays of 10, 20 and 30m correspond to (constant) multipath relative phases of approximately 198°, 36° and 234°, respectively (valid for the L1 carrier).

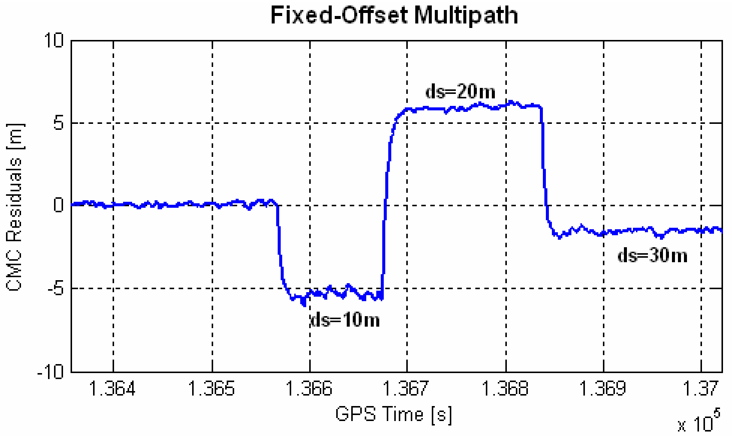

Figure 3-4: Effects of fixed-offset multipath on code minus carrier residuals.

Fixed-offset multipath can be deemed as a borderline case of the time-variant multipath case. If the frequency of the multipath variations becomes very low and approaches a value of zero, the sinusoidal appearance turns into a fixed-offset-like behavior.

The frequencies of multipath variations (i.e. the term $\Delta\omega_k$-$\Delta\omega_0$) depend on the Doppler differences between the signal components that – in turn – strongly depend on the mutual geometry of the satellite constellation and the reflector(s). In section 3.1.4, the frequencies of multipath variations that are expected to occur in a scenario with moving satellites and a static receiver will be derived.

3.1.3.3 Specular Multipath vs. Diffuse Multipath

Depending on the roughness of the reflecting surface, reflections can be termed as “specular” or “diffuse”. Specular multipath results from reflections on smooth surfaces, diffuse multipath is generated by reflectors with a rough surface. Figure 3-5 illustrates both types of reflections.

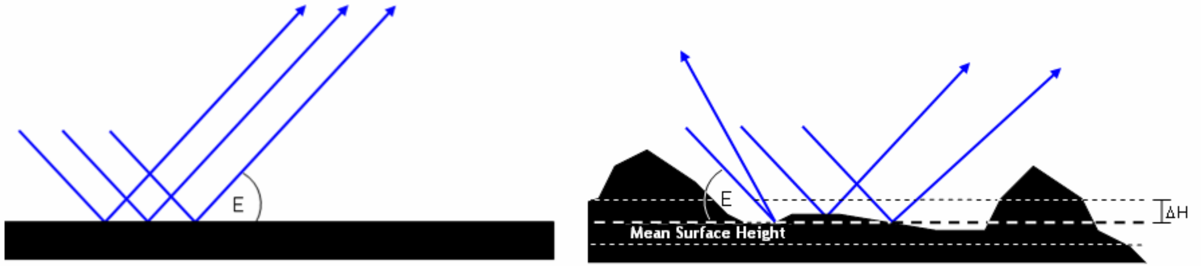

Figure 3-5: Specular reflection on a smooth surface (left illustration) vs. diffuse reflection on a rough surface (right illustration).

In case of diffuse reflection, the signal power is scattered in various directions. Furthermore, the phase relations between the signal paths illustrated in Figure 3-5 change. Thus, this type of reflection can be termed as non-directional and non-coherent. Whether or not a surface can be considered smooth or rough depends on the elevation angle E and the carrier wavelength λ. A rough surface can be characterized by the Rayleigh criterion (e.g. [BECKMANN and SPIZZICHINO 1987] or [KRAUS and SCHNEIDER 1988])

$$\Delta H \geq \frac{\lambda}{8 \sin E}, \qquad (12)$$

i.e. diffuse reflection occurs if ΔH fulfills this criterion and specular reflection can be expected if ΔH is smaller. Note that for ΔH, the standard deviation of the surface height around the local mean height within the first Fresnel zone is commonly used as input for the Rayleigh criterion ([Hannah 2001]). Figure 3-6a visualizes the Rayleigh criterion for an assumed carrier wavelength of λ=0.19m (L1). It should be noted, however, that this criterion allows only a qualitative statement about the occurrence of specular or diffuse reflections. The red curve must not be interpreted as a strict boundary between the two cases. Figure 3-6b illustrates the Rayleigh criterion for other carriers such as GPS L2, Galileo E6 and Galileo E5. Since the carrier wavelengths for L2, E6 and E5 do not differ significantly, there is almost no difference with respect to the Rayleigh criterion.

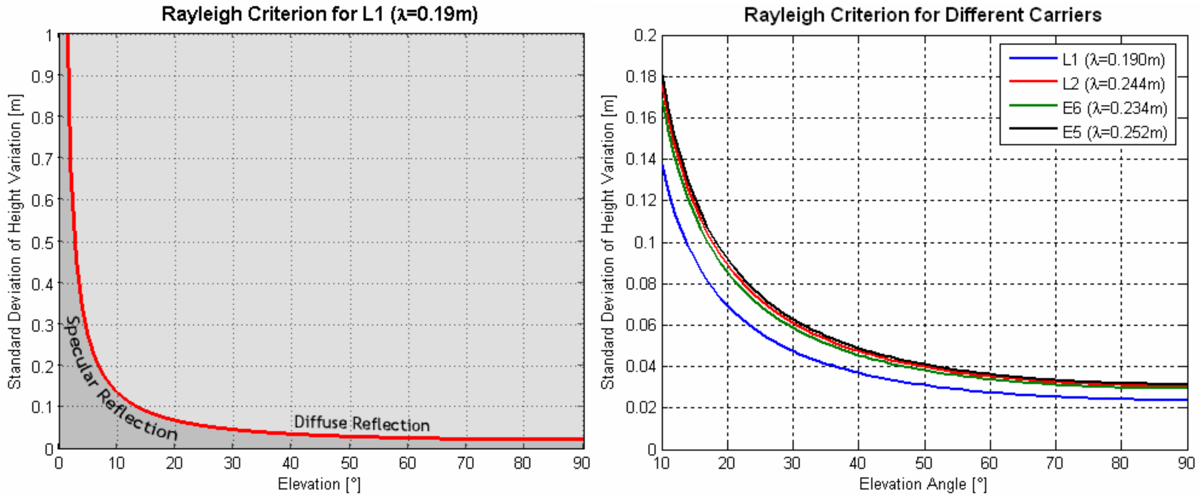

Figure 3-6: Visualization of the Rayleigh criterion for the L1 carrier and for other GNSS carriers. A similar diagram can be found in [Hannah 2001].

3.1.3.4 Diffraction

Even if the LOS signal is obstructed from view, some signal energy may reach the receiver. This is due to the fact that the signal can be diffracted at the edges of the obstructing object. This effect forces the signal to bend into the shadowed region so that despite the obstruction, the (attenuated) signal may be received in this region. Since diffracted signals deviate from their original signal path, diffraction can also be seen as a type of multipath. Figure 3-7 illustrates the geometric conditions for this type of multipath propagation.

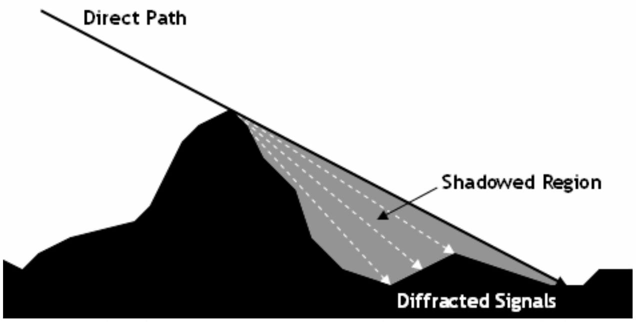

Figure 3-7: Shadowing effects resulting in signal diffraction.

In terms of Fresnel zone considerations, diffraction occurs if the first Fresnel zone is partially obstructed whereas complete signal blocking occurs if the obstructing object is larger than the first Fresnel zone (see section). A quantitative analysis of how strong diffracted signals are attenuated is given in section 3.1.5.

3.1.3.5 Hardware Induced Multipath

Multipath errors can also be induced by electronic components of a GNSS receiver (cables, amplifiers, filters or mixers). A discussion on this topic can be found in [KEITH 2000]. Figure 3-8 illustrates the possible origin of such effects.

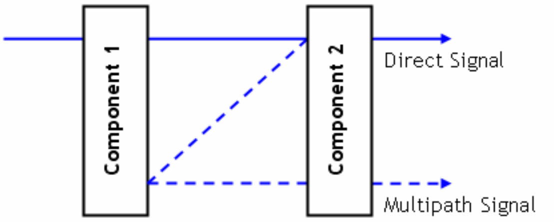

Figure 3-8: Possible origin of hardware induced multipath (adopted from [KEITH 2000]).

The signal may be reflected at the input of an electronic component back to the preceding component from where it is reflected again and possibly reaches the output of component #2. This twofold reflection creates a multipath signals that superimposes with the direct component. The reflections are caused by a so-called "impedance mismatch" between the different electronic components.

As it is the case with multipath due to reflecting objects in the vicinity of the receiver, the resulting multipath errors mainly depend on multipath delay, relative phase and relative amplitude. Relative amplitude can be expressed by means of the "voltage standing wave ratio" (VSWR) of each involved component. VSWR is a measure of how much power is reflected back from an electronic component when applying an external signal. VSWR is 1 if there is no reflection and >1 if the electronic component is a potential reflector. For the case of two electronic components (see Figure 3-8), the multipath relative amplitude can be expressed as follows ([KEITH 2000]):

$$\alpha = 20\log_{10}\left(\frac{(VSWR_1 - 1)(VSWR_2 - 1)}{(VSWR_1 + 1)(VSWR_2 + 1)}\right) \tag{13}$$

The simulations documented in [KEITH 2000] indicate that the impact of hardware induced multipath on the positioning performance is less than a meter (assuming VSWR values of 1.5 and 1.7, respectively).

3.1.4 The Frequency of Multipath Variations

Assuming a standard scenario with moving satellites and a static receiver, a sinusoidal variation of the multipath relative phase must be expected. As already shown in section 3.1.2, the phase and the amplitude of the compound signal will also reflect these variations. For a static user, the frequency f_M of the multipath variations (the "fading frequency") strongly depends on the actual satellite-reflector-receiver geometry. It can be computed as the temporal change of the multipath relative phase $\Delta\Phi_{M,k}+(\Delta\omega_k-\Delta\omega_0)t$ and can be expressed as follows:

$$f_M(t) = \frac{1}{2\pi}\cdot\frac{d(\Delta\Phi_{M,k} + (\Delta\omega_k - \Delta\omega_0)t)}{dt} = \frac{\Delta\omega_k - \Delta\omega_0}{2\pi} \tag{14}$$

The following sections provide a detailed derivation of the expected multipath frequencies for two cases, namely the general case of an arbitrary reflector position and the special case of ground multipath. The term $\Delta\Phi_{M,k}+(\Delta\omega_k-\Delta\omega_0)t$ will be replaced by $\Delta\phi_M$.

3.1.4.1 General Case: Arbitrary Reflector Position

As already described in [BECKER et al. 1994], the multipath relative phase can be expressed as a function of the satellite azimuth and elevation angles (A^S,E^S) and the reflector's azimuth and elevation angles (A_R,E_R) with respect to the local horizontal coordinate system illustrated in Figure 3-9:

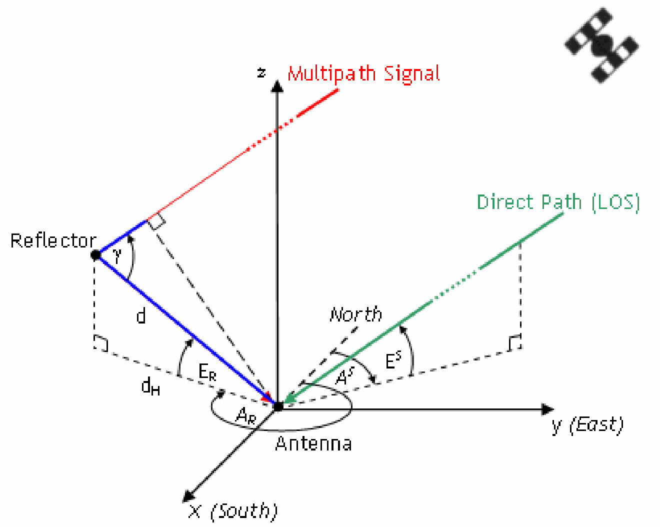

Figure 3-9: Geometric conditions for a satellite-reflector-antenna scenario.

The receiver is located in the origin of the coordinate system. With respect to this system, the satellite has the azimuth A^S and the elevation E^S. The reflector exhibits the elevation E_R and the azimuth A_R. The distance between the antenna and the reflector is denoted as d and d_H is its horizontal component. The geometric path delay ds is indicated by the blue portion of the signal path and can be expressed as follows:

$$ds(t) = d + d\cos\gamma(t) = d(1 + \cos\gamma(t)) \tag{15}$$

Due to the permanent motion of the satellites, the angle γ and the resulting geometric path delay ds are time-dependent. The multipath relative phase $\Delta\phi_M$ is a function of d and can be expressed as

$$\Delta\phi_M(t) = \frac{2\pi}{\lambda} ds(t) = \frac{2\pi}{\lambda}(d + d\cos\gamma(t)) = \frac{2\pi d}{\lambda}(1 + \cos\gamma(t)) \tag{16}$$

where λ is the carrier wavelength. The angle γ shall now be expressed as a function of the azimuth and elevation angles of the satellite and the reflector. For this purpose, the Cartesian coordinates of the satellite and the reflector are first to be expressed as a function of the corresponding azimuth and elevation angles with respect to the local horizontal coordinate system. It is assumed that the reflector azimuth and elevation do not change with time. In case that all azimuth and elevation angles are interpreted as spherical coordinates, the Cartesian coordinates of the satellite and the reflector can be expressed as follows:

$$\begin{aligned} x_{SAT} &= -r_{SAT}(t)\cdot\cos E^S(t)\cdot\cos A^S(t) & \qquad x_{REFL} &= -r_{REFL}\cdot\cos E_R\cdot\cos A_R \\ y_{SAT} &= r_{SAT}(t)\cdot\cos E^S(t)\cdot\sin A^S(t) & \qquad y_{REFL} &= r_{REFL}\cdot\cos E_R\cdot\sin A_R \\ z_{SAT} &= r_{SAT}(t)\cdot\sin E^S(t) & \qquad z_{REFL} &= r_{REFL}\cdot\sin E_R \end{aligned} \tag{17}$$

In the following, it is assumed that the Cartesian satellite and reflector coordinates are expressed as position vectors $\boldsymbol{r}_{SAT}$, $\boldsymbol{r}_{REFL}$ of unity length (r_{SAT}=r_{REFL}=1):

$$\vec{r}_{SAT} = \begin{pmatrix} -\cos E^S(t)\cos A^S(t) \\ \cos E^S(t)\sin A^S(t) \\ \sin E^S(t) \end{pmatrix} \qquad \vec{r}_{REFL} = \begin{pmatrix} -\cos E_R \cos A_R \\ \cos E_R \sin A_R \\ \sin E_R \end{pmatrix} \tag{18}$$

Both vectors are illustrated in Figure 3-10:

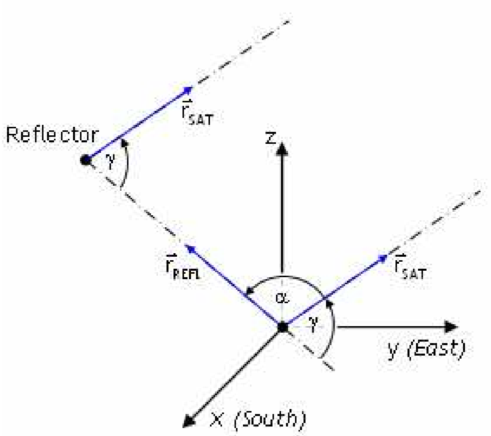

Figure 3-10: Vectors r_{SAT} and r_{REFL} with respect to the local horizontal coordinate system.

The angle between two vectors can be computed by means of their dot product. Thus, the angle α between the vectors $\boldsymbol{r_{SAT}}$ and $\boldsymbol{r_{REFL}}$ (which are of unity length) can be expressed as

$$\begin{aligned} \cos\alpha(t) &= \frac{\vec{r}_{SAT}\cdot\vec{r}_{REFL}}{\left\|\vec{r}_{SAT}\right\|\cdot\left\|\vec{r}_{REFL}\right\|} = \vec{r}_{SAT}\cdot\vec{r}_{REFL} \\ &= \cos E^S(t)\cos A^S(t)\cos E_R \cos A_R + \cos E^S(t)\sin A^S(t)\cos E_R \sin A_R + \sin E^S(t)\sin E_R \\ &= \cos E^S(t)\cos E_R\left(\cos A^S(t)\cos A_R + \sin A^S(t)\sin A_R\right) + \sin E^S(t)\sin E_R \\ &= \cos E^S(t)\cos E_R\left(\cos\left(A^S(t) - A_R\right)\right) + \sin E^S(t)\sin E_R \end{aligned} \tag{19}$$

As can be derived from Figure 3-10, the relationship between the angle α and the desired angle γ is simply γ=180°-α. The angle γ can therefore be expressed as

$$\begin{aligned} \cos\gamma(t) &= \cos(180° - \alpha) \\ &= -\cos\alpha \\ &= -\cos E^S(t)\cos E_R \cos[A^S(t) - A_R] - \sin E^S(t)\sin E_R \, . \end{aligned} \tag{20}$$

By inserting this expression into equation (16) and by expressing the distance *d* as a function of its horizontal component d_H and the reflector elevation E_R, the multipath relative phase $\Delta\phi_M$ takes on the following form:

$$\Delta\phi_M(t) = \frac{2\pi}{\lambda}\frac{d_H}{\cos E_R}\left\{1 - \cos E^S(t)\cos E_R \cos\left[A^S(t) - A_R\right] - \sin E^S(t)\sin E_R\right\} \tag{21}$$

Equation (21) differs from the results presented in [BECKER et al. 1994]. Further analysis of this discrepancy lead to the result that the formula introduced in this paper is incorrect. This is why the derivation of equation (21) has been presented in detail. By combining equations (14) and (21), the frequency f_M of the multipath variations can be computed as follows:

$$f_M(t) = \frac{d_H}{\lambda \cos E_R}\left\{\cos E_R \cos[A^S(t) - A_R]\sin[E^S(t)]\frac{dE^S(t)}{dt} + \cos[E^S(t)]\cos E_R \sin[A^S(t) - A_R]\frac{dA^S(t)}{dt} - \sin E_R \cos[E^S(t)]\frac{dE^S(t)}{dt}\right\} \quad (22)$$

3.1.4.2 Special Case: Ground Multipath

Ground multipath can be deemed as a special case of the multipath environment illustrated in Figure 3-9. In this case, equations (21) and (22) can be simplified according to the following considerations (see Figure 3-11 for verification):

- The satellite, the point of reflection and the antenna are assumed to be located in the same plane; as a result, the satellite azimuth is equal to the azimuth of the reflector (A^S=A_R).

- Due to the law of reflection (angle of incidence = angle of reflection), the angle γ can now be expressed as a function of the satellite elevation, namely

$$\gamma = 180^\circ - 2E^S \quad (23)$$

- Due to the permanent motion of the satellites, the horizontal distance between the antenna and the point of reflection is not constant. However, it can be expressed as a function of the height *h* of the antenna above the reflecting surface and the satellite elevation E^S according to

$$d_H = \frac{h}{\tan E^S(t)} \quad (24)$$

- The elevation E_R of the reflection point is simply the negative satellite elevation E^S (E_R=-E^S).

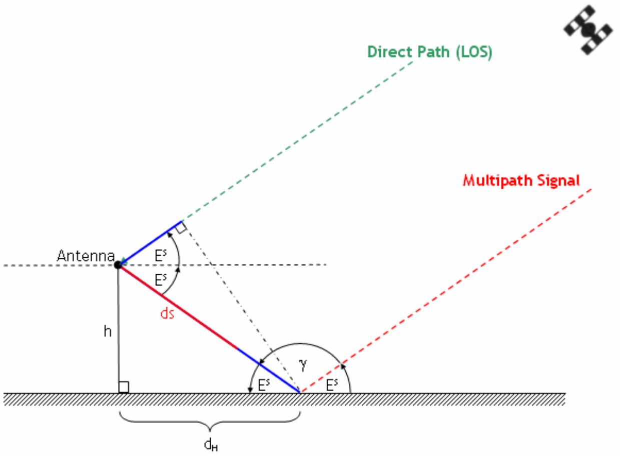

Figure 3-11: Geometrical situation in case of ground multipath.

Based on these assumptions, the geometric path delay *ds*, the multipath relative phase $\Delta\phi_M$ and the frequency f_M of the multipath variations simplify as follows:

$$ds(t) = d(1 + \cos\gamma(t)) = 2h\sin E^S(t) \quad (25)$$

$$\Delta\phi_M(t) = \frac{2\pi}{\lambda} ds(t) = \frac{4\pi h \sin E^S(t)}{\lambda} \tag{26}$$

$$f_M(t) = \frac{1}{2\pi} \cdot \frac{d\Delta\phi_M(t)}{dt} = \frac{2h\cos E^S(t)}{\lambda} \cdot \frac{dE^S(t)}{dt} \tag{27}$$

3.1.4.3 Occurring Frequencies for Different Multipath Environments

In order to get a deeper insight into the frequency of occurring multipath variations, some cases shall be examined in more detail. The analyses are based on a real satellite pass with the azimuth and elevation profile illustrated in Figure 3-12. For this pass, the occurring multipath frequencies and the corresponding cycle durations are plotted for different multipath environments, i.e. different locations of the reflector. In all scenarios, the azimuth and elevation gradients have been averaged over the entire pass, resulting in the values also listed in Figure 3-12:

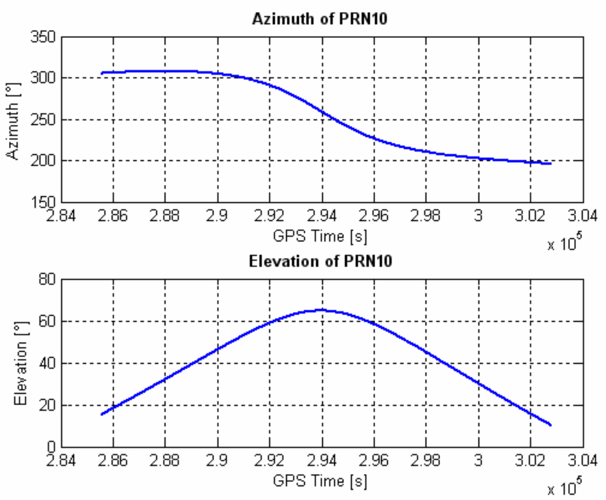

$$\frac{dA^S(t)}{dt} = -0.000110 \quad [\text{rad/s}]$$

$$\frac{dE^S(t)}{dt} = 0.000105 \quad [\text{rad/s}]$$

Figure 3-12: Typical azimuth and elevation profile for a complete satellite pass.

Case 1: Variation of Reflector Distance. The following diagram illustrates the frequency of the occurring multipath variations for fixed azimuth and elevation angles (A_R=120°, E_R=10°) of the reflector. The horizontal distance between the antenna and the reflector varies from 10m to 100m.

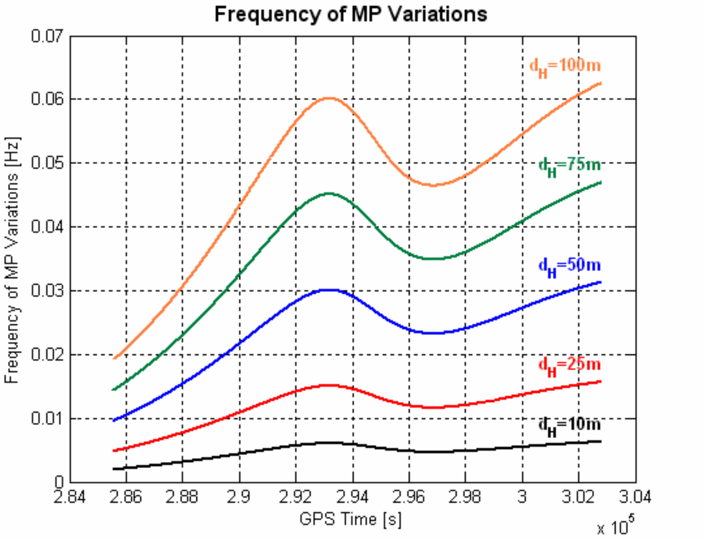

Figure 3-13: Occurring multipath frequencies for the satellite pass of PRN10 (A_R=120°, E_R=10°, varying horizontal distance d_H between antenna and reflector).

Figure 3-13 emphasizes the well-known fact that the frequency of the multipath variations becomes higher with increasing distance between the antenna and the reflector. Furthermore, also the frequency variations during the entire satellite pass become more distinct when the reflector is farther away from the antenna.

Case 2: Variation of Reflector Azimuth. Figure 3-14 illustrates the frequency of the occurring multipath variations for a fixed horizontal distance between the antenna and the reflector (d_H=75m) and a fixed elevation of E_R=10°. The azimuth A_R varies from 0° to 270°.

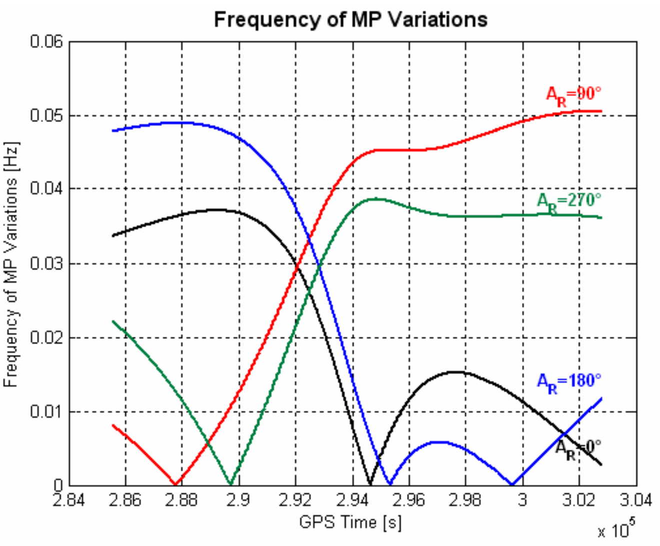

Figure 3-14: Occurring multipath frequencies for the satellite pass of PRN10.

Figure 3-14 indicates that the frequency of the occurring multipath variations strongly depends on the reflector's azimuth angle. The frequency profiles are significantly different subject to the azimuth angle A_R. Note that there are also situations where the multipath frequency becomes zero, resulting in theoretically infinite cycle durations. During these short periods of time, the occurring multipath can be termed as "fixed-offset" multipath.

Case 3: Variation of Reflector Elevation. The following diagram illustrates the frequency of the occurring multipath variations for a fixed horizontal distance between the antenna and the reflector (d_H=75m) and a fixed azimuth angle of A_R=120°. The elevation E_R varies from 5° to 60°.

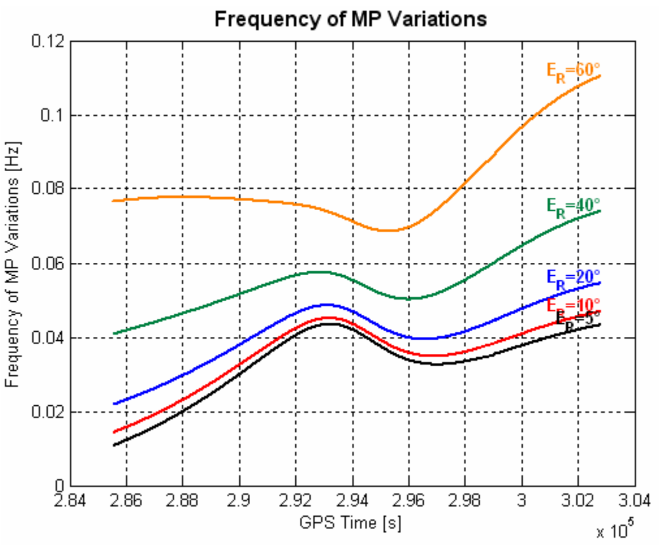

Figure 3-15: Occurring multipath frequencies for the satellite pass of PRN10 (d_H=75m, A_R=120°, varying reflector elevation E_R).

Similar to case 1, the frequencies of the occurring multipath variations increase with higher reflector elevation. This behavior is not limited to this special case, it can also be observed for other combinations of A_R and d_H.

Case 4: Ground Multipath. Figure 3-16 illustrates the frequency of the occurring multipath variations in case of ground multipath. As already mentioned, ground multipath is mainly characterized by identical azimuth angles of reflector and satellite (A^S=A_R) and by the fact that the reflector elevation is simply the (negative) satellite elevation (E_R=-E^S). The multipath frequency is plotted for different antenna heights *h* above the ground. Again, the frequency of the multipath variations becomes higher with increasing antenna height above the ground. Similar to case 1, the frequency variations during the entire satellite pass become more distinct when the antenna is higher above the reflecting surface.

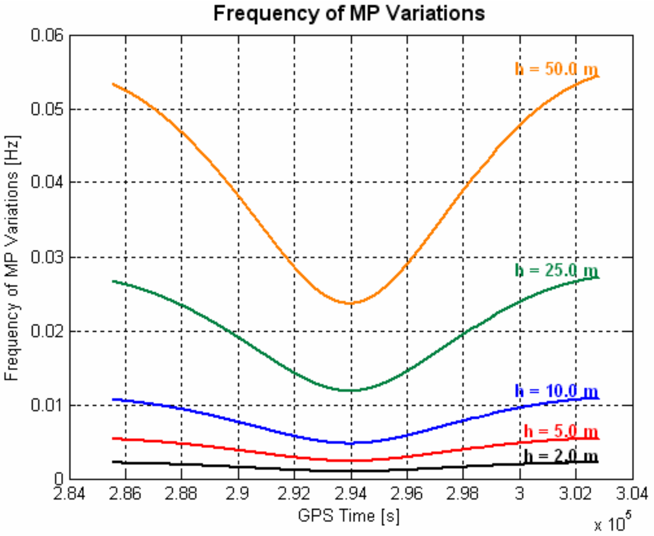

Figure 3-16: Occurring multipath frequencies for the satellite pass of PRN10 (ground multipath, antenna heights h).

In order to verify the frequency of the occurring multipath variations, ground multipath with an antenna height of 75m above the reflecting surface was simulated by means of a GPS hardware simulator. The satellite was observed during a time period of approximately 30 minutes. The azimuth and elevation profile as well as the expected (theoretical) multipath frequencies and cycle durations are illustrated in Figure 3-17.

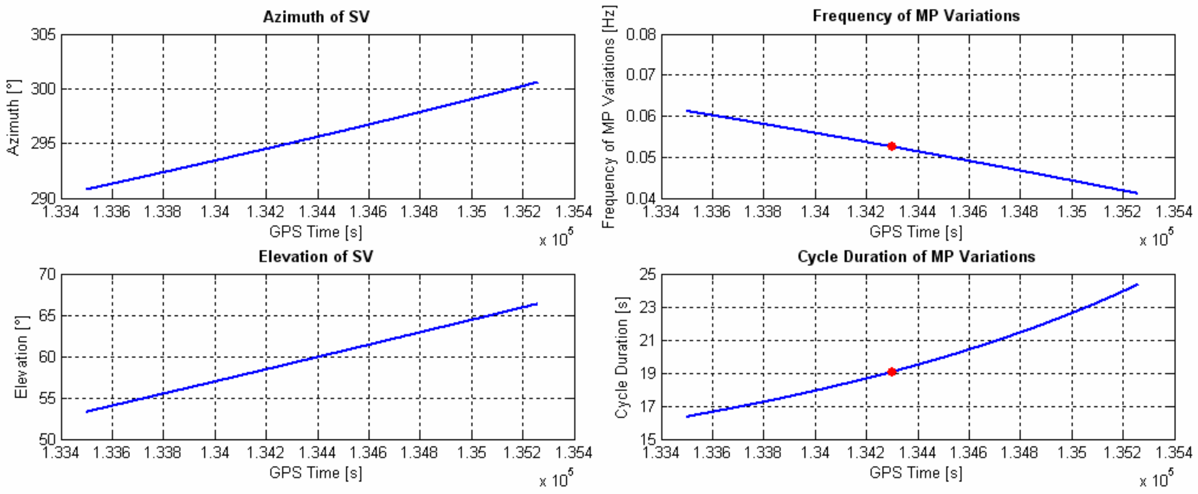

Figure 3-17: Azimuth and elevation profile as well as expected (theoretical) ground multipath characteristics for an antenna located 75m above a reflecting surface.

During the simulation, a multipath signal with a power of -12dB with respect to the direct signal was generated. In order to ensure that the multipath signal is really received by the antenna, an omni directional antenna phase pattern (0dB gain for all incident angles) was assumed. Code and carrier observations were recorded during the simulation in order to form the "code minus carrier" residuals illustrated in Figure 3-18.

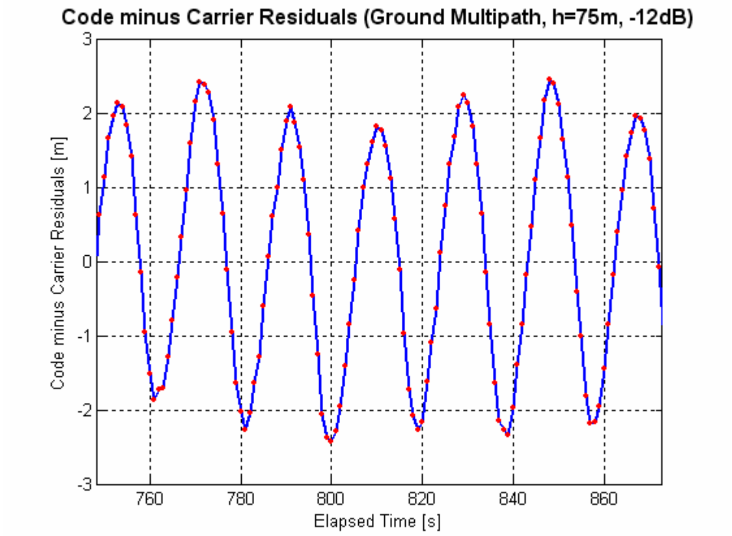

Figure 3-18: "Code minus carrier" residuals for GPS observations affected by ground multipath.

The "code minus carrier" residuals are computed at a GPS time of approximately 134300s. At this point in time, a multipath frequency of 0.0525Hz can be expected, resulting in a corresponding cycle duration of about 19s (see red spots in Figure 3-17). The "code minus carrier" residuals obtained from real measurements and illustrated in Figure 3-18 show a cycle duration of about 19s which perfectly confirms the theoretical prediction.

3.1.4.4 Maximum Fading Frequencies

There are several publications where estimations on the maximum occurring Doppler differences can be found (e.g. [VAN NEE 1992] or [EISSFELLER 1997]). Thus, assuming a static receiver, the maximum fading frequencies occur for a user at the equator and can be expressed either as a function of the reflector distance *d* [m] from the receiver

$$f_{M,max} = 1.38 \cdot 10^{-3} \frac{Hz}{m} \cdot d \tag{28}$$

(see [VAN NEE 1992]) or as a function of the geometric path delay *ds* [m] ([EISSFELLER 1997])

$$f_{M,max} \approx 1.13 \cdot 10^{-3} \frac{Hz}{m} \cdot ds \,. \tag{29}$$

Taking into account that multipath signals with path delays of larger than 1.5 chips (~440m) hardly affect the receiver's tracking loops (valid for the standard correlation technique, see section 3.2.3) the expected maximum fading frequency according to equation (29) is about 0.5Hz for a static user at the equator. For static users at other locations, the Doppler difference is always smaller. Another analysis that can be found in [HÖPER et al. 2001] predicts maximum fading frequencies of about 0.3Hz. It should be noted, however, that the fading frequency can be much larger for mobile users. For a user velocity of 15m/s, [VAN NEE 1992] states that the Doppler difference can take values up to 180Hz depending on the actual geometrical conditions.

3.1.5 Multipath Relative Amplitude

As will be shown in section 3.2.3, the relative power of the multipath signal (also referred to as “Signal-to-Multipath Ratio”, SMR) strongly determines the actual effects of multipath propagation on the signal tracking process within the receiver. Therefore, the multipath relative amplitude is a key parameter for the understanding and modeling of multipath propagation. According to [RODGERS 1992], the multipath relative amplitude α consists of four attenuation factors (in case that specular reflection is assumed):

$$\alpha = \eta_F \cdot \eta_R \cdot \eta_D \cdot \eta_A \tag{30}$$

η_F denotes the free space loss related to the extended signal path, η_R denotes the signal attenuation due to signal reflection, η_D is the depolarization loss and η_A the signal attenuation due to the antenna gain pattern. Since signal attenuation due to the additional free space loss is negligible (e.g. η_F=0.999975 for a path delay of 450m), it can be approximated by $\eta_F \approx 1$ and remain unconsidered.

3.1.5.1 Attenuation Due to Signal Reflection and Depolarization Loss

The GPS (and the future Galileo system as well) use right-hand circularly polarized signals (RHCP), a measure to eliminate the effects of Faraday rotation that are associated with the use of linearly polarized signals. RHCP is a special case of elliptical polarization, i.e. the electric and magnetic field of the electromagnetic wave are composed of two linearly polarized components, namely a horizontal component E_H and a vertical component E_V. The following illustration reveals both field components for the incident signal ($E_{H,I}$,$E_{V,I}$) and for the reflected wave ($E_{H,R}$,$E_{V,R}$):

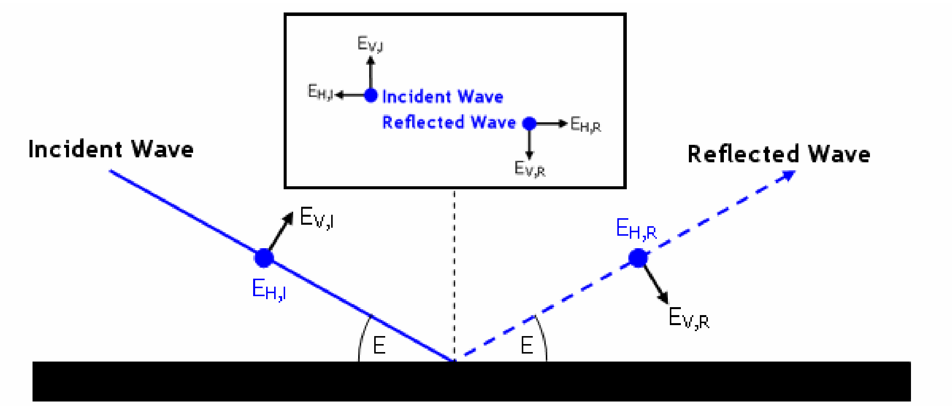

Figure 3-19: Electric field vectors for the incident and the reflected signal.

According to [BECKMANN and SPIZZICHINO 1987], the signal attenuation factors for the horizontally and vertically polarized components of the electric field can be expressed as a function of the elevation angle E:

$$\begin{aligned} \eta_H &= \frac{E_{H,R}}{E_{H,I}} = \frac{\sin E - \sqrt{Y^2 - \cos^2 E}}{\sin E + \sqrt{Y^2 - \cos^2 E}} \\ \eta_V &= \frac{E_{V,R}}{E_{V,I}} = \frac{Y^2 \sin E - \sqrt{Y^2 - \cos^2 E}}{Y^2 \sin E + \sqrt{Y^2 - \cos^2 E}} \end{aligned} \tag{31}$$

The (complex) term Y is defined as

$$Y = \sqrt{\frac{\varepsilon_R + j60\lambda\sigma}{\mu_R}}\,, \tag{32}$$

where ε_R is the dielectric constant (relative permittivity), μ_R the relative permeability, σ the conductivity of the reflective medium and λ the carrier wave length. Since the resulting signal attenuation η_R is a function of the horizontally and vertically polarized components, the following cases can be distinguished for the reflected signal:

- Elliptical polarization: η_H and η_V are different
- Circular polarization: η_H and η_V are equal
- Linear polarization: η_V is zero

As an alternative to the linear representation (η_H,η_V), η_R can be expressed as the sum of two circularly polarized components. These (complex) components are called "co-polarized" (Γ_0) and "cross-polarized" (Γ_X) and can be expressed as a function of the horizontally and vertically polarized components η_H and η_V ([Flock 1987]):

$$\Gamma_0 = \frac{\eta_H + \eta_V}{2}; \quad \Gamma_X = \frac{\eta_H - \eta_V}{2} \tag{33}$$

The resulting signal attenuation η_R due to the reflection process as based on equations (31) and (32) can be expressed as follows ([Eissfeller 1997]):

$$\eta_R = \sqrt{\frac{1}{2}\left(|\eta_H|^2 + |\eta_V|^2\right)} \tag{34}$$

Figure 3-20 illustrates the horizontal, vertical and circular components of the coefficient η_R, assuming conductivity and permittivity values of ε_R=3 and σ=2·10^{-5} S/m (characteristic values for concrete). Note that only the magnitude of the complex coefficients is plotted as a function of the elevation angle. Both diagrams are valid for an incident RHCP GNSS signal.

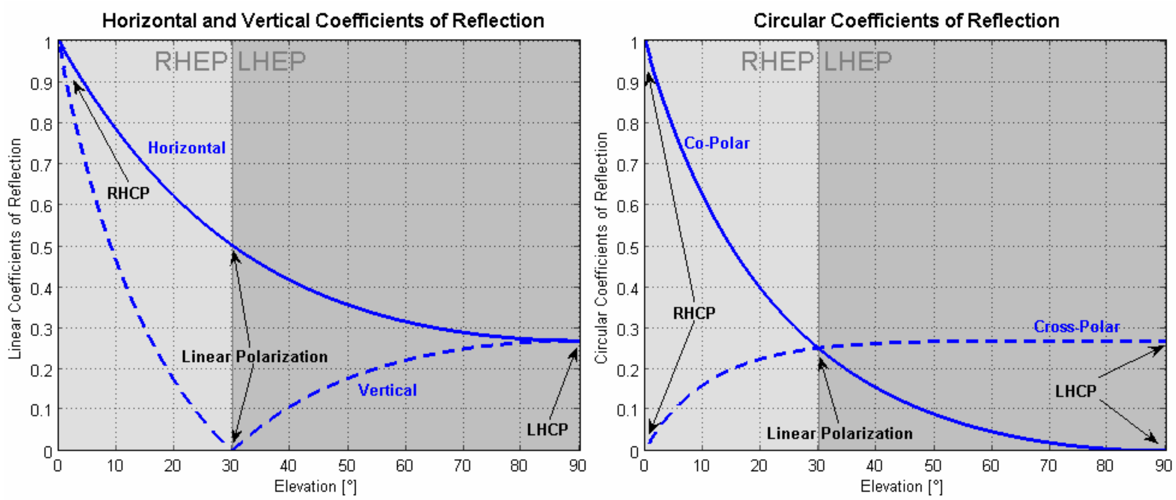

Figure 3-20: Horizontal, vertical and circular components of the coefficient of reflection for an incident RHCP signal.

For an elevation of E=0°, the reflected signal is RHCP, i.e. the horizontal and vertical components of the coefficient of reflection are equal, the co-polar component is 1 and the cross-polar component is zero. For small signal elevations, the reflected signal becomes right-hand elliptically polarized (RHEP), showing different magnitudes for the linear and circular components of the coefficient of reflection. At E=30°, the vertical component becomes zero and both circular components are equal. This is where the signal becomes linearly polarized. The point where the vertical component η_V becomes zero is called Brewster angle. This is also the point where the polarization changes from right-hand to left-hand. Thus, for elevations greater than the Brewster angle, the reflected signal becomes left-hand elliptically polarized (LHEP) and reaches circular polarization at E=90° (LHCP).

Another constituent of equation (30) is the depolarization loss η_D. Since GNSS antennas are designed for the reception of RHCP and the polarization may change during the reflection process, the reflected signal (that may not be RHCP anymore) can be further attenuated due to the RHCP antenna characteristic. For an incident RHCP signal, this effect can be expressed in the form of a coupled coefficient of reflection ([HANNAH 2001]):

$$(\eta_R \cdot \eta_D)_{RHCP} = \left(|\Gamma_0| + 10^{-\frac{K}{20}} \cdot |\Gamma_X| \right) e^{-j\pi} \tag{35}$$

K is the antenna LHCP rejection ratio (expressed in [dB]) that can be modeled as a function of the elevation (and azimuth) angle or considered constant if an omni directional antenna characteristic for both polarization components is assumed. According to [HANNAH 2001], typical values for *K* are 10-11dB. For an incident LHCP signal – a case that can occur after a reflection where the signal polarization changed from RHCP to LHCP – the coupled coefficient of reflection can be expressed as follows ([HANNAH 2001]):

$$(\eta_R \cdot \eta_D)_{LHCP} = \left(10^{\frac{K}{20}} \cdot |\Gamma_0| + |\Gamma_X| \right) e^{-j\pi} \tag{36}$$

3.1.5.2 Attenuation Due to Antenna Gain Pattern Influences

The last factor that has to be considered is the influence of the antenna gain pattern. Since GNSS antenna patterns are typically not omni directional, the antenna gain is usually expressed as a function of the elevation angle. Typical values for η_A are 0.5 (-3dB) near the horizon and 2 (+3dB) near the zenith (however, actual values depend on the antenna type). Thus, depending on the location of the potential reflectors, a multipath signal can even be amplified (η_A>1).

3.1.5.3 Multipath Relative Amplitudes in Case of Diffuse Reflection

In case that diffuse reflections are present, they can be accounted for by applying a magnitude reduction factor ρ_S, so that the horizontally and vertically polarized components of the electric field (equations (31)) can be modified as follows ([FLOCK 1987]):

$$\begin{aligned} \eta_H^* &= \rho_S \eta_H \\ \eta_V^* &= \rho_S \eta_V \end{aligned} \tag{37}$$

with

$$\rho_S = \exp\left(-\frac{1}{2} \Delta H^2 \right) I_0 \left(\frac{1}{2} \Delta H^2 \right). \tag{38}$$

In equation (38), I_0 is the modified Bessel function of zero order and ΔH the surface roughness height as defined in section 3.1.3.3.

3.1.6 Minimum Size of Reflecting Surface

In order to cause reflections, a reflector has to be sufficiently large. The minimum size of a reflector that is required to cause reflections can be estimated by considering the Fresnel zone concept, a criterion to define an unobstructed line-of-sight communication link. It depends on various parameters like carrier wavelength, signal elevation and the distance between the antenna and the reflecting surface.

3.1.6.1 Fresnel Zone Concept

An unobstructed and undisturbed line-of-sight communication link can be described in the form of Fresnel ellipsoids. A Fresnel ellipsoid has the transmitter *T* and the receiver *R* as focal points. The size of the n^{th} Fresnel ellipsoid depends on the distance *d* between the two focal points and on the carrier wavelength λ and fulfills the following equation ([KLUKAS 2004]):

$$a + b < d + \frac{n\lambda}{2} \tag{39}$$

The 1st Fresnel ellipsoid is defined by n=1. This case plays an important role because it defines the region where most of the transmitted energy passes through and which should be free of obstruction ([BOITHIAS 1987]).

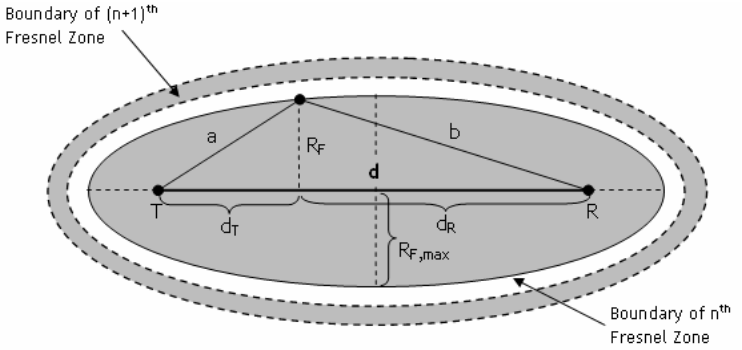

Figure 3-21: Definition of Fresnel ellipsoids.

The semi-minor axis R_F of the first Fresnel ellipsoid is a function of the distance *d* between transmitter and receiver and the carrier wavelength λ ([BOITHIAS 1987]). It describes the "height" of the first Fresnel ellipsoid in the middle of the signal path:

$$R_{F,max} = \frac{1}{2}\sqrt{\lambda d} \tag{40}$$

At any other point along the signal path, the height R_F of the first Fresnel ellipsoid can be expressed as follows ([FLOCK 1979]):

$$R_{F,max} = \sqrt{\frac{\lambda d_T d_R}{d}} \tag{41}$$

Any object that is larger than the first Fresnel zone leads to complete signal blockage. However, if the first Fresnel zone is partially obstructed, signal diffraction effects must be expected.

3.1.6.2 Effective Fresnel Zone for a Planar Reflector

Fresnel zones can be used to estimate the minimum size a reflector must have to be able to reflect a sufficient amount of energy. Figure 3-22 illustrates the case of a planar reflector. The satellite is located at *T* and the signal would be received by the virtual receiver *R'* if the reflecting surface was not present. *T* and *R'* define the first Fresnel ellipsoid as plotted in Figure 3-22. The effective Fresnel zone that causes signal reflection is the intersection of a planar reflector with the first Fresnel ellipsoid. Its shape and dimensions depend on the elevation angle *E*, the height h_1 and h_2 and the carrier wavelength λ.

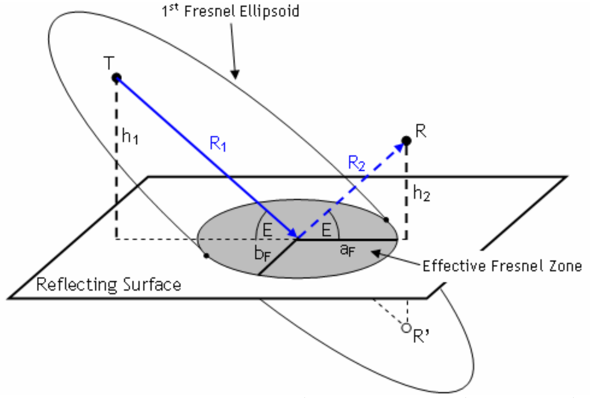

Figure 3-22: Definition of first Fresnel zone on a planar reflecting surface.

According to [EISSFELLER 1997], the semi-major and semi-minor axis of the effective Fresnel zone a_F and b_F can be expressed as follows:

$$b_F \approx \sqrt{n\lambda R_2} = \sqrt{\frac{n\lambda h_2}{\sin E}} \quad \text{and} \quad a_F \approx \frac{b_F}{\sin E} = \sqrt{\frac{n\lambda h_2}{\sin^3 E}} \tag{42}$$

Figure 3-23 illustrates the size of the effective Fresnel zone and the numerical eccentricity e_{num} as a function of the signal elevation *E*. These quantities can be computed according to

$$A_F = \pi \cdot a_F \cdot b_F \qquad\qquad e_{num} = \frac{\sqrt{a_F^2 - b_F^2}}{a_F} \tag{43}$$

By inserting equation (42) into equation (43), it can be shown that the numerical eccentricity does not depend on the antenna height h_2.

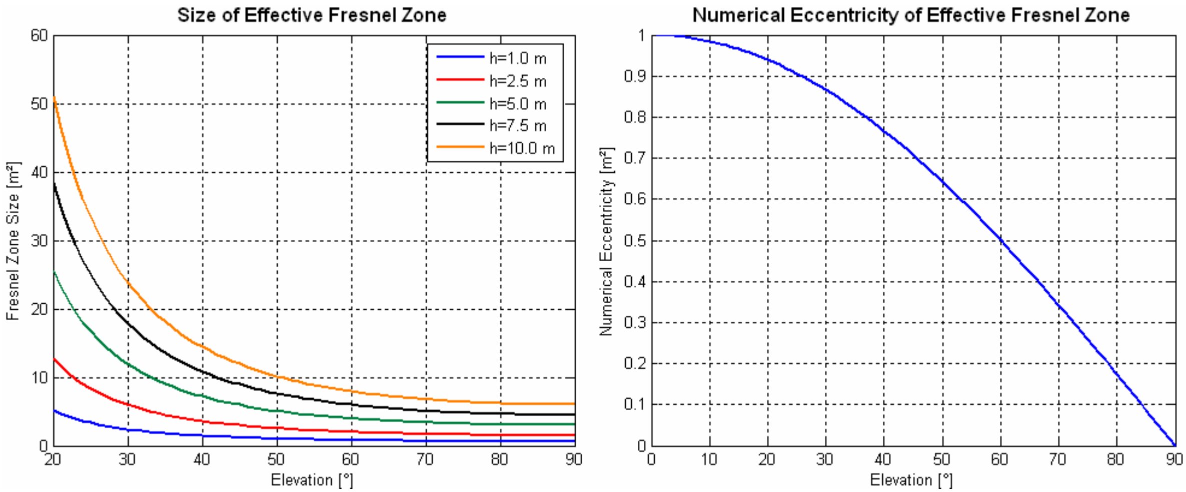

Figure 3-23: Size of effective Fresnel zone for different antenna heights and numerical eccentricity of effective Fresnel zone as a function of the elevation angle.

For the case of a planar reflecting surface, the size of the Fresnel zone decreases with increasing elevation angle. At the same time, the numerical eccentricity of the effective Fresnel zone also decreases leading to a circular shape of the Fresnel ellipse for E=90°. For this elevation angle, the size of the ellipse reaches its minimum. For h_2=1m, the minimum size of the Fresnel ellipse is A~0.6m^2. Smaller reflectors will not lead to a sufficient amount of reflected energy. For higher values of h_2, the size of the Fresnel ellipse is always larger. It is obvious that especially for low elevation angles, large reflectors are required to produce undesired reflections so that in theory, it is more likely to see multipath on highly-elevated signals than for low elevation angles.

It can be shown that for a vertical reflector, the sizes of the effective Fresnel zones are the same as for a horizontal reflector. However, the elevation angles related to these sizes are different. The same is true for the eccentricity of the Fresnel ellipse. In case of a vertical reflector, the effective Fresnel zone has circular shape for E=0°. In order to consider a vertical reflector, the *sin(E)*-terms of equation (42) have to be replaced by *cos(E)*-terms.

3.2 Effects on Signal Tracking

3.2.1 Basic Receiver Architecture

Before dealing with aspects of signal tracking and the influence of multipath on the signal processing process, the basic architecture of a GNSS receiver is presented at first. Figure 3-24 illustrates a block diagram of a typical receiver architecture.

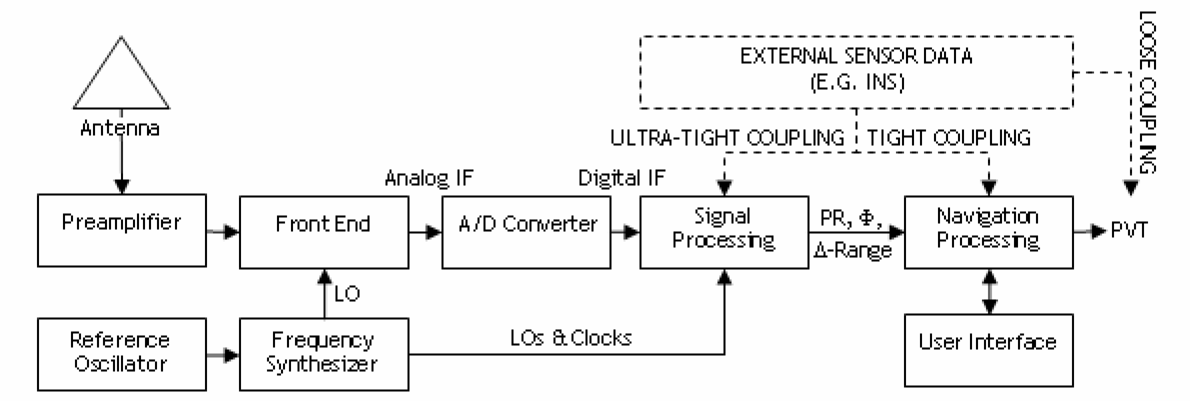

Figure 3-24: Block diagram of a generic GNSS receiver.

Antenna. As GNSS signals are right-hand circularly polarized, the antenna has to use this polarization as well. Further desired requirements w.r.t. GNSS antennas are that they have a suitable pattern (signal tracking from the zenith to the horizon for all azimuths), are able to mitigate multipath and/or jamming signals and show only small antenna phase center variations. Several antenna types are able to receive RHCP signals. The most common antenna type is the microstrip antenna. Multipath rejection can be achieved by using special antennas such as choke-ring antennas, phased-array antennas or multipath limiting antennas (MLA's).

Preamplifier. The preamplifier section may be part of the antenna hardware and consists of a low-noise amplifier (LNA), filters for jamming and interference rejection and burnout protection. The preamplifier has a typical gain of 25-40dB ([BRAASCH and VAN DIERENDONCK, 1999]).

Front-End. This section performs all analog signal processing tasks such as filtering (suppression of out-of-band interference), further amplification and down-conversion to an intermediate frequency (IF). By means of a frequency synthesizer whose generated frequencies are derived from the reference oscillator, the analog RF signal is down-converted using either one or several steps (single-stage vs. multiple-stage conversion). Finally, the IF signal is converted to baseband by mixing it with two LOs at the nominal IF, the second having a phase-shift of 90° with respect to the other. This process constitutes the signal's I- and Q-components (can also be performed after A/D conversion).

A/D Conversion. The baseband I- and Q-signal components are digitized in the A/D conversion section. This process comprises sampling with a sampling frequency which fulfills the Nyquist criterion and quantization. For quantization, single- and multi-bit conversion may be used. While most low-cost receivers use the single-bit approach, 1.5 to 3-bit-sampling can typically be found in high-end receivers. Sampling frequencies typically range from 2-20MHz ([Braasch and Van Dierendonck 1999]). The quantization process always results in signal degradation that depends on the number of quantization levels and on other parameters like IF bandwidth. For narrow IF bandwidths and single-bit quantization, signal degradation up to 3.5dB may occur ([Braasch and Van Dierendonck 1999],[Van Dierendonck 1996]).

Signal Processing. Digital signal processing includes Doppler removal, mixing of the I- and Q-data streams with early, prompt and late versions of the ranging codes, accumulation of the mixed I- and Q-samples during a "predetection integration interval" (formation of correlation values), discriminator-based code tracking by means of a Delay Lock Loop (DLL) and carrier tracking by means of a Phase Lock Loop (PLL) or Frequency Lock Loop (FLL). Signal acquisition and data demodulation are also performed in this unit. The signal processing unit provides pseudoranges PR, carrier phases Φ and Δ-Ranges as basic GNSS observables. Section 3.2.2 provides a more detailed overview on the signal tracking process.

Navigation Processing. The basic GNSS observables are used to compute a navigation (PVT) solution. This can be achieved by solving the basic GNSS observation equations by means of a least-squares adjustment or by applying more advanced methods such as Kalman filtering.

GNSS receivers can be coupled with external data, such as INS data or other sensors (e.g. altimeters). Depending on where exactly external data is incorporated into the data stream, the process is called "loose coupling", "tight coupling" or "ultra-tight coupling" (following the terminology introduced in [Alban 2003]). Loose coupling combines the PVT solution obtained with the GNSS receiver with navigation solutions obtained by other systems (e.g. INS, LORAN-C or GLONASS) to compute a combined PVT solution. Tight coupling combines the basic GNSS observables (pseudoranges, Doppler, or carrier phases) with data generated by external (inertial) sensors. By means of ultra-tight coupling, external data can be used to reduce the influence of signal dynamics within the tracking loops (e.g. by feeding INS-derived acceleration values into the signal processing unit). By this measure, smaller loop noise bandwidths can be used resulting in decreased influence of thermal noise.

Typically, a combination of hard- and software is used within the signal processing unit to determine the desired observables. In recent years, however, software-based implementations of all signal processing tasks became feasible and more popular. In this case, all processing steps after the A/D conversion are software-based. Such an approach is called "Software Receiver" (see e.g. [Pany et al. 2006]).

3.2.2 Signal Tracking Basics

3.2.2.1 Signal Acquisition

Signal acquisition is performed in the receiver's signal processing unit. Following the notation given in [MISRA and ENGE 2001], the sampled signal s_l (not yet separated into the I- and Q-samples) can be written as follows:

$$\begin{aligned} s_l &= \sqrt{P}D(t_l-\tau)x(t_l-\tau)\cos\left[2\pi(f_{IF}+f_D)t_l+\delta\theta\right] \\ t_l &= lT_s, \quad l = 0,1,2,3,\ldots \end{aligned} \tag{44}$$

$\sqrt{P}$ denotes the signal amplitude, *D* the navigation data message, *x* the ranging code and τ the signal propagation time (including propagation errors). The intermediate frequency is denoted by f_{IF}, the Doppler shift by f_D and the carrier phase offset by $\delta\theta$. T_s is the time between two successive samples and t_l is the sampling time.

Signal acquisition is a global search for the exact values of the signal propagation time τ and the Doppler frequency f_D. Without having a priori information, the receiver has to perform a search over the entire code-Doppler space, compute correlation values for all possible combinations of code phases τ and Doppler frequencies f_D, and find a correlation peak from which the initial values for τ and f_D can be derived. This type of acquisition is called "cold start". The time required for acquisition depends on the size of the search region (code length and occurring Doppler frequencies), the number of available channels, the number of correlators per channel, the acquisition algorithm and the signal conditions (SNR). Depending on the actual implementation of the acquisition process, cold start may take up to several minutes. Reacquisition, a situation where a signal had been acquired but the receiver has lost lock temporarily, can be achieved much faster (typically within a few seconds), because the receiver already has a priori information about the current position and the clock offset.

3.2.2.2 Code and Carrier Tracking

After A/D conversion, the digitized signal samples are mixed with in-phase (0° phase shift) and quadra-phase outputs (90° phase shift) of a numerically controlled oscillator (which is the carrier NCO as illustrated in Figure 3-25). By this measure, the signal is divided into an *I* and a *Q* data stream. As part of the carrier tracking loop, the carrier NCO is constantly adjusted such that it matches the phase or the frequency of the received signal.

After this first mixing process which is sometimes referred to as "carrier wipeoff", the *I* and *Q* samples are mixed with early (*E*), late (*L*) and prompt (*P*) versions of the ranging code which are generated in the code generator. By accumulation/integration of the resulting data streams during the predetection integration time interval, the desired correlation values (denoted as I_L, I_P, I_E, Q_L, Q_P and Q_E) are formed. In a next step, suitable code and phase discriminators can be derived from these *I* and *Q* samples. The discriminator functions are used to compute an error signal which is – after passing a loop filter - fed back to the code and carrier NCO which are adjusted accordingly to maintain code, phase or frequency lock. In addition to the pure function of maintaining phase or frequency lock, the navigation data can be recovered and demodulated during the carrier tracking process. Furthermore, carrier loop measurements can be fed back into the code loop. This process is called carrier-aiding. It can improve the code tracking robustness by reducing the influence of signal dynamics and allows the use of narrow code tracking loop bandwidths (<1Hz) thus reducing the influence of thermal noise.

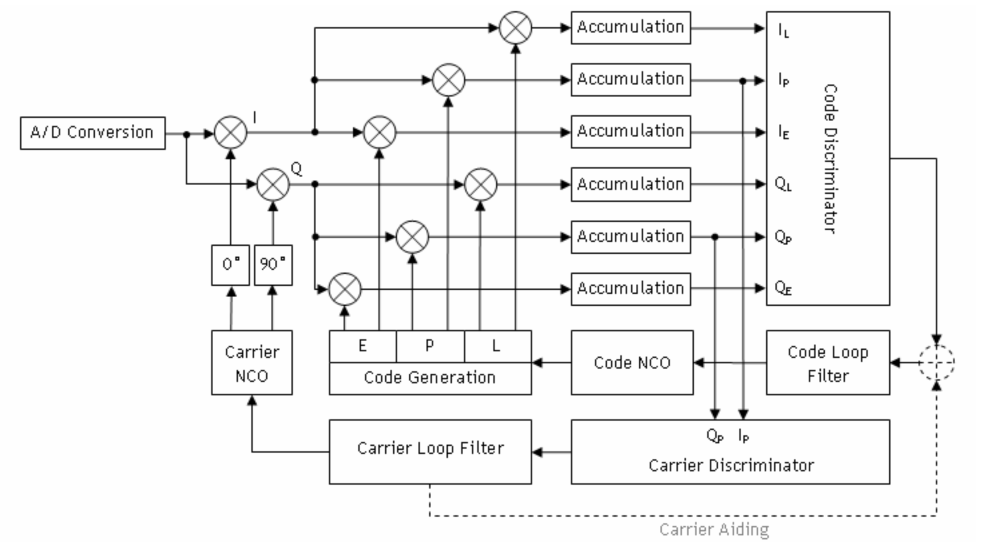

Figure 3-25: Block diagram for code and carrier tracking.

Following the notations introduced in equation (3) and those used in [VAN DIERENDONCK et al. 1992] and [EISSFELLER 1997], the correlator outputs I_L, I_P, I_E, Q_L, Q_P and Q_E can be expressed as follows (the spacing between early and late code is denoted as *d*):

$$I_E = AD(t-\tau_0)R(\tau_0-\tau-d/2)\cos(\theta_0-\theta)+\eta_{I,E} \tag{45}$$

$$I_P = AD(t-\tau_0)R(\tau_0-\tau)\cos(\theta_0-\theta)+\eta_{I,P} \tag{46}$$

$$I_L = AD(t-\tau_0)R(\tau_0-\tau+d/2)\cos(\theta_0-\theta)+\eta_{I,L} \tag{47}$$

$$Q_E = AD(t-\tau_0)R(\tau_0-\tau-d/2)\sin(\theta_0-\theta)+\eta_{Q,E} \tag{48}$$

$$Q_P = AD(t-\tau_0)R(\tau_0-\tau)\sin(\theta_0-\theta)+\eta_{Q,P} \tag{49}$$

$$Q_L = AD(t-\tau_0)R(\tau_0-\tau+d/2)\sin(\theta_0-\theta)+\eta_{Q,L} \tag{50}$$

The amplitude can be expressed as $A=\sqrt{2\cdot SNR\cdot T}$, where $SNR\cdot T$ is the signal-to-noise ratio for the predetection bandwidth $1/T$ [Hz]. *R* denotes the correlation process between the incoming signal and the internally generated early, late and prompt versions of the reference code and **D** the navigation data stream. The noise influences in each channel are denoted by η. Equations (45)-(50) contain the code tracking error τ_0-τ and the phase tracking error θ_0-θ which have to be driven to zero by the tracking loops. The correlator outputs can be used to set up the following common code, phase and frequency discriminators *D* ([VAN DIERENDONCK 1996]):

Code Discriminators:

Early-minus-late (coherent)

$$D_C = (I_E - I_L)\,\mathrm{sign}(I_P) \tag{51}$$

Early-minus-late power (non-coherent)

$$D_C = (I_E^2 + Q_E^2) - (I_L^2 + Q_L^2) \tag{52}$$

Dot product (non-coherent)

$$D_C = (I_E - I_L)I_P + (Q_E - Q_L)Q_P \tag{53}$$

Phase Discriminators:

Costas discriminator

$$D_{Ph} = I_P Q_P \tag{54}$$

Decision-directed Costas discriminator

$$D_{Ph} = Q_P \operatorname{sign}(I_P) \tag{55}$$

Arctangent discriminator

$$D_{Ph} = \arctan\left(\frac{Q_P}{I_P}\right) \tag{56}$$

Frequency Discriminators:

Cross-product discriminator

$$D_f = I_P(i-1)Q_P(i) - I_P(i)Q_P(i-1) \tag{57}$$

Decision-directed cross-product discriminator

$$D_f = \left[I_P(i-1)Q_P(i) - I_P(i)Q_P(i-1)\right]\operatorname{sign}\left[I_P(i-1)I_P(i) + Q_P(i-1)Q_P(i)\right] \tag{58}$$

Differential arctangent discriminator

$$D_f = \arctan\left(\frac{Q_P(i)}{I_P(i)}\right) - \arctan\left(\frac{Q_P(i-1)}{I_P(i-1)}\right) \tag{59}$$

In contrast to the code and phase discriminators, the frequency discriminators use I and Q samples of both the current integration interval *i* and the previous interval *i-1*. It should be noted that all discriminators have to be scaled such that the computed discriminator value equals the actual tracking error (at least for small tracking errors).

The following sections provide an overview how some of these discriminators are affected by multipath. In such a case, the correlator outputs (45)–(50) contain *N* additional multipath components (now without consideration of the noise terms η and assuming that the code and phase tracking errors are denoted by $\Delta\tau=\tau_0-\tau$ and $\Delta\theta=\theta_0-\theta$, respectively):

$$I_E = AD(t-\tau_0)R(\Delta\tau - d/2)\cos(\Delta\theta) + A\sum_{k=1}^{N}\alpha_k D(t-\tau_k)R(\Delta\tau-\tau_k - d/2)\cos(\Delta\theta) \tag{60}$$

$$I_P = AD(t-\tau_0)R(\Delta\tau)\cos(\Delta\theta) + A\sum_{k=1}^{N}\alpha_k D(t-\tau_k)R(\Delta\tau-\tau_k)\cos(\Delta\theta) \tag{61}$$

$$I_L = AD(t-\tau_0)R(\Delta\tau + d/2)\cos(\Delta\theta) + A\sum_{k=1}^{N}\alpha_k D(t-\tau_k)R(\Delta\tau-\tau_k + d/2)\cos(\Delta\theta) \tag{62}$$

$$Q_E = AD(t-\tau_0)R(\Delta\tau - d/2)\sin(\Delta\theta) + A\sum_{k=1}^{N}\alpha_k D(t-\tau_k)R(\Delta\tau-\tau_k - d/2)\sin(\Delta\theta) \tag{63}$$

$$Q_P = AD(t-\tau_0)R(\Delta\tau)\sin(\Delta\theta) + A\sum_{k=1}^{N}\alpha_k D(t-\tau_k)R(\Delta\tau-\tau_k)\sin(\Delta\theta) \tag{64}$$

$$Q_L = AD(t-\tau_0)R(\Delta\tau + d/2)\sin(\Delta\theta) + A\sum_{k=1}^{N}\alpha_k D(t-\tau_k)R(\Delta\tau-\tau_k + d/2)\sin(\Delta\theta) \tag{65}$$

The variables α_k, τ_k and θ_k (contained in the term $\Delta\theta$ of the multipath components) denote the multipath relative amplitude, the multipath delay and the multipath relative phase of the k^{th} multipath component, respectively ($k\geq1$).

3.2.3 Code Multipath

Based on the definition of the three code discriminators (51)-(53) and the multipath-affected correlator outputs (60)-(65), the discriminator functions in the presence of multipath can be set up. They take on the following form (see also [EISSFELLER 1997]):

Early-minus-late (coherent)

$$\begin{aligned} D_C(\Delta\tau) &= A[R(\Delta\tau - \tfrac{d}{2}) - R(\Delta\tau + \tfrac{d}{2})]\cos(\Delta\theta) \\ &\quad + A\sum_{k=1}^{N}\alpha_k[R(\Delta\tau - \tau_k - \tfrac{d}{2}) - R(\Delta\tau - \tau_k + \tfrac{d}{2})]\cos[\Delta\theta + \Delta\Phi_k + (\Delta\omega_k - \Delta\omega_0)t] \end{aligned} \tag{66}$$

Early-minus-late power (non-coherent)

$$\begin{aligned} D_C(\Delta\tau) &= A^2[R^2(\Delta\tau - \tfrac{d}{2}) - R^2(\Delta\tau + \tfrac{d}{2})] \\ &\quad + A^2\sum_{k=1}^{N}\alpha_k^2[R^2(\Delta\tau - \tau_k - \tfrac{d}{2}) - R^2(\Delta\tau - \tau_k + \tfrac{d}{2})] \\ &\quad + 2A^2\sum_{\substack{i,j\\ i\neq j}}^{N}\alpha_i\alpha_j[R(\Delta\tau - \tau_i - \tfrac{d}{2})R(\Delta\tau - \tau_j - \tfrac{d}{2}) - R(\Delta\tau - \tau_i + \tfrac{d}{2})R(\Delta\tau - \tau_j + \tfrac{d}{2})] \\ &\quad \times\cos[\Delta\Phi_j - \Delta\Phi_i + (\Delta\omega_j - \Delta\omega_i)t] \end{aligned} \tag{67}$$

Dot product (non-coherent)

$$\begin{aligned} D_C(\Delta\tau) &= A^2[R(\Delta\tau - \tfrac{d}{2}) - R(\Delta\tau + \tfrac{d}{2})]R(\Delta\tau) \\ &\quad + A^2\sum_{k=1}^{N}\alpha_k^2[R(\Delta\tau - \tau_k - \tfrac{d}{2}) - R(\Delta\tau - \tau_k + \tfrac{d}{2})]R(\Delta\tau - \tau_k) \\ &\quad + A^2\sum_{\substack{i,j\\ i\neq j}}^{N}\alpha_i\alpha_j[R(\Delta\tau - \tau_i - \tfrac{d}{2}) - R(\Delta\tau - \tau_i + \tfrac{d}{2})]R(\Delta\tau - \tau_j) \\ &\quad \times\cos[\Delta\Phi_j - \Delta\Phi_i + (\Delta\omega_j - \Delta\omega_i)t] \end{aligned} \tag{68}$$

$\Delta\Phi_k+(\Delta\omega_k-\Delta\omega_0)t$ is the time-varying multipath relative phase. Note that the term $D(t-\tau_k)$ does not appear in any of the above equations (it can be set to unity). The reason is that in case of coherent code tracking, it can be assumed that the data has already been demodulated in the carrier tracking loop. For the other two discriminator implementations the data bit stream is squared and thus takes on a value of 1.

Assuming only one single reflector, a vanishing phase tracking error ($\Delta\theta\approx 0$) and worst case values for the multipath relative phase (±180°), the code multipath errors $\Delta\tau$ can be expressed as a function of the multipath delay τ_k, resulting in a so-called multipath error envelope, a common way to illustrate code multipath errors. Figure 3-26 illustrates the coherent early-minus-late code discriminator and the resulting multipath error envelope for the GPS C/A code signal, assuming a chip spacing of 1 chip and a multipath relative amplitude of α=0.5. For the computation of the correlation function, a bandwidth of 16MHz was assumed.

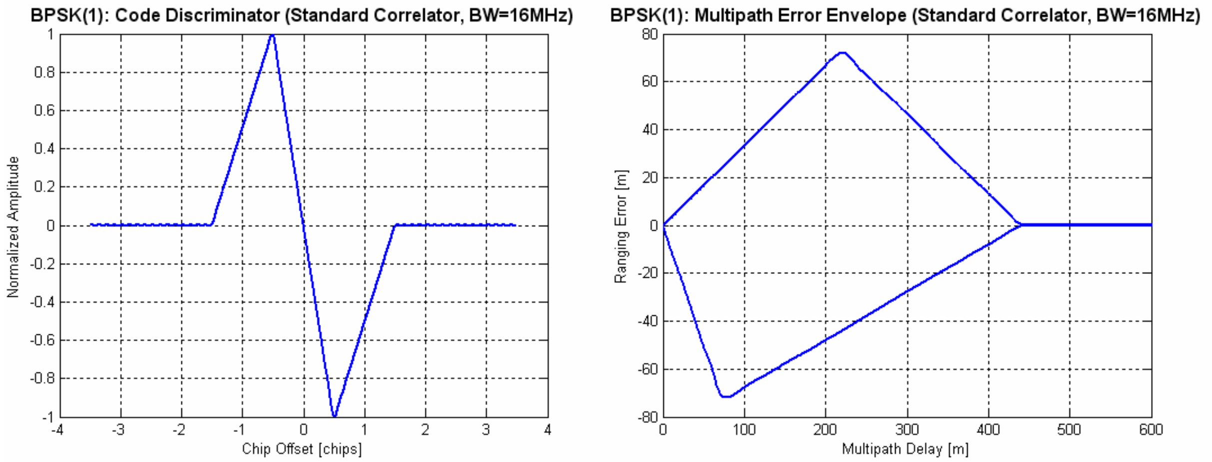

Figure 3-26: Coherent early minus late code discriminator and resulting multipath error envelope for a BPSK(1) signal representing the GPS C/A code. A chip spacing of d=1 and a multipath relative amplitude of α=0.5 have been assumed.

The multipath error envelopes for the non-coherent code discriminators are nearly the same as for the coherent case, so that the differences between the three discriminators with respect to their multipath performance are only marginal.

3.2.4 Carrier Multipath

Similar to the code discriminators, the phase discriminators can also be set up by inserting the expressions of the multipath affected correlator outputs into equations (54)-(56). Assuming that the navigation data bits have already been demodulated (D=1) and the multipath relative phase $\Delta\Phi_k+(\Delta\omega_k-\Delta\omega_0)t$ is subtracted from $\Delta\theta$ rather than added to it (as can be found in [KELLY et al. 2003] or [BRAASCH 1996]), the *arctangent* discriminator can be expressed as follows:

$$D_{Ph}(\Delta\theta)=\arctan\left(\frac{R(\Delta\tau)\sin(\Delta\theta)+\sum_{k=1}^{N}\alpha_k R(\Delta\tau-\tau_k)\sin[\Delta\theta-(\Delta\Phi_k+(\Delta\omega_k-\Delta\omega_0)t)]}{R(\Delta\tau)\cos(\Delta\theta)+\sum_{k=1}^{N}\alpha_k R(\Delta\tau-\tau_k)\cos[\Delta\theta-(\Delta\Phi_k+(\Delta\omega_k-\Delta\omega_0)t)]}\right) \quad (69)$$

By assuming one single multipath signal with the multipath relative amplitude of α_M, a path delay of τ_M, and by replacing $\Delta\Phi_k+(\Delta\omega_k-\Delta\omega_0)t$ with ϕ_M, equation (69) simplifies to

$$D_{Ph}(\Delta\theta)=\arctan\left(\frac{R(\Delta\tau)\sin(\Delta\theta)+\alpha_M R(\Delta\tau-\tau_M)\sin(\Delta\theta-\phi_M)}{R(\Delta\tau)\cos(\Delta\theta)+\alpha_M R(\Delta\tau-\tau_M)\cos(\Delta\theta-\phi_M)}\right) \quad (70)$$

The expected carrier multipath error can be obtained by zeroing the discriminator (i.e. $D_{Ph}(\Delta\theta)=0$). This equation holds true if the argument of the *arctan* function is zero.

$$\begin{gathered}\frac{R(\Delta\tau)\sin(\Delta\theta)+\alpha_M R(\Delta\tau-\tau_M)\sin(\Delta\theta-\phi_M)}{R(\Delta\tau)\cos(\Delta\theta)+\alpha_M R(\Delta\tau-\tau_M)\cos(\Delta\theta-\phi_M)}=0\\ \Leftrightarrow\\ R(\Delta\tau)\sin(\Delta\theta)+\alpha_M R(\Delta\tau-\tau_M)\sin(\Delta\theta-\phi_M)=0\end{gathered} \quad (71)$$

Equation (71) can be solved for the carrier tracking error $\Delta\theta$, which can be expressed as follows:

$$\Delta\theta = \arctan\left(\frac{\alpha_M R(\Delta\tau - \tau_M)\sin(\phi_M)}{R(\Delta\tau) + \alpha_M R(\Delta\tau - \tau_M)\cos(\phi_M)}\right) \tag{72}$$

The carrier multipath error $\Delta\theta$ depends on the multipath relative amplitude α, the correlation function R and the geometric path delay τ_M. In case that no code multipath is considered ($R(\Delta\tau)=R(\Delta\tau-\tau_M)=1$), equation (72) simplifies to the well-known expression

$$\Delta\theta = \arctan\left(\frac{\alpha_M \sin(\phi_M)}{1 + \alpha_M \cos(\phi_M)}\right). \tag{73}$$

This expression is identical to the carrier multipath error derived in section 3.1.2 (see derivation of equation (8)). The resulting carrier phase error as a function of the multipath relative phase is illustrated in Figure 3-2. The carrier multipath errors for the GPS L1 signal as a function of the geometric path delay is shown in the following diagram (derived from equation (72) and expressed in [chips]). The multipath relative phase ϕ_M was computed strictly from the geometric path delay τ_M ($\phi_M=2\pi\tau_M/\lambda$).

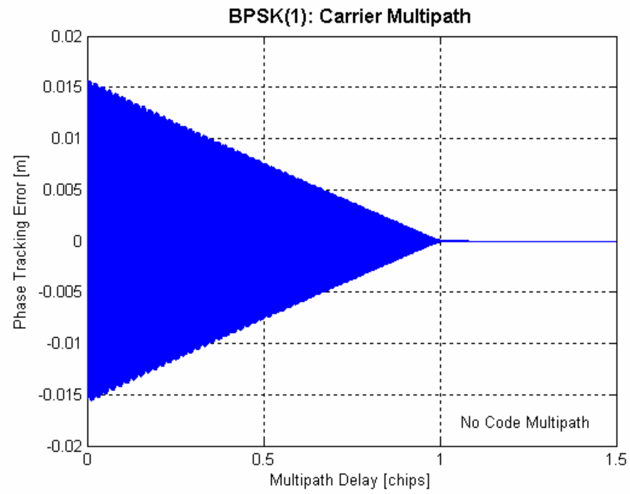

Figure 3-27: Expected carrier multipath errors for the GPS L1 signal assuming a multipath relative amplitude of α_M=0.5.

It should be noted that the Costas detector (which is not addressed in detail in this section) shows the same behavior as the *arctangent* detector.

3.2.5 Mean Multipath Errors

Using the notation of equation (72) and assuming the presence of one single multipath signal only, the coherent early-minus-late code discriminator can be expressed as follows:

$$\begin{aligned} D_C(\Delta\tau) &= A[R(\Delta\tau - \frac{d}{2}) - R(\Delta\tau + \frac{d}{2})]\cos(\Delta\theta) \\ &+ A\alpha_M[R(\Delta\tau - \tau_M - \frac{d}{2}) - R(\Delta\tau - \tau_M + \frac{d}{2})]\cos(\phi_M - \Delta\theta) \end{aligned} \tag{74}$$

The $\cos(\phi_M - \Delta\theta)$ term is responsible for the fact that the code multipath errors do not average out to zero over time, i.e. that the expected long-term mean multipath error is different from zero. This term becomes negative only if the difference between the multipath relative phase ϕ_M and the phase tracking error $\Delta\theta$ is larger than 90°, otherwise the cosine term becomes positive. Figure 3-28 illustrates the regions for which the phase differences are larger and smaller than 90°.

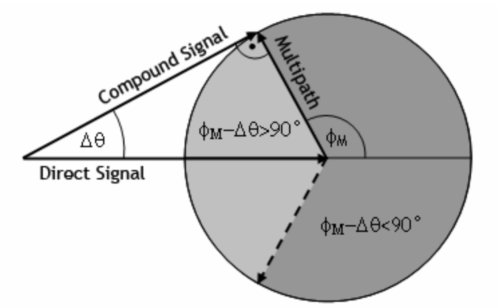

Figure 3-28: Regions where the cosine of the difference between the multipath relative phase ϕ_M and the multipath error $\Delta\theta$ becomes negative (light grey) and positive (dark grey). A similar diagram can be found in [KELLY et al. 2003].

The region for which the phase difference is smaller than 90° and the term $cos(\phi_M - \Delta\theta)$ becomes positive is larger than the region for which the cosine term is negative. Assuming that the multipath relative phase ϕ_M varies constantly with time, the cosine term (and thus the resulting multipath errors) will be positive when averaging over a sufficiently long period of time (several cycles).

4. Multipath Mitigation Techniques

This chapter provides an overview on the most important approaches for multipath mitigation. Although the main focus is on receiver-internal techniques, the use of post-processing techniques or special antennas for multipath mitigation is considered as well. The chapter starts with a description of the most common mitigation techniques for code multipath.

Throughout this chapter, the BPSK(1) (representing the current GPS C/A-Code) signal is used to illustrate the multipath performance of each technique. For the computation of the underlying correlation function and code discriminators, a pre-correlation bandwidth of 16 MHz and an ideal band-pass filter is assumed. A detailed multipath performance which also considers future Galileo signals can be found in section 5.2.

4.1 Mitigation of Code Multipath

4.1.1 Narrow Correlation

The first approach to reduce multipath effects is the narrow correlation technique. This technique has been introduced to GPS receivers by NovAtel Inc. Instead of using a standard correlator with a chip spacing of 1 chip between early and late code, the term “narrow correlation” typically indicates the use of any chip spacing less than d=1. One of the basic papers on this tracking technique ([Van Dierendonck et al. 1992]) suggests a spacing of d=0.1 chips to build up the discriminator function. This value can also be found in many other publications. The code discriminator and the corresponding multipath performance for the 0.1-chip Narrow Correlator is illustrated in Figure 4-1.

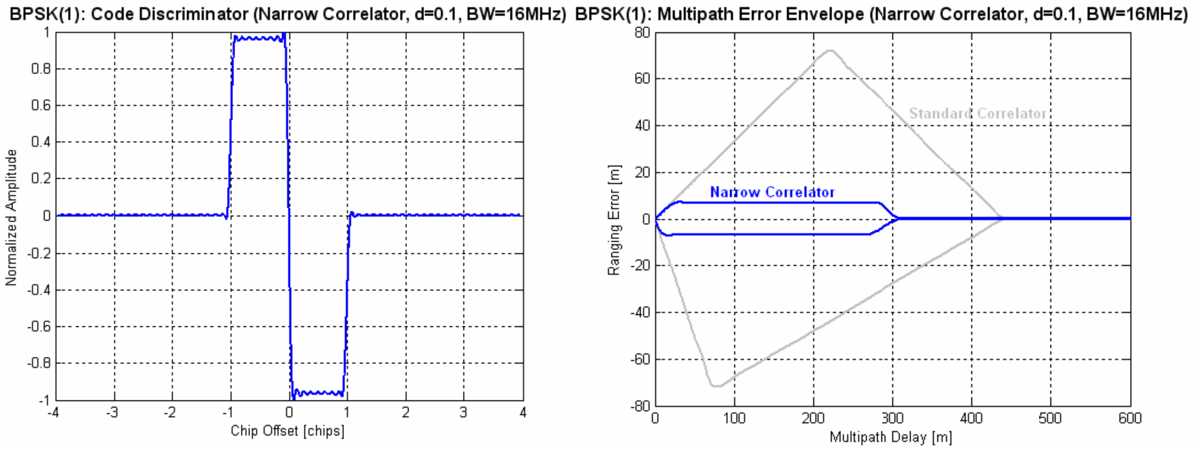

Figure 4-1: Code discriminator and multipath error envelope for the 0.1 chip Narrow Correlator. For comparison, the multipath error envelope of the standard (wide) correlator is also plotted (gray curve).

Compared to the standard correlation technique, the multipath performance can be enhanced significantly by using the narrow correlation technique. The maximum multipath error is proportional to the chip spacing *d*, so that by using a spacing of d=0.1, the maximum ranging error can be reduced by a factor of ten compared to the wide correlator (d=1). Another advantage of the Narrow Correlator is that the ranging error becomes zero at a geometric path delay of about 1 chip. The wide correlator, on the other hand is sensitive to path delays up to 1.5 chips. Moreover, the narrow correlator shows less thermal noise than the standard correlator, because the influence of thermal noise is also directly proportional to the chip spacing (see e.g. [Van Dierendonck 1996]).

4.1.2 Double Delta Correlator

The term "Double Delta (ΔΔ) Correlator" is a general expression for special code discriminators which are formed by two correlator pairs instead of only one. The general tracking concept is described in detail in [McGraw and Braasch 1999], where this type of correlator is called "High Resolution Correlator" (HRC). As will be discussed below, also Ashtech's Strobe Correlator™ and NovAtel's Pulse Aperture Correlator™ (PAC) are implementations of the ΔΔ correlation concept.

4.1.2.1 High Resolution and Strobe Correlator

The ΔΔ code discriminator can be set up by forming a linear combination of two early and two late correlators. The basic concept is illustrated in Figure 4-2, where the spacing between E_1 and L_1 is referred to as *d* and the spacing between E_2 and L_2 is assumed to be 2*d*.

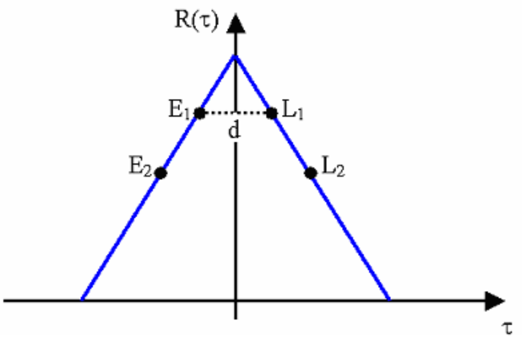

Figure 4-2: General concept of the ΔΔ correlator.

In general, several code discriminators may be set up by forming different combinations out of these 4 correlators. In [McGraw and Braasch 1999], the following combination was used to build up the code discriminator D_{HRC}:

$$D_{HRC} = (E_1 - L_1) - \frac{1}{2}(E_2 - L_2) \tag{75}$$

Since the differences $(E_1\text{-}L_1)$ and $(E_2\text{-}L_2)$ can be interpreted as narrow correlators, equation (75) can be rewritten as follows:

$$D_{HRC} = \text{Narrow}(d) - \frac{1}{2}\text{Narrow}(2d) \tag{76}$$

This discriminator function has the same shape as that of the Strobe Correlator™, which has been introduced to Ashtech's GPS receivers. With consideration of the chip spacing definition used above, the Strobe Correlator™ ([Garin and Rousseau 1996], [Garin et al. 1997]) can be expressed as follows:

$$\begin{aligned} D_{STROBE} &= 2\text{Narrow}(d) - \text{Narrow}(2d) \\ &= 2 \cdot (E_1 - L_1) - (E_2 - L_2) \\ &= 2 \cdot D_{HRC} \end{aligned} \tag{77}$$

The code discriminators represented by equations (76) and (77) are illustrated in Figure 4-3. There, a chip spacing of *d*=0.1 between E_1 and L_1 has been assumed (as introduced in [Garin et al. 1997], smaller spacings such as *d*=0.05 are also suggested in some publications):

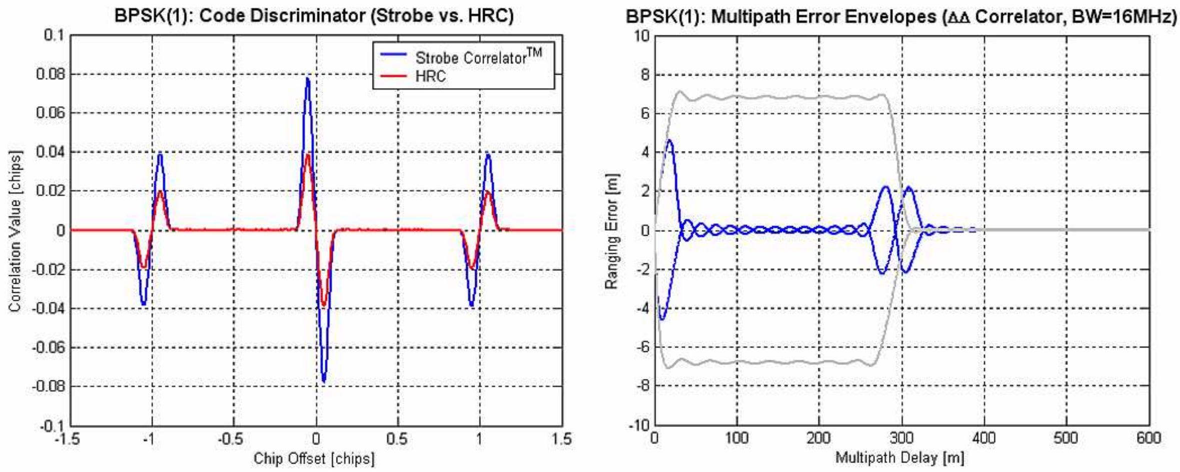

Figure 4-3: Code discriminators and multipath error envelopes for the ΔΔ correlator (chip spacing between E1 and L1: d=0.1). Note the multipath error envelope of the 0.1-chip Narrow Correlator (gray curve) for comparison.

Since the code multipath performance only depends on the shape of the discriminator function and not on its relative amplitude, both discriminators will result in identical code multipath error envelopes. The resulting code multipath performance for the ΔΔ correlator is also illustrated in Figure 4-3.

The ΔΔ correlator exhibits a very good overall multipath performance. It is only sensitive to short- and long-delay multipath and results in small maximum ranging errors. For path delays between 40 and 250m, the multipath error is almost zero. Note that this behavior is not representative for all kinds of GNSS signals. In case that BOC signals are used, the multipath error envelopes will show additional peaks for medium-delay multipath.

Another implementation of the ΔΔ correlator seems to be the Pulse Aperture Correlator^{TM} (PAC) introduced by NovAtel Inc. Although no technical details about this correlation technique have been published, a closer look at the multipath error envelope (published in [NovAtel Inc. 2002] reveals a high degree of similarity to the performance of the ΔΔ correlator.

4.1.2.2 Narrow Correlator^{TM} vs. HRC/Strobe

Both the Narrow and the Strobe correlation technique result in maximum ranging errors of the same order of magnitude. It can be shown, however, that the observations obtained with the Narrow Correlator^{TM} are less noisy than the Strobe/HRC observations. A detailed noise analysis carried out in [McGraw and Braasch 1999] indicates that there is a 3dB noise penalty for the HRC compared to a conventional dot product code detector.

This result has been verified by means of two receivers operating with narrow and Strobe correlation techniques, respectively. Both receivers were connected to the same antenna. The observations which were expected to be affected by multipath were processed on a “code minus carrier” basis (CMC) to visualize the signal variations caused by multipath. The resulting CMC residuals for both correlation techniques are illustrated in Figure 4-4. They are nearly identical in shape and amplitude so that both diagrams show a high degree of correlation. The only significant difference between the two data sets is that the Strobe observations show a significantly increased influence of noise.

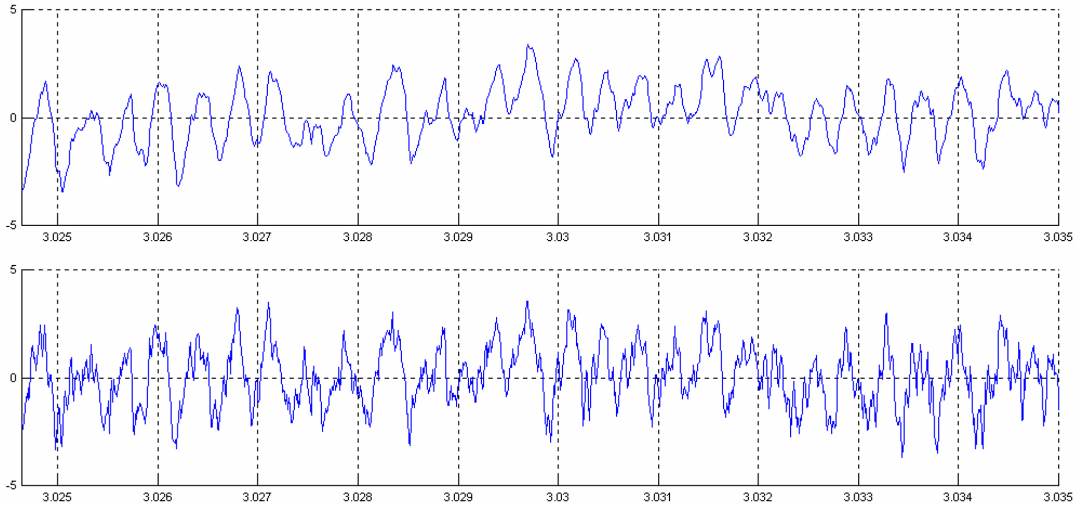

Figure 4-4: Example of code multipath, recorded simultaneously with two receivers using the narrow correlator (upper diagram) and the Strobe correlator (lower diagram), respectively.

4.1.3 Early Late Slope Technique (ELS)

This multipath mitigation technique can be easily explained by considering the signal's correlation function. The general idea is to determine the slope at both sides of the correlation function's central peak ([TOWNSEND and FENTON 1994]). Once both slopes are known, they can be used to compute a pseudorange correction *T* that can be applied to the measured pseudorange. This mitigation technique has temporarily been used in some of NovAtel's GPS receivers, where it has been called "Multipath Elimination Technique". In the following, the computation of the pseudorange correction will be described in detail.

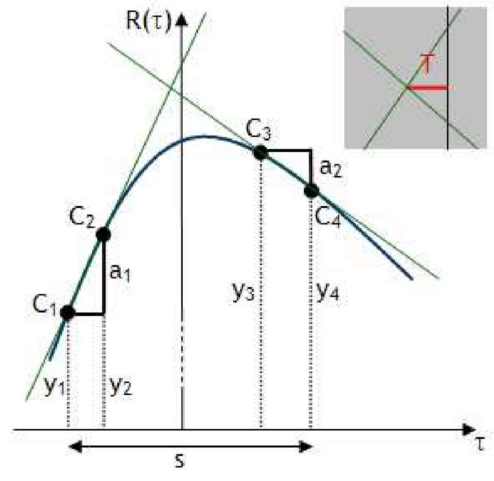

Figure 4-5: Computation of a pseudorange correction *T* by analyzing the slopes on both sides of the correlation function.

The slope on each side of the correlation function is determined by means of 4 correlators (C_1…C_4) which have dedicated τ-coordinates (τ_1…τ_4). These correlators are used to determine the corresponding correlation values (y_1…y_4). By use of (τ_1…τ_4) and (y_1…y_4), the slopes a_1 and a_2 can be determined. With that information, two first order polynomials (defined by C_1, C_2 and C_3, C_4, respectively) can be set up. The τ-coordinate of the intersection of these two straight lines can be determined as follows ([TOWNSEND and FENTON 1994]):

$$T = \frac{y_1 - y_2 + {}^{s}\!/_{2}\,(a_1 + a_2)}{a_1 - a_2} \tag{78}$$

Figure 4-5 illustrates the peak of a (band-limited) correlation function which is distorted due to the influence of multipath. As a result, the correlation peak is not at τ=0. The multipath performance of this technique can be determined by comparing the pseudorange correction *T* with the actual peak location. It turns out that the shape of the resulting error envelopes strongly depends on the correlator positions. In order to illustrate this fact, the following envelopes for the BPSK(1) signal have been plotted with different correlator configurations:

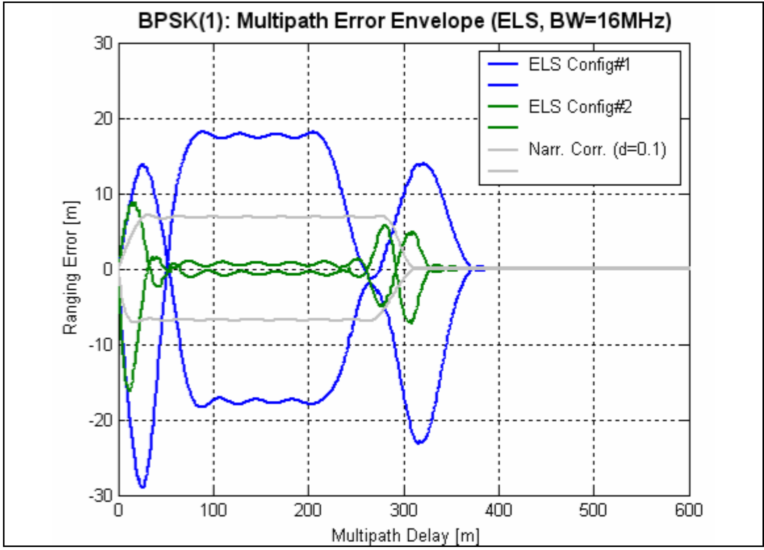

Configuration	
#1	#2
τ_1 = -0.25	τ_1 = -0.10
τ_2 = -0.10	τ_2 = -0.06
τ_3 = +0.10	τ_3 = +0.06
τ_4 = +0.25	τ_4 = +0.10

Figure 4-6: Multipath error envelopes for two different ELS implementations. Note the multipath error envelope of the 0.1-chip Narrow Correlator (gray curve) for comparison.

Obviously, there are significant differences with respect to the multipath performance subject to the used correlator configuration. Whereas the multipath performance for configuration #1 is much poorer compared to that of the 0.1-chip Narrow Correlator, configuration #2 leads to much better results, especially in case of medium-delay multipath. As a result, the multipath error envelopes obtained with this technique are only valid for a given correlator configuration and different configurations should be used for different signals to optimize their multipath performance.

4.1.4 Early/Early Tracking (Version 1)

The basic concept of this correlation technique can be found in [Van Dierendonck and Braasch 1997]. The main purpose is to find a tracking point that is not distorted by multipath. To achieve this, two correlators E_1 and E_2 are located on the early slope of the correlation function. A graphical illustration of this concept is given in Figure 4-7:

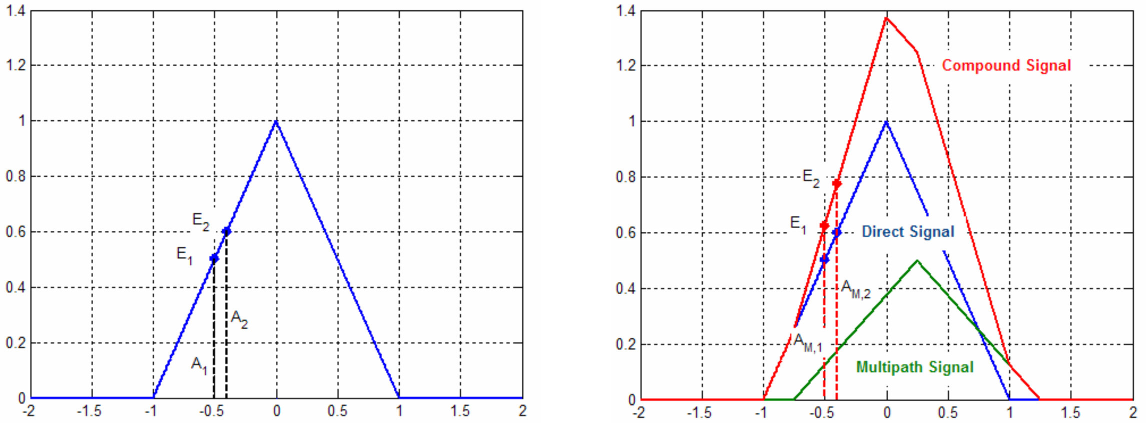

Figure 4-7: Basic E_1/E_2 tracking concept.

In case that the actual position of the two correlators E_1, E_2 and the shape of the correlation function is known, the amplitudes at both correlator positions can be used to set up an error function for this correlation technique.

In case that the undistorted correlation function (blue curve) is considered first, the amplitudes of both correlators are given by A_1 and A_2, respectively. The ideal ratio of both amplitudes can be expressed by $R=A_2/A_1$ (undistorted case, no multipath present). In the presence of multipath, however, the actual amplitudes $A_{M,1}$ and $A_{M,2}$ will be observed. The resulting ranging error can then be computed by means of the following error function ([Van Dierendonck and Braasch 1997]):

$$\Delta R = A_{M,2} - R \cdot A_{M,1} \tag{79}$$

If the resulting correlation function is undistorted between E_1 and E_2, the error function becomes $\Delta R=A_2-(A_2/A_1)A_1=0$. Since multipath signals always arrive after the direct signal, the very first portion of the correlation function's leading edge will not be distorted. From this point of view, it is desirable to set E_1 and E_2 as early as possible to avoid short delay multipath. On the other hand, the noise performance suffers when E_1 and E_2 are shifted to the left slope of the correlation function. As a result, a trade-off between multipath and noise mitigation is necessary (see [Van Dierendonck and Braasch 1997]).

The performance of this multipath mitigation technique is illustrated in Figure 4-8 (blue curve). The tracking point was set to τ=-0.5 and a chip spacing between E_1 and E_2 of 0.1 chip was assumed so that the two correlators are located at τ_1=-0.55 and τ_2=-0.45, respectively.

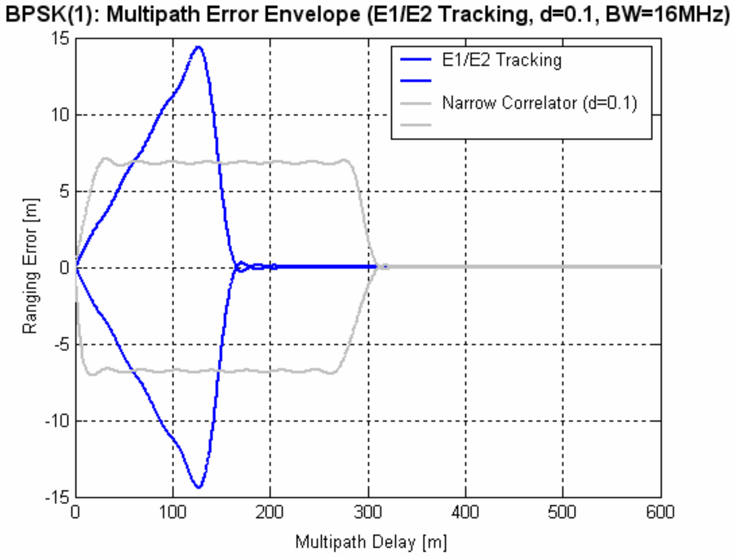

Figure 4-8: Multipath error envelope for BPSK(1), processed with an E_1/E_2 tracker (tracking points τ_1=-0.55 and τ_2=-0.45). Note the multipath error envelope of the 0.1-chip Narrow Correlator (gray curve) for comparison.

As expected, the resulting ranging error decreases to zero for geometric path delays of greater than approximately 1+E_2 (expressed in [m]), in this case for path delays grater than ~160m. Compared to the 0.1-chip Narrow Correlator, the E_1/E_2 tracker produces significantly larger ranging errors but, on the other hand, is less sensitive to short-delay multipath.

4.1.5 Early/Early Tracking (Version 2)

Another implementation which is different from this basic approach can be found in [Mattos 1996]. Implementation details are also discussed in [Winkel 2003]. The implementation uses two early correlation functions $R_{E1}(\tau)$ and $R_{E2}(\tau)$ at the points E_1 and E_2 to set up the following discriminator function:

$$D(\tau) = \eta - \frac{R_{E2}(\tau)}{R_{E1}(\tau)} \tag{80}$$

For a given tracking point τ_0, the parameter η can be expressed as follows [Winkel 2003]:

$$\eta = \frac{\tau_0 - d + T_c}{\tau_0 + T_c} \tag{81}$$

with d being the correlator spacing between E_1 and E_2 and T_c the chip length of code. The discriminator function and the resulting multipath error envelopes for this implementation of the E_1/E_2 tracker are illustrated in Figure 4-9. For both diagrams, the correlator spacing is d=0.1 and the tracking point is set to τ_0=-0.5.

Figure 4-9 also illustrates the multipath error envelope for the 0.1-chip Narrow Correlator (grey curve). Note that the E_1/E_2 tracker outperforms the narrow correlator implementation for all geometric path delays.

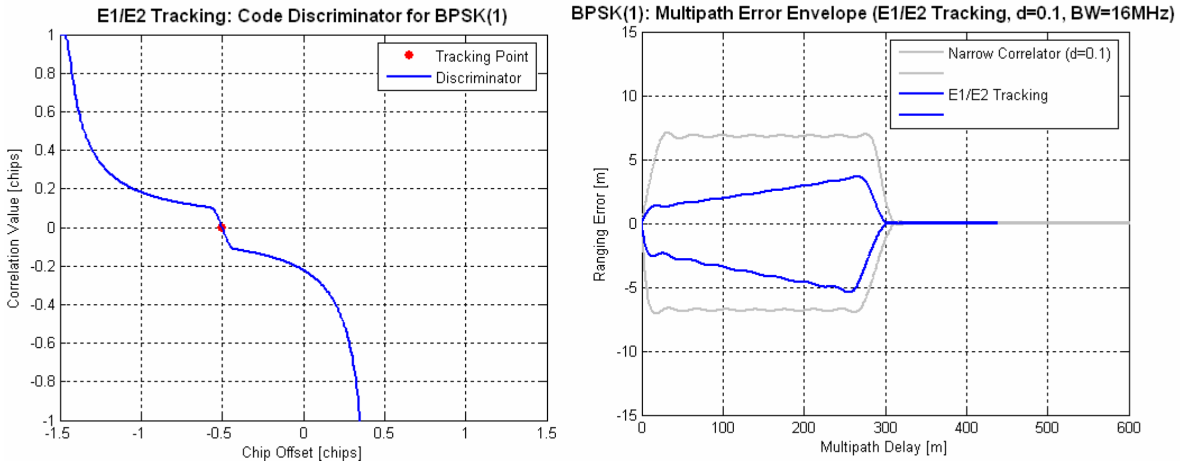

Figure 4-9: Code discriminator (left diagram) and multipath error envelope (right diagram) for BPSK(1), processed with an E_1/E_2 tracker, tracking point τ=-0.5 chips, d=0.1 chips.

4.1.6 Nth Derivative Correlator

The discriminator function for this correlation technique is built up by taking the n^{th} derivative of the correlation function. As long as n is an odd number, the (undistorted) discriminator function is zero at the tracking point. In general, it is also possible to use higher-order derivatives of the correlation function (e.g. the 3rd derivative) or linear combinations of several derivatives. For the following illustrations, the 1st derivative of the correlation function is used as discriminator function.

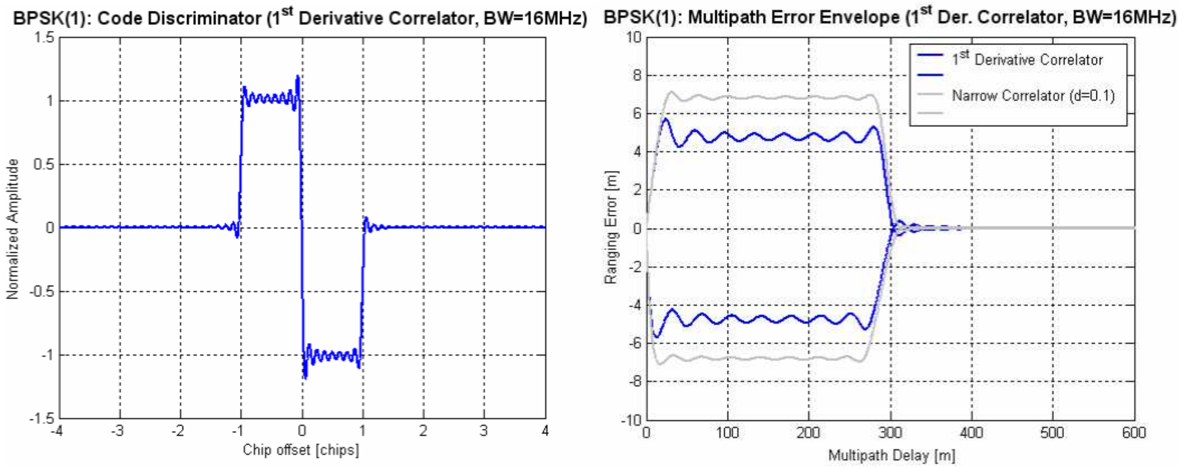

Figure 4-10: Code discriminator and multipath error envelope for the 1st Derivative correlator. Note the multipath error envelope of the 0.1-chip Narrow Correlator (gray curve) for comparison.

Compared to the 0.1-chip Narrow Correlator, the first derivative correlator shows a similar behavior, producing slightly smaller maximum ranging errors over the entire range of geometric path delays. The concept of using a derivative of the correlation function to set up a code discriminator is related to the technique of using modified correlator reference waveforms to mitigate multipath ([WEILL 1997b]).

4.1.7 Carrier Smoothing

4.1.7.1 Smoothing Algorithm

By means of simultaneous processing of code and carrier observations, both measurements can be combined to obtain a "carrier smoothed pseudorange". This approach benefits from the fact that the carrier observations are less affected by noise compared to the code observations and are thus more accurate. Therefore, code noise (and code multipath) can be significantly reduced by means of the carrier smoothing process. The smoothing algorithm can be expressed as follows (see e.g. [LUO et al. 2000]):

$$\begin{gathered} PR_{sm}(k) = \left[\frac{1}{B}\right] PR_{raw}(k) + \left[\frac{B-1}{B}\right] PR_{proj}(k) \\ PR_{proj}(k) = PR_{sm}(k-1) + \underbrace{\phi(k) - \phi(k-1)}_{\Delta PR(k)} \\ B = \frac{S}{T} \end{gathered} \tag{82}$$

Equation (82) makes use of the following notations:

k	Current epoch
$PR_{raw}(k)$	Observed pseudorange at epoch k
$PR_{sm}(k)$	Smoothed pseudorange at epoch k
$PR_{proj}(k)$	Projected pseudorange at epoch k, computed as the sum of the previous smoothed pseudorange and the difference $\Delta PR(k)$ between successive pseudoranges derived from successive carrier observations $\phi(k)$ and $\phi(k-1)$
S	Smoothing time constant [s]
T	Data update interval [s]

According to equation (82), the smoothed pseudoranges are a weighted average of the observed and already smoothed pseudoranges. The basic smoothing concept was first introduced by R. Hatch and it is therefore often termed as Hatch-Filter ([HATCH 1986]). The result of such a smoothing process is illustrated in Figure 4-11, where code noise is smoothed by using different time constants. The data update interval is T=1s in all cases.

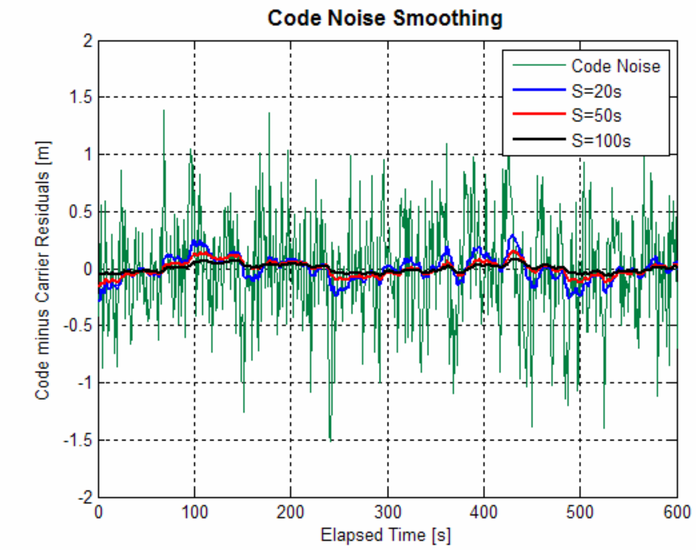

Figure 4-11: Smoothing of code noise by using different time constants.

It is obvious that the smoothed code noise depends on the time constant *S*. Longer time-constants generally result in better smoothing performance. However, this is only true as long as the ionospheric path delay is more or less constant during the smoothing process. If the ionospheric path delay varies, the performance of the smoothing process is always limited. Such aspects will be described in section 4.1.7.2. In addition to the smoothing of code noise, this method can also be used to smooth out signal variations caused by code multipath. Figure 4-12 illustrates a multipath smoothing process. Again, time constants of 20s, 50s and 100s are used.

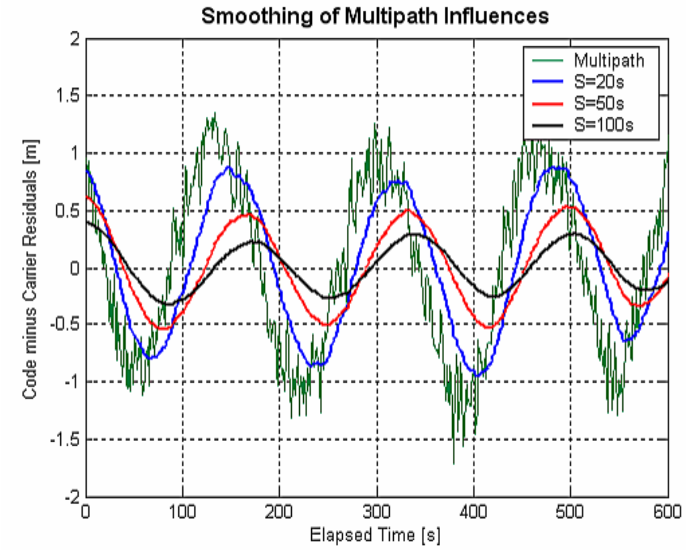

Figure 4-12: Smoothing of code multipath by using different time constants.

It is obvious that the multipath amplitudes can be reduced significantly by means of the smoothing process. As it is the case for code noise smoothing, the performance of the smoothing process in the presence of multipath depends on the smoothing time constant *S*. The longer these time constants the more efficient the reduction of occurring multipath amplitudes.

4.1.7.2 Theoretical Accuracy and Performance Limitations

4.1.7.2.1 Standard Deviation of Smoothed Pseudoranges

Summarizing the different parts of equation (82), the *kth* smoothed pseudorange can be expressed as follows:

$$PR_{sm}(k) = \left(\frac{1}{B}\right) PR_{raw}(k) + \left(\frac{B-1}{B}\right)\left[PR_{sm}(k-1) + \Delta PR(k)\right] \tag{83}$$

Based on equation (83) and the law of error propagation, the theoretical standard deviation of a smoothed pseudorange can be derived. Assuming that the observed pseudorange PR_{raw}, the $(k\text{-}1)^{th}$ smoothed pseudorange $PR_{sm,k-1}$ and the pseudorange difference ΔPR_{k-1} are uncorrelated, the variance of the k^{th} smoothed pseudorange can be expressed as follows:

$$\sigma^2_{sm,k} = \left(\frac{1}{B}\right)^2 \sigma^2_{raw} + \left(\frac{B-1}{B}\right)^2 \sigma^2_{sm,k-1} + \left(\frac{B-1}{B}\right)^2 \sigma^2_{\Delta PR,k-1} \tag{84}$$

Equation (84) can be simplified by assuming that the variance of the k^{th} and the $(k\text{-}1)^{th}$ smoothed pseudorange are the same:

$$\sigma^2_{sm,k} = \sigma^2_{sm,k-1} \tag{85}$$

Furthermore, error-free pseudorange differences can be assumed:

$$\sigma^2_{\Delta PR,k-1} = 0 \tag{86}$$

This is a valid approximation, because the ΔPRs are derived from carrier observations which are much more accurate than the code observations. After these simplifications, equation (84) takes on the following form:

$$\sigma^2_{sm,k} = \left(\frac{1}{B}\right)^2 \sigma^2_{raw} + \left(\frac{B-1}{B}\right)^2 \sigma^2_{sm,k} \tag{87}$$

After solving this equation for $\sigma_{sm,k}$, the standard deviation of the k^{th} smoothed pseudorange can be expressed as

$$\sigma_{sm,k} = \sqrt{\frac{1}{2B-1}}\sigma_{raw} = \sqrt{\frac{T}{2S-T}}\sigma_{raw} \approx \sqrt{\frac{T}{2S}}\sigma_{raw}\,. \tag{88}$$

The last simplification accounts for the fact that the smoothing time constant S is usually much larger than the data update interval T. The same result can be found in [HWANG 1998].

4.1.7.2.2 Limitations

In general, the carrier smoothing process is an effective way of reducing code noise and code multipath. In some cases, however, the smoothing process will cause undesired errors. In the following, three critical aspects will be discussed in more detail, namely the influence of slow multipath variations, ionospheric influences and effects of signal dynamics on the smoothing process in the presence of multipath.

Frequency of Multipath Variations. Assuming a static user, the frequency f_M of the multipath variations strongly depends on the actual satellite-reflector-receiver geometry. The expected frequencies of multipath variations have already been computed in section 3.1.4. It has been shown that the variations become more rapid if the distance between the reflector and the receiver increases. Equation (22) provides a general expression for the frequency of multipath variations. Assuming that the satellite and the reflector have the same azimuth angle (A^S-A_R=0), equation (22) simplifies to:

$$f_M(t) = \frac{d_H}{\lambda \cos E_R} \frac{dE^S(t)}{dt} \left\{ \cos E_R \sin[E^S(t)] - \sin E_R \cos[E^S(t)] \right\} \qquad (89)$$

For a rough assessment of occurring frequencies, mean values for the satellite elevation angle and the rate of change of this angle can be considered. In section 3.1.4, a mean rate of change of the satellite elevation of ~0.000105 rad/s has been derived from a typical satellite pass. Assuming a mean satellite elevation angle of E^S=45°, a carrier wave length of 0.19m and a reflector elevation of E_R=10°, the following multipath periods/frequencies can be computed for various antenna-reflector distances d_H:

Horizontal distance d_H from reflector	1 m	2 m	5 m	10 m
Period *T* of multipath variations	~52 min	~26 min	~ 10 min	~ 5 min
Frequency *f* of multipath variations	0.0003 Hz	0.0006 Hz	0.0016 Hz	0.0032 Hz

Table 4-1: Expected frequencies of multipath variations.

With respect to the carrier smoothing process, these very long multipath periods occurring for short-delay multipath may cause problems. For many applications, a smoothing time constant of 100s is proposed (e.g. in [RTCA 1993]). This value can also be found in many other publications, especially in publications related to airborne GNSS applications. The problem is that such a relatively small smoothing constant cannot effectively smooth out multipath variations with long periods as those listed in Table 4-1. This effect is illustrated in Figure 4-13, where the result of two carrier smoothing simulations is shown. The first simulation (left diagram) considers high-frequency multipath variations whereas the second one (right diagram) bases on a multipath period of 960s, corresponding to a horizontal distance d_H of approximately 3.2m from the reflector. For both simulations, a time constant of *S*=100s has been used and the amplitude of the multipath variations is assumed to be 3m.

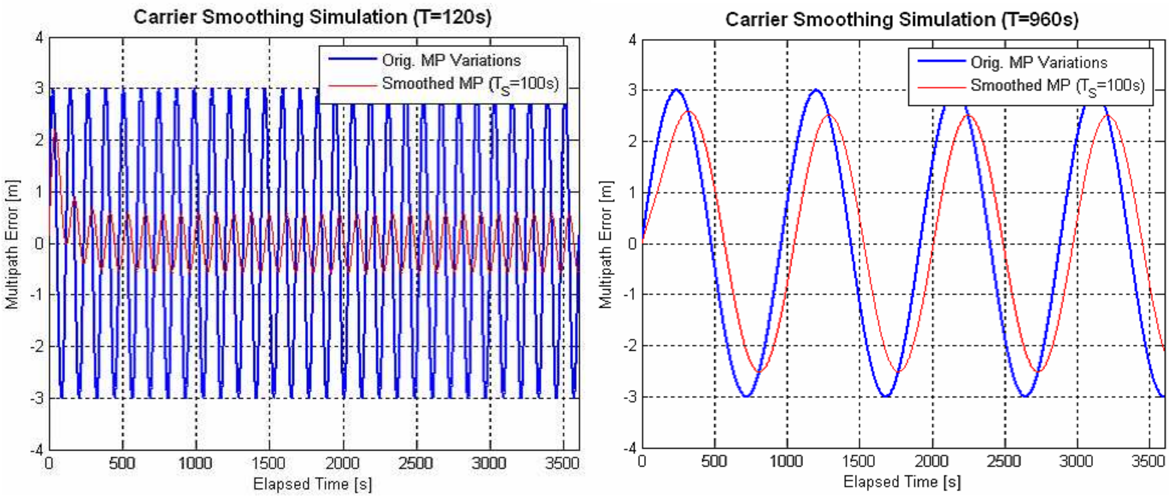

Figure 4-13: Efficiency of the carrier smoothing process for different frequencies of multipath (the same smoothing constants of T_S=100s have been used for both simulations).

Figure 4-13 clearly visualizes the problems that occur when applying the carrier smoothing process with relatively short smoothing constants to very slow-varying multipath. In this case, the multipath variations cannot be reduced significantly (right diagram). On the other hand, high-frequency multipath, which generally occurs for longer path delays, can be reduced significantly (left diagram). It should be noted that the smoothing efficiency does not depend on the amplitude of the multipath variations. As a result, it is uncertain that smoothing short-delay multipath with relatively short time constants results in a significant performance enhancement. One possible solution is to use longer time constants. However, this may lead to ranging errors in case of varying ionospheric conditions.

Ionospheric Influences. One well-known impact on the carrier smoothing performance are smoothing errors due to varying ionospheric conditions. This aspect has been addressed in several publications. An extensive discussion of this subject is provided in [HWANG 1998], where it is shown that ionospheric influences result in residual ranging errors that are proportional to the smoothing time constant. According to [HWANG 1998], the resulting ranging error ΔI caused by a time-varying ionospheric divergence I_d [m/s] depends on the smoothing time constant S and can be expressed as follows:

$$\Delta I = 2 \cdot S \cdot I_d \tag{90}$$

The effect is illustrated in Figure 4-14, where the ionospheric divergence trend has been visualized by computing code minus carrier residuals (green curve). The time series has been smoothed by using different time constants. The residual smoothing errors are due to the fact, that the smoothing process cannot "follow" the ionospheric trend. This results in significant ranging errors which become larger when the time constant is increased.

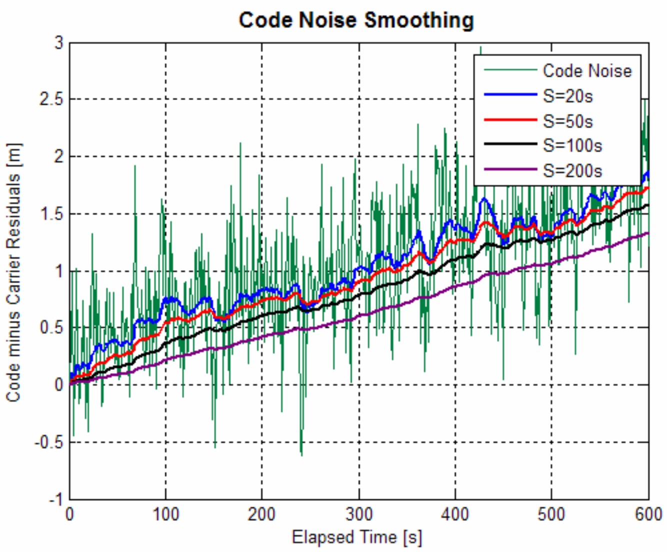

Figure 4-14: Effect of time-varying ionospheric conditions on the carrier smoothing process.

Obviously, the code noise can be smoothed more efficiently by using longer time constants. On the other hand, with an increasing smoothing constant, the residual smoothing error also increases. That's why constants of no more than 100s are normally used for the smoothing process. In general, it is difficult to predict actual ionospheric conditions for a given location at a given point in time. However, time-varying ionospheric conditions degrading the carrier smoothing performance must be expected in the following cases:

- Observations during hours around sunrise and sunset due to diurnal variations of the electron density
- In case of the occurrence of geomagnetic storms (frequently occurs in years of increased solar activity)

- Observations in regions along the magnetic equator (in this area, the strongest large-scale TEC gradients can be observed)
- Occurrence of Medium-Scale Traveling Ionospheric Disturbances (MSTIDs) that can be observed frequently even in mid-latitude regions ([WANNINGER 2000])

As a result, temporal ionospheric variations are expected to occur frequently; they cannot be assumed to be non-existent from the outset. For a single-frequency user, varying ionospheric conditions cause additional issues with respect to reducing multipath effects. As it has been shown in the previous section, rather long smoothing constants (e.g. several hundred seconds) must be used to reduce short-delay multipath effects effectively. On the other hand, in order to avoid ranging errors due to ionospheric effects, relatively low time constants are needed. As a result, in case that the user has to deal with short-delay multipath and varying ionospheric conditions, it is impossible to get a significant performance enhancement by the carrier smoothing process; carrier smoothing becomes nearly worthless in such cases. The reasons can be summarized as follows:

- If a small smoothing constant is used, ionospheric influences become less important but low-frequency multipath variations cannot be smoothed out effectively.
- If a very large smoothing constant is used, even low-frequency multipath variations can be smoothed out, but, on the other hand, a relatively large additional error is induced by the ionospheric influences.

It must be stated, however, that this quandary can be solved by using dual frequency measurements. By this measure, the ionospheric influence can be removed and large smoothing constants can be used without producing significant residual errors ([HWANG 1998]). However, even in the future, not every user will be equipped with a dual frequency receiver. In such a case, the issues mentioned above cannot be overcome easily.

Signal Dynamics. So far, the discussions on the potential of carrier smoothing for mitigating multipath assumed that the multipath variations change relatively slowly. This assumption holds true in case of static or low dynamic conditions. In high dynamic environments, however, the impact of multipath differs from that observed in static or low dynamic cases. The actual multipath performance in a dynamic environment strongly depends on the occurring multipath phase rates. An extensive analysis of the effect of high multipath phase rates can be found in [KELLY et al. 2003]. According to this publication, the influence of a slowly varying multipath phase is negligible; that's why techniques like carrier smoothing can generally reduce multipath variations (except for the situations discussed above). However, as can be shown, certain fast multipath phase rates can induce ranging biases which depend on the actual DLL implementation (coherent vs. non-coherent). According to [KELLY et al. 2003], fading frequencies can be grouped into the categories listed in Table 4-2:

Cat. No.	Category	Characterization	Impact
1	Slow-fading multipath	Multipath relative Doppler shift smaller than the DLL loop noise bandwidth	Time-varying range errors
2	Fast-fading multipath	Multipath relative Doppler shift larger than the DLL loop noise bandwidth	Loop filter removes multipath variations through averaging, but range biases may occur
3	Very fast-fading multipath	Relative Doppler larger than accumulation rate of correlators (betw. 50 and 1000Hz)	No impact, multipath averaged out completely

Table 4-2: Categories of multipath fading frequencies.

Cat. 1 multipath is the one that has been discussed extensively so far. The time-varying errors produced by this type of multipath can in general be reduced by techniques like carrier smoothing. On the other hand, Cat.3 multipath has no impact on the multipath performance, because multipath variations are completely averaged out during the tracking process. As it is shown in [KELLY et al. 2003], Cat. 2 multipath results in range biases which depend on the geometric path delay, the multipath relative amplitude and the type of DLL used for tracking. For a non-coherent (early-minus-late power) DLL, a signal-to-multipath ratio (SMR) of 3dB and a fading frequency of 10Hz, biases of up to 7.5m have been observed for short-delay multipath. Since this type of multipath signal does not result in (periodic) signal variations, it cannot be reduced by carrier smoothing. As a result, when considering dynamic environments, significant multipath errors (up to several meters) can occur that cannot be smoothed out.

4.1.7.3 Summary

The previous section tried to highlight the limitations and shortcomings of the carrier smoothing approach. It became clear that carrier smoothing is not a suitable approach for reducing multipath effects in any situation. Especially in environments with very short-delay multipath signals and changing ionospheric conditions, there is no suitable time constant that ensures significant reduction of multipath influences. The benefits and drawbacks of using carrier smoothing for multipath mitigation are summarized in the following table:

Benefits	Drawbacks
Significant reduction of multipath effects (in case that the smoothing time constant is large enough compared to the frequency of the multipath variations)	Range biases in case of changing ionospheric influences (for single-frequency users)
	Unsuitable in case of long-periodic multipath variations and varying ionospheric conditions (choice of any smoothing constant will lead to smoothing errors)
	Fast-fading multipath results in range biases that cannot be smoothed out

Table 4-3: Benefits and limitations of carrier smoothing used for multipath mitigation.

4.1.8 Multipath Estimating Delay Lock Loop (MEDLL)

In the mid 1990s, a novel multipath mitigation technique was developed and proposed by NovAtel. It is called Multipath Estimating Delay Lock Loop (MEDLL) and bases on the maximum-likelihood (ML) estimation technique. Basic publications on this subject are [VAN NEE et al. 1994], [TOWNSEND et al. 1995a] and [TOWNSEND et al. 1995b]. The aim is to estimate the main multipath parameters (multipath relative phase and amplitude as well as the multipath delay) which can be expressed in the form of the signal model

$$r(t) = \sum_{i=0}^{N} \alpha_i p(t - \tau_i)\cos(\omega t + \phi_i) + n(t), \tag{91}$$

where $N+1$ is the number of signal components (direct path plus N multipath signals), $p(t)$ denotes the ranging code and the navigation data, $n(t)$ the influence of thermal noise and α_i, τ_i and ϕ_i are the amplitude, the time delay and the relative phases of the i^{th} signal component, respectively. The direct signal component is obtained for i=0. In conventional tracking loops, only the delay τ_0 and phase ϕ_0 of the LOS signal component are estimated. However, in addition to the LOS signal parameters, the MEDLL technique also tries to estimate the multipath parameters. If these estimates are denoted as $\hat{\alpha}_i, \hat{\tau}_i$ and $\hat{\phi}_i$, the estimated signal can be expressed as

$$s(t)=\sum_{i=0}^{N}\hat{\alpha}_i p(t-\hat{\tau}_i)\cos(\omega t+\hat{\phi}_i)\,. \tag{92}$$

In the sense of ML theory, the correct estimates of $\hat{\alpha}_i, \hat{\tau}_i$ and $\hat{\phi}_i$ have to minimize the mean square error $\Lambda(\hat{\alpha}_i, \hat{\tau}_i, \hat{\phi}_i)$ which is defined as an integral over the observation period [t-T,t] ([VAN NEE et al. 1994]):

$$\Lambda(\hat{\alpha}_i,\hat{\tau}_i,\hat{\phi}_i)=\int_{t-T}^{T}[r(t)-s(t)]^2\,dt \tag{93}$$

In general, equation (93) can be solved by forming the partial derivatives of Λ with respect to the estimates $\hat{\alpha}_i, \hat{\tau}_i$ and $\hat{\phi}_i$, and setting them to zero. The resulting equations are a function of a (undistorted) reference correlation function from which the distorted correlation functions corresponding to each multipath signal are subtracted (see [VAN NEE et al. 1994] for details). Expressed in a simplified manner, the MEDLL approach finds a set of *N+1* correlation functions which – if added – provide the best possible fit to the actual (possibly distorted) correlation function. The approach can also be seen as a decomposition of the correlation function into its direct and multipath constituents where all estimated multipath-affected components of the signal's correlation function are consecutively subtracted from the observed (and distorted) correlation function. After having carried out these steps with all considered multipath components, the remaining correlation function is used to obtain an optimal estimate of the current code tracking error.

By taking a closer look at the underlying problem, it turns out that the solution of equation (93) for the parameter $\hat{\tau}_i$ incorporates a search for its maximum in the τ-domain. This is why the correlation function has to be sampled by a rather large amount of correlators. The amount of available correlators and the number of multipath signals considered determine the complexity of the corresponding computations (concerning the number of mathematical operations to execute). To limit the associated computational burden, NovAtel's first MEDLL receivers worked with 12 correlators per channel and assumed the existence of three signal components (N=2, direct path plus two multipath components).

The potential of mitigating code multipath (i.e. to find the correct estimates for $\hat{\tau}_i$) strongly depends on the amount of available correlators. Considering the configuration with 12 correlators and two assumed multipath signals, the remaining code multipath errors are similar to those obtained with Double Delta implementations (e.g. Strobe correlator) or to those obtained with a standard 1-chip correlation technique processing the GPS P-Code signal. Thus, the MEDLL technique is still sensitive to short-delay multipath. Multipath with longer path delays (>~30m), however, can be mitigated efficiently ([TOWNSEND et al. 1995a]).

MEDLL is not the only ML estimation approach suitable to decompose the received signal into its direct and multipath constituents. The Multipath Mitigation Technology (MMT) is an efficient implementation of the two-path ML estimator (which assumes the direct signal plus one single multipath component) and has been developed by Dr. Lawrence Weill in the late 1990s. It represents a lower bound of the pseudorange estimation error in the presence of multipath. It has been treated extensively in many of Weill's recent publications (e.g. [WEILL 2002a] or [WEILL 2003a]) or in his patent specification ([WEILL and FISHER 2002b]). The topic is also discussed in [AVILA-RODRIGUEZ et al. 2006] presenting lower error bounds for different Galileo signal options in the presence of multipath. The MMT is used in conjunction with a novel multipath mitigation technique introduced by NovAtel in 2005 (Vision Correlator, see section 4.1.10.1 or [FENTON and JONES 2005] for details).

4.1.9 Using Wavelets for Multipath Mitigation

This sections shows how wavelet processing can be used to mitigate code multipath. The basic idea is discussed in [ZHANG and BARTONE 2004] and uses code minus carrier observations in conjunction with wavelet decomposition, a technique which is called Wave-Smooth^{TM}. In the following, the associated processing steps are described in more detail. A brief introduction on the most important aspects of wavelet analysis is given in chapter 10 of this thesis (Appendix C).

The first step is the formation of ionosphere-free code and carrier observations, a prerequisite for applying wavelet processing techniques. In case that dual frequency measurements are available, the code observations ρ_{f1}, ρ_{f2} and the carrier observations ϕ_{f1}, ϕ_{f2} can be combined according to

$$\rho^* = \frac{f_1^2}{f_1^2 - f_2^2}\rho_{f1} - \frac{f_2^2}{f_1^2 - f_2^2}\rho_{f2} \tag{94}$$

$$\phi^* = \frac{f_1^2}{f_1^2 - f_2^2}\phi_{f1} - \frac{f_2^2}{f_1^2 - f_2^2}\phi_{f2}, \tag{95}$$

where ρ^* and ϕ^* denote the iono-free code and carrier observations and f_1 and f_2 are the center frequencies to which the code and carrier measurements are related (it is assumed that $f_1 > f_2$). As a next step, the (iono-free) code minus carrier (CMC) observable is formed for every epoch *k*. Due to the integer carrier phase ambiguity, the CMC is biased.

$$\begin{aligned} CMC_{biased,k} &= \rho_k^* - \phi_k^* \\ &= -N_\phi + M_{\rho,k} - M_{\phi,k} + \varepsilon_{\rho,k} - \varepsilon_{\phi,k} \end{aligned} \tag{96}$$

In addition to the ambiguity term N_ϕ, equation (96) contains the influences of code and carrier multipath (M_ρ and M_ϕ) as well as the noise influences ε_ρ and ε_ϕ. In order to remove the existing bias, all CMC values within a time window τ are averaged and subtracted from the biased CMC values. For sufficient large values of τ, these processing steps can be summarized as follows:

$$\begin{aligned} CMC_{unbiased,k} &= CMC_{biased,k} - \frac{\sum_{j=k-\tau+1}^{k} CMC_{biased,j}}{\tau} \\ &= M_{\rho,k} - M_{\phi,k} + \varepsilon_{\rho,k} - \varepsilon_{\phi,k} \end{aligned} \tag{97}$$

The results are (unbiased) CMC residuals which can be further processed by means of wavelet decomposition. The basic concept is to decompose the signal (all CMC residuals within the time window τ in this case) into an approximation *a* and different levels of details *d*. This process can be expressed in the form of

$$CMC_{unbiased} = a_n + \sum_{i=1}^{n} d_n , \tag{98}$$

where *n* is the decomposition level. The approximation a_n of the CMC residuals contains the low frequency component of the signal and determines its general behavior (e.g. existing trends would be clearly visible in a_n). On the other hand, the details d_n contain the high frequency contents of the signal (i.e. the noise influence in the CMC residuals). Compared to the influence of noise, multipath influences have commonly lower frequencies and should be visible in the approximation a_n. Therefore, only a_n is used in the next step to reconstruct the signal. As the process of reconstructing the signal is carried out only with the low frequency component of the original signal, the reconstructed signal is a smoothed version of the original CMC residuals. As already stated, the decomposition process is carried out for all CMC data within the time window τ. The last data point $a_{n,k}$ serves as a multipath correction $\Delta\rho$ which can be subtracted from the original CMC residual at epoch k, resulting in the corrected CMC residual $CMC_{unbiased,k,corr}$:

$$\Delta\rho = a_{n,k} \tag{99}$$

$$CMC_{unbiased,k,corr} = CMC_{unbiased,k} - \Delta\rho \tag{100}$$

The multipath correction $\Delta\rho$ can be subtracted from the original code phase measurement to mitigate the existing code multipath error. Figure 4-15 illustrates the basic principle of this multipath mitigation technique. The upper diagram shows the unbiased CMC residuals as obtained from equation (97). At the beginning, the residuals are affected by thermal noise only. As from t=240s, multipath influences result in sinusoidal signal variations.

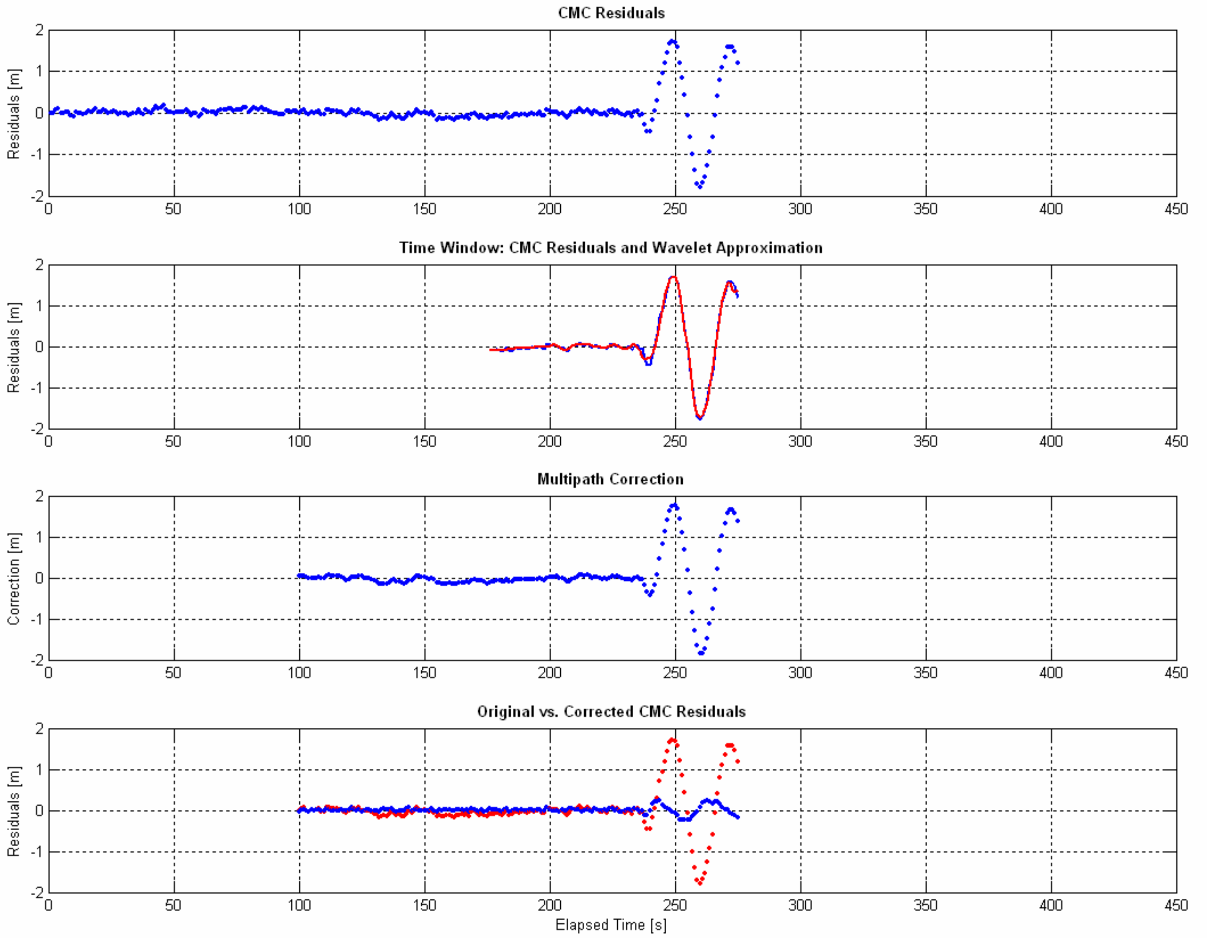

Figure 4-15: Multipath mitigation by signal decomposition.

Figure 4-15b illustrates the same CMC residuals during a time window of τ=100s (blue) together with the result of a wavelet decomposition of these residuals (red, decomposition level n=2, no details, mother wavelet: Daubechies 4). The third diagram shows the multipath correction $\Delta\rho$ (the value of the last data point of the wavelet decomposition process). Finally, the lower diagram compares the original CMC data (red) with the corrected CMC data (according to equation (100)). In this case, the original multipath variations of ±1.8m can be reduced to around ±0.2m (nearly 90% multipath reduction). It should be noted, however, that the actual performance depends on a variety of parameters like the size of the time window τ, the decomposition level n and the mother wavelet being used.

For best results, these parameters should be adjusted to the current multipath conditions, i.e. that the occurring fading frequencies should be known in advance. To achieve this, [ZHANG and BARTONE 2004] propose to apply a spectrogram analysis to the CMC residuals to identify the different frequency components. After that, the decomposition level can be adjusted accordingly.

4.1.10 Other Approaches

4.1.10.1 Vision Correlator

In 2005, NovAtel Inc. presented a new technique to mitigate multipath. In contrast to special code discriminators that are derived from two or several correlation values, the new approach analyzes the code chip transitions in the time domain. It is called Vision Correlator ([FENTON and JONES 2005]) and uses a dedicated number of sample points (the so-called "Vision Correlator vector") to sample a chip transition. In order to filter out the influence of noise, successive chip transitions are super-imposed during a specific time interval. The main advantage of analyzing chip transitions is that they are distorted more intensely than the correlation function. Based on a reference function representing an undistorted chip transition, the sample points are used to estimate code delay, amplitude and carrier phase of the direct path and one or more multipath signals. The mathematics behind this approach are very similar to the computations that have to be carried out for mitigating multipath with the MEDLL technique. According to [FENTON and JONES 2005], the Vision Correlator performs much better than the Narrow Correlator or the Pulse Aperture Correlator. It allows efficient mitigation of short-delay multipath. For multipath delays <4m, it results in smaller maximum multipath errors than other mitigation techniques.

4.1.10.2 Exploiting Day-To-Day Repeatability and SNR Data

One possible way to mitigate code multipath is to take advantage of the day-to-day repeatability of multipath influences. This approach requires recorded GNSS data from previous days and is a suitable approach for reference stations with only slight day-to-day changes of the multipath environment. The basic idea for multipath mitigation is to compute (iono-free) CMC residuals taken during the same period of a sidereal day. During these periods of time, the satellite constellations related to the two time series are assumed to be identical. The CMC residuals can be differenced, thus removing the signal characteristics that are common to both time series. Multipath influences are expected to occur at the same points in (sidereal) time and to show similar patterns that cancel out by differencing both time series. As has been shown in [SLEEWAEGEN 1997], the efficiency of this multipath mitigation method can be enhanced by exploiting SNR data as determined by the receiver. [SLEEWAEGEN 1997] showed that the SNR variations caused by multipath are in phase with the multipath-induced code error. Based on a scaling factor that relates the observed SNR data to a multipath error, the standard deviation of the code error (obtained from differenced CMC residuals) can be reduced by ~30% compared to the "day-to-day repeatability method".

4.1.10.3 A Posteriori Multipath Estimation (APME)

In contrast to the standard implementation of using an early, punctual and late code replica to form the code discriminator function, this method uses an additional late correlator to perform signal amplitude measurements and to compute an estimate of the expected multipath error ([SLEEWAEGEN and BOON 2001]). The approach seems to perform better than the Narrow Correlator and for some combinations of geometric path delay and multipath relative amplitude even better than the Strobe correlator. Especially for short-delay multipath and weak multipath signals, the APME outperforms the Strobe correlator.

4.1.10.4 Tracking Error Compensator (TrEC)

The Tracking Error Compensator (TrEC) takes advantage of the fact that some regions of the signal's correlation function do not show temporal variations as the multipath parameters change. These regions are invariant to multipath influences and are therefore called "multipath invariant" regions (MPI). They are located at the plateaus of the correlation function. Since the ideal shape of the correlation functions for all GPS satellites is known, the theoretical location of these MPI regions are known as well. The general idea as well as a general TrEC algorithm can be found in [PHELTS and ENGE 2000a] and [PHELTS and ENGE 2000b]. The basic steps to mitigate multipath using the TrEC technique are as follows:

- Computation of ideal correlation functions for each satellite.
- Selection of an MPI point and computation of the ideal distance between the peak of the ideal correlation function and the selected MPI point (to be carried out for all satellites, results are stored in a look-up table).
- During satellite tracking, the ideal distance to the MPI point is used to search this point on the actual correlation function by means of two or several additional correlators.
- Once identified, the ideal distance between the MPI point and the correlation peak (derived from look-up table entries) is compared to the actual distance (as obtained by means of the additional correlators). The difference between both measurements is used to correct the tracking loop output.

As it has been pointed out in [PHELTS and ENGE 2000a], the TrEC approach is an efficient multipath mitigation technique especially for narrowband receivers for which the traditional mitigation techniques still result in rather large maximum ranging errors. Furthermore, the TrEC approach is an efficient mean to mitigate short-delay multipath.

4.1.10.5 Special Antennas

In order to reduce the influences of multipath before these signal reach the signal processing unit of the receiver, special antennas have been developed. This section provides an overview of the most important developments.

Choke Ring. Choke rings are a rather simple means to mitigate multipath. They are ground planes consisting of several concentric rings that are located around the GNSS antenna. In theory, the resulting grooves are able to cancel out the primary and secondary wave of a reflected signal. This can be achieved if the groove's depth is approximately equal to ¼ of the carrier wavelength. This is why choke rings are normally designed for a dedicated carrier frequency. However, so-called dual-depth choke rings have also been developed in the past ([FILIPPOV et al. 1998] and [FILIPPOV et al. 1999]).

Multipath Limiting Antenna (MLA). Multipath Limiting Antennas consist of two distinct antennas/antenna patterns. A high-zenith antenna (HZA) is used for high elevation satellites (>30°) and the signals of low elevation satellites are tracked by another pattern with sufficient gain between ~5-35 degrees. The gain patterns of both antennas are complementary in the sense that the HZA exhibits very low gain for low elevation angles; the second pattern, however, is characterized by high antenna gain for low elevation angles. Both antennas are connected to their own receiving unit and a special processing facility is used to combine the pseudorange and carrier phase observations of the two antennas/receivers into one so-called "virtual receiver" measurement. This concept provides less noisy measurements for low elevation satellites and reduces multipath effects ([NORMARK et al. 2002] and [THORNBERG et al. 2003]).

Phased-Array Antennas. A phased array is an array of several antennas which can be steered in such a way that the effective antenna pattern is reinforced in a desired direction and suppressed in undesired directions. This process is also called “beam forming” and allows the antenna to create an antenna beam which exactly points towards the satellite (i.e. the antenna gain is very high in this direction). On the other hand, zero gain can be generated for other (undesired) directions. Since multipath signals commonly arrive from directions different to that of the concerned satellite, multipath signals can be suppressed effectively. In order to account for the movement of the satellites, the antenna beams have to be steered accordingly (adaptive beam forming).

4.2 Mitigation of Carrier Multipath

Only few receiver internal correlation techniques are suitable for carrier multipath mitigation. The most promising techniques are the Double-Delta ($\Delta\Delta$) or High Resolution Correlator ([McGraw and Braasch 1999]) and the Multipath Estimation Delay Lock Loop (MEDLL). The potentialities of these two approaches for carrier multipath mitigation are described below. Furthermore, there are some post processing approaches using SNR observations or antenna arrays to mitigate carrier multipath.

4.2.1 High Resolution Correlator (HRC)

The general concept of the HRC has already been discussed in section 4.1.2. There, five correlators (2 early correlators, 2 late correlators and the punctual one) have been introduced. With respect to carrier tracking, the interest is focused on the punctual correlator. The HRC concept proposes the formation of a synthesized punctual correlator, which can be expressed as follows ([McGraw and Braasch 1999]):

$$P_{HRC} = 2P - (E_1 + L_1) \tag{101}$$

Assuming that an *arctangent* detector is used for carrier tracking, the carrier multipath performance can be analyzed by means of equation (72). Figure 4-16a illustrates the standard and the high resolution correlator P_{HRC} for the BPSK(1) signal and the resulting carrier multipath errors are illustrated in Figure 4-16b.

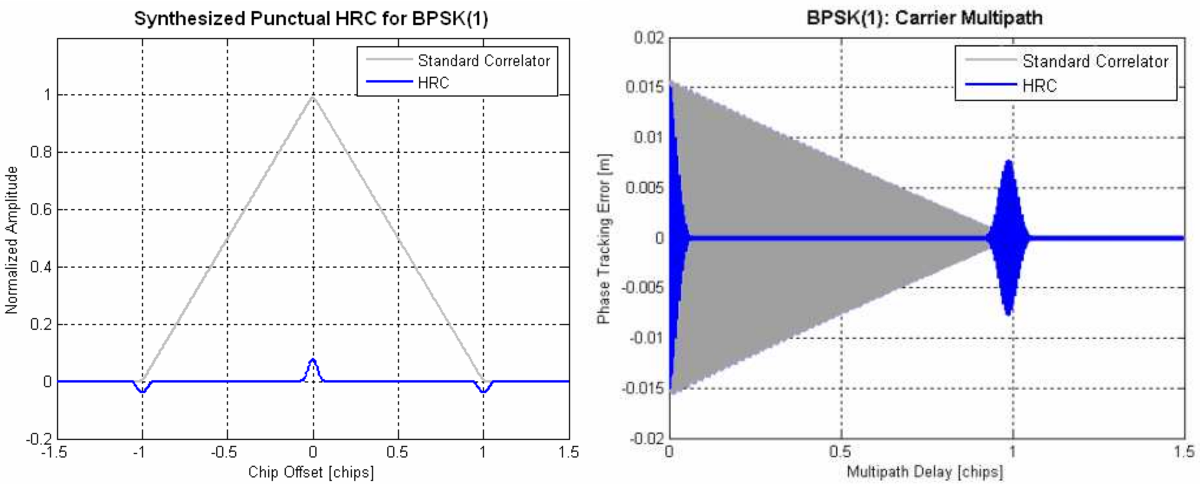

Figure 4-16: Punctual HRC and resulting carrier multipath performance for BPSK(1) (blue curves). The standard correlator and its resulting carrier multipath errors are plotted as grey curves.

Figure 4-16b clearly illustrates the performance enhancement when using the HRC. In fact, the maximum carrier multipath error is the same for both correlators. However, it rapidly decreases and becomes almost zero for a wide range of medium geometric path delays. Only for path delays around 1 chip (~293m for BPSK(1)), the multipath errors for the HRC are larger than for the standard correlator.

4.2.2 MEDLL

In addition to the High Resolution Correlator (HRC), only the Multipath Estimation Delay Lock Loop is able to mitigate carrier multipath. Figure 4-17 illustrates the theoretical performance of the MEDLL technology with respect to carrier multipath mitigation. Obviously, this technique performs much better than the standard phase discriminator ([TOWNSEND et al. 1995a]).

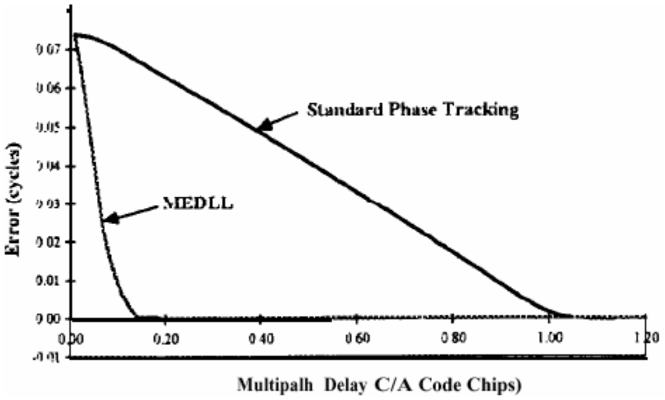

Figure 4-17: Theoretical performance of the MEDLL for carrier multipath mitigation (compared to standard phase tracking).[1]

However, as has also been shown in [TOWNSEND et al. 1995a], the actual performance is somewhat poorer, i.e. in practice, carrier phase errors do also exist for larger geometric path delays than indicated by Figure 4-17.

4.2.3 Other Approaches

4.2.3.1 Multi-Antenna Spatial Processing

Carrier multipath mitigation can also be achieved by post-processing of recorded data. One possible approach is the so-called multi-antenna spatial processing ([RAY et al. 1998]). This technique makes use of several closely-spaced antennas and bases on the following assumptions:

- The antennas are arranged in the form of a small antenna array (20-30cm in diameter), so that multipath can be considered correlated for all antennas
- All occurring reflections are attributed to one single reflector (i.e. only one multipath signal is considered)

Figure 4-18 illustrates a typical setup for this approach. The antenna array consists of 6 antennas (A_0-A_5) with the center antenna A_0 being used as the reference antenna. The observables are the (observed) single carrier phase differences between A_1-A_5 and the reference antenna A_0 to one satellite.

---

[1] adopted from [TOWNSEND et al. 1995a]

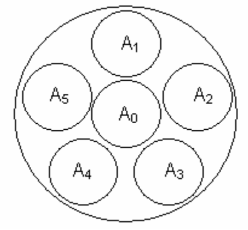

Figure 4-18: Possible antenna array for multi-antenna spatial processing.

By means of a least-squares adjustment, the attenuation factor α, the multipath relative phase as well as azimuth and elevation of the assumed reflector can be estimated. By means of the estimated multipath relative phase, the expected phase differences between two antennas can be computed and the observed differences can be corrected accordingly. According to [RAY et al. 1998], carrier multipath can be reduced by up to 70% with this approach.

4.2.3.2 Use of SNR Data

Also SNR data can be exploited for the purpose of carrier multipath mitigation. One possible approach that has been proposed in [AXELRAD et al. 1994] uses corrected SNR data in conjunction with spectral analysis to compute estimated phase errors with which the observed carrier phases can be corrected.

As a first step, the observed SNR data has to be corrected for the influence of satellite motion. Therefore, the signal's azimuth and elevation as well as the antenna pattern have to be considered. The remaining fluctuations in the SNR values are mainly due to multipath. The next step is to carry out a spectral analysis to determine the number of present multipath signals. This information can be used to model the SNR residuals as a function of the multipath relative amplitudes and frequencies. By means of an adjustment process, the attenuation factors and the multipath relative phase can be estimated. As a final step, this information is used to compute expected phase errors due to multipath which serve as corrections for the observed carrier phases. It should be noted, however, that the sign of the correction is principally unknown. For the derivation of the correct sign, two simultaneously observing receivers are needed ([AXELRAD et al. 1994]).

By means of this technique, the standard deviation of single difference residuals between two receivers could be reduced by about 20% ([AXELRAD et al. 1994]). The performance of this technique can be further enhanced by refinement of the underlying models ([COMP and AXELRAD 1996]). However, as measured by the effort that is necessary to compute the carrier phase corrections, the multipath error reduction potential of this technique is limited. This is due to the fact that the proposed approach bases on several assumptions that can barely be assumed for real GNSS data:

- The amplitude of the direct signal is constant during a certain period of time
- The amplitudes of the multipath signals are constant during a certain period of time
- The frequency of the multipath variations is constant during a certain period of time
- The antenna pattern is relatively homogeneous and not very sensitive to small changes of the signal's azimuth and elevation

5. Multipath Performance for GPS and Galileo

5.1 Criteria for Multipath Performance Assessment

Past and present activities in the field of GPS modernization or the development of the European Galileo system aim at the enhancement of the overall navigation performance by providing better navigation signals compared to those that are available today. A very promising approach is the optimization of the modulation schemes of the present signals by introducing new chip waveforms or combinations of different waveforms. It has been shown that significant enhancements can be achieved in terms of code noise, tracking robustness or susceptibility to multipath and to narrow and wide band interference by changing the modulation scheme ([AVILA-RODRIGUEZ et al. 2005] or [HEIN et al. 2005]. Additionally, thanks to better satellite and receiver hardware, hardware-induced error sources can be reduced more efficiently as well. Furthermore, if it is considered that new civil signals will be available for the modernized GPS and Galileo in the near future, important error sources like the ionospheric error will become less important, because the users will be able to eliminate them by computing ionospheric corrections based on dual-frequency observations, by making use of A-GNSS capabilities or by processing SBAS signals.

Despite this potential of performance enhancement, multipath still remains the dominant error source and the limiting factor for many applications. Multipath is the major inevitable source of error contributing to the overall error budget and - given its random nature - the most difficult to mitigate. Therefore, multipath performance analyses played a significant role during the signal definition phase of Galileo and are being considered for possible future optimizations. Together with noise and interference considerations, multipath was one of the most important design drivers for the Galileo baseline signal structure that we have today. Also for future signal optimization efforts, multipath performance will play a major role. Therefore, a meaningful methodology to derive typical, meaningful and realistic multipath errors has to be provided in order to estimate the contribution of multipath to the overall error budget.

A very common approach to describe the effects of specular multipath is the computation of multipath error envelopes (as used in the previous sections to illustrate the potentials of different multipath mitigation techniques). Despite the simplifications assumed in this model (consideration of one single multipath signal, dedicated multipath relative amplitude, no shadowing effects), multipath error envelopes are very well suited to compare the multipath performance of different signals because the appearance of the resulting error envelopes directly reflects differences in modulation schemes or chipping rates.

Apart from the computation of multipath error envelopes, there are also other, more complex models that consider more than one multipath signal in different multipath environments. The most complex ones are statistical channel models. The following section starts with a brief description of such a statistical model. Based on model parameters for different environments, the resulting multipath errors will be computed for the current GPS C/A code as well as for two former Galileo L1 signal candidates. It is assumed that the multipath errors obtained with this model are typical for the underlying environment and can serve as a reference for the subsequent analyses. Thereafter, much simpler multipath models as well as the computation of multipath errors based on multipath error envelopes are discussed in detail.

The main objective is to determine whether or not a particular approach of computing multipath errors leads to errors comparable to those obtained by the rather complex statistical models and whether or not these models can be replaced by simplified ones. The main motivation is to provide methods for assessing the multipath performance of a dedicated signal/receiver/environment combination and to provide the necessary means for the computation of realistic multipath errors that can be used as an input for GNSS error budget computations.

5.1.1 Signal Scenario

In order to visualize the different criteria of multipath performance assessment, three sample signals will be used, namely the BPSK(1) representing the current GPS C/A code, the BOC(1,1) and the CBCS(20%), a former candidate signal for the optimization of the Galileo OS signal on L1 (see [AVILA-RODRIGUEZ et al. 2005] and [HEIN et al. 2005] for details). The autocorrelation functions of these signals are illustrated in Figure 5-1. They are based on a pre-correlation bandwidth of 24 MHz.

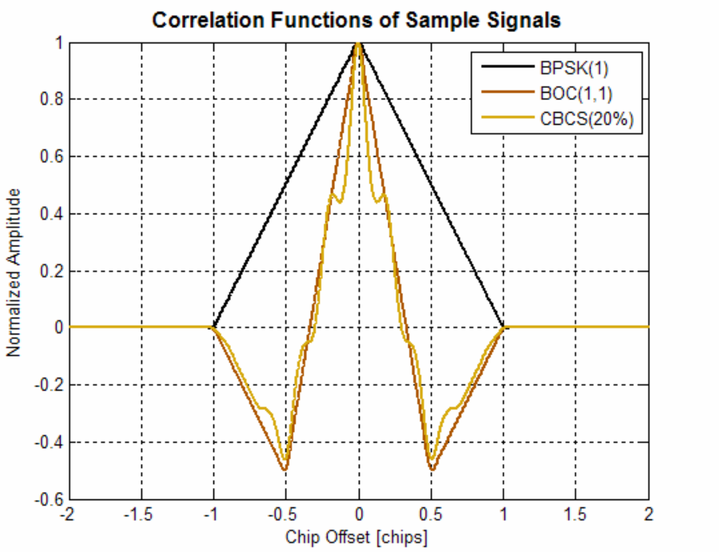

Figure 5-1: Autocorrelation function for the three sample signals.

5.1.2 Signal Processing

In order to compute the influence of code multipath, two different implementations of a delay lock loop have been considered, namely a coherent early minus late (E-L) and a non-coherent early minus late power (E-L-P) implementation. According to [BRAASCH 1996] or [KELLY 2003], the coherent (E-L) discriminator function in the presence of multipath can be expressed as

$$\begin{aligned} D_{coh}(\tau) = & \left[R\left(\tau + d/2\right) - R\left(\tau - d/2\right)\right]\cos(\theta_c) \\ & + \sum_{i=1}^{M} \alpha_i \left[R\left(\tau + d/2 - \delta_i\right) - R\left(\tau - d/2 - \delta_i\right)\right]\cos(\theta_{m,i} - \theta_c) \end{aligned} \quad (102)$$

where $R(\tau)$ denotes the correlation function, d is the correlator spacing and α_i, δ_i and θ_i are the relative amplitude, the path delay and the relative phase of the i^{th} multipath signal, respectively. M indicates the number of multipath signals. θ_c is the phase of the composite signal and can be expressed as follows (extension of the formula given in [BRAASCH 1996] for multiple reflections):

$$\tan(\theta_c) = \frac{\sum_{i=1}^{M} \alpha_i R(\tau - \delta_i)\sin(\theta_{m,i})}{R(\tau) + \sum_{i=1}^{M} \alpha_i R(\tau - \delta_i)\cos(\theta_{m,i})} \tag{103}$$

The non-coherent (E-L-P) discriminator function in the presence of multipath can be expressed as ([Kelly 2003]):

$$D_{noncoh}(\tau) = \left| \sum_{i=0}^{M} \alpha_i R\left(\tau + d/2 - \delta_i\right) e^{j\theta_0} \right|^2 - \left| \sum_{i=0}^{M} \alpha_i R\left(\tau - d/2 - \delta_i\right) e^{j\theta_0} \right|^2 \tag{104}$$

Note that the direct signal is obtained for $i=0$, $\delta_0=0$, $\theta_0=0$ and $\alpha_0=1$ (normalized amplitude). For the computation of multipath influences, a chip-spacing of $d=0.1$ will be used throughout this chapter. The reason of using the same chip spacing for all signals is to base all computations on the same assumptions. However, future GNSS receivers will probably use different chip spacings for the GPS and the Galileo signals, resulting in a multipath performance different from the one computed in the following sections.

5.1.3 Multipath Errors Based on Statistical Channel Models

The most realistic but also the most complex approach to assess the multipath performance of a given signal/receiver combination is to consider not only the signal characteristics and the receiver architecture but also different multipath environments and different elevation angles. However, this requires exact knowledge of the multipath propagation channel under various conditions. Based on extensive measurement campaigns, such channel models have been derived in the past (e.g. [Jahn et al. 1996] or [Lutz et al. 2000]), or are currently being developed ([Steingaß and Lehner 2003/2004]). For the following determination of typical multipath errors that are valid for a dedicated environment, the wide band channel model for land mobile satellite services (LMS) presented in [Jahn et al. 1996] and [Lutz et al. 2000] has been used. This model provides general distributions for the number of occurring multipath signals, their corresponding path delays and relative amplitudes as well as associated model parameters for different environments and elevation angles. Effects like shadowing are also taken into account by modeling the amplitude of the line-of-sight (LOS) component.

The model distinguishes between three types of signals, namely the direct path, near reflections and far reflections. The amplitude of the direct path follows either a Rice distribution (LOS) or a Rayleigh distribution in case of shadowing. The number of near and far echoes is Poisson-distributed, and their amplitudes follow a Rayleigh distribution. The delays τ of the near multipath signals are distributed exponentially and can be expressed as

$$P_{SCM}(\tau) = \frac{1}{\tau_0} e^{-\frac{\tau}{\tau_0}}, \tag{105}$$

where τ_0 denotes the typical path delay in a specific environment. In contrast to the near multipath signals, the far echoes are uniformly distributed. The path delay distribution expressed in equation (105) will also be used for other models discussed later in this chapter. Figure 5-2 illustrates the typical distribution of path delays and amplitudes for a rural environment (based on 1.000 simulation runs) as obtained from the statistical LMS channel model.

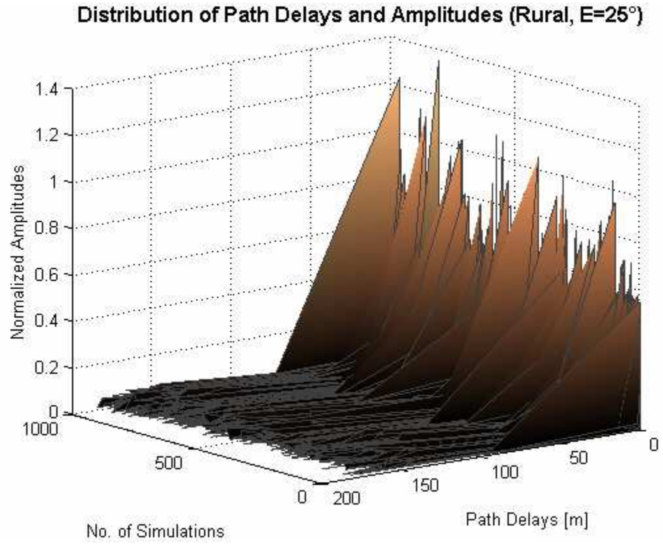

Figure 5-2: Typical distribution of path delays and amplitudes in a rural environment for an elevation of E=25°.

Based on the LMS model parameters presented in [JAHN et al. 1996], some important environmental characteristics can be derived. The following diagrams illustrate mean signal-to-multipath ratios (SMR), typical path delays, the number of occurring multipath signals and the percentage of time during which multipath has to be expected for several environments and elevation angles. They have been derived on the basis of 100.000 simulation runs.

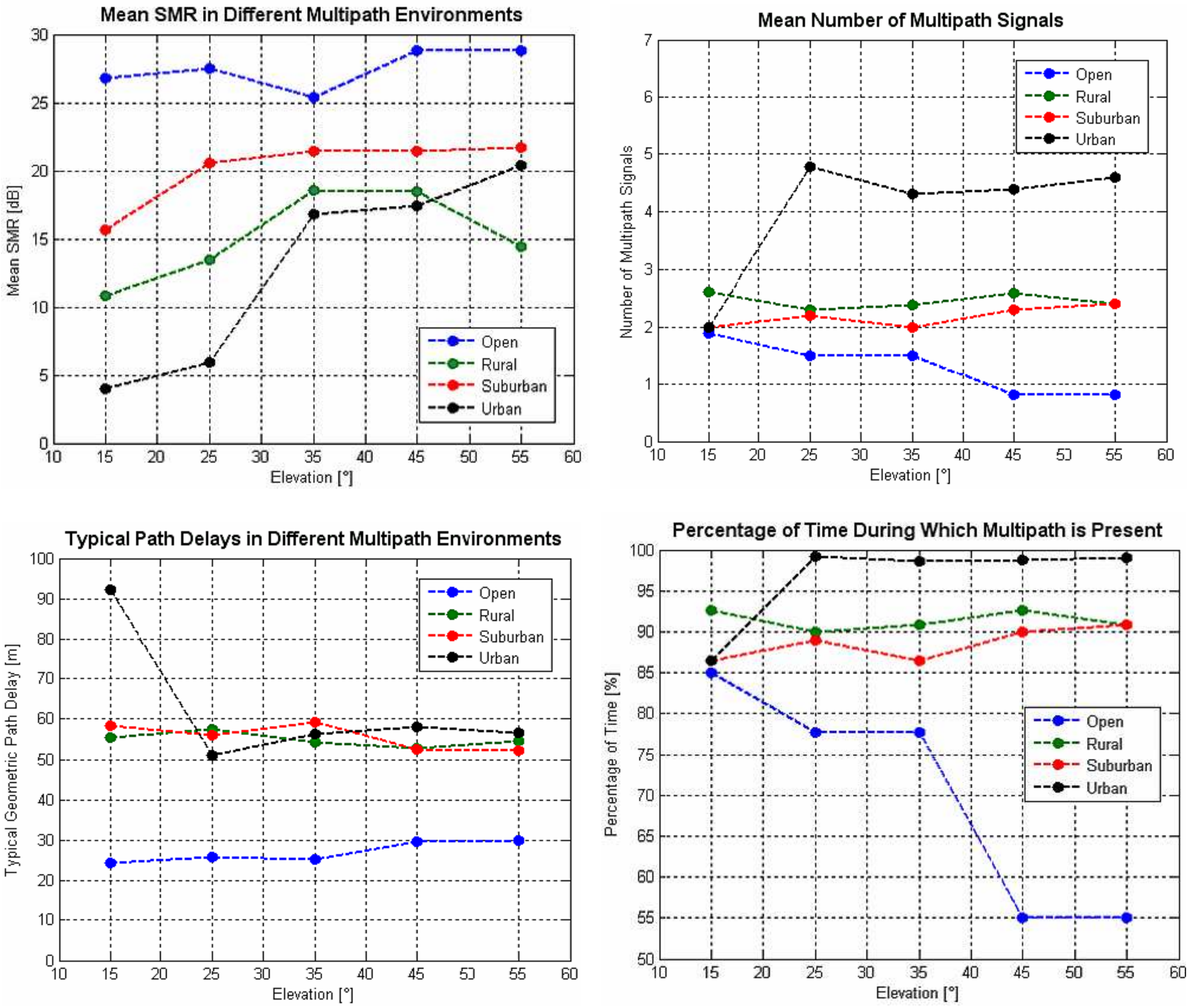

Figure 5-3: Mean SMR, number of multipath signals, typical path delays and frequency of occurrence of multipath signals in different environments.

As expected, the urban environment is the worst environment with respect to multipath propagation. It is characterized by the strongest multipath and the largest number of multipath signals. Furthermore, there are almost no periods of time without the presence of one or several multipath signals. Interestingly, the typical path delays do not seem to depend significantly on the elevation angle (exception: urban environment at low elevation angles). With the exception of the mean SMR values, rural and suburban environments seem to have similar characteristics with respect to multipath propagation. Note that, according to [Jahn et al. 1996], rural environments are mainly characterized by trees and forests located along the rural highways. In order to reduce the complexity of subsequent analyses, the computations of multipath errors will be carried out for an elevation angle of E=25°. In this case, the following multipath characteristics can be derived from Figure 5-3:

	Multipath Characteristics (E=25°)	
Environment	**Mean SMR**	**Typ. Path Delay**
Open	27.5 dB	26 m
Rural	13.5 dB	57 m
Suburban	20.5 dB	56 m
Urban	6.0 dB	51 m

Table 5-1: Multipath characteristics for different multipath environments at E=25°.

Based on the environmental multipath characteristics illustrated in Figure 5-3 and the signal processing steps introduced in section 5.1.2, the typical multipath performance of each sample signal can be computed. This includes the following steps:

- Computation of the LOS amplitude with consideration of temporary shadowing effects
- Computation of the number of occurring multipath signals
- Computation of relative amplitudes and path delays for each multipath signal
- Computation of multipath relative phases
- Computation of discriminator functions according to equations (102) and (104)
- Determination of resulting multipath error (analysis of zero-crossing of the discriminator function)

These steps have to be carried out for a large number of simulations. The results of such an analysis are illustrated in Figure 5-4a, where the multipath errors for the three sample signals are plotted for each simulation run. Note that the multipath relative phases were not computed directly from the geometric path delay but generated randomly. This accounts for possible phase jumps caused by the reflector which can hardly be modeled ([Van Nee 1992]) and the fact that scatterers at different distances are uncorrelated.

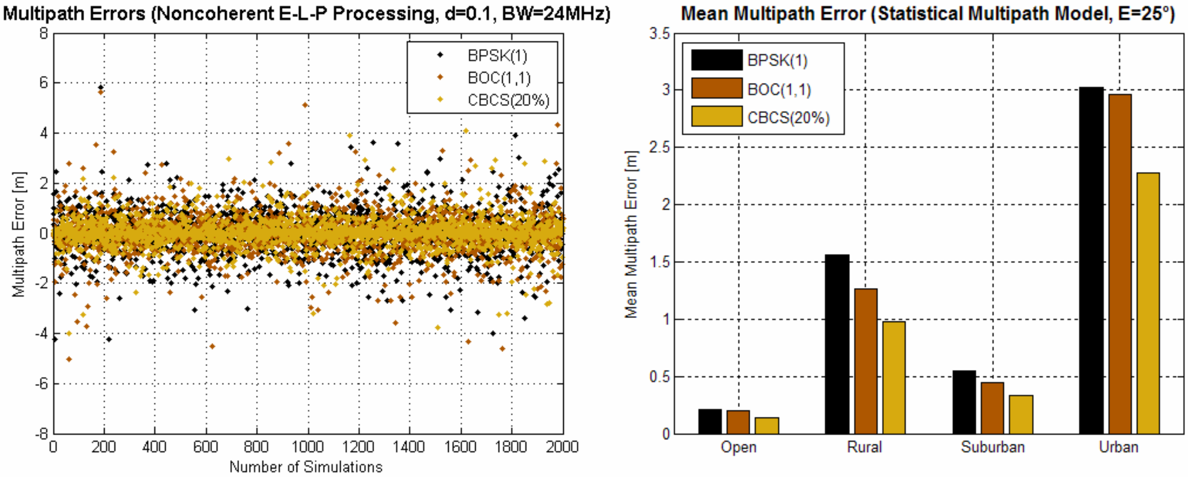

Figure 5-4: Distribution of multipath errors for the three sample signals and derived mean multipath errors, based on 2.000 simulations and a non-coherent discriminator function.

Based on these computations and the obtained error distributions, typical multipath errors can be derived by either computing RMS values or standard deviations or by determining a suitable mean value. In the following, typical multipath errors will always be defined as mean values obtained by averaging the absolute (unsigned) values of the error distribution. According to this definition, the typical (mean) multipath errors as illustrated in Figure 5-4b have been computed for the three sample signals on the basis of 2.000 simulation runs. They are plotted for all four environments assuming an elevation angle of E=25°. Since it turned out that the resulting mean errors are nearly identical for the coherent and the non-coherent case, only the non-coherent case has been considered.

In all environments, the CBCS shows the best multipath performance followed by the BOC(1,1) and the BPSK(1). As expected, the urban environment causes the largest multipath errors. Except for the rural environment, the multipath performance of the BPSK(1) and the BOC(1,1) does not seem to differ significantly.

The main benefit of using statistical channel models is that they allow the computation of multipath errors under realistic conditions by integrating information about the multipath environment and by considering different elevation angles. As a result, both qualitative and quantitative statements about the expected multipath performance can be obtained. On the other hand, statistical channel models are very complex and require time consuming and laborious data processing.

5.1.4 Multipath Errors Based on Power-Delay-Profiles

Another multipath model that also considers multiple reflections was proposed in [VAN NEE 1992]. Instead of using detailed statistical information about the propagation channel, it assumes a rather simple power-delay profile $P_{PDP}(\tau)$. This distribution can be obtained by simply applying a factor p_0 to equation (105):

$$P_{PDP}(\tau) = p_0 P_{SCM}(\tau) = \frac{p_0}{\tau_0} e^{-\frac{\tau}{\tau_0}} \tag{106}$$

Again, the typical multipath delay is denoted by τ_0 and p_0 is the total amount of multipath power originating from all multipath sources. The model assumes the presence of an arbitrary number of multipath signals equidistantly distributed between $\tau = 0$ and $\tau = \tau_{max}$.

There is of course an indirect link to the consideration of different multipath environments. In case that their characteristics are known (namely typical SMRs and multipath delays, e.g. derived from diagrams like Figure 5-3), these parameters can be used to characterize the power-delay distribution described by equation (106). In order to compute typical multipath errors from such a power-delay profile, a total amount of 100 reflectors have been assumed. Since a chip-spacing of d=0.1 only causes multipath errors if the geometric path delays are smaller than ~1.05 chips (at least in theory), the 100 reflectors have been distributed equidistantly between path delays of τ=0 and τ_{max}=1.05 chips. The spacing between adjacent path delays is denoted as $\Delta\tau$. Based on the assumed value of p_0 and the typical path delay τ_0 (according to Table 5-1) the power $p_i(\tau_i)$ of the i^{th} multipath signal can be computed as

$$p_i(\tau_i) = P_{PDP}(\tau_i) \cdot \Delta\tau \tag{107}$$

Thus, the power of the i^{th} multipath signal is simply the area enclosed by the power delay profile P_{PDP} at $\tau = \tau_i$ for a path delay step of $\Delta\tau$ (see Figure 5-5).

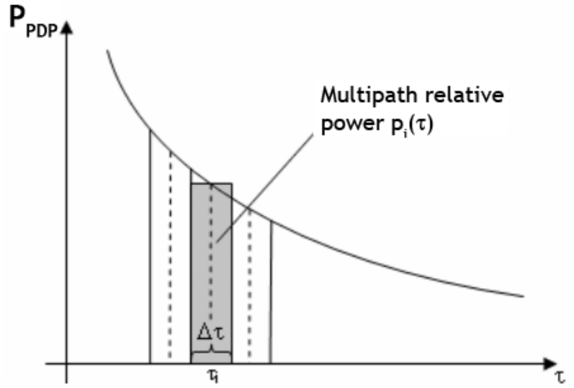

Figure 5-5: Determination of multipath relative power levels.

Based on the relationship between signal power and signal amplitude, the corresponding multipath relative amplitudes α_i can be expressed as

$$\alpha_i(\tau_i) = \sqrt{2p_i(\tau_i)}\,. \tag{108}$$

All other computational steps (generation of random multipath relative phases, computation of discriminator functions and determination of resulting multipath errors) are identical to the procedures described in the previous section. Figure 5-6 illustrates the mean multipath errors obtained by this model (average of unsigned multipath errors over all simulations). The multipath errors for all three sample signals are plotted as a function of the typical path delay, assuming a mean SMR of 13.5dB (representative for the rural environment). The error obtained for each value of τ_0 is the mean multipath error averaged over 1.000 simulation runs. Since the mean errors are plotted as a function of the typical multipath delay, representative multipath errors for all environments with a typical SMR of 13.5dB can be derived from Figure 5-6.

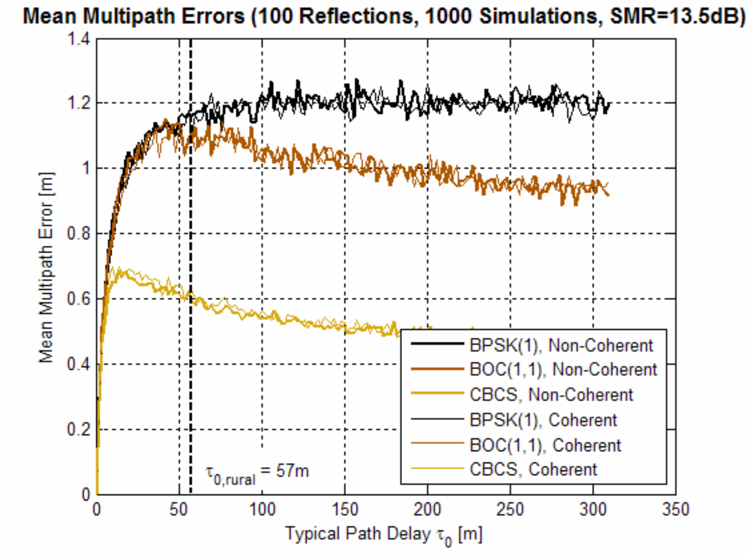

Figure 5-6: Computation of mean multipath errors as a function of the typical path delay τ_0.

Typical multipath errors for the rural environment (τ_0=57m) are ~1.2m for the BPSK(1), ~1.1m for the BOC(1,1) and ~0.6m for the CBCS, respectively. The multipath errors illustrated in Figure 5-6 have been computed for the coherent as well as for the non-coherent case. Again, both DLL implementations result in nearly identical mean multipath errors. Multipath errors for all other environments can be obtained by computing diagrams like Figure 5-6 for all relevant SMRs and by extracting the resulting errors at the typical path delay associated with each environment. The results are summarized in Figure 5-7. Again, the mean multipath errors reflect the conditions at an elevation of E=25°.

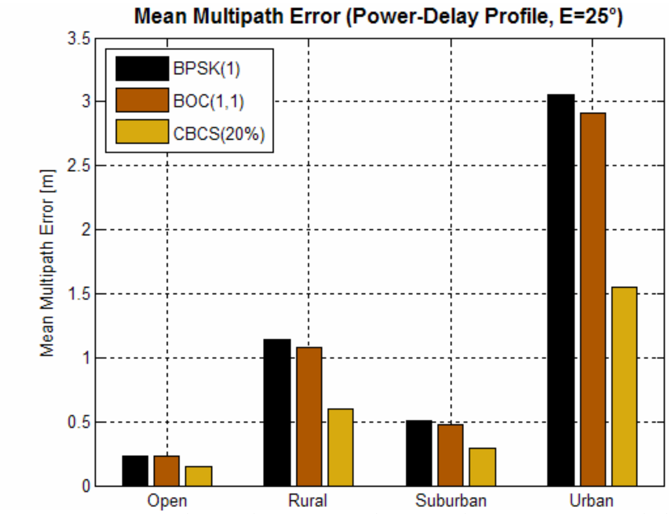

Figure 5-7: Mean multipath errors obtained from power-delay profiles.

The results obtained by this model are very similar to those obtained by the more complex statistical channel model (from both a qualitative and a quantitative point of view). Again, the CBCS shows the best multipath performance followed by the BOC(1,1) and the BPSK(1). The previous results that indicated only little differences between the performance of the BPSK(1) and the BOC(1,1) can be confirmed by this model. Modeling of multipath propagation based on power-delay profiles is not as complex as using statistical channel models. The main reason is that instead of using several distributions (for amplitudes, delays and number of signals) only one distribution is needed. Nevertheless, the model leads to similar results and can also be used to compare different signals with respect to their multipath performance. However, quantitative results comparable to those of the statistical channel model can only be obtained if some environmental characteristics are known (mean SMR and typical path delays).

5.1.5 Multipath Error Envelopes

A common way of illustrating the multipath performance of a given signal/receiver combination is the computation of its multipath error envelope. It represents the influence of one single multipath signal with a dedicated relative amplitude (usually α=0.5) that is constant for all considered geometric path delays. Figure 5-8 illustrates multipath error envelopes for all three sample signals. Different environments are considered by using typical multipath relative amplitudes derived from the SMRs listed in Table 5-1.

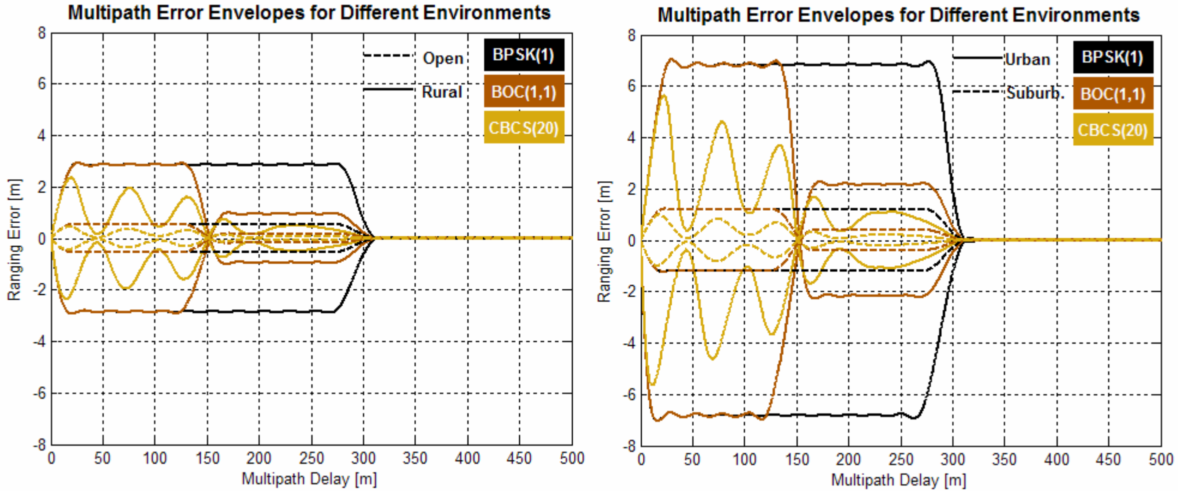

Figure 5-8: Multipath performance for the three sample signals in open, rural, urban and suburban environments (valid for E=25° and a correlator spacing of d=0.1).

As can be derived from Figure 5-8, the multipath performance of the three signals can be rated as follows:

- The BPSK(1) and the BOC(1,1) show the same multipath performance for short- and medium-delay multipath; only for long-delay multipath, BOC(1,1) outperforms BPSK(1).
- The CBCS outperforms the other two signals for all geometric path delays.

This general behavior is common to all environments, because the only difference between the computations is that different multipath relative amplitudes were used, i.e. the multipath errors are scaled differently. The main benefit of using multipath error envelopes as a criterion for multipath performance assessment is that these graphs clearly reflect differences in the structure of the underlying signals. Thus, the multipath performance of different signals under identical conditions can be directly compared with respect to each other. On the other hand, analyses of error envelopes allow only general statements about the multipath performance, because they are only valid for a dedicated scenario (constant relative amplitude, one single multipath signal and dedicated receiver architecture). In addition, qualitative statements must often differentiate short-, medium- and long-delay multipath performance. Furthermore, it is difficult to extract meaningful typical multipath errors from these envelopes. To overcome these limitations, the envelopes can be further modified or processed to allow a better understanding of the actual multipath performance under realistic conditions, to provide better means for comparing the multipath performance of different signals or correlation techniques and to be able to derive typical and meaningful multipath error contributions to the overall error budget. To achieve these goals, the following criteria can be considered:

5.1.5.1 Area Enclosed by Multipath Error Envelope

One possible approach to further analyze a given multipath error envelope is to compute the areas enclosed by the envelope. The result of such a computation for the three sample signals (based on the envelopes illustrated in Figure 5-8) is shown in Figure 5-9. In order to allow a better comparison between the signals, the area obtained for the BPSK(1) has been normalized to unity.

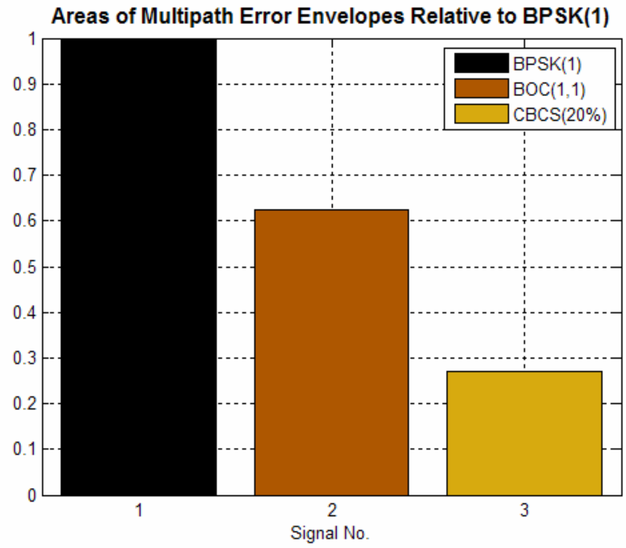

Figure 5-9: Comparison of areas enclosed by multipath error envelopes.

In general, it can be assumed that smaller envelope areas indicate a better multipath performance. According to this criterion, the CBCS shows the best code multipath performance, followed by the BOC(1,1) and the BPSK(1). Due to the fact that the areas for the BOC(1,1) and the CBCS are relative to that obtained for the BPSK(1), the results illustrated in Figure 5-9 are identical for all envelopes plotted in Figure 10 and Figure 11 and are thus independent of the multipath environment. Qualitative performance assessments with consideration of different environments could be carried out by comparing absolute area values instead of normalizing one area to unity.

Since these computations base on the envelopes themselves, differences in the structure of the underlying signals affect the area computation directly. Furthermore, this approach allows a more general multipath performance assessment because the results represent the multipath performance for all geometric path delays. However, typical multipath errors cannot be extracted from the derived areas. Therefore, this approach is mainly suited for qualitative comparisons.

5.1.5.2 Running Average of Multipath Error Envelope

A more reliable way for multipath performance assessment is the computation of the running average of an envelope. For this purpose, only the absolute envelope values are considered and their cumulative sum is used to compute average ranging errors. Within the framework of this thesis, the mean value of the in-phase and the unsigned 180° phase shift component of the multipath error envelopes are used to compute the running averages. Figure 5-10 illustrates the result of such a computation for the three sample signals based on the envelope for the rural environment illustrated in Figure 5-8.

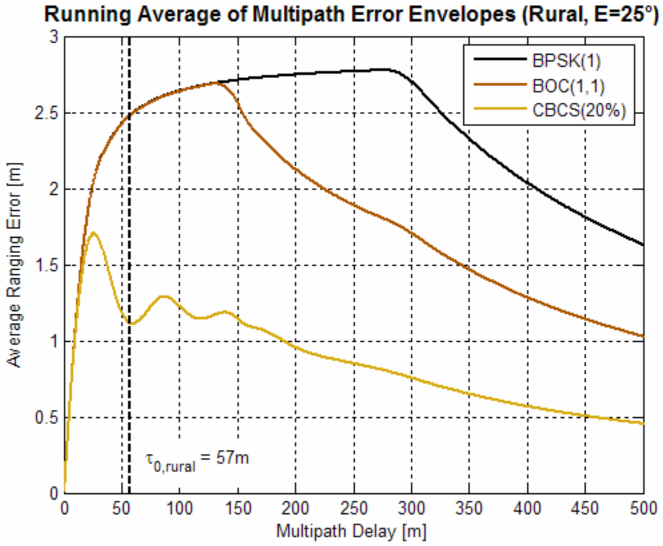

Figure 5-10: Comparison of running averages of multipath error envelopes (rural environment).

Since running averages are also computed directly from the error envelopes, the results also reflect the differences between the different signals. A good multipath performance is characterized by a small maximum average value and a rapid decrease towards zero. Based on this criterion, the CBCS shows the best overall multipath performance with respect to code multipath, followed by the BOC(1,1) and the BPSK(1).

In contrast to the computation of the area enclosed by the envelope, the running averages contain information about the susceptibility to multipath at different path delays. Moreover, it is possible to derive mean multipath errors from diagrams like Figure 5-10 by determining the ordinate value of the running average at a certain path delay, e.g. at path delays τ_0 which are representative for a dedicated environment. The obtained value can be interpreted as an average multipath error resulting from multipath signals with path delays between τ=0 and τ=τ_0. Longer path delays remain unconsidered in this model (a reasonable simplification as most multipath is short-delay multipath, see Figure 5-2).

For the rural environment illustrated in Figure 5-10, this method leads to average multipath errors of about 2.5m for the BPSK(1) and the BOC(1,1) and ~1.2m for the CBCS signal. These values reinforce the results obtained by visual inspection of the error envelopes which indicate identical performance of BPSK(1) and BOC(1,1) in case of short-delay multipath. The determination of mean multipath errors by analyzing running average plots for all environments (derived from the envelopes illustrated in Figure 5-8) at an elevation of 25° leads to the following results:

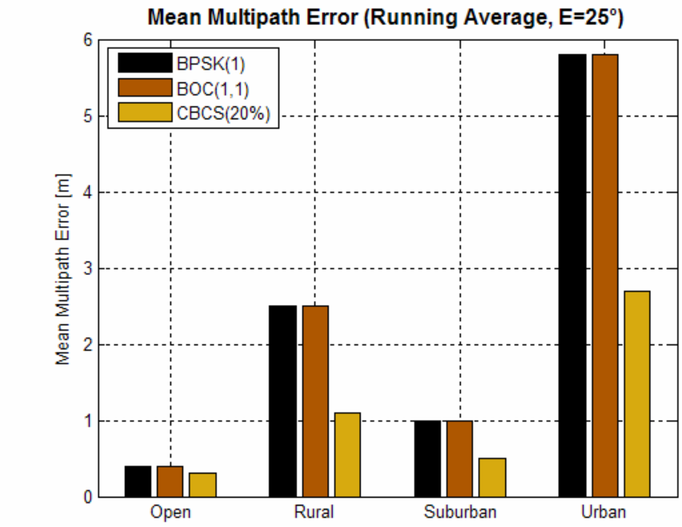

Figure 5-11: Mean multipath errors as extracted from running average plots.

Except for the open environment, the CBCS signal performs much better than the other two signals. Since only typical multipath delays τ_0 (short path delays) are considered, the BPSK(1) and the BOC(1,1) show identical multipath performance in all environments.

Since the computation of running averages is based on multipath error envelopes, no complex and extensive preparatory computations are necessary. It should be noted, however, that multipath errors derived from running average plots still base on one single reflection with a dedicated relative amplitude. Furthermore, if different multipath environments are to be considered, their fundamental characteristics (typical SMRs and path delays) have to be known. The main benefit of computing and analyzing running average plots is that both qualitative and quantitative conclusions can be drawn. However, the mean multipath errors obtained from the computation of running averages do not match with those obtained from the statistical channel model or from suitable power-delay profiles. As a result, this approach does not seem to be suitable for the derivation of typical and meaningful multipath errors.

5.1.6 Weighted Multipath Error Envelopes

Weighting Scheme No.1. Another approach to modify a multipath error envelope is to scale it according to a distribution of path delays and amplitudes. With equation (105) such a delay distribution $P_1=P_{SCM}(\tau)$ has been used for the statistical channel model. Further assuming that the multipath power $p(\tau_i)$ is related to the mean relative amplitude $\alpha(\tau_i)$ according to equation (108), an amplitude distribution $P_2(\tau)$ can be defined by replacing $p(\tau_i)$ of equation (108) with equation (106). Both distributions can be expressed as

$$P_1(\tau) = \frac{1}{\tau_0} e^{-\frac{\tau}{\tau_0}} \qquad P_2(\tau) = \frac{\alpha_0}{\sqrt{\tau_0}} e^{-\frac{\tau}{2\tau_0}} \tag{109}$$

where $P_1(\tau)$ models the multipath delays and $P_2(\tau)$ the multipath amplitudes, using the coefficient of reflection α_0 and a typical path delay τ_0 for the considered multipath environment. Similar to the statistical channel model discussed above, this model takes into account that short-delay multipath occurs more frequently than long-delay multipath and that long geometrical path delays result in relatively weak multipath signals (compared to nearby reflections). Based on equations (109), the combined distribution $D_1(\tau)$ of multipath delays and amplitudes can be expressed as follows:

$$D_1(\tau) = P_1(\tau) \cdot P_2(\tau) = \frac{\alpha_0}{\tau_0\sqrt{\tau_0}} e^{-\frac{3\tau}{2\tau_0}} \tag{110}$$

This model can now be used to modify (scale) the multipath error envelopes $E(\tau)$. Since the coefficient of reflection α_0 can already be considered for the computation of the multipath error envelope itself, it can be set to unity and the modified combined distribution

$$D_1'(\tau) = \frac{1}{\tau_0\sqrt{\tau_0}} e^{-\frac{3\tau}{2\tau_0}} \tag{111}$$

can be used for further analysis. In order to obtain scaled envelopes where the ranging errors are expressed in [m], equation (111) has to be normalized such that $D_1'(\tau{=}0)=1$, resulting in weighted multipath error envelopes $E_1'(\tau)$ which can be expressed as follows:

$$E_1'(\tau) = \frac{E(\tau) \cdot D_1'(\tau)}{D_1'(\tau = 0)} = E(\tau) \cdot e^{-\frac{3\tau}{2\tau_0}} \tag{112}$$

Figure 5-12 illustrates resulting weighted error envelopes for a typical path delay of τ_0=57m and an SMR of 13.5 dB, again representing the rural environment.

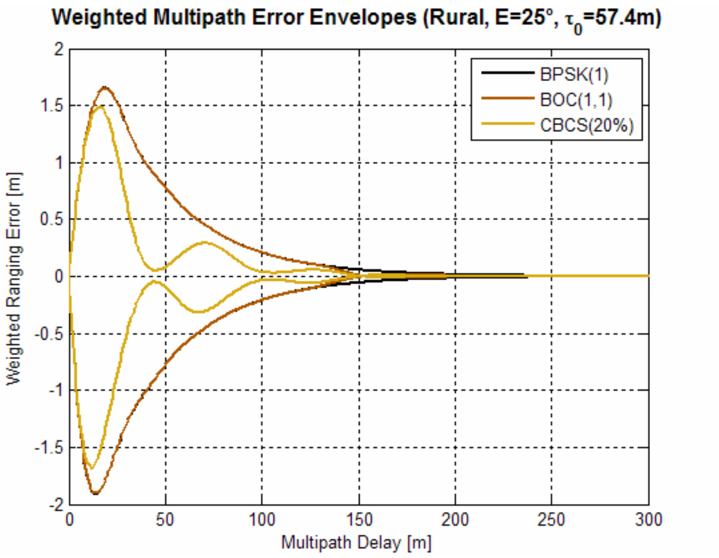

Figure 5-12: Comparison of weighted multipath error envelopes for the three sample signals.

According to this criterion, there is no significant difference between the BPSK(1) and the BOC(1,1). The CBCS, however, outperforms the other two signals due to its good short-delay multipath performance. The qualitative results obtained by an appropriate scaling of multipath error envelopes are similar to those obtained by the more complex statistical channel model and the power-delay profile approach. However, the analysis of weighted multipath error envelopes does not allow the derivation of typical (mean) multipath errors, because the envelopes always represent a worst case scenario. Thus, multipath errors extracted directly from these plots are worst case errors that are valid for a dedicated path delay.

Weighting Scheme No.2. Alternatively, the power-delay profile (106) can be used to scale the original envelopes. Assuming that p_0 corresponds to the SMR from which the multipath relative amplitude α_0 can be computed, the distribution $D_2(\tau)$ can be expressed as

$$D_2(\tau) = \frac{\alpha_0}{\tau_0} e^{-\frac{\tau}{\tau_0}} . \tag{113}$$

After normalization, the weighted multipath error envelopes $E_2'(\tau)$ can be computed according to

$$E_2'(\tau) = \frac{E(\tau) \cdot D_2(\tau)}{D_2(\tau = 0)} = E(\tau) \cdot e^{-\frac{\tau}{\tau_0}} . \tag{114}$$

5.1.6.1 Area Enclosed by Weighted Multipath Error Envelopes

A fairly good qualitative multipath performance assessment can be obtained by computation of the areas enclosed by the weighted multipath error envelopes. Based on the weighted envelopes of Figure 5-12 (rural environment, E=25°, weighting scheme No. 1), the following normalized areas have been computed.

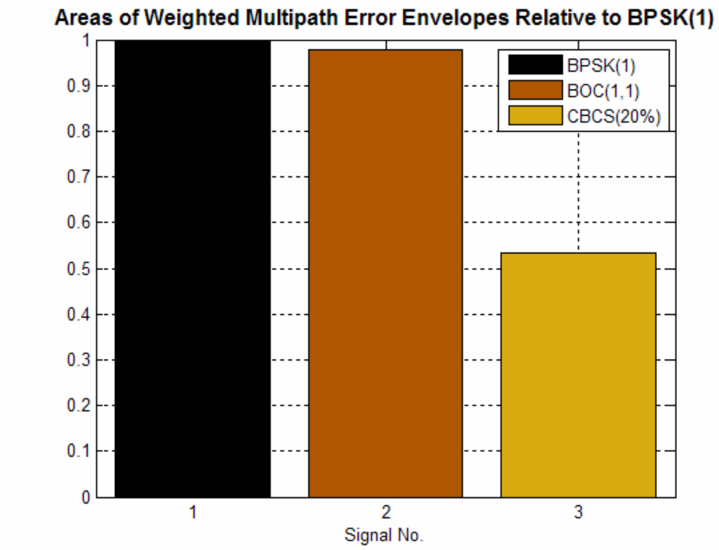

Figure 5-13: Comparison of areas enclosed by weighted multipath error envelopes (weighting scheme No.1, rural environment, E=25°).

Alternatively, instead of normalizing the first envelope area to unity, absolute area values can be computed to allow a better understanding of the multipath performance in different environments. When normalized areas are used, there are only insignificant differences between the different multipath environments.

5.1.6.2 Running Averages of Weighted Multipath Error Envelopes

Based on weighted envelopes like the ones illustrated in Figure 5-12, the running averages can be computed as well. Figure 5-14 illustrates the running averages of the weighted multipath error envelopes for the rural environment.

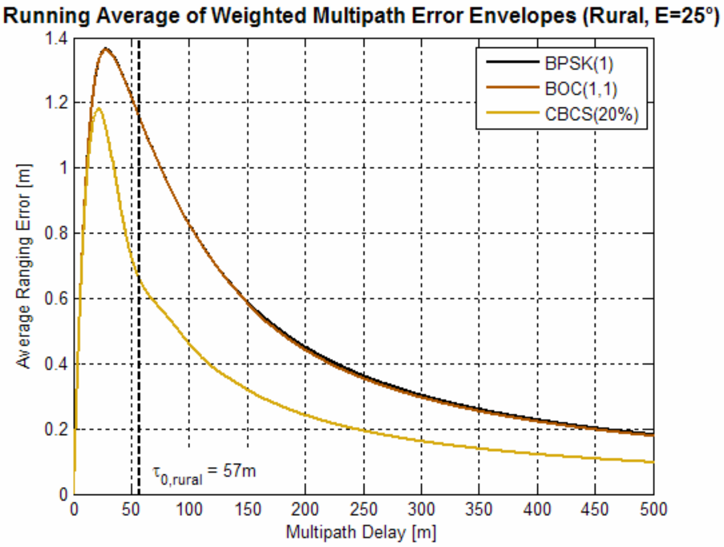

Figure 5-14: Multipath performance based on weighted envelopes (weighting scheme No.1).

Again, mean multipath errors can be extracted by determining the ordinate value of the running average at a certain path delay, e.g. at path delays τ_0 which are representative for the considered multipath environment. This leads to a mean multipath error of ~0.7m for the CBCS and ~1.2m for the BPSK(1) and the BOC(1,1). Mean multipath errors for all environments derived from running average plots based on weighted envelopes are given in Figure 5-15a (weighting scheme No.1) and in Figure 5-15b (weighting scheme No.2).

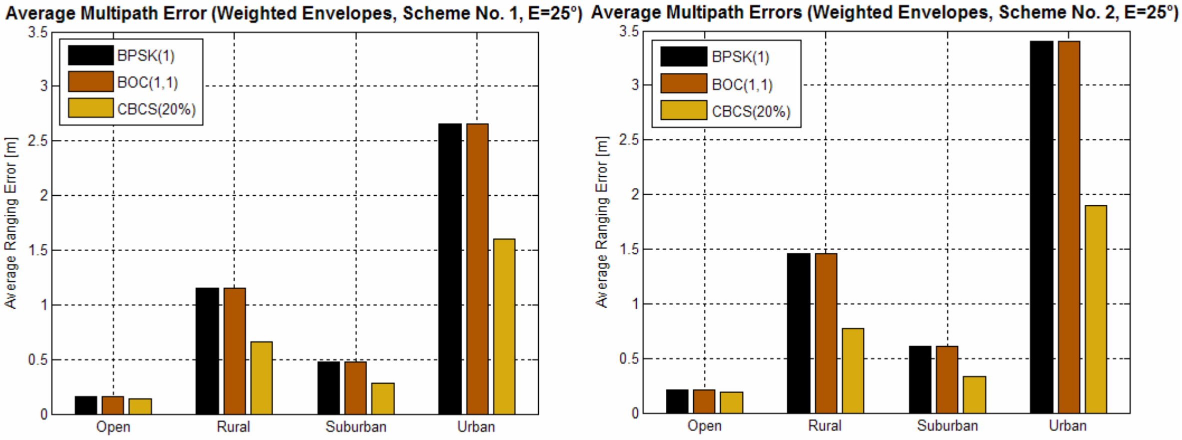

Figure 5-15: Mean multipath errors based on the analysis of weighted running average plots (left diagram: weighting scheme No.1, right diagram: weighting scheme No.2).

Both weighting schemes result in mean multipath errors that are of the same order. The mean errors derived from envelopes weighted by scheme No. 2 are without exception larger than those obtained from weighting scheme No. 1. The most important result is that the mean multipath errors derived by this method are of the same order as those obtained by the statistical channel model or derived from average power-delay profiles. It seems that this approach is suitable to derive typical and meaningful mean multipath errors for different environments (provided that their main characteristics in terms of typical SMR and typical path delays are known). The approach of scaling envelopes is much less complex than carrying out a multitude of simulations and deriving the required mean values statistically. In contrast to the more complex approaches (statistical channel models/power-delay profiles), modeling of multipath propagation by assuming one single reflection and by weighting the resulting multipath error envelopes with a suitable scaling function seems to be an adequate approach to obtain meaningful multipath errors.

5.1.7 Summary

Several models that characterize GNSS multipath propagation have been discussed and analyzed with respect to their potential of providing meaningful and realistic values for occurring multipath errors. All models are suitable for comparing different GNSS signals with respect to their multipath performance. Starting with the most complex and realistic model (the statistical channel model), its main characteristics have been used as input for all other models/approaches throughout this chapter. While all models allow qualitative statements about the multipath performance of a given signal/receiver combination, only three of them have the potential to provide meaningful multipath errors that can be used as input for the computation of GNSS error budgets. Against this background, the most important approaches are:

- Computation of mean multipath errors derived from statistical channel models (SCM)
- Computation of mean multipath errors derived from power-delay profiles (PDP)
- Computation of mean multipath errors derived from running average plots based on weighted multipath error envelopes (with consideration of different weighting schemes, RAW1 and RAW2)

Figure 5-16 summarizes the mean multipath errors obtained from these models. The different models lead to multipath errors of the same order, so that any of these models seems to be suitable to compute realistic and meaningful multipath errors. It should be noted, however, that these results could only be obtained because the main multipath characteristics derived from the statistical channel model served as input for all other models.

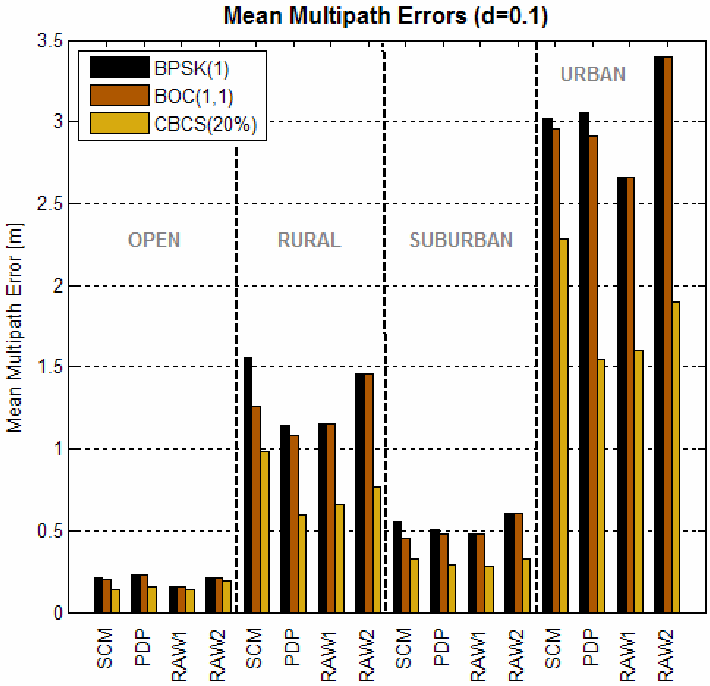

Figure 5-16: Comparison of mean multipath errors obtained from different multipath models (narrow correlation, d=0.1, E=25°).

Recall that for the computation of the mean multipath errors summarized in Figure 5-16, the same chip spacing has been assumed for each signal. All qualitative statements comparing the multipath performance of the BPSK, the BOC and the CBCS are based on this assumption. The main motivation for this work, however, was not to compare the multipath performance of different signals with respect to each other, but to show that different approaches to compute multipath errors lead to similar results. As can be illustrated by means of Figure 5-17 and Figure 5-18, consideration of a different chip spacing for all three signals (d=0.05) or consideration of a different tracking technique (a 0.1/0.2 chip ΔΔ implementation in this case) leads to the same qualitative results that the mean multipath errors obtained from the different multipath models are of the same order.

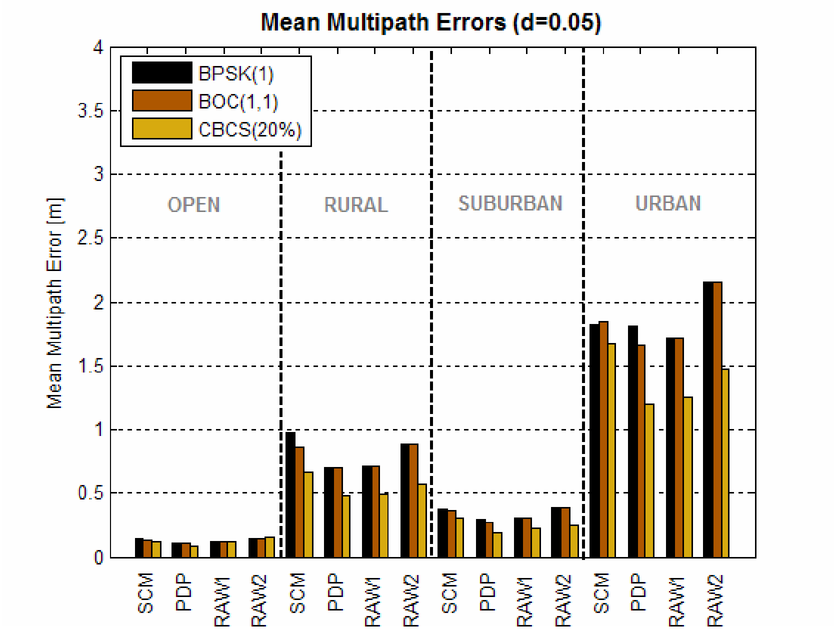

Figure 5-17: Comparison of mean multipath errors obtained from different multipath models (narrow correlation, d=0.05, E=25°).

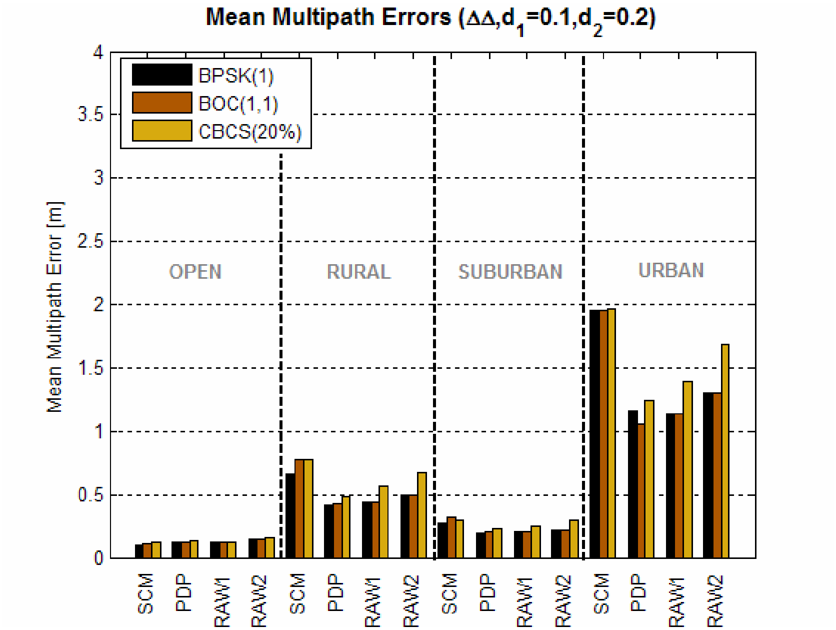

Figure 5-18: Comparison of mean multipath errors obtained from different multipath models (0.1/0.2 chip Double Delta correlator, E=25°).

With respect to the complexity of each model, the approach of using running average plots based on weighted multipath error envelopes seems to be the most efficient one. Table 5-2 summarizes all methods for multipath performance assessment discussed in this chapter. It differentiates between the potential of providing qualitative and meaningful (typical and realistic) quantitative results. Approaches that allow derivation of worst-case multipath errors (multipath error envelopes) or result in multipath errors that are not of the same order as those obtained by the approaches illustrated in Figure 5-16, were rated negatively in Table 5-2.

Summary: Methods for Multipath Performance Assessment		
Approach	**Qualitative Assessment**	**Quantitative Assessment**
Statistical Channel Models	YES	YES
Power-Delay Profiles	YES	YES
Weighted Multipath Error Env.	YES	NO
Running Averages	YES	YES
Areas	YES	NO
Multipath Error Envelopes	YES	NO
Running Averages	YES	NO
Areas	YES	NO

Table 5-2: Summary of methods for multipath performance assessment.

It should finally be noted that there are also other (empirical) multipath models. One approach, which has previously been used to compute the contribution of multipath errors to the UERE budget for the modernized GPS ([Kovach 2000]), is based on the RTCA/DO-245 document which contains “Minimum Aviation System Performance Standards (MASPS) for the Local Area Augmentation System (LAAS)” ([RTCA Special Committee 1993]). Such models have not been considered in this analysis because the resulting multipath errors are based on special assumptions (use of multipath-limiting antennas, consideration of specific multipath environments, averaging of observations over several antennas, and application of carrier smoothing algorithms). Therefore, the results of such models can hardly be compared to the ones obtained from the models discussed in this chapter.

5.2 Expected Code Multipath Errors

Based on the computation of running average multipath errors as obtained from weighted multipath error envelopes, mean code multipath errors have been computed for a signal scenario representing the current planning status of Galileo and considering the civil L5 signal of the modernized GPS. As it has been shown in the previous sections, weighting scheme no. 2 leads to slightly larger mean multipath errors than weighting scheme no. 1 and is thus used for the subsequent analysis (to ensure a worst case analysis). The computation is carried out for the following signals of the frequency bands L1, E6 and E5/L5 (under consideration of the signal characteristics listed in Table 5-3 and Table 5-4):

Signal/Receiver Parameters	**L1**			
Frequency Band	L1 (GPS)	E2-L1-E1 (OS)	E2-L1-E1 (OS)	E2-L1-E1 (PRS)
Center Frequency [MHz]	1575.42	1575.42	1575.42	1575.42
Carrier Wavelength [m]	0.190	0.190	0.190	0.190
Modulation Scheme	BPSK(1)	BOC(1,1)	MBOC(6,1,1/11)	$BOC_{cos}(15,2.5)$
Chip. Rate [Mcps]	1.023	1.023	1.023	2.56
Chip Length [m]	293.05	293.05	293.05	117.22
Pre Corr. Bandwidth [MHz]	24	24	24	40

Table 5-3: Considered signals at L1.

Signal/Receiver Parameters	**E6**		**E5/L5**	
Frequency Band	E6 (CS)	E6 (PRS)	GPS L5	E5ab (OS)
Center Frequency [MHz]	1278.75	1278.75	1176.45	1191.80
Carrier Wavelength [m]	0.234	0.234	0.255	0.252
Modulation Scheme	BPSK(5)	$BOC_{cos}(10,5)$	BPSK(10)	AltBOC(15,10)
Chip. Rate [Mcps]	2.56	2.56	10.23	10.23
Chip Length [m]	58.61	58.61	29.31	29.31
Pre Corr. Bandwidth [MHz]	24	40	24	51[2]

Table 5-4: Considered signals at E6 and E5/L5.

---

[2] results in same code multipath errors as separate processing of E5a or E5b with a bandwidth of 24MHz

The MBOC modulation is foreseen as a replacement for the BOC(1,1) which was the first baseline for the Galileo L1 OS signal. It is a combination of a BOC(1,1) and a BOC(6,1) with the BOC(6,1) having 1/11 of the power of BOC(1,1). The MBOC is the result of an optimization process aimed at enhancing the performance of the OS on L1. The MBOC modulation is also foreseen for the fourth civil GPS signal on L1 (L1C).

Mean code multipath errors have been computed for the Narrow Correlator, assuming a correlator spacing of 0.1 chips, and for a Double Delta implementation using correlator spacings of 0.2 and 0.1 chips. Both correlation techniques are common approaches to mitigate code multipath.

As will be shown below, the expected multipath errors are rather small in some cases (especially when the open environment is considered) and of the same order as the thermal noise influence. In order to get an idea of the ratio between code noise and multipath, the influence of thermal noise for each signal is computed in the form of the so-called Cramer-Rao Bound, a lower bound for the thermal noise influence that does not depend on the correlation value and that can be computed by using the following expression ([SPILKER 1996d]):

$$\sigma_{CRLB}^2 = \frac{c^2 B_{DLL}}{4\pi^2 f_c^2 \, C/N_0 \int_{-B_{IF}}^{B_{IF}} f^2 \left|S(f)\right|^2 df} \tag{115}$$

The Cramer-Rao Lower Bound depends on the speed of light c, the code chipping rate f_c, the noise bandwidth B_{DLL} of the code tracking loop, the carrier frequency f, the single-sided signal bandwidth at baseband B_{IF}, the (normalized) power spectral density $S(f)$ and the C/N_0.

A noise influence of the order of the Cramer-Rao bound can be achieved by using a coherent early minus late correlator (such as the Narrow Correlator) with an appropriate correlator spacing. In such a case, the noise performance of the Narrow Correlator is very close to this theoretical lower bound. It is therefore used to assess the noise performance for the Narrow Correlator as illustrated below. For the code noise computations, a C/N_0 of 45dBHz has been assumed.

As stated in [MCGRAW and BRAASCH 1999] and already discussed in section 4.1.2.2, the use of a Double Delta correlator results in a noise increase of 3dB. The code noise computations for this correlation technique can therefore also be based on the computation of the Cramer-Rao Lower Bound by using a C/N_0 of 42dBHz instead of the 45dBHz as assumed for the Narrow Correlator. The resulting noise levels are approximately 40% higher than those obtained for the Narrow Correlator, a percentage that is also cited in [SLEEWAGEN and BOON 2001].

5.2.1 Narrow Correlator

The expected mean code multipath errors for the 0.1 chip narrow correlator are illustrated in Figure 5-19. The code noise influence for all signals is illustrated in the form of transparent grey bars. Since they base on a certain C/N_0, they are independent from the multipath environment and are also assumed independent from the elevation angle E.

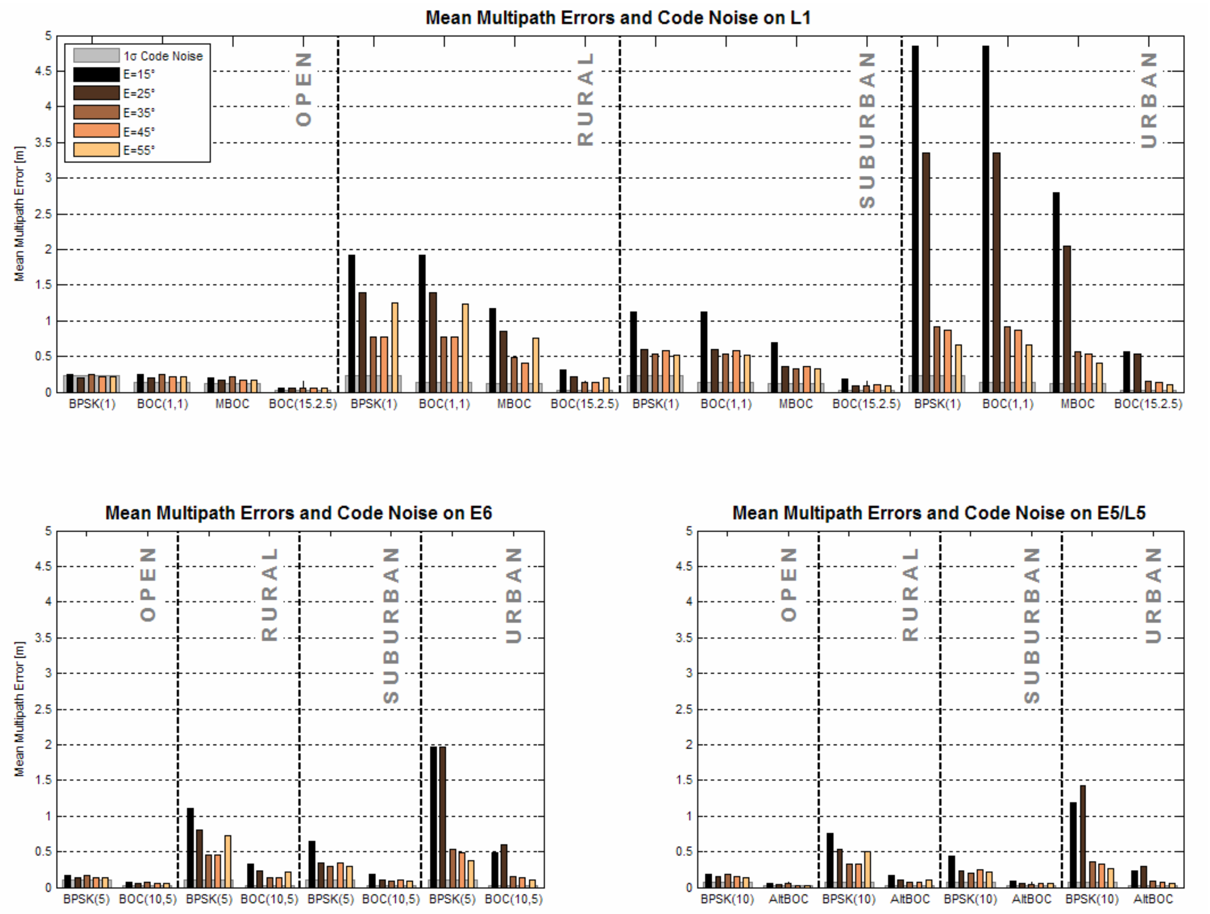

Figure 5-19: Expected mean code multipath errors and code noise for the 0.1 chip narrow correlator. The code noise influence represents the Cramer-Rao Lower Bound and was computed assuming a C/N_0 of 45dBHz.

The results illustrated in Figure 5-19 can be summarized as follows:

- At L1, the expected code multipath errors for BPSK(1) and BOC(1,1) are exactly the same. As a result, the former baseline signal for the Galileo Open Service at L1 does not outperform the GPS C/A code signal with respect to code multipath.
- Compared to BOC(1,1), the optimized MBOC signal shows a significantly better code multipath performance (smaller multipath error).
- As expected, the PRS signal at L1 outperforms all other L1 signals (smallest multipath error).
- At E6, the PRS signal (BOC_{cos}(10,5)) clearly outperforms the CS signal (BPSK(5)).
- At L5/E5, the Galileo Open Service signal AltBOC(15,10) clearly outperforms the GPS L5 signal BPSK(10).
- At L1, mean multipath errors up to ~4.9m have to be expected.
- At E6, mean multipath errors up to ~2.0m have to be expected.
- At L5/E5, mean multipath errors up to ~1.4m have to be expected.
- As expected, the largest mean code multipath errors typically occur in urban environments.
- The mean multipath errors that have to be expected in the open environment are of the same order as the influence of thermal noise.

5.2.2 Double-Delta Correlator

The expected mean code multipath errors for the double-delta implementation are illustrated in Figure 5-20. As in the previous section, the code noise influence for all signals is illustrated in the form of transparent grey bars. It has been computed by carrying out the same computations as for the Narrow Correlator, but using a reduced C/N_0 of 42dBHz.

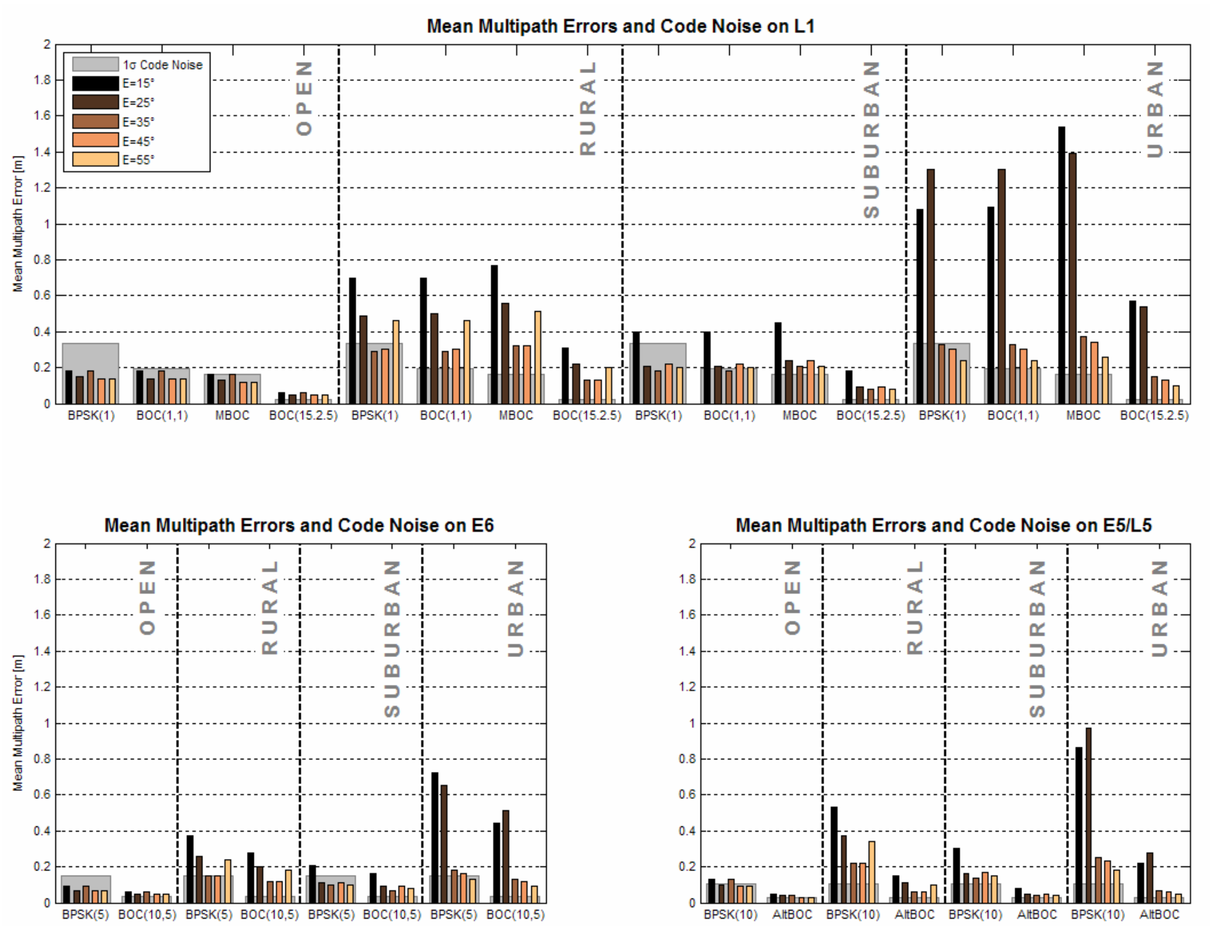

Figure 5-20: Expected mean code multipath errors and code noise for a Double Delta correlator implementation. The code noise influence can be obtained by increasing the values obtained for the 0.1 chip narrow correlator by ~40%.

A first comparison between the expected mean code multipath errors obtained from the narrow correlator and those obtained from the double-delta correlator shows that for any signal, signal elevation and multipath environment, the use of the double-delta correlator results in equal or smaller mean multipath errors. Further results can be summarized as follows:

- At L1, the expected code multipath errors for BPSK(1) and BOC(1,1) are exactly the same. Similar to the case of the narrow correlator (see previous section), the former baseline signal for the Galileo Open Service at L1 does not outperform the GPS C/A code signal with respect to code multipath.
- In contrast to the multipath performance of the narrow correlator, the optimized MBOC signal does not show superior code multipath performance; the expected mean code multipath errors may even be larger than for BPSK(1) or BOC(1,1).
- The PRS signal at L1 outperforms all other L1 signals (smallest multipath error)
- At E6, the PRS signal outperforms the CS signal (but not as clearly as in the narrow correlator case).

- At L5/E5, the Galileo Open Service signal AltBOC(15,10) outperforms the GPS L5 signal BPSK(10).
- At L1, mean multipath errors up to ~1.5m have to be expected.
- At E6, mean multipath errors up to ~0.7m have to be expected.
- At L5/E5, mean multipath errors up to ~1.0m have to be expected, i.e. using the 0.2/0.1 chip double-delta correlator, code multipath errors at L5/E5 may be larger than at E6.
- Due to the increased influence of thermal noise when using a Double Delta correlator, typical multipath errors may be of the same order or even smaller as the expected code noise. As can be derived from Figure 5-20, this is the case for all signals at all elevation angles in the open environment. However, such cases also occur in other environments (e.g. for the BPSK(1) signal in suburban and even in urban environments).

5.2.3 Iono-Free Linear Combinations

Mean code multipath errors have also been computed for some iono-free linear combinations. Such combinations are based on pseudorange observations obtained from two or more frequencies. In case that code observations PR_1 and PR_2 at carrier frequencies f_1 and f_2 (with $f_1 > f_2$) are available, the iono-free linear combination can be expressed as

$$\begin{aligned}\rho^* &= \underbrace{\frac{f_1^2}{(f_1^2 - f_2^2)}}_{A} PR_1 - \underbrace{\frac{f_2^2}{(f_1^2 - f_2^2)}}_{B} PR_2 \\ &= A \cdot PR_1 - B \cdot PR_2\end{aligned} \tag{116}$$

This linear combination only eliminates the ionospheric path delay. All other error sources (clock errors, ephemeris errors, tropospheric errors and noise) are still present in this observable. Moreover, the linear combination is significantly noisier than the pseudoranges measured at either frequency. According to the law of error propagation, the standard deviation of the iono-free pseudorange ρ^* can be expressed as follows:

$$\sigma_{\rho^*} = \sqrt{A^2 \sigma_{PR_1}^2 + B^2 \sigma_{PR_2}^2} \tag{117}$$

Assuming that the pseudorange noise terms σ_{PR1} and σ_{PR2} are equal ($\sigma_{PR1} = \sigma_{PR2}$) and uncorrelated, equation (117) simplifies to

$$\sigma_{\rho^*} = \sqrt{A^2 \sigma_{PR}^2 + B^2 \sigma_{PR}^2} = \sqrt{A^2 + B^2} \cdot \sigma_{PR} = C \cdot \sigma_{PR}\,. \tag{118}$$

Although the simplification $\sigma_{PR1} = \sigma_{PR2}$ is not valid in most cases, it can be used to demonstrate the significant increase of thermal noise when using iono-free linear combinations. For the signal scenario listed in Table 5-3 and Table 5-4, the following factors *C* must be expected:

Signal Combinations			**Increase of Thermal Noise**		
Freq. Bands	**Signal No. 1**	**Signal No. 2**	**A**	**B**	**C**
L1/E5a/L5	BPSK(1)	BPSK(10)	2.26	1.26	**2.59**
	BOC(1,1) or MBOC or $BOC_{cos}(15,2.5)$	AltBOC(15,10)	2.34	1.34	**2.69**
E6/E5	BPSK(5) or $BOC_{cos}(10,5)$	AltBOC(15,10)	7.61	6.61	**10.08**
L1/E6	BOC(1,1) or $BOC_{cos}(15,2.5)$ or MBOC	BPSK(5)	2.93	1.93	**3.51**
	$BOC_{cos}(15,2.5)$ or MBOC	$BOC_{cos}(10,5)$	2.93	1.93	**3.51**

Table 5-5: Increase of thermal noise for iono-free linear combinations (factor C).

The expected mean code multipath errors for iono-free linear combinations can be calculated by replacing σ_{PR1} and σ_{PR2} in equation (117) with the mean code multipath errors for the single frequency case (e.g. as computed in section 5.2.1). Since the combined code noise (and code multipath) is smaller for a large frequency separation than for a small one, the following multipath analysis was carried out only for the following signal combinations.

Case ID	L1	E5a/L5
Case 1	BPSK(1)	BPSK(10)
Case 2	BOC(1,1)	AltBOC(15,10)
Case 3	MBOC(6,1,1/11)	AltBOC(15,10)
Case 4	BOC$_{cos}$(15,2.5)	AltBOC(15,10)

Table 5-6: Considered iono-free linear combinations between L1 and E5a/L5.

Case 1 represents the linear combination that can be formed by using the signals of the modernized GPS. Case 2-4 are the possible options related to Galileo. The expected mean code multipath errors for these scenarios are summarized in the following diagram (assuming the use of a 0.1 chip narrow correlator for code tracking). The expected code noise errors are computed by means of equation (117), where the pseudorange noise terms σ_{PR1} and σ_{PR2} represent the Cramer-Rao Lower Bound as computed in section 5.2.1.

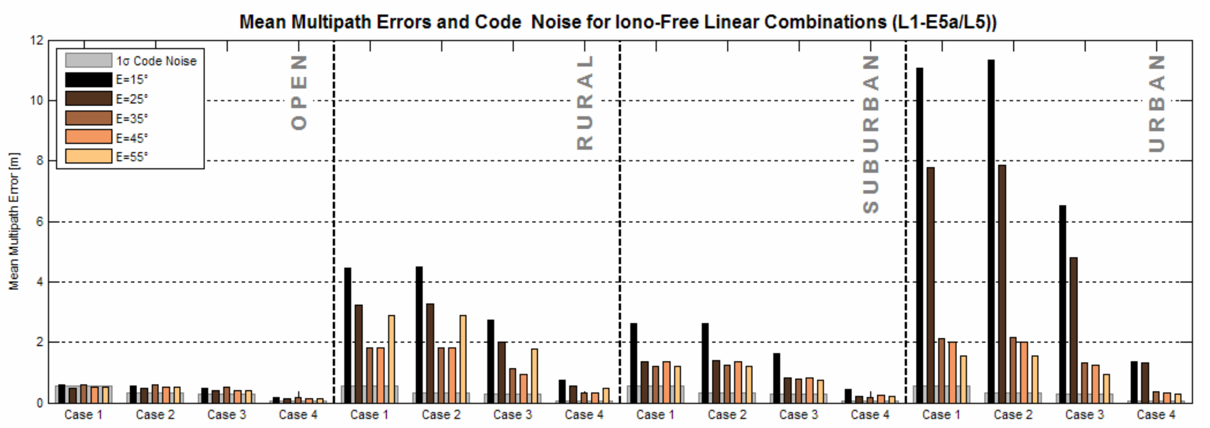

Figure 5-21: Expected mean code multipath errors for four iono-free linear combinations.

Whatever environment is considered, the use of the BPSK(1)/BPSK(10) and the BOC(1,1)/AltBOC(15,10) combination result in nearly identical multipath errors. Interestingly, the expected code multipath errors can be reduced significantly by using the optimized MBOC instead of BOC(1,1) in combination with the AltBOC(15,10) (case 3). The smallest code multipath errors can be expected when using the BOC$_{cos}$(15,2.5) / AltBOC(15,10) combination (case 4).

When using iono-free linear combinations in conjunction with the 0.1 chip narrow correlator, typical code multipath errors up to ~11.3m have to be expected (urban environment). For open environments, errors up to ~0.6m have to be expected. For the other environments, the corresponding errors are ~4.5m (rural) and ~2.6m (suburban).

5.3 Expected Carrier Multipath Errors

As already discussed and illustrated in section 3.2.4, the expected carrier multipath errors for dedicated geometric path delays depend on the shape of the correlation function. However, maximum carrier phase errors due to multipath always occur for short path delays (theoretically for τ=0) and for a multipath relative amplitude of α=1. Under these conditions, the maximum carrier multipath only depends on the carrier frequency and cannot exceed one fourth of the carrier wavelength (λ/4, see also section 3.1.2). The maximum carrier multipath errors for different carrier frequencies are listed in Table 5-7.

Frequency Band	Carrier Frequency	Carrier Wavelength	Max. Carr. Multipath
E1/L1	1575.42 MHz	0.190 m	~48 mm
L2	1227.60 MHz	0.244 m	~61 mm
E6	1278.75 MHz	0.234 m	~59 mm
E5a/L5	1176.45 MHz	0.255 m	~64 mm
E5b	1207.14 MHz	0.248 m	~62 mm
E5a/E5b	1191.80 MHz	0.252 m	~63 mm

Table 5-7: Maximum carrier multipath error for different carrier frequencies.

It should be noted, however, that the actual carrier multipath errors are expected to be smaller than indicated in Table 5-7. Considering the typical SMR values for the different multipath environments (see Table 5-1), the following worst-case carrier multipath errors can be expected for the GPS/Galileo signals on L1, E6 and E5ab/L5.

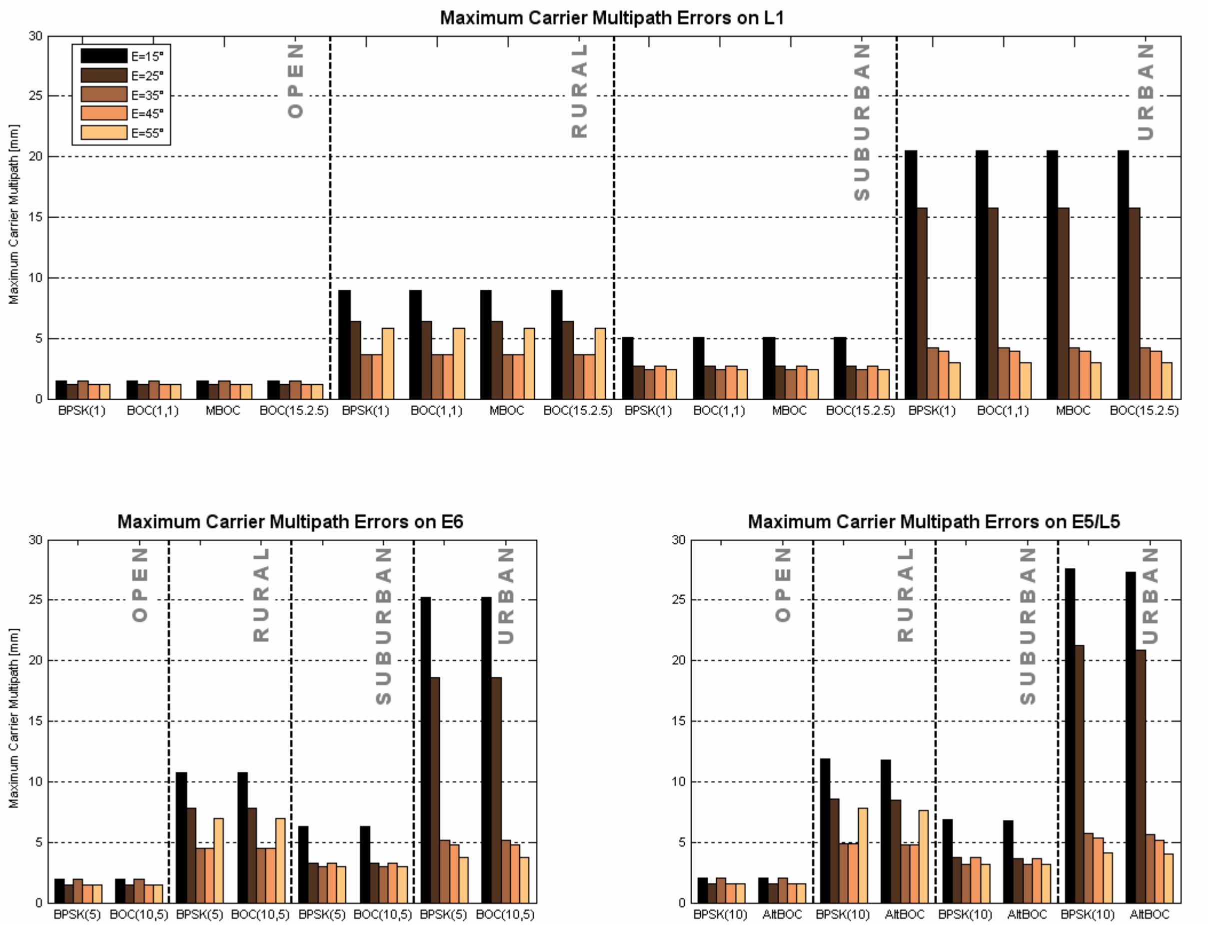

Figure 5-22: Worst-case carrier multipath errors on L1, E6 and E5/L5.

The multipath errors have been derived from carrier multipath error envelopes at τ=0 (where maximum errors occur). At zero path delay, the resulting carrier multipath only depends on the assumed SMR value and on the carrier frequency. It does neither depend on the modulation scheme nor on the correlation technique, i.e. that the maximum carrier multipath errors illustrated in Figure 5-22 are valid for standard carrier tracking as well as for HRC tracking approaches. Hence, assuming a certain multipath environment and a dedicated carrier frequency, the errors at dedicated elevation angles are the same for all signals in this frequency band. Slight differences between two signals only occur for the BPSK(10) and the AltBOC(15,10) signal at E5ab/L5, because both signals have slightly different carrier frequencies.

At L1, the maximum carrier multipath errors are ~2mm (open environment), ~9mm (rural environment), ~5mm (suburban environment) and ~21mm for the urban environment. Maximum errors at E6 are ~2mm (open), ~11m (rural), ~6mm (suburban) and ~25mm (urban). At E5/L5, maximum errors of ~2mm (open), ~12mm (rural), ~7mm (suburban) and ~28mm (urban) must be expected. All errors occur for small elevation angles (E=15°). The largest errors must be expected in the urban environment. In such environments, errors up to ~21mm must be expected at L1 and up to ~25mm and ~28mm for E6 and E5/L5, respectively. In summary, maximum carrier multipath errors between ~1mm and ~28mm must be expected for the signals and multipath environments considered in Figure 5-22.

Part II.

Multipath Detection Techniques and Monitoring Approaches

The second part of this thesis covers various aspects of multipath detection and monitoring. Chapter 6 contains an overview of current multipath detection and monitoring approaches. In this context, techniques like "code minus carrier" monitoring, SNR monitoring, the use of differenced observations or spectral and wavelet analysis are discussed with respect to their benefits and drawbacks or their real-time capability. In chapter 7, a completely new approach for real-time multipath monitoring by processing multi-correlator observations will be introduced. So far, multi-correlator observations have primarily been used for the detection of satellite signal failures ("Evil Waveforms"). The proposed multipath monitoring scheme makes use of the same basic observations as used for the detection of Evil Waveforms and utilizes them for the purposes of real-time multipath monitoring. The objective is to provide the user with instant information whether or not a signal is affected by multipath. The proposed monitoring scheme has been implemented in the form of a Matlab-based software called RTMM (Real-Time Multipath Monitor) which has been used to verify the monitoring approach and to determine its sensitivity. Further topics are discussions on how the monitoring approach can be further optimized or a detailed discussion on the benefits and the shortcomings of this approach.

6. Multipath Detection and Monitoring

This section provides an overview of several approaches to monitor multipath effects. Multipath monitoring might be useful for antenna siting applications or as part of a signal quality monitoring system. The approaches discussed in this chapter are:

- Code minus carrier (CMC) monitoring
- SNR (C/N_0) monitoring
- Differencing observations (e.g. single or double differences)
- Multipath Estimating Delay Lock Loop (MEDLL)
- Receiver Autonomous Integrity Monitoring (RAIM)
- Spectral analysis
- Wavelet analysis

All approaches are discussed with respect to their benefits and drawbacks, including the potential of providing real time information on the presence of multipath influences. The term “real time” does not only cover the fact that a monitoring algorithm can be implemented as a real time algorithm, it is – in the context of this thesis – rather defined as the ability to detect multipath as soon as it appears (instant detection). An algorithm that analyzes a set of *N* previous observations, for example, may be implemented in real time, but as the result of this analysis is derived from the last *N* observations, there may not be any information if the current observation is influenced by multipath. In the following sections, such approaches are characterized as “near real time”.

6.1 Code minus Carrier (CMC) Monitoring

One method of multipath monitoring is differencing the code and carrier observations. Both observations may be affected by multipath. However, carrier multipath is much smaller than code multipath, so that the influences of carrier multipath become hidden in the ‘code minus carrier’ observations. As a result, the CMC approach is suitable for monitoring code multipath but not for monitoring carrier multipath. Table 6-1 lists the observation equations for code and carrier observations:

<table>
<tr><th colspan="2">Observation Equations</th></tr>
<tr><th>Pseudorange</th><th>Carrier Phase</th></tr>
<tr><td>$PR = R + c(dt - dT) + d_I + d_T + \varepsilon_{PR}$</td><td>$\Phi = R + c(dt - dT) - d_I + d_T + \lambda N + \varepsilon_{\Phi}$</td></tr>
<tr><td colspan="2">R Geometric distance between the user and the satellite that can be expressed by the Cartesian coordinates of satellite and user. Hence, R contains the unknown user position and the satellite position (including ephemeris errors).
dt Satellite clock error
dT Receiver clock error
d_I Ionospheric path delay
(different signs for code and carrier observations due to ionospheric dispersion)
d_T Tropospheric path delay
N Integer phase ambiguities
λ Carrier wave length
ε_{PR},ε_{Φ} Code/carrier noise and other error sources like code/carrier multipath</td></tr>
</table>

Table 6-1: Observation equations for code and carrier measurements.

Differencing code and phase measurements leads to the ‘code minus carrier’ (CMC) observable:

$$\begin{aligned} CMC &= PR - \Phi \\ CMC &= 2d_I - \lambda N + \varepsilon_{PR} - \varepsilon_{\Phi} \end{aligned} \tag{119}$$

Formation of CMC eliminates the clock errors, the tropospheric path delay and the ephemeris errors. Due to the ionospheric dispersion, the resulting observable contains twice the ionospheric path delay, the carrier ambiguities, the combined code and phase noise and the combined code and carrier multipath. Carrier multipath effects are relatively small, so that mainly code multipath is visible in the CMC observations. In case that the ionospheric path delay significantly changes with time, the CMC observations will show a long-periodic trend which can be eliminated by either using dual-frequency observations or by filtering the CMC observations as introduced in the following section.

6.1.1 Filtering of CMC Observations

In order to be able to detect possible multipath influences reliably, it is necessary to eliminate the long-periodic ionospheric trend and to smooth out the influence of thermal noise. To accomplish that task, a digital band-pass filter can be applied to the data. A filter that is commonly used for this purpose is a high-order Butterworth filter. The frequency bounds of the filter must be chosen such that all typically multipath-related frequencies pass the filter. The filter process can be described as follows (adopted from [HAMMING 1983]):

$$CMC_{fil,i} = \sum_{k=0}^{n} a_k \cdot CMC_{i-k} - \sum_{k=1}^{n} b_k \cdot CMC_{fil,i-k} \tag{120}$$

In equation (120), a_k and b_k are the filter coefficients, CMC_i the original ‘Code minus Carrier’ observations at epoch i, $CMC_{fil,i}$ the filtered ‘Code minus Carrier’ observations at epoch i and n the filter order. Note that the CMC observable contains the integer phase ambiguity N, so that it is sensitive to cycle-slips. In a practical implementation, a cycle-slip detection and repair algorithm can be implemented or the filter process can be reset after a cycle-slip has been detected. The filter coefficients are a function of the sampling rate, the cutoff-frequencies and the filter order. A detailed description on how to calculate the filter coefficients can be found in [HAMMING 1983].

Equation (120) indicates that the i^{th} filtered CMC value is formed by use of already filtered data. The filter order n determines how many previously filtered observations are used. Assuming a filter of order n=8, the filter process uses the last 8 previously filtered CMC values to compute the filtered value at the current epoch. Due to this fact and due to an occurring phase shift between the original and filtered data (which is a normal behavior for filtered data), multipath cannot be detected in real-time. Figure 6-1 illustrates an example of a filter process based on simulated CMC observations.

In Figure 6-1, the ionospheric influence is modeled as a second order polynomial, a sinusoidal function has been applied to model multipath (amplitude: 1m) and random numbers uniformly distributed between 0 and 1 have been added to account for the influence of thermal noise. The filtered observations are indicated by the green curve that only shows the influence of multipath. The thermal noise has been smoothed out and the ionospheric trend has been removed by the filter process.

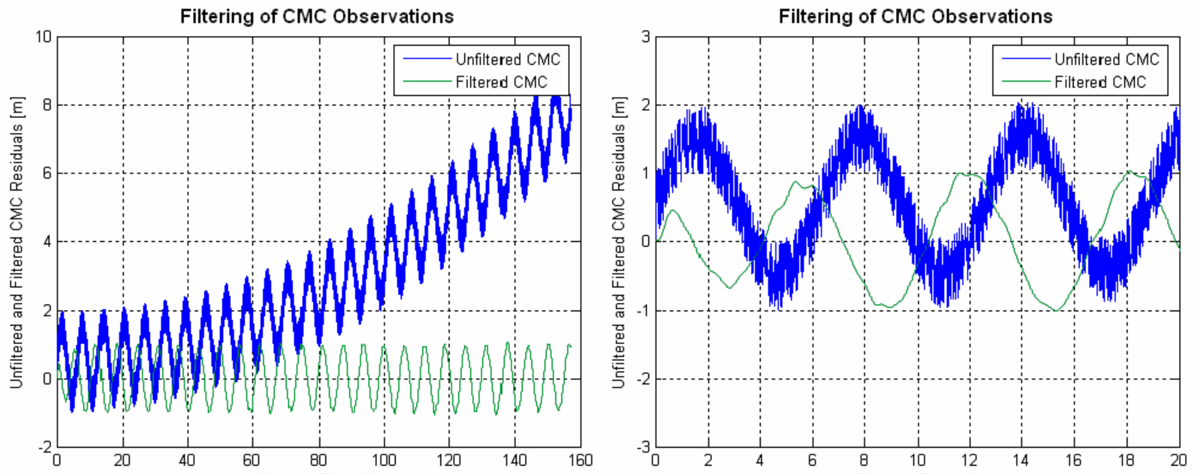

Figure 6-1: Filtering of simulated CMC observations by means of an 8th order Butterworth filter.

Using real GNSS data, the implemented filter needs a rather long time to initialize itself. Figure 6-2 illustrates this behavior by comparing unfiltered CMC data (upper diagram) with a filtered version of the same data set (lower diagram). The data set has been obtained from a GPS hardware simulator. For visualization purposes, the ionospheric influence and the carrier ambiguities have been removed from the unfiltered data. The filter input, however, contained the ionospheric influence and results in the filtered data set.

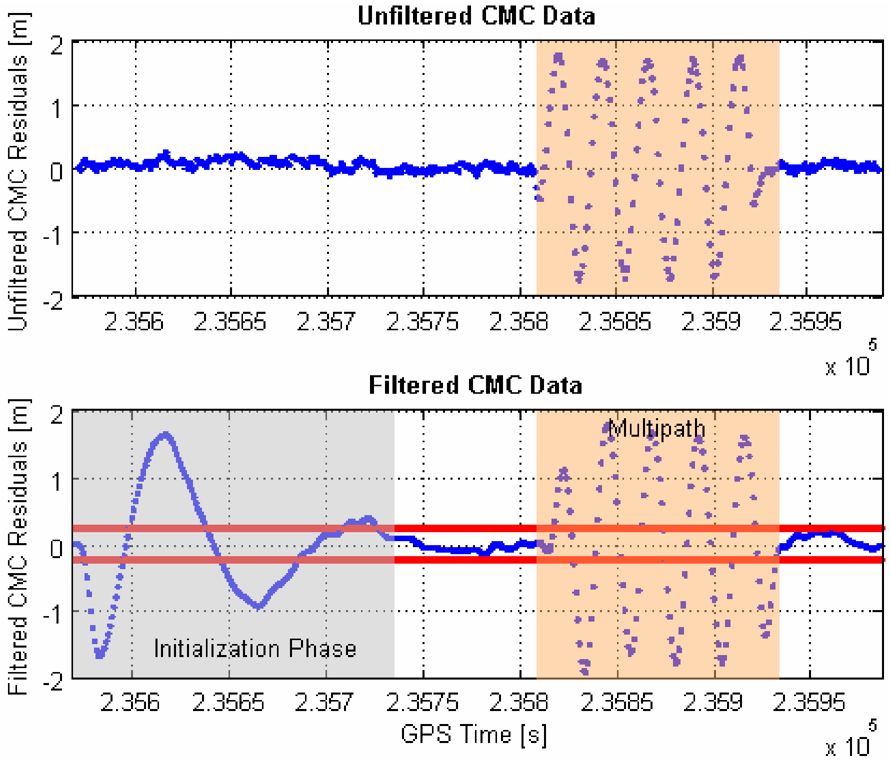

Figure 6-2: Initialization phase and multipath detection using an 8th order Butterworth filter.

Based on the filtered data set, multipath monitoring can be performed by comparing the filtered CMC residuals with a threshold that represents the expected influence of thermal noise on the CMC observations (see section 6.1.2 for details). Filtered CMC residuals exceeding this threshold can be regarded as multipath-affected.

The long initialization phase illustrated in Figure 6-2 is not the only practical issue. As already mentioned, this monitoring approach is also sensitive to cycle-slips. This would either require a cycle-slip detection and repair algorithm or a reset of the filter process after a cycle-slip is detected. The first approach would increase the method's complexity and computational load, a reset of the filter process would induce another initialization phase during which multipath detection is impossible. Moreover, the algorithm is very sensitive to data gaps which have to be handled in a similar manner as cycle-slips.

6.1.2 Monitor Thresholds

The CMC observations contain the influence of code and phase noise. However, code noise is the predominant effect. Therefore, in case that the actual discriminator implementation of the monitoring receiver is known, the noise variance of the underlying code discriminator can be used to set up the monitor thresholds. The dot-product discriminator, for example, has a closed-loop noise standard deviation of

$$\sigma_T = T_C \cdot \sqrt{\frac{B_L d}{2 \cdot SNR}\left(1+\frac{1}{T \cdot SNR}\right)}\ [m], \tag{121}$$

where T_C [m] is the code chip length, B_L [Hz] the code loop noise bandwidth, d the correlator spacing and T [s] the pre-detection integration time ([Van Dierendonck 1996]). The SNR can be expressed as a function of the C/N_0 [dB-Hz] in the form $SNR = 10^{C/10N_o}$. The monitoring thresholds can be implemented as

$$thres_{CMC} = \pm m_{exp}\sigma_T, \tag{122}$$

where m_{exp} is a threshold expansion factor that determines the false-alarm rate of the monitor implementation. Note that the setup of realistic monitoring thresholds by using equations (121) and (122) requires a fairly good knowledge of the receiver architecture (discriminator, loop noise bandwidth, correlator spacing, integration time). It should also be noted that due to the band-pass filter characteristics, the filtered CMC observations are less affected by thermal noise.

6.2 SNR Monitoring

Two different approaches can be used to implement an SNR (or C/N_0) based multipath monitoring algorithm. The first one bases on the computation of a theoretical (expected) C/N_0 as obtained from link budget considerations, the second approach bases on polynomials describing the expected C/N_0 as a function of the elevation angle obtained from calibration measurements.

6.2.1 Based on Link Budget Computations

In general, the expected C/N_0 as computed by a receiver can be determined by performing link budget computations. The simplest expression for the expected C/N_0 is the ratio between the received power P_S and the total spectral noise density N_0 ([Misra and Enge 2001]):

$$C/N_{0,exp} = \frac{P_S\,[W]}{N_0\,[W/Hz]} = \frac{P_T G_T G_R}{4\pi R^2 L_A} \cdot \frac{\lambda^2}{4\pi} \cdot \frac{1}{N_0}\ [dBHz] \tag{123}$$

In equation (123), P_T is the transmit power of the satellite signal, G_T and G_R are the antenna gain patterns of the transmitting antenna and the user antenna, λ is the carrier wavelength, atmospheric losses are considered by the term L_A and R denotes the distance between the satellite and the user antenna. The total spectral noise density N_0 can be expressed by BOLTZMANN's constant k and the equivalent noise temperature T_{eq} as

$$N_0 = kT_{eq}\,[\mathrm{W/Hz}]. \tag{124}$$

Although rather simple, this approach comprises some practical issues. To obtain an accurate estimation of the expected C/N_0, parameters like the antenna gains G_T and G_R must be known precisely (as a function of the signal elevation or even azimuth and elevation). Moreover, it is not possible to quantify the atmospheric losses in real time. Furthermore, the spectral noise density N_0 depends on the receiver hardware, whose noise characteristics may not be known precisely as well. There are also additional parameters affecting the actual C/N_0 that are not considered in equation (123) such as de-pointing or polarization mismatch losses. Therefore, recording C/N_0 profiles during a calibration campaign seems to be a more practical approach (see next section).

6.2.2 Based on Recorded C/N_0 Profiles

This approach requires a calibration campaign during which the C/N_0 observations of each satellite are recorded during one or several entire passes. Based on the obtained C/N_0 profiles, the expected C/N_0 can be expressed in the form of a k^{th} order polynomial as a function of the elevation angle E or – if the antenna pattern is not rotation-symmetric with respect to the local plumb line – as a function of azimuth A and elevation E:

$$C/N_0\,(E)_{exp} = \sum_{n=0}^{k} a_n E^n \tag{125}$$

$$C/N_0\,(A,E)_{exp} = \sum_{j=0}^{s} a_j f_j(A,E) \tag{126}$$

In equation (125), a_n are the coefficients of the k^{th} order polynomial. The index s in equation (126) depends on the order of the underlying polynomial. Assuming that the antenna pattern can be modeled as a second order polynomial (k=2, s=5), equations (125) and (126) can be expressed as follows:

$$C/N_0\,(E)_{exp} = a_0 + a_1E + a_2E^2 \tag{127}$$

$$\begin{aligned} C/N_0\,(A,E)_{exp} &= a_0 + a_1f_1(A,E) + a_2f_2(A,E) + a_3f_3(A,E) + a_4f_4(A,E) + a_5f_5(A,E) \\ &= a_0 + a_1A + a_2E + a_3A^2 + a_4E^2 + a_5AE \end{aligned} \tag{128}$$

The coefficients can be derived by applying a univariate or bivariate regression on the pattern data. Alternatively, look-up tables (LUTs) can be derived from the C/N_0 profiles if any azimuth-dependency must be expected. Once the coefficients are known or the LUTs are available, the expected C/N_0 can be computed by inserting the current satellite position in the sky (azimuth and elevation or elevation only).

6.2.3 Monitor Thresholds

Based on the computation of expected C/N_0 values, the monitor thresholds can be computed by making use of the theoretical standard deviation of the C/N_0 observable.

According to [PANY and EISSFELLER 2006], the variance of the C/N_0 can be expressed as follows:

$$\sigma^2_{C/N_0,exp} = \frac{1}{T^2 M}\left(1+2T\,C/N_{0,exp}\right) \tag{129}$$

T is the coherent integration time and *M* the total number of integrations to obtain the C/N_0 estimation. For GPS receivers, a typical value for the integration time is T=0.02s that corresponds with the inverse data rate of 50Hz. An integration time of T=0.02s together with M=8 showed a good match between the theoretically derived variance and the empirically derived variance as obtained from a C/N_0 time series recorded with a NovAtel receiver. These values serve as a basis for the subsequent analyses and monitoring implementations. The monitoring thresholds $thres_{C/N0}$ can be implemented as

$$thres_{C/N_0} = C/N_{0,exp} \pm m_{exp}\sigma_{C/N_0,exp}\,, \tag{130}$$

where m_{exp} is a so-called threshold expansion factor that determines the false-alarm rate of the monitoring implementation. Figure 6-3 illustrates a C/N_0 profile of PRN5 as obtained from a GPS hardware simulator. In order to determine the expected C/N_0 as a function of the elevation angle, a 3rd order polynomial was fitted to the data (green solid line). This allows the computation of the expected C/N_0 as a function of the elevation angle according to equation (125) and the theoretical variance of the expected C/N_0 according to equation (129). For the definition of the monitor thresholds (red dashed lines), a threshold expansion factor of m_{exp}=8 has been assumed. The theoretical sensitivity of this monitoring approach is discussed in section 7.11 where it is compared to the sensitivity of a novel monitoring approach that uses multi-correlator observations to detect distortions of the signal's correlation function.

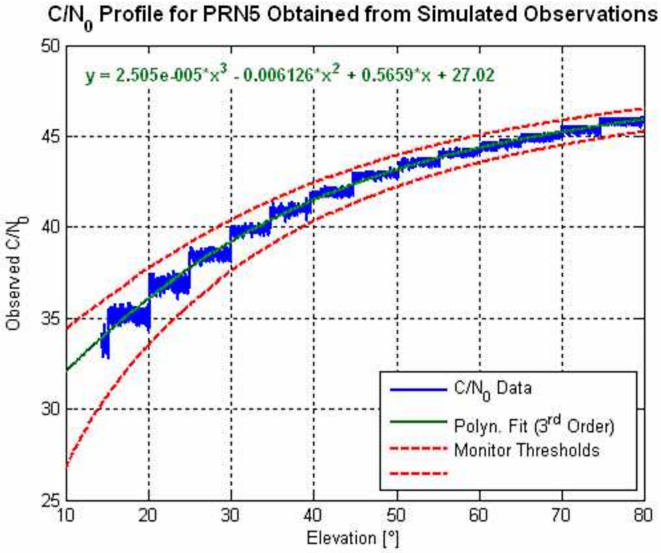

Figure 6-3: C/N_0 profile, 3rd order polynomial fit and monitor thresholds for PRN5 as obtained from simulated GPS observations.

Figure 6-4 illustrates the multipath monitoring process for the same data set which has already been used in section 6.1. The lower diagram shows the variations of the observed C/N_0 due to multipath (blue), the expected C/N_0 (green) and the monitor thresholds (red lines, assuming an expansion factor of m_{exp}=5 in this case).

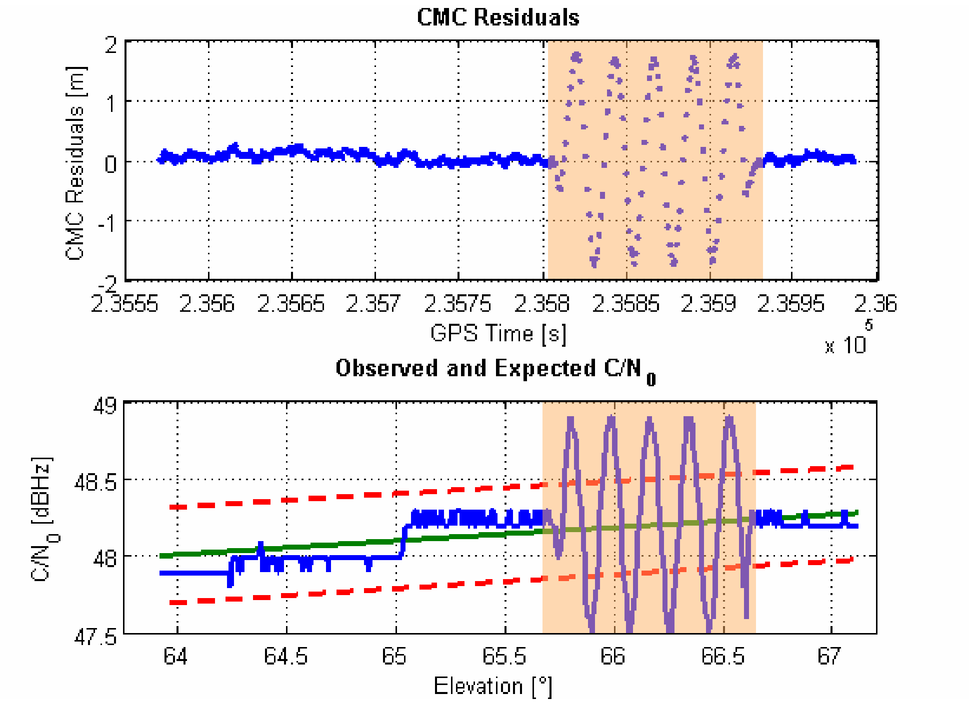

Figure 6-4: Multipath monitoring by analyzing the observed C/N$_0$.

6.3 Formation of Differences Between Observations

Real-time multipath monitoring can also be achieved by using two separate receivers which are located in the vicinity of each other. In such a scenario, the observations (code and/or carrier observations) of both receivers can be differenced, thus eliminating or at least reducing certain error sources. However, the approach of differencing code and carrier observations offers additional drawbacks:

- Since multipath effects are typically not spatially correlated, the differences will show the *combined* multipath influence at *both* antennas. As a result, it is impossible to determine the multipath effects at one specific antenna site (exception: multipath effects can be completely excluded for one of the two receivers which is normally not the case).
- In order to achieve real-time signal monitoring, both receivers must have the capability to transmit and/or receive data from the other receiver in real-time.
- In case that carrier multipath is to be monitored in real-time, the carrier phase ambiguities have to be considered and determined instantly. Moreover, the monitor is sensitive to cycle-slips, so that the carrier ambiguities have to be re-calculated after the occurrence of a cycle-slip.

In the following sections, several approaches of differencing observations will be presented. All differencing approaches are suitable to detect multipath effects but not to mitigate them.

6.3.1 Single Differences

Single differences are formed by differencing code or carrier observations of two receivers that observe the same satellite simultaneously. The general concept is illustrated in Table 6-2. The resulting observation equations for code and carrier measurements base on the general observation equations introduced in Table 6-1 and are listed in Table 6-2:

<table>
<tr><th colspan="2">Single Differences: Observation Equations</th></tr>
<tr><td>**Pseudorange**
$\Delta PR = \Delta R - c\Delta dT + \Delta d_I + \Delta d_T + \varepsilon_{PR}$</td><td>**Carrier Phase**
$\Delta\Phi = \Delta R - c\Delta dT - \Delta d_I + \Delta d_T + \lambda\Delta N + \varepsilon_{\Phi}$</td></tr>
<tr><td colspan="2">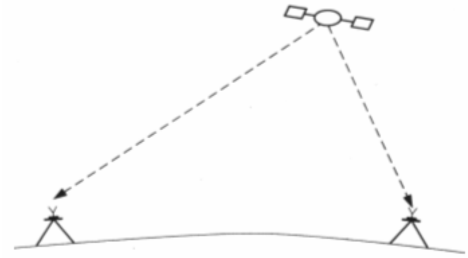</td></tr>
</table>

Table 6-2: General concept and observation equations for the formation of single differences.[3]

By means of the differencing process, the satellite clock error can be eliminated completely. Furthermore, the ephemeris error (contained in ΔR) can be minimized. The same is true for the tropospheric and ionospheric ranging errors Δd_T and Δd_I, as long as the baseline between both receivers is not too long and the atmospheric conditions are nearly identical for both receivers. The receiver clock errors can be eliminated by synchronizing both receiver clocks. In case that carrier multipath is to be monitored in real time, the carrier ambiguities have to be determined constantly. By using multi-frequency receivers, the ionospheric path delay can also be applied immediately. The remaining residuals will only show the influence of noise and multipath. As already mentioned, the visible multipath variations result from the combined influence on both antennas. Multipath influences at one specific antenna may be even stronger.

6.3.2 Double Differences

Double differences are formed by subtracting the single differences (formed for each receiver according to the principle presented in the previous section) of two satellites for each point in time. The general concept is illustrated in Table 6-3. Again, the resulting observation equations for code and carrier measurements base on the general observation equations already introduced in Table 6-1 and are listed in Table 6-3:

<table>
<tr><th colspan="2">Double Differences: Observation Equations</th></tr>
<tr><td>**Pseudorange**
$\nabla\Delta PR = \nabla\Delta R + \nabla\Delta d_I + \nabla\Delta d_T + \varepsilon_{PR}$</td><td>**Carrier Phase**
$\nabla\Delta\Phi = \nabla\Delta R - \nabla\Delta d_I + \nabla\Delta d_T + \lambda\nabla\Delta N + \varepsilon_{\Phi}$</td></tr>
<tr><td colspan="2">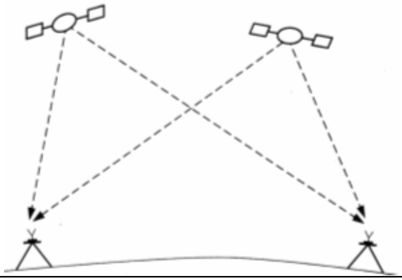</td></tr>
</table>

Table 6-3: Observation equations for the formation of single differences.[4]

By means of this differencing approach, both the satellite clock and the receiver clock errors can be eliminated completely. As it is the case for the formation of single differences, the ephemeris error (contained in ΔR) can be minimized. The same is true for the tropospheric and ionospheric ranging errors Δd_T and Δd_I (assuming a reasonable baseline length). In case that carrier multipath is to be monitored in real time, the carrier ambiguities have to be instantly available. By using multi-frequency receivers, the ionospheric path delay

---

[3] Illustration adopted from [Bauer 1997]

[4] Illustration adopted from [Bauer 1997]

can also be applied immediately. The remaining residuals will only show the influence of noise and multipath. Again, the visible multipath variations result from the combined influence at both antennas. Multipath influences on one specific antenna may be stronger than observed.

6.3.3 Differencing Multi-Frequency Observations

As it is the case for the previous two approaches, differencing of multi-frequency observations also requires two receivers. The basic concept can be found in [GEORGIADOU and KLEUSBERG 1988] and bases on the observation equations listed in Table 6-4. In this case, dual frequency observations (GPS code and carrier observations on L1 and L2 in this example) are used to detect multipath influences:

Multi-Frequency Observation Equations	
Pseudorange	**Carrier Phase**
$PR_{L1} = R + c(dt - dT) + d_{I,L1} + d_T + \varepsilon_{PR,L1}$	$\Phi_{L1} = R + c(dt - dT) - d_{I,L1} + d_T + \lambda N_{L1} + \varepsilon_{\Phi,L1}$
$PR_{L2} = R + c(dt - dT) + d_{I,L2} + d_T + \varepsilon_{PR,L2}$	$\Phi_{L2} = R + c(dt - dT) - d_{I,L2} + d_T + \lambda N_{L2} + \varepsilon_{\Phi,L2}$

Table 6-4: Observation equations for dual-frequency measurements.

The following parameters do not depend on the carrier frequency and cancel out by subtracting the L1- and L2-observations:

- Geometric range between the satellite and the user
- Ephemeris error (contained in R)
- Satellite and receiver clock errors
- Tropospheric path delay

Due to the dispersive nature of the ionosphere, the differenced ionospheric path delay between L1 and L2 is the dominant remaining error influence. Additionally, the (differenced) carrier ambiguities have to be considered when subtracting dual-frequency carrier observations. Differencing pseudorange and carrier observations for the two frequencies results in the following equations:

Carrier: $$\Phi_{L1} - \Phi_{L2} = \underbrace{d_{I,L2} - d_{I,L1}}_{\Delta_\Phi} + \underbrace{\lambda(N_{L1} - N_{L2})}_{N_\Delta} + \underbrace{\varepsilon_{\Phi,L1} - \varepsilon_{\Phi,L2}}_{\varepsilon_\Delta} \qquad (131)$$

Code: $$PR_{L1} - PR_{L2} = \underbrace{d_{I,L1} - d_{I,L2}}_{\Delta_{PR}} + \underbrace{\varepsilon_{PR,L1} - \varepsilon_{PR,L2}}_{\varepsilon_\Delta} \qquad (132)$$

Rearranging these equations leads to the differences *Δ* of the ionospheric path delays:

Carrier: $$\Delta_\Phi = \Phi_{L1} - \Phi_{L2} - N_\Delta + \varepsilon_\Delta \qquad (133)$$

Code: $$\Delta_{PR} = PR_{L1} - PR_{L2} + \varepsilon_\Delta \qquad (134)$$

Equation (133) contains the combined carrier ambiguities, which have to be removed instantly in case that carrier multipath effects have to be monitored in real time. After removing these ambiguities, both observations (133) and (134) will mainly show changes in the ionospheric path delay including superimposed multipath effects. Since the changes of ionospheric condition do not significantly vary for two observation sites with a relatively short baseline, such variations can be minimized by differencing equations (133) and (134) for two receivers. The main drawback of this approach, however, is that the monitored multipath variations are the result of the combined influence at both antennas.

6.4 Wavelets

In this section, three possible approaches to perform multipath detection and monitoring by means of wavelets are introduced. The first two approaches are based on the Continuous Wavelet Transformation (CWT) and make use of wavelet coefficients to detect multipath variations. The third approach bases on the signal decomposition method already mentioned in section 4.1.9. A brief introduction of some important aspects of wavelet analysis is given in chapter 10 (Appendix C).

6.4.1 Visual Inspection of Wavelet Coefficients

A first method of wavelet-based multipath detection is the computation of wavelet coefficients for different scales and positions of the underlying mother wavelet (CWT). The absolute value of these coefficients can be plotted as a function of the wavelet position (or time) and the scale of the wavelet. Large coefficients at certain scales indicate a high degree of similarity between the (scaled) wavelet and the original signal. As all wavelets have a mean value of zero and since occurring multipath variations also tend to show this behavior, large coefficients at certain scales indicate the presence of multipath. Small coefficients, on the other hand, indicate a low level of similarity between the underlying wavelet and the signal and thus indicate the presence of thermal noise only.

Figure 6-5 illustrates the results of such an analysis for a CMC data set which is partially affected by multipath. The wavelet coefficients have been computed for scales between 1 and 32 over the entire observation period using Matlab’s Wavelet Toolbox. The biorthogonal wavelet No. 1.3 has been used as mother wavelet. The region where the largest wavelet coefficients can be observed nicely corresponds to the period where multipath variations are visible in the CMC residuals.

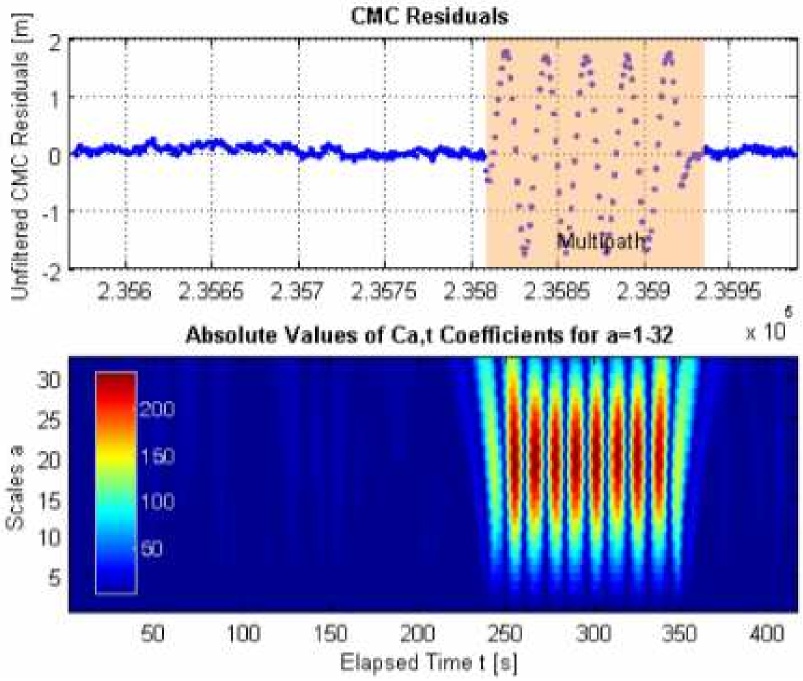

Figure 6-5: Multipath monitoring by computation and visual inspection of wavelet coefficients.

This method still works even if the amplitude of the multipath influences are of the same order as the thermal noise. Such a case is illustrated in Figure 6-6, where the results of the multipath detection process in the presence of weak multipath are shown. Despite the fact that the multipath amplitude is very low, the resulting signal variation is clearly visible in the visualization of the wavelet coefficients.

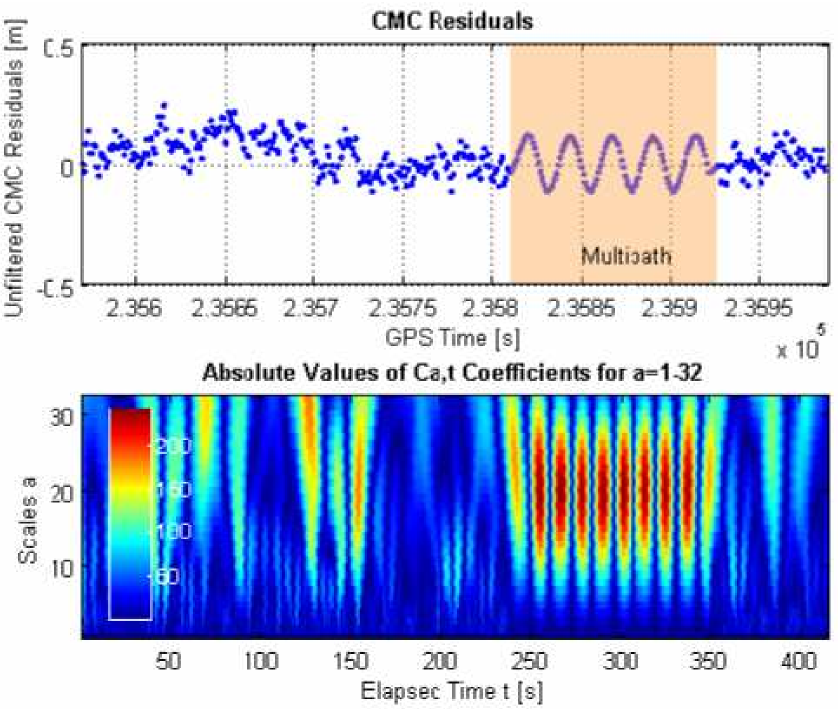

Figure 6-6: Result of the multipath detection process in case of weak multipath.

Note that the use of other mother wavelets leads to similar results. The main difference between the results illustrated in Figure 6-5 and Figure 6-6 and the ones obtained by using other mother wavelets is that the maximum coefficients occur at different scales (see Figure 6-7 for a comparison of the detection results when using other mother wavelets).

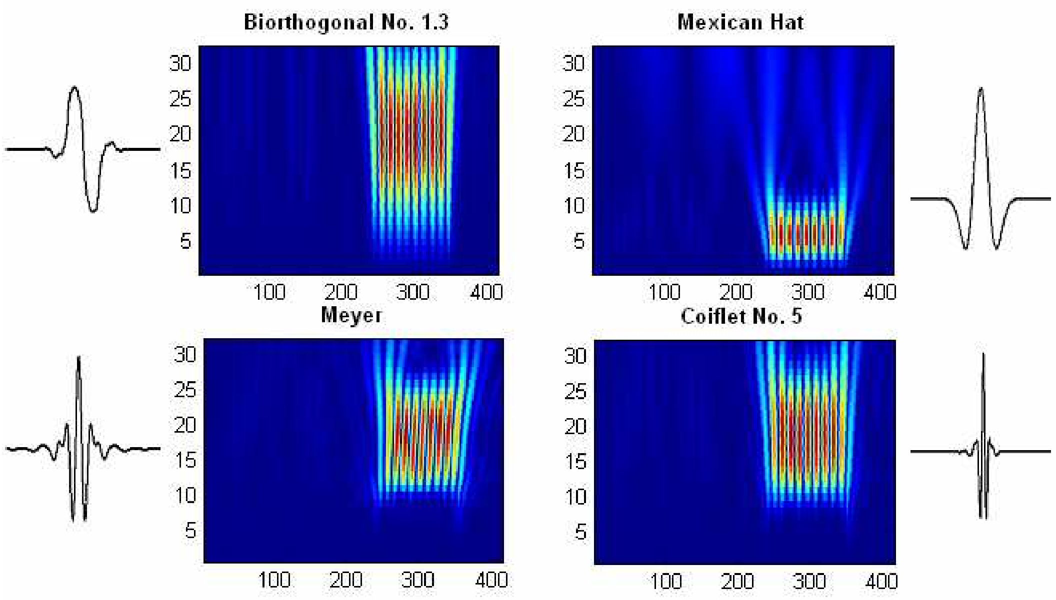

Figure 6-7: Use of different mother wavelets for multipath detection.

This method is best suited for post-processing purposes. As wavelet processing includes the entire observation period and since multipath is detected by visual inspection, it is not possible to implement it as a real time multipath monitor. Moreover, this method does only provide reasonable results if the original data is unbiased, i.e. that the residuals have to be computed before performing the analysis. Furthermore, for best results, any existing ionospheric trend should be removed from the data before applying the wavelet transform. In general, wavelet analysis is not restricted to CMC observations. If all existing trends and biases are removed from the original data, also SNR data or differenced observations (single or double differences) can be analyzed by means of wavelets. Note, however, that whenever carrier observations are involved, the process is sensitive to cycle-slips.

6.4.2 CWT Coefficients for Moving Time Window

The computation of CWT coefficients can also be used for a near real time implementation of a multipath monitor. To achieve this, a data history of N original data samples must be set up. This time window contains the last N-1 data samples (epochs t_{k-N+1} to t_{k-1}) plus the data sample for the current epoch t_k. For this subset of data, the wavelet coefficients are computed and the coefficients of the current epoch only (but at all considered scales) are used to compute a multipath indicator. After that, the time window is shifted to the right (now containing data samples between epoch t_{k-N+2} and t_{k+1}) and the computation of the multipath indicator is repeated. By doing so, the multipath indicator can be computed for every epoch after the time window has been filled (initialization phase).

The basic concept is further illustrated in Figure 6-8. The time window consists of the last 100 samples of the CMC residuals illustrated in the upper diagram. The wavelet coefficients for these 100 samples for scales 1-32 are plotted in the second diagram. In this case, the multipath indicator is the difference between the maximum and minimum wavelet coefficient that occurs for the current epoch t_k (other ways to establish a suitable multipath indicator are also possible). It is then compared to a threshold which indicates if the input signal is affected by multipath (lower diagram).

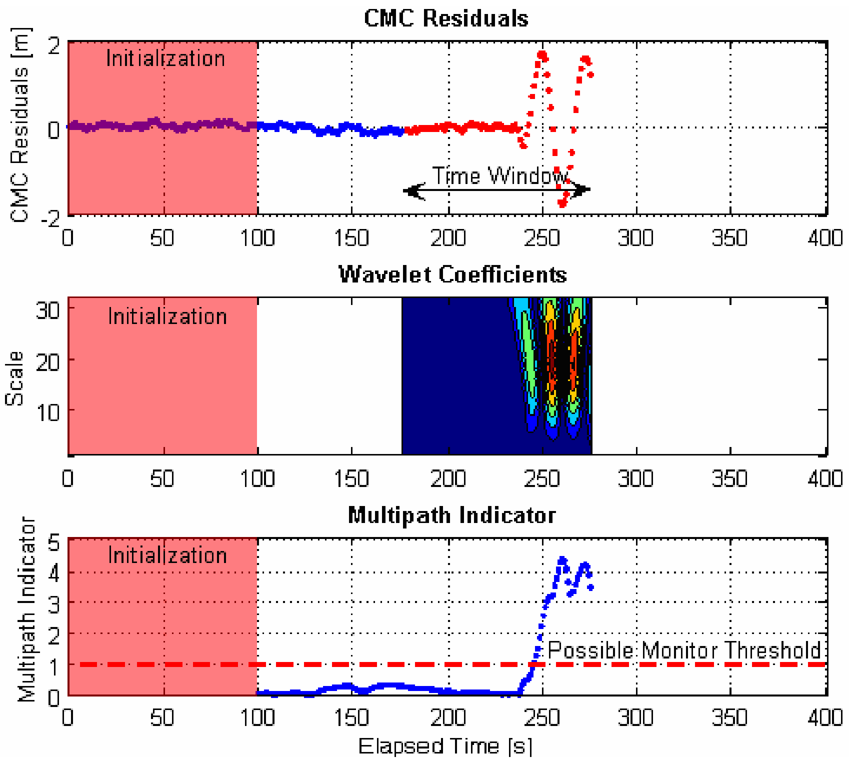

Figure 6-8: Multipath monitoring by computing CWT coefficients for a moving time window.

Despite its ability to detect and monitor multipath influences in near real time, this approach has also some shortcomings. Again, the input data must be unbiased and free of cycle-slips, and for best results, any existing ionospheric trend should be removed (e.g. by using dual frequency data). In fact, multipath detection generally works in the presence of a ionospheric trend. In this case, however, the monitor threshold depends on temporal ionospheric path delay changes which can hardly be predicted. The use of a data history results in an initialization phase during which multipath detection is impossible. Finally, the threshold depends on the mother wavelet used to compute the wavelet coefficients and also on how the multipath indicator is defined. Therefore, the monitor thresholds must be determined (calibrated) by processing multipath-free data.

6.4.3 Signal Decomposition

In section 4.1.9, wavelet processing in conjunction with the use of CMC observables has been introduced as a possible approach to mitigate code multipath. As this method is able to produce a pseudorange correction, this correction can – together with a suitable threshold – be used as an indicator for the presence of code multipath. The general concept is illustrated in Figure 6-9.

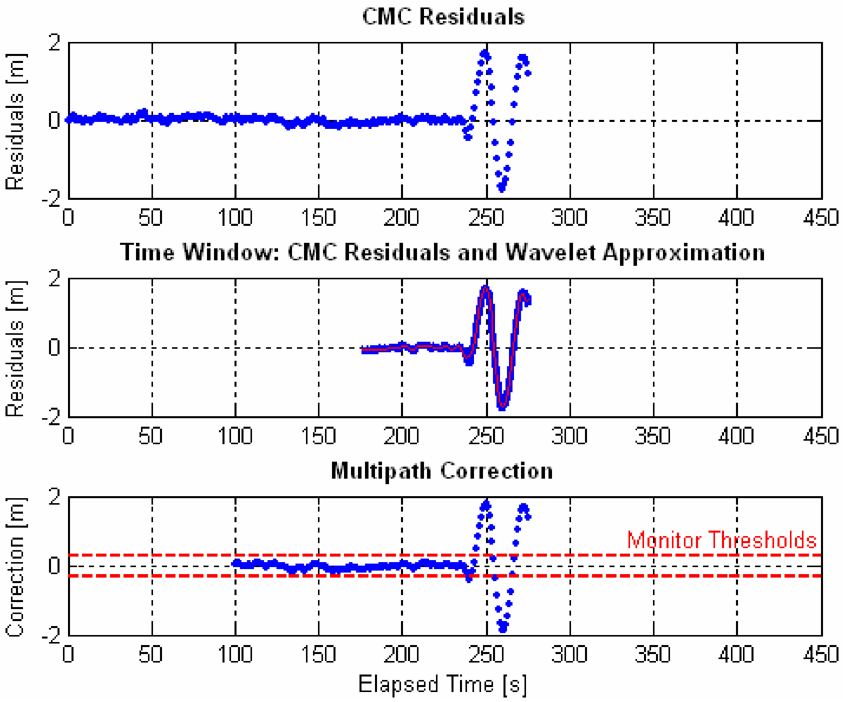

Figure 6-9: Multipath monitoring by analyzing multipath corrections obtained by means of wavelet decomposition.

The upper diagram shows the CMC residuals as obtained after the bias removal (as described in section 4.1.9). The second diagram shows the CMC residuals during a time window of 100s (blue) together with the result of a wavelet decomposition of these residuals (red curve, approximation at decomposition level 2, no details, mother wavelet: Daubechies No. 4). The lower diagram shows a correction value obtained from the last data point of the wavelet approximation. If the correction exceeds a certain threshold, the presence of multipath can be postulated. Since in the absence of multipath, the correction terms mainly contain the effects of thermal noise, the same threshold as proposed in section 6.1.2 can be used (see equation (121)).

Like for other wavelet-based multipath monitoring approaches, the input data must be unbiased and free of cycle-slips and ionospheric influences. Again, the use of a data history results in an initialization phase during which multipath detection is impossible. Note that the actual performance depends on the selection of the time window size (filter constant), the wavelet decomposition level and the mother wavelet being used. For best results, these parameters have to be adjusted in accordance with the actual multipath environment (expected multipath frequencies) whose exact characteristics can hardly be predicted. On the other hand, in contrast to other low-pass filters (e.g. the Hatch filter for obtaining carrier-smoothed pseudoranges or the band-pass filter introduced in section 6.1.1), the use of wavelets allows very efficient smoothing of code observations showing almost no transient effects and phase shifts between original and smoothed data. However, multipath monitoring can be done in near real time only.

6.5 Other Algorithms

6.5.1 Receiver Autonomous Integrity Monitoring (RAIM)

RAIM is a receiver-internal technique to assess the integrity of a GNSS signal and plays a significant role in safety-critical GNSS applications. There are several possible RAIM implementations, which can be divided into methods for Fault Detection (FD) and Fault Detection and Exclusion (FDE). In addition to pure failure detection, FDE methods are able to identify the affected signal and exclude it from navigation processing. Another classification distinguishes between snapshot schemes using measurements of the current epoch, and averaging schemes using both past and present measurements. RAIM requires a certain number of redundant pseudorange observations. For FD, a minimum of 5 observations are required, FDE requires at least 6 observations.

A basic implementation for fault detection is the so-called Range-Comparison Method. As a first step, four observations are used to compute a position solution. Based on the known coordinates of the remaining satellites, this solution can be used to compute their predicted ranges. As a final step, the differences between the predicted ranges and the observed pseudoranges to the remaining satellites are formed and compared to a suitable threshold indicating a possible signal failure. The so-called Least-Squares-Residuals Method forms the least squares solution for all visible satellites and predicts the ranges to all of them. By differencing predicted and observed ranges, a set of range residuals can be set up that are used to compute a failure indicator called SSE ([BROWN 1992]) which is then compared to a suitable threshold. As [BROWN 1992] shows, both methods as well as a third one called Parity Method are mathematically identical. In this manner, RAIM has the potential to detect and – in case that FDE schemes are applied – mitigate multipath influences. To achieve this, however, a minimum number of signals must be available and have to be processed simultaneously. Moreover, for efficient multipath detection, the threshold settings have to be adjusted to serve this purpose. Typical thresholds are in the order of >50m which is too large to detect short-delay multipath ([GARIN 2005]).

6.5.2 Multipath Estimating Delay Lock Loop (MEDLL)

The MEDLL approach has already been introduced and discussed in section 4.1.8 as a method for mitigating code multipath. Due to its capability of estimating the multipath parameters (multipath delay, relative phase and relative amplitude) for a specified number of multipath components, it is also suitable for multipath detection purposes. The MEDLL approach bases on the analysis of the correlation peak by sampling the correlation function with a rather large number of correlators (the actual number of necessary correlators depends on the number of multipath components that need to be estimated). The computations can be performed on an epoch-by-epoch basis without using information from previous epochs, so that in general, MEDLL can be implemented in real-time. Despite its ability to detect and mitigate multipath in real-time, the main drawbacks of this approach are that it requires a large amount of correlators and that a real-time implementation requires high computing power.

6.5.3 Spectral Analysis

6.5.3.1 Frequency Analysis Based on CMC Observations

Since multipath influences typically result in variations of the CMC observable, these variations can be analyzed by transforming the (multipath-affected) CMC observations into the frequency domain and by analyzing the resulting spectrum from which the dominant fading frequencies can be derived. Together with a suitable detector function and a corresponding threshold, multipath influences can be detected.

Such an approach for the detection of multipath influences at DGPS reference stations has been described in [HÖPER et al. 2001]. Herein, the last 512 CMC samples are used as an input for an FFT transformation. In order to detect variations with frequencies up to 0.5Hz (representing an expected maximum of occurring fading frequencies, see 3.1.4.4) the signal has to be sampled with 1Hz (theorem of Shannon), the common output data rate of a GNSS receiver. Possible (long-periodic) ionospheric variations have to be taken into account as well by omitting very low frequencies. [HÖPER et al. 2001] suggest to omit ionospheric-induced variations with cycle durations of 5 minutes or longer. From the resulting (discrete and band-limited) spectrum, a detector function is set up that forms a ratio between the maximum spectral value and the mean of all other values. This ratio is compared to a threshold indicating whether or not there is multipath on the signal.

The main benefit of this approach is that it works with one single receiver and one single satellite signal, i.e. no differencing between receivers and/or satellites is necessary. As a result, the multipath influence can be unambiguously assigned to a signal. On the other hand, this approach requires a data history, is sensitive to cycle-slips, is only able to detect code multipath and has some computational burden. Although the algorithm can be implemented in real-time, the method does not really provide real-time information about the multipath influence at a dedicated point in time, because the current output of the detector function bases on the previous 512 observations. Strictly speaking, the monitoring result is just an indication if there were multipath influences during the past 512 seconds.

6.5.3.2 Spectral Analysis of Differenced Observations

Differencing observations as described in sections 6.3.1 and 6.3.2 may also show periodic variations due to multipath and can therefore be analyzed with respect to their spectral characteristics. A possible algorithm may look quite the same as the one introduced in the previous section. In contrast to the CMC observations, single or double differences do hardly contain ionospheric influences, i.e. it is not necessary to consider a band-limited spectrum. As it is the case for the CMC observations, the multipath detection algorithm can be implemented in real time. However, there is still no exact information when the multipath signal exactly occurs, because the monitor only provides information about past multipath influences.

6.6 Summary

Table 6-5 lists all monitoring approaches discussed in the previous sections and compares them with respect to their benefits and drawbacks, real-time capability and complexity.

Monitoring Approach		Real-Time Capability	Complexity/ Comp. Load	Benefits	Drawbacks
Code m. Carrier (CMC)		No[5]	Moderate (use of band-pass filter)	Noise reduction and elimination of ionospheric trend (by suitable pass-band)	Data history, sensitive to cycle-slips and data gaps, phase-shift of filtered data, detection of code multipath only
SNR Monitoring		Yes	Moderate	High sensitivity for short-delay multipath (see section 7.11)	Calibration required
Differencing		Yes	Moderate to high (carrier ambiguity fixing)	Detection of code and carrier multipath	2 receivers with data link required, carrier ambiguity resolution, detects combined multipath influences only
RAIM		Yes	Moderate	Allows multipath monitoring and mitigation	Minimum of N+1(2) signals required for detection (exclusion)[6]
MEDLL		Yes	High	Multipath monitoring and mitigation, estimation of multipath parameters	Many correlators required, high computational load, dedicated number of multipath signals must be assumed
Spectral Analysis	CMC observations	No[5]	Moderate to high (FFT analysis)	Requires only one receiver and standard code and carrier observations	Data history, initialization phase, sensitive to cycle-slips, detection of code multipath only, ionospheric variations have to be considered
	Differenced observations			No ionospheric influences to be considered	Data history, initialization phase, 2 receivers required, data link for near-real-time implementation, detects combined multipath influences only
Wavelets (CMC obs.)	CWT coeff. (visual insp.)	No	High (wavelet analysis)	Requires only one receiver and standard code and carrier observations, good sensitivity (detection of weak multipath)	Data must be unbiased and free of cycle-slips, ionospheric trend should be removed, post-processing only
	CWT coeff. (time wind.)	No[5]		Near real time implementation	Data history, data must be unbiased and free of cycle-slips, ionospheric trend should be removed (dual frequency data), threshold depends on mother wavelet and multipath indicator
	Signal decomp.			Efficient smoothing of code observations (no transient effects, no phase shift between original and smoothed data)	Data history required, sensitive to cycle-slips, performance depends on mother wavelet, approximation level and filter constant (interrelation with multipath environment)

Table 6-5: Comparison of different approaches for multipath detection and monitoring.

By means of multi-correlator observations, it is possible to design a multipath monitoring system that overcomes most of the drawbacks listed in Table 6-5 (insensitive to cycle-slips, no minimum number of visible satellites required, low computational load by using only few correlators, unambiguous identification of affected signal). The detailed design and the performance of this monitoring approach will be the topic of the following chapter.

---

[5] Near real time only

[6] N denotes the number of unknowns in the observation equations

7. Development of a Real-Time Multipath Monitor (RTMM)

7.1 Introduction

In this chapter, a novel approach for the detection of multipath signals in real-time is introduced. It makes use of the multi-correlator technique, which samples the signal's correlation function with a distinct number of correlators and is thus able to detect deviations from its "nominal" shape.

So far, this technique has primarily been used for the detection of "Evil Waveforms". In general, the term "Evil Waveform" refers to anomalous signals transmitted by a satellite. Such an "Evil Waveform" occurred in 1993 for the first time when an anomalous "behavior" of SV19 had been observed. An analysis of differential position accuracies based on code pseudorange observations led to an accuracy of 50cm without and 2-8m with consideration of SV 19. The power spectrum of the anomalous signal revealed a large spike at the center frequency instead of showing a normal *sinc* function shape. In 1994, the reason for this anomalous behavior had finally been identified as a failure in the satellite's signal generation and transmission hardware ([PHELTS 2001]).

Anomalous signals like those observed with SV19 always result from failures of the analogue and/or digital signal generating hardware onboard a satellite ([PHELTS 2001]). Evil waveforms can pose an integrity threat to any GNSS user. Especially for airborne users with high integrity requirements (e.g. during the landing phase of an aircraft), such signal failures can cause unacceptable errors. As a consequence, current satellite based augmentation systems like LAAS or WAAS include some Signal Quality Monitoring (SQM) concepts to protect airborne users against such threats.

The SV 19 event led to the development of several candidate threat models to explain the observed anomalous behavior. By means of these analyses, three primary threats to the satellite signal had been identified, all of them producing an anomalous peak to the signal's correlation function ([JAKAB 1999], [PHELTS 2001]):

- Flattening of the correlation peak: This leads to plateaus around the correlation peak, resulting in regions of zero discriminator gain.
- Distortions of the correlation function in the form of asymmetries and oscillations.
- Occurrence of additional peaks: This may cause the receiver to track the wrong peak.

As the presence of evil waveforms always results in a distortion of the signal's correlation function, one possible approach is to monitor the incoming signal by means of several correlators which are placed at distinct locations along its correlation function. By means of this technique, the actual shape of the correlation function can be compared to its "nominal" shape. Since the correlators used for monitoring purposes are usually placed around the peak of the correlation function, the obtained observations are also called "Correlation Peak Observations".

To the knowledge of the author, only some of NovAtel's GPS receivers as well as commercial software receivers provide multi-correlator observations at present. To obtain multi-correlator functionality, the standard NovAtel receivers have to be equipped with a special SQM firmware. The number and the exact location of available correlators depend on the receiver family and the available SQM firmware version. An overview of available correlator configurations is provided in section 7.2.1.

In order to detect evil waveforms, the correlator configuration illustrated in Figure 7-1 can be used. This configuration is provided by NovAtel's SQM firmware v447s17 for OEM3 receivers and consists of eight correlators located on and around the peak of the correlation function (3 early - 1 punctual - 4 late correlators).

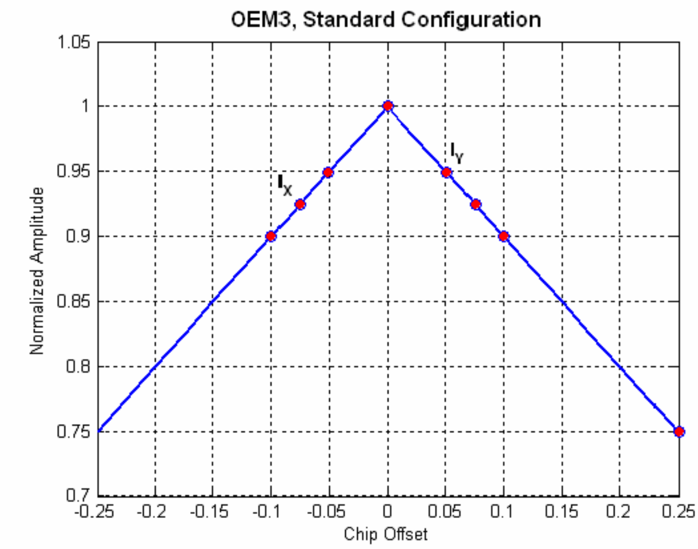

Figure 7-1: Possible correlator configuration for the detection of evil waveforms.

The red correlators can be used to set up a variety of so-called test metrics. By determination of the correlation value for each correlator, different combinations can be formed. Some of them (but by far not all possible ones) are listed in Table 7-1. Such test metrics are currently being used in the University of Stanford IMT to detect evil waveforms (see e.g. [PULLEN et al. 2000/2002], [PHELTS 2000/2003], [NORMARK et al. 2001/2002], [LUO et al. 2000], [MITELMAN et al. 2000], [AKOS et al. 2000]).

Type of Test	Formation	Example
Delta Tests	$\Delta = \frac{I_{-X} - I_{+X}}{I_0} - \frac{I_{-Y} - I_{+Y}}{I_0} - \mu_\Delta$	$M1: \frac{I_{-0.075} - I_{+0.075}}{I_0} - \frac{I_{-0.05} - I_{+0.05}}{I_0} - \mu_{M1}$ $M2: \frac{I_{-0.1} - I_{+0.1}}{I_0} - \frac{I_{-0.05} - I_{+0.05}}{I_0} - \mu_{M2}$
Symmetric Ratio Tests	$R_{I_{\pm X}} = \frac{I_{-X} + I_{+X}}{I_0} - \mu_R$	$M3: \frac{I_{-0.05} + I_{+0.05}}{I_0} - \mu_{M3}$ $M4: \frac{I_{-0.075} + I_{+0.075}}{I_0} - \mu_{M4}$
Negative Ratio Tests	$R_{I_{-X}} = \frac{I_{-X}}{I_0} - \mu_R$	$M5: \frac{I_{-0.1}}{I_0} - \mu_{M5}$ $M6: \frac{I_{-0.075}}{I_0} - \mu_{M6}$
Positive Ratio Tests	$R_{I_{+X}} = \frac{I_{+X}}{I_0} - \mu_R$	$M7: \frac{I_{+0.075}}{I_0} - \mu_{M7}$ $M8: \frac{I_{+0.1}}{I_0} - \mu_{M8}$

Table 7-1: Test metrics used to detect satellite signal failures. The symbol μ accounts for the mean value of each test metric, so that the resulting metrics have zero-mean.

Table 7-2 lists some theoretical metric values for PRN13. Note that these values are only valid in case that infinite pre-correlation bandwidth is assumed and in case that the correlation functions' side lobes (minor correlation peaks at spacings <-1 and >+1) and the influence of noise are neglected.

	Metric No.	Metric Value
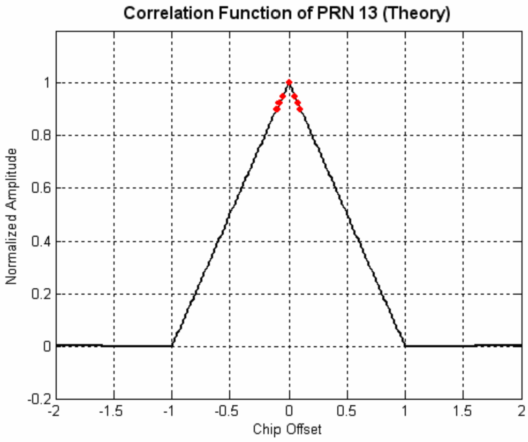	M1	0.00000
	M2	0.00000
	M3	0.94885
	M4	0.92500
	M5	0.90000
	M6	0.92500
	M7	0.92500
	M8	0.90000

Table 7-2: Theoretical correlation function and metric values for PRN13.

In reality, correlation peak distortions due to minor correlation peaks (depending on PRN code) and due to receiver pre-correlation filtering (which results in a rounded correlation peak and in an asymmetric correlation function) have to be considered as well. Both effects are illustrated in Table 7-3.

	Metric No.	Metric Value
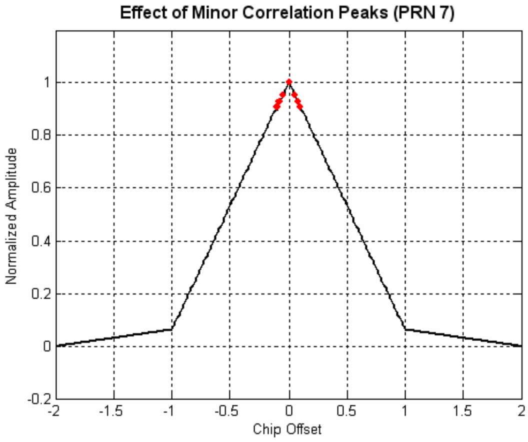	M1	0.00000
	M2	0.00000
	M3	0.95205
	M4	0.92969
	M5	0.90626
	M6	0.92969
	M7	0.92969
	M8	0.90626
	Metric No.	Metric Value
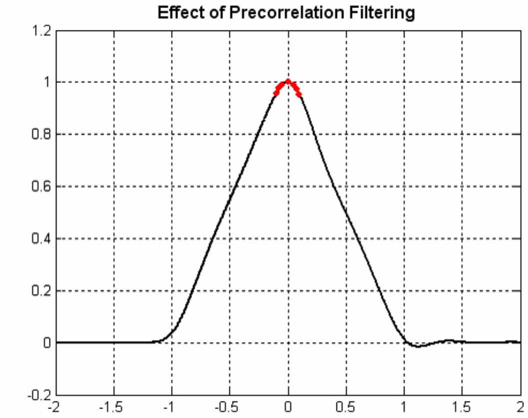	M1	4.8273e-004
	M2	0.0014
	M3	0.9879
	M4	0.9745
	M5	0.9575
	M6	0.9752
	M7	0.9738
	M8	0.9542

Table 7-3: Effect of minor correlation peaks and pre-correlation filtering on the metric values.

Both effects result in a “natural” correlation peak distortion, which depends on the satellite being tracked (PRN number) and on the receiver characteristics (pre-correlation bandwidth, type of filter). In order to account for these effects, each test metric has to be corrected by its long-term mean μ. These mean values can be determined by calculating the average value of the metrics over a long period of time carrying out field calibration measurements in a multipath- and interference-free environment.

The following diagrams illustrate metric M5 (as defined in Table 7-1, but without consideration of its long-term mean value) computed from correlation peak observations of PRN13 during an SQM calibration campaign carried out in August 2003. A whole satellite pass was recorded (rising-culmination-setting, elevation mask: 10°). As expected, the mean value of the metric (red line in Figure 7-2a) differs from the theoretical value listed in Table 7-2. At low elevation angles, the metric clearly shows the influence of noise and multipath. For the purposes of signal failure detection, these effects have to be reduced in order to detect a signal failure reliably. Otherwise, such a faulty signal could remain hidden in the noise floor. The most common approach to reduce the effects of noise and multipath is data smoothing, i.e. a Hatch or a FIR filter is applied to the data ([MITELMAN et al. 2000]).

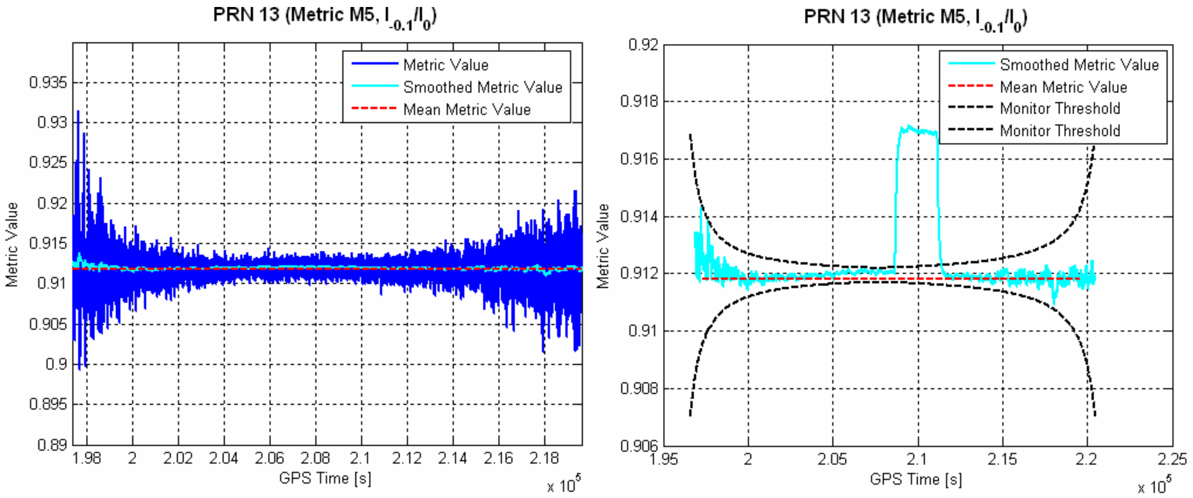

Figure 7-2: Test metric M5 during a complete pass of PRN13. A Hatch-Filter with a time constant of 100s has been applied to obtain the smoothed time series.

In order to implement an SQM at a specific site, all satellites have to be observed during their entire passes. Based on the correlation peak observations carried out during the observation period, smoothed time series of suitable test metrics are computed (as illustrated in Figure 7-2). Based on these metric observations, which are still influenced by noise and – in most cases – also by multipath, suitable monitor thresholds have to be computed. These thresholds have to account for all multipath effects at the specific site as well as for the gain pattern of the selected antenna. For the computation of these thresholds, certain assumptions with respect to false alarm and missed-detection probabilities have to be considered. Furthermore, it has to be assumed that no signal failures occur during such a calibration campaign ([VAN DIERENDONCK et al. 2000], [SCHUSTER BRUCE et al. 2000]).

The result of such a threshold computation is illustrated in Figure 7-2b. As a minimum requirement, the monitor thresholds have to be chosen such that the smoothed metric values do not exceed its corresponding threshold. Figure 7-2b also illustrates the occurrence of a (simulated) signal failure. The signal failure is assumed to last 2500 seconds and to create a metric offset of 0.005. This results in a metric value that is well above the monitor threshold. As a result, the signal failure can be easily detected in this case. Note that the signal failure “produces” a maximum metric value of ~0.917. If the unsmoothed time series of Figure 7-2a had been used for the threshold derivation, the failure may have remained undetected (at least for low elevation angles where the influence of noise and multipath is rather large). This is the reason why the low-pass filter is applied to these metric observations.

The threshold derivation itself is a very laborious and time-consuming process. The main reasons can be summarized as follows:

- Thresholds are site-dependent, i.e. they must be selected according to the actual multipath conditions at a specific site
- Thresholds depend on the antenna pattern
- False alarm and missed-detection-probabilities have to be taken into account (at least if the signal quality monitor is designed for airborne applications)
- Thresholds must be computed for all visible satellites and for all metrics that are to be monitored

The main drawback of this SQM approach is that the monitor thresholds derived from the calibration measurements are only valid for the selected site and the selected antenna. Once the monitor station has to be moved to another site or another antenna is used, the calibration process needs to be repeated and the monitor thresholds have to be computed anew. Nevertheless, this technique is currently used in the University of Stanford Integrity Monitoring Test Environment (IMT) in order to detect satellite signal failures. During the past few years, detailed information about SQM by means of correlation peak measurements and the formation of test metrics have been published in form of many papers or theses (e.g. [PULLEN et al. 2000], [PULLEN et al. 2002], [PHELTS 2000], [PHELTS 2001], [PHELTS 2003], [NORMARK et al. 2001], [NORMARK et al. 2002], [LUO et al. 2000], [MITELMAN et al. 2000], [AKOS et al. 2000]).

By using correlation peak observations, it is also possible to detect multipath signals in real time. In the following sections, the basic concept of such a real-time multipath monitoring system – which also bases on the formation of suitable test metrics - will be developed.

7.2 Hardware Aspects

7.2.1 Multi-Correlator Firmware

All experiments, measurements and simulations described in this chapter were carried out with two NovAtel receivers (OEM3/OEM4). Both receivers provide multi-correlator observations via a modified receiver firmware.

For the OEM3 receiver (NovAtel ProPak) two different multi-correlator firmware versions have been used. The first version (v447s18) unifies all available correlators on one single tracking channel, so that a specific satellite signal can be tracked with 48 correlators. The main drawback of this firmware version is that only one signal at a time can be analyzed. As a result, positioning is not possible when using this configuration; it has not been considered for the development of the multipath monitor.

With a second OEM3 firmware version (v447s17), only 8 correlators per channel are used to sample the signal's correlation function, resulting in a total amount of 6 channels that can be observed simultaneously. The main benefit of this firmware is that up to 6 signals can be tracked simultaneously and positioning is feasible as well. The positions of the 8 correlators near the correlation peak are according to Figure 7-1. The correlator positions are fixed and cannot be changed.

The multi-correlator firmware for the OEM4 receiver (v1.212S19) provides 8 channels with 10 correlation peak observations per channel. Different correlator positions can be realized by selecting one of four different configurations. The exact correlator positions for each of these configurations are listed in the following table.

Samples	NARROW	ULTRANARROW	ULTRANARROW2	ULTRANARROWPAC
I	(-0.204600)	-0.102300	(-0.204600)	-0.102300
	(-0.102300)	-0.076725	(-0.102300)	-0.076725
	-0.076725	-0.051150	-0.076725	-0.051150
	-0.025575	-0.025575	-0.025575	-0.025575
	0.000000	0.025575	0.000000	0.025575
	0.025575	0.051150	0.025575	0.051150
	0.076725	0.076725	0.076725	0.076725
		0.102300		0.102300
Q	-0.102300	-0.102300	-0.102300	-0.102300
	-0.076725	-0.025575	-0.025575	-0.025575
	0.000000		0.000000	

Table 7-4: Available correlator configurations. The bracketed correlator positions cannot be used for monitoring purposes (they represent early minus late correlation values).

The configurations NARROW and ULTRANARROW2 provide 7(5) I- and 3 Q-Samples. The difference between the two configurations is that one Q-Sample is taken at a different correlator position. As the multipath monitor will only use I-Samples, both configurations can be considered identical. The configurations ULTRANARROW and ULTRANARROWPAC only differ with respect to the tracking technique. ULTRANARROW uses an Early-Late discriminator whereas ULTRANARROWPAC tracks the signal using a Strobe/Double Delta discriminator implementation. Both configurations provide correlator outputs at the same correlator positions, so that only two of the four configurations are relevant for the implementation of the multipath monitor (e.g. NARROW and ULTRANARROW).

Depending on the available correlator configuration, a large number of tests can be set up. The metrics introduced in Table 7-1 represent only a subset of all possible metrics. Since it can be assumed that some metrics are more suitable for multipath monitoring than others, it is important to start with a large amount of metrics and then to reduce the number of metrics by eliminating those that turn out to be unsuitable (this process is described in detail in section 7.4). Table 7-5 lists the formation criteria of all linear test metrics which have been considered in this chapter. I_X, I_Y and I_Z represent correlation peak observations for arbitrary code offsets X, Y and Z, respectively.

Type of Test Metric	Formation	Examples	Remarks
Delta-Tests	$\frac{(I_{-X}-I_{+X})-(I_{-Y}-I_{+Y})}{I_Z}$	$\frac{I_{-0.075}-I_{+0.075}}{I_0}-\frac{I_{-0.05}-I_{+0.05}}{I_0}$ $\frac{I_{-0.075}-I_{+0.075}}{I_{+0.1}}-\frac{I_{-0.05}-I_{+0.05}}{I_{+0.1}}$	Requires two correlator pairs, I_Z can be any available I-Sample
Symmetric Ratio Tests	$\frac{(I_{-X}-I_{+X})}{I_Y}$	$\frac{I_{-0.05}-I_{+0.05}}{I_0}$ or $\frac{I_{-0.05}-I_{+0.05}}{I_{-0.075}}$	Requires one correlator pair, I_Y can be any available I-Sample
Simple Ratio Tests	$\frac{I_X}{I_Y}$ and $\frac{I_Y}{I_X}$	$\frac{I_{+0.25}}{I_{-0.1}}$ or $\frac{I_0}{I_{-0.075}}$	Ratios in all combinations
Differential Ratio Tests	$\frac{(I_X-I_Y)}{I_Z}$	$\frac{(I_{-0.1}-I_{+0.25})}{I_{+0.05}}$	Numerator: Differences in all combinations Denominator: any available I-Sample

Table 7-5: Formation of linear test metrics.

The following table provides a comparison between the correlator configurations considered for this thesis. The configurations are compared with respect to the number of available channels and correlator locations. In addition, the table also lists the number of possible test metrics (provided that the metrics are formed according to the formation criteria in Table 7-5). The last column indicates whether or not logging of correlation peak observations is supported by NovAtel's logging and receiver control software "GPSolution".

	Configuration	No. of Channels	No. of Metrics	GPSolution Logging
OEM3	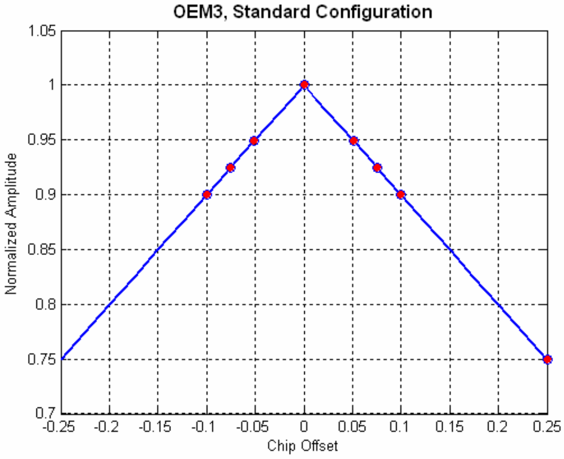 OEM3, Standard Configuration	6	328	no
OEM4	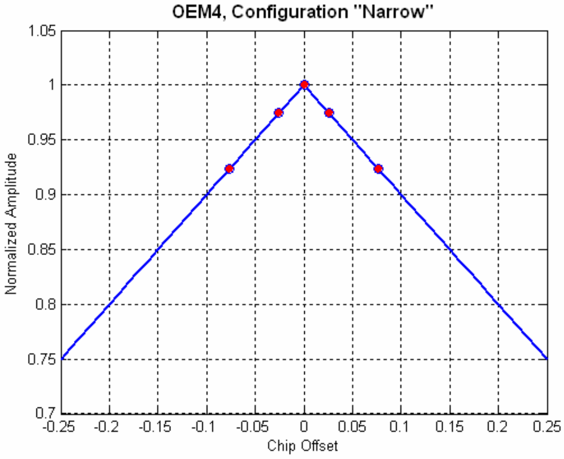 OEM4, Configuration "Narrow"	8	81	yes
	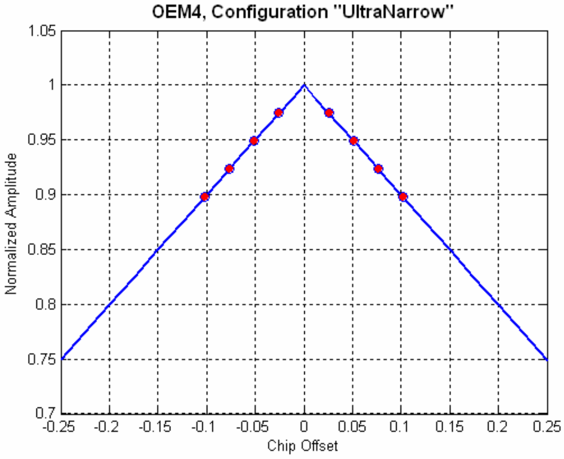 OEM4, Configuration "UltraNarrow"	8	360	yes

Table 7-6: Considered correlator configurations for the purpose of multipath monitoring.

7.2.2 Signal Simulator

During the development phase of the multipath monitor, a reliable signal source was required. For these purposes, a GPS hardware simulator was used (STR4760, Spirent Communications). This approach allowed the definition of a dedicated multipath environment and ensured reproducible scenarios. As will be discussed later on, the implementation of the multipath monitor requires a priori knowledge of the long-term mean values of each considered test metric. In principle, a GPS hardware simulator can be used to determine this information. However, it turned out that there are differences between the mean values obtained from simulator observations and those obtained from real-world data (see e.g. [SCHUSTER BRUCE et al. 2000]). As a consequence, the actual implementation of the proposed multipath monitor has to be based on real-world observation data. Nevertheless, the GPS hardware simulator has been used for concept verification and performance tests. Therefore, the long-term mean metric values have been derived from both simulator and real GPS data.

7.3 Concept Development

Test metrics like those introduced in Table 7-5 are currently being used for the detection of satellite signal failures. However, they can also be used for the purposes of real-time multipath monitoring because signal failures and multipath signals both result in a deformed correlation function. Therefore, the first step is to examine the influence of multipath signals on the test metrics.

This **first step** is performed on the basis of modeled correlation functions for the direct path and for one single multipath signal. The basic concept is illustrated in Figure 7-3, where the correlation function for the direct signal component is represented by the blue curve. The multipath signal is illustrated in the form of the green curve, showing an offset with respect to the direct path due to its extended path length (denoted as geometric path delay and expressed in [chips]) and reduced amplitude. Superimposition of both signal components results in the compound signal represented by the red curve, which is a distorted version of the correlation function for the direct path. In order to point out the influence on a dedicated test metric, the first correlator configuration presented in Table 7-6 is also plotted (OEM3 STANDARD). As a result of the distortion of the correlation function due to the influence of multipath, the correlation values for the indicated correlator positions and thus the metrics themselves (howsoever they are formed) are affected by multipath as well.

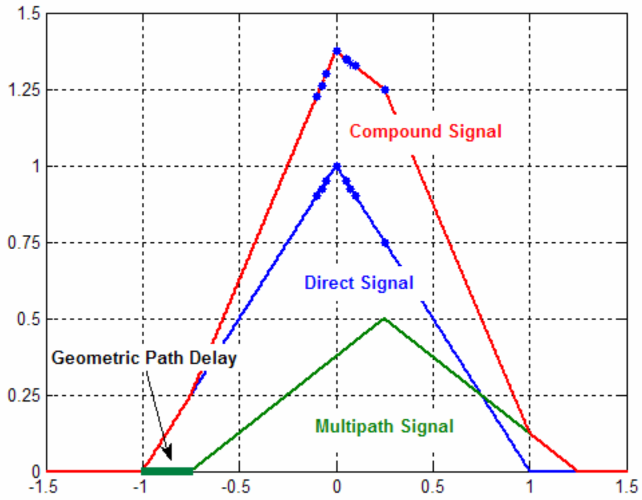

Example:

$$M = \frac{I_{+0.25}}{I_0}$$

Metric value for undistorted signal:

$$M = \frac{0.75}{1} = 0.75$$

Metric value for multipath-affected (compound) signal:

$$M = \frac{1.250}{1.375} \approx 0.909$$

Figure 7-3: Superimposition of direct signal and multipath component and impact on correlation peak observations.

The influence of multipath on a dedicated test metric can be visualized as a function of the geometric path delay

- By first assuming a multipath relative amplitude

- By superimposition of the correlation functions for the direct path and the multipath signal as presented in Figure 7-3
- By determination of the correlation values for the correlators used for monitoring the correlation peak
- By computation of the metric value for the metric of interest.

In case this procedure is repeated for any geometric path delay between 0 and 2 and in case that different multipath relative phases are considered as well, the multipath influence for a dedicated test metric can be illustrated as a function of the geometric path delay as shown in Figure 7-4. The diagrams illustrate the influence of one single multipath on two sample metrics. The computations were carried out for multipath relative amplitudes of 0.5 (purple curve), 0.25 (grey curve) and 0.1 (blue curve), respectively. For modeling the underlying correlation function, a pre-correlation bandwidth of 16 MHz and an ideal band pass filter were assumed. The modeled correlation function is assumed to be unaffected by thermal noise. It should be noted that the metrics were corrected for their long-term mean values, so that the metric values represent the deviation from their nominal means.[7]

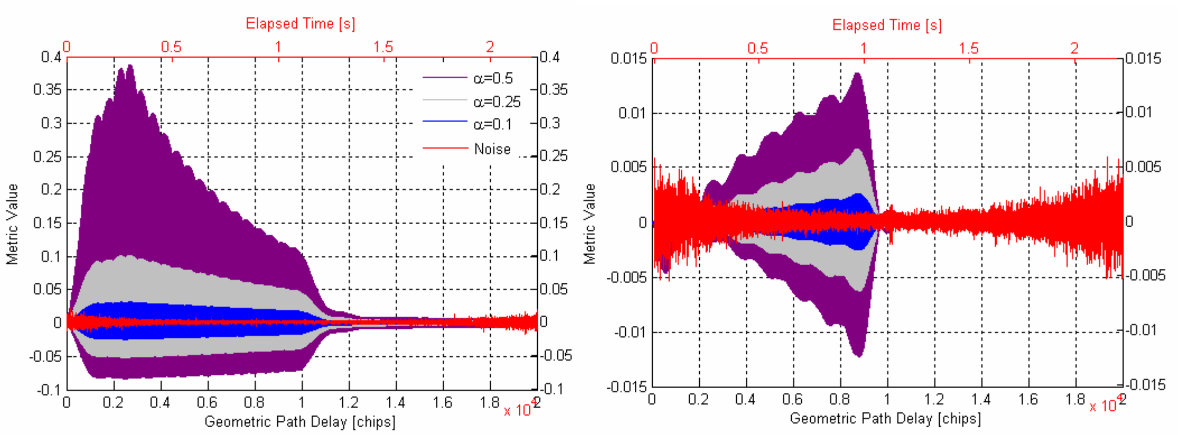

Figure 7-4: Values of two sample test metrics in the presence of a single multipath signal (as a function of the geometric multipath delay) assuming different relative amplitudes (0.5 (purple), 0.25 (gray) and 0.1 (blue)). The red curve illustrates the influence of thermal noise.

As a **second step**, the influence of thermal noise on the test metrics was evaluated. For this purpose, undistorted correlation peak observations influenced by thermal noise only were recorded by using a GPS hardware simulator. In order to account for increased noise at low elevation angles, a suitable antenna gain pattern was modeled and considered for the simulation. A dedicated satellite (PRN 21 in this case) was observed during its complete pass and the obtained metric data - representing the influence of thermal noise - was added to the illustration of the corresponding theoretical multipath errors for this metric (red data in Figure 7-4). Note that the indicated noise floor is a function of time and not a function of the geometric path delay.

The **general idea** for the implementation of a real-time multipath monitor is to constantly monitor each test metric and to compare each value with a threshold that indicates should the metric value exceed its corresponding noise level. If the metric value exceeds this threshold, it is assumed that the test metric is not only affected by noise but also by other interfering signals (mainly by multipath, less frequently by signal failures). This basic idea is illustrated in Figure 7-5, where the influence of noise and multipath on the second sample metric of Figure 7-4 is again plotted for multipath relative amplitudes of 0.5, 0.25 and 0.1, respectively.

---

[7] In the following, the diagrams that visualize the influence of multipath on a test metric will be termed as „multipath error envelopes“ or simply „envelopes“ (although the actual multipath error is plotted and not only its envelope).

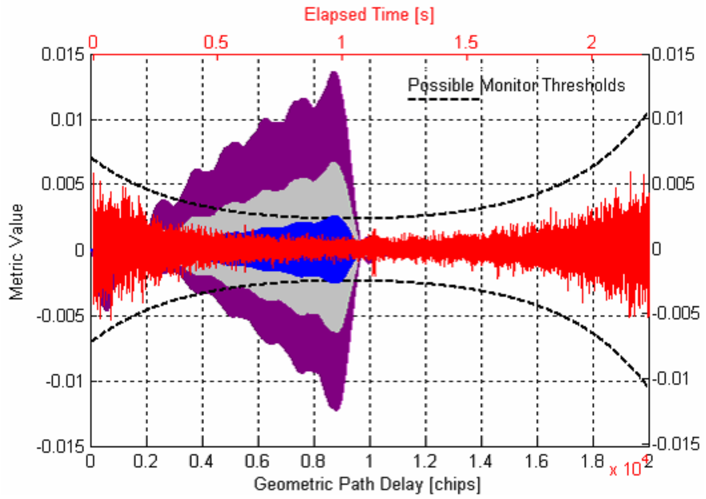

Figure 7-5: Multipath vs. thermal noise. The noise data was obtained from a GPS hardware simulator for a complete satellite pass. Note that the noise is a function of time (upper scale) and NOT a function of the path delay.

As can be derived from Figure 7-5, the thermal noise of the metric is well below the maximum multipath errors for all multipath cases discussed above - at least for sufficient high elevation angles. As a result, it should be feasible to detect such multipath signals (at least in case they produce their maximum errors) by determination of a suitable monitor threshold. It should be noted, however, that the threshold that will serve as a multipath indicator has to be sufficiently higher than the noise level in order to avoid false alarms caused by unexpectedly high fluctuations of the metric values. Nevertheless, by means of this approach, it should be feasible to detect multipath signals with relative amplitudes of more than 0.1. A more detailed performance analysis for this approach is given in section 7.7.

Since the metric error caused by multipath strongly depends on the actual geometric path delays, it is always possible that even a strong multipath signal causes metric values which are within the noise floor. It is clear that such multipath signals cannot be detected by means of this method. On the other hand, the resulting ranging error caused by multipath is usually very small in such cases because the correlation function is not severely distorted. As will be shown in section 7.7, this statement does not hold true for very short path delays. For longer path delays, however, it is not really necessary to detect multipath signals which are hidden in the noise floor, so that in most cases the proposed multipath monitor only detects multipath signals with significant negative impact on the ranging accuracy.

A closer look at Figure 7-4 reveals two additional aspects. First, it seems that some metrics are sensitive to short-delay multipath whereas others are more sensitive to long-delay multipath. The first sample metric (left diagram in Figure 7-4) shows its maximum metric values for path delays of about 0.25 chips. They decrease for longer path delays. The second sample metric (right diagram), however, shows very small metric values for short path delays but when it comes to longer path delays, the metric value increases and reaches its maximum values for a path delay of about 0.9 chips. Second, it seems that some metrics are more suitable for multipath detection than others. The maximum values of the first envelope are by far higher above the noise floor than it is the case for the second sample metric (at least for multipath relative amplitudes of 0.5 and 0.25). According to this criterion, the first sample metric is more suitable for multipath detection.

Such aspects are taken into account in the following section, where the large amount of available test metrics is to be reduced to obtain a set of most suitable metrics for the purposes of real-time multipath monitoring.

7.4 Metric Selection

Although a very large number of (linear) test metrics can be set up by combining two or more correlation peak observations, not all of these metrics are suitable for multipath monitoring. Besides, for implementing the multipath monitor, it is neither required nor desired to have such a large number of tests. If we assume to have 328 available tests for the OEM3 STANDARD correlator configuration and 10 visible satellites, the monitor would have to carry out over 3000 metric computations (plus consecutive computations) per epoch – a rather time consuming process. Mainly two aspects can be used to reduce the number of test metrics:

- Metrics whose maximum multipath-affected metric values are not sufficiently high above the corresponding noise floor can remain unconsidered. Thus, one measure could be the computation of a “multipath-to-noise” (M/N) ratio based on simulated multipath envelopes and the corresponding noise influence for each metric. Metrics with low M/N ratios can be down-weighted with respect to those showing high M/N ratios.
- Furthermore, it must be assumed that some metrics are correlated, i.e. if there are two correlated metrics and the first metric detects a multipath signal, the second one will most likely do the same. Together with the computation of M/N ratios, this aspect provides another approach of reducing the amount of test metrics: if two metrics are found to be correlated, the metric with the lower M/N ratio can be omitted.

Both criteria – the computation of M/N ratios and the consideration of correlations between test metrics – are addressed in the following sections.

7.4.1 Multipath-To-Noise Ratio

The computation of a “multipath-to-noise” ratio (M/N) is a measure to assess a metric’s capability for multipath detection. There are different possibilities to define such ratios. Within the framework of this thesis, the M/N ratio is defined as the maximum absolute metric value of the i^{th} simulated multipath error envelope $M_{i,MP}$ divided by the standard deviation of the corresponding noise floor $N_{M,i}$. It can be expressed as follows:

$$\frac{M}{N} = \frac{\max\left(\left|M_{i,MP}\right|\right)}{\mathrm{std}(N_{M_i})} \tag{135}$$

M/N ratios can either be derived from diagrams like Figure 7-5 where the standard deviation of the noise floor characterizes the noise influence during the entire satellite pass (at low and high elevation angles) or by computing theoretical noise variances that can be expressed as a function of the C/N_0 (see sections 7.4.3 and 7.5.1). High M/N ratios indicate that the maximum of the error envelopes is relatively far above the noise floor whereas very low ratios indicate that the envelopes do not significantly exceed the corresponding noise level. As a consequence, metrics showing high ratios are assumed to be more suitable for detecting multipath signals.

By computation of M/N ratios for all possible metrics and by sorting the resulting list in descending order, a preliminary metric ranking can be obtained. The metrics on top of the list are the most promising ones with respect to their sensitivity for multipath monitoring. Within the framework of this thesis, the noise influence and the corresponding M/N ratios always base on the computation of the metrics’ theoretical noise variances.

7.4.2 Correlation of Test Metrics

The computation of correlations between test metrics will be carried out exemplarily for a subset of 13 test metrics which all use the punctual I-Sample I_0 for normalization. The considered metrics base on the OEM3 STANDARD configuration and are denoted as m_1-m_{13}. The computation bases on the law of error propagation and starts with the observation equations:

Δ-Tests	Symmetric Ratio Tests	Asymmetric Ratio Tests
$m_1 = \frac{I_{-0.075} - I_{+0.075} - I_{-0.05} + I_{+0.05}}{I_0} = \frac{Z_{m01}}{I_0}$ $m_2 = \frac{I_{-0.1} - I_{+0.1} - I_{-0.05} + I_{+0.05}}{I_0} = \frac{Z_{m02}}{I_0}$ $m_3 = \frac{I_{-0.1} - I_{+0.1} - I_{-0.075} + I_{+0.075}}{I_0} = \frac{Z_{m03}}{I_0}$	$m_4 = \frac{I_{-0.05} - I_{+0.05}}{I_0} = \frac{Z_{m04}}{I_0}$ $m_5 = \frac{I_{-0.075} - I_{+0.075}}{I_0} = \frac{Z_{m05}}{I_0}$ $m_6 = \frac{I_{-0.1} - I_{+0.1}}{I_0} = \frac{Z_{m06}}{I_0}$	$m_7 = \frac{I_{-0.1}}{I_0} = \frac{Z_{m07}}{I_0}$ $m_{12} = \frac{I_{+0.1}}{I_0} = \frac{Z_{m12}}{I_0}$ $m_8 = \frac{I_{-0.075}}{I_0} = \frac{Z_{m08}}{I_0}$ $m_{11} = \frac{I_{+0.075}}{I_0} = \frac{Z_{m11}}{I_0}$ $m_9 = \frac{I_{-0.05}}{I_0} = \frac{Z_{m09}}{I_0}$ $m_{10} = \frac{I_{+0.05}}{I_0} = \frac{Z_{m10}}{I_0}$ $m_{13} = \frac{I_{+0.25}}{I_0} = \frac{Z_{m13}}{I_0}$

Table 7-7: Observation equations for 13 linear test metrics.

The partial derivatives of the test metrics with respect to the observed I-samples (Matrix *A*) are as follows:

$$A = \begin{bmatrix}
\frac{\partial m_1}{\partial I_{-0.1}} & \frac{\partial m_1}{\partial I_{-0.075}} & \frac{\partial m_1}{\partial I_{-0.05}} & \frac{\partial m_1}{\partial I_0} & \frac{\partial m_1}{\partial I_{+0.05}} & \frac{\partial m_1}{\partial I_{+0.075}} & \frac{\partial m_1}{\partial I_{+0.1}} & \frac{\partial m_1}{\partial I_{+0.25}} \\
\frac{\partial m_2}{\partial I_{-0.1}} & \frac{\partial m_2}{\partial I_{-0.075}} & \frac{\partial m_2}{\partial I_{-0.05}} & \frac{\partial m_2}{\partial I_0} & \frac{\partial m_2}{\partial I_{+0.05}} & \frac{\partial m_2}{\partial I_{+0.075}} & \frac{\partial m_2}{\partial I_{+0.1}} & \frac{\partial m_2}{\partial I_{+0.25}} \\
\frac{\partial m_3}{\partial I_{-0.1}} & \frac{\partial m_3}{\partial I_{-0.075}} & \frac{\partial m_3}{\partial I_{-0.05}} & \frac{\partial m_3}{\partial I_0} & \frac{\partial m_3}{\partial I_{+0.05}} & \frac{\partial m_3}{\partial I_{+0.075}} & \frac{\partial m_3}{\partial I_{+0.1}} & \frac{\partial m_3}{\partial I_{+0.25}} \\
\frac{\partial m_4}{\partial I_{-0.1}} & \frac{\partial m_4}{\partial I_{-0.075}} & \frac{\partial m_4}{\partial I_{-0.05}} & \frac{\partial m_4}{\partial I_0} & \frac{\partial m_4}{\partial I_{+0.05}} & \frac{\partial m_4}{\partial I_{+0.075}} & \frac{\partial m_4}{\partial I_{+0.1}} & \frac{\partial m_4}{\partial I_{+0.25}} \\
\frac{\partial m_5}{\partial I_{-0.1}} & \frac{\partial m_5}{\partial I_{-0.075}} & \frac{\partial m_5}{\partial I_{-0.05}} & \frac{\partial m_5}{\partial I_0} & \frac{\partial m_5}{\partial I_{+0.05}} & \frac{\partial m_5}{\partial I_{+0.075}} & \frac{\partial m_5}{\partial I_{+0.1}} & \frac{\partial m_5}{\partial I_{+0.25}} \\
\frac{\partial m_6}{\partial I_{-0.1}} & \frac{\partial m_6}{\partial I_{-0.075}} & \frac{\partial m_6}{\partial I_{-0.05}} & \frac{\partial m_6}{\partial I_0} & \frac{\partial m_6}{\partial I_{+0.05}} & \frac{\partial m_6}{\partial I_{+0.075}} & \frac{\partial m_6}{\partial I_{+0.1}} & \frac{\partial m_6}{\partial I_{+0.25}} \\
\frac{\partial m_7}{\partial I_{-0.1}} & \frac{\partial m_7}{\partial I_{-0.075}} & \frac{\partial m_7}{\partial I_{-0.05}} & \frac{\partial m_7}{\partial I_0} & \frac{\partial m_7}{\partial I_{+0.05}} & \frac{\partial m_7}{\partial I_{+0.075}} & \frac{\partial m_7}{\partial I_{+0.1}} & \frac{\partial m_7}{\partial I_{+0.25}} \\
\frac{\partial m_8}{\partial I_{-0.1}} & \frac{\partial m_8}{\partial I_{-0.075}} & \frac{\partial m_8}{\partial I_{-0.05}} & \frac{\partial m_8}{\partial I_0} & \frac{\partial m_8}{\partial I_{+0.05}} & \frac{\partial m_8}{\partial I_{+0.075}} & \frac{\partial m_8}{\partial I_{+0.1}} & \frac{\partial m_8}{\partial I_{+0.25}} \\
\frac{\partial m_9}{\partial I_{-0.1}} & \frac{\partial m_9}{\partial I_{-0.075}} & \frac{\partial m_9}{\partial I_{-0.05}} & \frac{\partial m_9}{\partial I_0} & \frac{\partial m_9}{\partial I_{+0.05}} & \frac{\partial m_9}{\partial I_{+0.075}} & \frac{\partial m_9}{\partial I_{+0.1}} & \frac{\partial m_9}{\partial I_{+0.25}} \\
\frac{\partial m_{10}}{\partial I_{-0.1}} & \frac{\partial m_{10}}{\partial I_{-0.075}} & \frac{\partial m_{10}}{\partial I_{-0.05}} & \frac{\partial m_{10}}{\partial I_0} & \frac{\partial m_{10}}{\partial I_{+0.05}} & \frac{\partial m_{10}}{\partial I_{+0.075}} & \frac{\partial m_{10}}{\partial I_{+0.1}} & \frac{\partial m_{10}}{\partial I_{+0.25}} \\
\frac{\partial m_{11}}{\partial I_{-0.1}} & \frac{\partial m_{11}}{\partial I_{-0.075}} & \frac{\partial m_{11}}{\partial I_{-0.05}} & \frac{\partial m_{11}}{\partial I_0} & \frac{\partial m_{11}}{\partial I_{+0.05}} & \frac{\partial m_{11}}{\partial I_{+0.075}} & \frac{\partial m_{11}}{\partial I_{+0.1}} & \frac{\partial m_{11}}{\partial I_{+0.25}} \\
\frac{\partial m_{12}}{\partial I_{-0.1}} & \frac{\partial m_{12}}{\partial I_{-0.075}} & \frac{\partial m_{12}}{\partial I_{-0.05}} & \frac{\partial m_{12}}{\partial I_0} & \frac{\partial m_{12}}{\partial I_{+0.05}} & \frac{\partial m_{12}}{\partial I_{+0.075}} & \frac{\partial m_{12}}{\partial I_{+0.1}} & \frac{\partial m_{12}}{\partial I_{+0.25}} \\
\frac{\partial m_{13}}{\partial I_{-0.1}} & \frac{\partial m_{13}}{\partial I_{-0.075}} & \frac{\partial m_{13}}{\partial I_{-0.05}} & \frac{\partial m_{13}}{\partial I_0} & \frac{\partial m_{13}}{\partial I_{+0.05}} & \frac{\partial m_{13}}{\partial I_{+0.075}} & \frac{\partial m_{13}}{\partial I_{+0.1}} & \frac{\partial m_{13}}{\partial I_{+0.25}}
\end{bmatrix} = \begin{bmatrix}
0 & \frac{1}{I_0} & -\frac{1}{I_0} & -\frac{Z_{m1}}{I_0^2} & \frac{1}{I_0} & -\frac{1}{I_0} & 0 & 0 \\
\frac{1}{I_0} & 0 & -\frac{1}{I_0} & -\frac{Z_{m2}}{I_0^2} & \frac{1}{I_0} & 0 & -\frac{1}{I_0} & 0 \\
\frac{1}{I_0} & -\frac{1}{I_0} & 0 & -\frac{Z_{m3}}{I_0^2} & 0 & \frac{1}{I_0} & -\frac{1}{I_0} & 0 \\
0 & 0 & \frac{1}{I_0} & -\frac{Z_{m4}}{I_0^2} & -\frac{1}{I_0} & 0 & 0 & 0 \\
0 & \frac{1}{I_0} & 0 & -\frac{Z_{m5}}{I_0^2} & 0 & -\frac{1}{I_0} & 0 & 0 \\
\frac{1}{I_0} & 0 & 0 & -\frac{Z_{m6}}{I_0^2} & 0 & 0 & -\frac{1}{I_0} & 0 \\
\frac{1}{I_0} & 0 & 0 & -\frac{I_{-0.1}}{I_0^2} & 0 & 0 & 0 & 0 \\
0 & \frac{1}{I_0} & 0 & -\frac{I_{-0.075}}{I_0^2} & 0 & 0 & 0 & 0 \\
0 & 0 & \frac{1}{I_0} & -\frac{I_{-0.05}}{I_0^2} & 0 & 0 & 0 & 0 \\
0 & 0 & 0 & -\frac{I_{+0.05}}{I_0^2} & \frac{1}{I_0} & 0 & 0 & 0 \\
0 & 0 & 0 & -\frac{I_{+0.075}}{I_0^2} & 0 & \frac{1}{I_0} & 0 & 0 \\
0 & 0 & 0 & -\frac{I_{+0.1}}{I_0^2} & 0 & 0 & \frac{1}{I_0} & 0 \\
0 & 0 & 0 & -\frac{I_{+0.25}}{I_0^2} & 0 & 0 & 0 & \frac{1}{I_0}
\end{bmatrix} \tag{136}$$

A is a *(n x m)* matrix, where *n* is the number of observation equations and *m* the number of available correlators. The I-samples can be treated as Gaussian variables having the following mean μ_I, variance σ_I^2 and covariance $\sigma_{I1,I2}$ properties [SLEEWAGEN and BOON 2001]:

$$\begin{aligned}
\mu_I &= \sqrt{2 \cdot \text{SNR} \cdot T} \cdot R(d_I) \approx \sqrt{2 \cdot \text{SNR} \cdot T} \cdot (1 - d_I) \\
\sigma_I^2 &= 1 \\
\sigma_{I_1,I_2} &= R(d_{I1,I2}) \approx 1 - d_{I1,I2}
\end{aligned} \tag{137}$$

d_I is the correlator spacing between an arbitrary I-sample and the punctual I-sample I_0 and $d_{I1,I2}$ is the correlator spacing between two arbitrary I-samples I_1 and I_2. $R(d)$ is the normalized correlation amplitude at $\tau=d$. Assuming an ideal correlation function of triangular shape, *R(d)* is simply equal to (*1-d*). Moreover, *T* is the accumulation time and SNR the signal-to-noise ratio that is related to the C/N$_0$ reported by the receiver via

$$\mathrm{SNR} = 10^{\frac{C/N_0}{10}} . \tag{138}$$

By substituting the I-Samples of equation (136) with the mean value of equation (137), the Jacobian matrix *A* can be expressed as follows:

$$A = \frac{1}{\sqrt{2 \cdot \mathrm{SNR} \cdot T}} \begin{bmatrix} 0 & \frac{1}{R(0)} & -\frac{1}{R(0)} & -\frac{R(-0.075)-R(0.075)-R(-0.05)+R(0.05)}{R^2(0)} & \frac{1}{R(0)} & -\frac{1}{R(0)} & 0 & 0 \\ \frac{1}{R(0)} & 0 & -\frac{1}{R(0)} & \frac{R(-0.1)-R(0.1)-R(-0.05)+R(0.05)}{R^2(0)} & \frac{1}{R(0)} & 0 & -\frac{1}{R(0)} & 0 \\ \frac{1}{R(0)} & -\frac{1}{R(0)} & 0 & \frac{R(-0.1)-R(0.1)-R(-0.075)+R(0.075)}{R^2(0)} & 0 & \frac{1}{R(0)} & -\frac{1}{R(0)} & 0 \\ 0 & 0 & \frac{1}{R(0)} & \frac{R(-0.05)-R(0.05)}{R^2(0)} & -\frac{1}{R(0)} & 0 & 0 & 0 \\ 0 & \frac{1}{R(0)} & 0 & \frac{R(-0.075)-R(0.075)}{R^2(0)} & 0 & -\frac{1}{R(0)} & 0 & 0 \\ \frac{1}{R(0)} & 0 & 0 & \frac{R(-0.1)-R(0.1)}{R^2(0)} & 0 & 0 & -\frac{1}{R(0)} & 0 \\ \frac{1}{R(0)} & 0 & 0 & \frac{R(-0.1)}{R^2(0)} & 0 & 0 & 0 & 0 \\ 0 & \frac{1}{R(0)} & 0 & \frac{R(-0.075)}{R^2(0)} & 0 & 0 & 0 & 0 \\ 0 & 0 & \frac{1}{R(0)} & \frac{R(-0.05)}{R^2(0)} & 0 & 0 & 0 & 0 \\ 0 & 0 & 0 & \frac{R(0.05)}{R^2(0)} & \frac{1}{R(0)} & 0 & 0 & 0 \\ 0 & 0 & 0 & \frac{R(0.075)}{R^2(0)} & 0 & \frac{1}{R(0)} & 0 & 0 \\ 0 & 0 & 0 & \frac{R(0.1)}{R^2(0)} & 0 & 0 & \frac{1}{R(0)} & 0 \\ 0 & 0 & 0 & \frac{R(0.25)}{R^2(0)} & 0 & 0 & 0 & \frac{1}{R(0)} \end{bmatrix} \tag{139}$$

The variance-covariance matrix for the observations (I-Samples) is a square matrix (*m* x *m*) and consists of the observations' variances σ^2_I=1 and the corresponding co-variances $\sigma_{I1,I2}$ = $R(d_{I1,I2})$ as introduced in equation (137):

$$D(l) = \begin{bmatrix} \sigma^2_{I_{-0.1}} & \sigma_{I_{-0.1,-0.075}} & \sigma_{I_{-0.1,-0.05}} & \sigma_{I_{-0.1,0}} & \sigma_{I_{-0.1,+0.05}} & \sigma_{I_{-0.1,+0.075}} & \sigma_{I_{-0.1,+0.1}} & \sigma_{I_{-0.1,+0.25}} \\ & \sigma^2_{I_{-0.075}} & \sigma_{I_{-0.075,-0.05}} & \sigma_{I_{-0.075,0}} & \sigma_{I_{-0.075,+0.05}} & \sigma_{I_{-0.075,+0.075}} & \sigma_{I_{-0.075,+0.1}} & \sigma_{I_{-0.075,+0.25}} \\ & & \sigma^2_{I_{-0.05}} & \sigma_{I_{-0.05,0}} & \sigma_{I_{-0.05,+0.05}} & \sigma_{I_{-0.05,+0.075}} & \sigma_{I_{-0.05,+0.1}} & \sigma_{I_{-0.05,+0.25}} \\ & & & \sigma^2_{I_0} & \sigma_{I_{0,+0.05}} & \sigma_{I_{0,+0.075}} & \sigma_{I_{0,+0.1}} & \sigma_{I_{0,+0.25}} \\ & & & & \sigma^2_{I_{+0.05}} & \sigma_{I_{0.05,+0.075}} & \sigma_{I_{0.05,+0.1}} & \sigma_{I_{+0.05,+0.25}} \\ & & & \% & & \sigma^2_{I_{+0.075}} & \sigma_{I_{0.075,+0.1}} & \sigma_{I_{+0.075,+0.25}} \\ & & & & & & \sigma^2_{I_{+0.1}} & \sigma_{I_{+0.1,+0.25}} \\ & & & & & & & \sigma^2_{I_{+0.25}} \end{bmatrix} \tag{140}$$

$$D(l) = \begin{bmatrix} 1 & R(0.025) & R(0.05) & R(0.1) & R(0.15) & R(0.175) & R(0.2) & R(0.35) \\ R(0.025) & 1 & R(0.025) & R(0.075) & R(0.125) & R(0.15) & R(0.175) & R(0.325) \\ R(0.05) & R(0.025) & 1 & R(0.05) & R(0.1) & R(0.125) & R(0.15) & R(0.3) \\ R(0.1) & R(0.075) & R(0.05) & 1 & R(0.05) & R(0.075) & R(0.1) & R(0.25) \\ R(0.15) & R(0.125) & R(0.1) & R(0.05) & 1 & R(0.025) & R(0.05) & R(0.2) \\ R(0.175) & R(0.15) & R(0.125) & R(0.075) & R(0.025) & 1 & R(0.025) & R(0.175) \\ R(0.2) & R(0.175) & R(0.15) & R(0.1) & R(0.05) & R(0.025) & 1 & R(0.15) \\ R(0.35) & R(0.325) & R(0.3) & R(0.25) & R(0.2) & R(0.175) & R(0.15) & 1 \end{bmatrix} \tag{141}$$

According to the law of error propagation, the resulting variance-covariance matrix *D(m)* of the considered test metrics can the computed as:

$$D(m) = A \cdot D(l) \cdot A^T \tag{142}$$

with *D(m)* being an (*n* x *n*)-matrix with the following structure:

$$D(m) = \frac{1}{2 \cdot SNR \cdot T} \begin{bmatrix}
\sigma^2_{m1} & \sigma_{m1m2} & \sigma_{m1m3} & \sigma_{m1m4} & \sigma_{m1m5} & \sigma_{m1m6} & \sigma_{m1m7} & \sigma_{m1m8} & \sigma_{m1m9} & \sigma_{m1m10} & \sigma_{m1m11} & \sigma_{m1m12} & \sigma_{m1m13} \\
 & \sigma^2_{m2} & \sigma_{m2m3} & \sigma_{m2m4} & \sigma_{m2m5} & \sigma_{m2m6} & \sigma_{m2m7} & \sigma_{m2m8} & \sigma_{m2m9} & \sigma_{m2m10} & \sigma_{m2m11} & \sigma_{m2m12} & \sigma_{m2m13} \\
 & & \sigma^2_{m3} & \sigma_{m3m4} & \sigma_{m3m5} & \sigma_{m3m6} & \sigma_{m3m7} & \sigma_{m3m8} & \sigma_{m3m9} & \sigma_{m3m10} & \sigma_{m3m11} & \sigma_{m3m12} & \sigma_{m3m13} \\
 & & & \sigma^2_{m4} & \sigma_{m4m5} & \sigma_{m4m6} & \sigma_{m4m7} & \sigma_{m4m8} & \sigma_{m4m9} & \sigma_{m4m10} & \sigma_{m4m11} & \sigma_{m4m12} & \sigma_{m4m13} \\
 & & & & \sigma^2_{m5} & \sigma_{m5m6} & \sigma_{m5m7} & \sigma_{m5m8} & \sigma_{m5m9} & \sigma_{m5m10} & \sigma_{m5m11} & \sigma_{m5m12} & \sigma_{m5m13} \\
 & & & & & \sigma^2_{m6} & \sigma_{m6m7} & \sigma_{m6m8} & \sigma_{m6m9} & \sigma_{m6m10} & \sigma_{m6m11} & \sigma_{m6m12} & \sigma_{m6m13} \\
 & & & & & & \sigma^2_{m7} & \sigma_{m7m8} & \sigma_{m7m9} & \sigma_{m7m10} & \sigma_{m7m11} & \sigma_{m7m12} & \sigma_{m7m13} \\
 & & & & & & & \sigma^2_{m8} & \sigma_{m8m9} & \sigma_{m8m10} & \sigma_{m8m11} & \sigma_{m8m12} & \sigma_{m8m13} \\
 & & & & & & & & \sigma^2_{m9} & \sigma_{m9m10} & \sigma_{m9m11} & \sigma_{m9m12} & \sigma_{m9m13} \\
 & & & & \% & & & & & \sigma^2_{m10} & \sigma_{m10m11} & \sigma_{m10m12} & \sigma_{m10m13} \\
 & & & & & & & & & & \sigma^2_{m11} & \sigma_{m11m12} & \sigma_{m11m13} \\
 & & & & & & & & & & & \sigma^2_{m12} & \sigma_{m12m13} \\
 & & & & & & & & & & & & \sigma^2_{m13}
\end{bmatrix} \tag{143}$$

Equation (143) does not only allow the derivation of correlations between metric pairs but also contains the theoretical noise variances $\sigma_{m,i}{}^2$ for each metric. The correlation ρ between two test metrics m_i and m_j can be computed by

$$\rho_{m_i m_j} = \frac{\sigma_{m_i m_j}}{\sigma_{m_i} \sigma_{m_j}} \tag{144}$$

The accuracy of these computations depends on the a priori knowledge of the shape of the correlation function. In case that the shape of the correlation function is completely unknown, *R(d)* can be approximated by (*1-d*). Exact correlation values *R(d)* require a priori information on the pre-correlation bandwidth and on type and order of the band limiting filter. In addition, the results also depend on the PRN codes to some extent (due to minor correlation peaks) and therefore vary for different satellites. Within the framework of this thesis, it is assumed that only the pre-correlation bandwidth is known (which is 16MHz for the OEM3 and ~18MHz for the OEM4 receiver). Neither minor correlation peaks nor a special type of band pass filter is assumed. As a result, the correlation function from which the correlation values *R(d)* are computed is symmetric and represents the result of an ideal band pass filter. Figure 7-6 illustrates the correlation function which serves as a basis for the subsequent computations of correlation coefficients and theoretical noise variances:

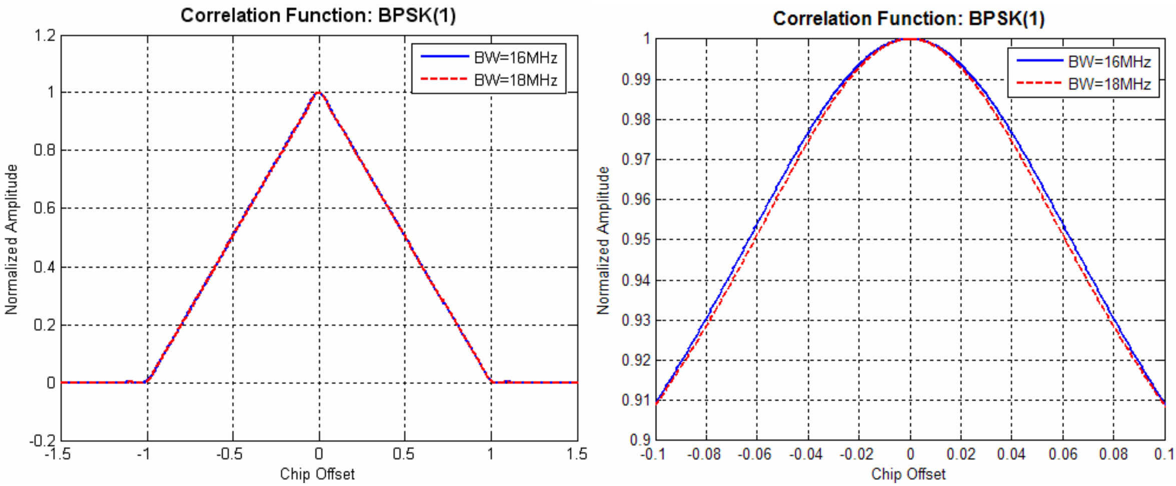

Figure 7-6: Correlation function used to compute the theoretical noise variances of the OEM3 (BW=16MHz) and OEM4 (BW=18MHz) test metrics. The differences between both functions become more evident in the right diagram where only the peak region is illustrated.

Taking into account the correlation function shapes illustrated in Figure 7-6, the correlation values *R(d)* can be determined and inserted into equations (139)-(141). The correlations $\rho_{mi,mj}$ can be arranged in the form of a matrix of correlation coefficients (also an (*n* x *n*)-matrix) that takes on the following form:

	m_1	m_2	m_3	m_4	m_5	m_6	m_7	m_8	m_9	m_{10}	m_{11}	m_{12}	m_{13}
m_1	1.00	0.96	0.85	0.31	0.64	0.82	0.61	0.47	0.26	-0.26	-0.47	-0.61	-0.41
m_2	0.96	1.00	0.96	0.15	0.49	0.73	0.54	0.36	0.12	-0.12	-0.36	-0.54	-0.41
m_3	0.85	0.96	1.00	-0.03	0.30	0.59	0.43	0.22	-0.02	0.02	-0.22	-0.43	-0.39
m_4	0.31	0.15	-0.03	1.00	0.93	0.78	0.58	0.69	0.82	-0.82	-0.69	-0.58	-0.36
m_5	0.64	0.49	0.30	0.93	1.00	0.95	0.70	0.74	0.76	-0.76	-0.74	-0.70	-0.45
m_6	0.82	0.73	0.59	0.78	0.95	1.00	0.74	0.71	0.64	-0.64	-0.71	-0.74	-0.51
m_7	0.61	0.54	0.43	0.58	0.70	0.74	1.00	0.95	0.81	-0.14	-0.10	-0.10	-0.12
m_8	0.47	0.36	0.22	0.69	0.74	0.71	0.95	1.00	0.94	-0.19	-0.11	-0.10	-0.12
m_9	0.26	0.12	-0.02	0.82	0.76	0.64	0.81	0.94	1.00	-0.33	-0.19	-0.14	-0.14
m_{10}	-0.26	-0.12	0.02	-0.82	-0.76	-0.64	-0.14	-0.19	-0.33	1.00	0.94	0.81	0.45
m_{11}	-0.47	-0.36	-0.22	-0.69	-0.74	-0.71	-0.10	-0.11	-0.19	0.94	1.00	0.95	0.55
m_{12}	-0.61	-0.54	-0.43	-0.58	-0.70	-0.74	-0.10	-0.10	-0.14	0.81	0.95	1.00	0.63
m_{13}	-0.41	-0.41	-0.39	-0.36	-0.45	-0.51	-0.12	-0.12	-0.14	0.45	0.55	0.63	1.00

🟩 Weak Corr. (p<=0.6) ⬜ Mod. Corr. (0.6<p<=0.8) 🟥 High Corr. (p>0.8)

Table 7-8: Correlations between linear test metrics m_1 - m_{13}.

Table 7-8 visualizes the correlations between the metrics listed in Table 7-7. The matrix is symmetrical with respect to its diagonal and contains the correlation coefficients calculated according to equation (144). The degree of correlation between metric pairs is indicated by different colors. There are a few metric pairs which are highly correlated, whereas the majority of metric combinations show only weak to moderate correlations.

7.4.3 Theoretical Noise Variances

As already mentioned, the M/N ratios shall serve as a basis for the determination of suitable test metrics that can be implemented in the real time multipath monitor. The noise influence can be quantified by the theoretical noise variances which can be extracted from the diagonal elements of the variance-covariance matrix *D(m)* (equation (143)):

$$\sigma^2_{\text{noise},i} = \frac{\sigma^2_{m_i}}{2 \cdot \text{SNR} \cdot \text{T}} \tag{145}$$

The theoretical noise variances depend on the SNR and thus on the current C/N_0 as reported by the receiver. They also depend on the accumulation time during which the I-Samples are integrated. The shorter the accumulation time, the noisier the observations. The OEM3/OEM4 multi-correlator receivers both work with an accumulation time of 1s.

The noise variances do not only serve as a means to determine the most suitable test metrics, they can also be used to compute instant monitor thresholds. These thresholds always have to account for the current influence of thermal noise. The higher this influence, the higher the thresholds must be. The computation of theoretical noise variances is an excellent way to compute monitor thresholds because they depend on the current C/N_0 that characterizes the current noise influence.

7.4.4 Metric Selection Algorithm

The computation of theoretical noise influences, the computation of *M/N* ratios and the consideration of correlations between test metrics can be used to reduce the number of metrics required for multipath monitoring. Based on the underlying correlator configuration, the metric selection process is carried out as follows:

- Determination of all possible metrics according to Table 7-5
- Computation of theoretical multipath error envelopes for all possible metrics
- Computation of theoretical noise variances for each metric
- Computation and sorting of *M/N* ratios for each metric's envelope/noise combination, resulting in a "metric ranking" that indicates the most promising metrics
- Computation of correlation coefficients for all metric combinations; this results in a correlation matrix like the one illustrated in Table 7-8
- Determination of all highly correlated metric pairs (correlations >0.8, red-colored elements in Table 7-8, resulting in a list of highly correlated metric pairs

So far, all steps listed above are necessary pre-computations. The actual metric selection process uses the metric ranking (based on *M/N* ratios) and the list of highly correlated metric pairs. Both lists – based on the metrics m_1-m_{13} (Table 7-7) - are illustrated in the following table. For the computation of the M/N ratios, a multipath relative amplitude of α=0.5 and a C/N_0 of 45dBHz has been assumed.

Metric Ranking	
Metric *m*	***M/N***
13	133.16
12	101.17
11	**90.15**
10	**80.08**
6	76.17
5	**68.29**
1	**64.23**
2	**62.71**
4	**58.60**
3	**57.77**
7	29.82
8	**27.41**
9	**25.97**

Highly Correlated Metric Pairs		
Metric m_i	**Metric m_j**	**Coeff. of Corr.**
1	2	0.96
1	3	0.85
1	6	0.82
2	3	0.96
4	5	0.93
4	9	0.82
4	10	0.82
5	6	0.95
7	8	0.95
7	9	0.81
8	9	0.94
10	11	0.94
10	12	0.81
11	12	0.95

Table 7-9: Metric ranking and correlated metric pairs for m_1-m_{13}.

The objective of the metric selection process is to obtain a set of metrics that are not highly correlated with respect to each other and at the same time provide a high M/N ratio. To achieve this, the M/N ratios of all highly correlated metric pairs are compared. The metric showing the lower *M/N* ratio is deleted from the metric ranking. By successively doing so with all entries in the "correlated metric pairs" list, only uncorrelated or weakly to moderately correlated metrics remain considered. In the above case, all metrics except m_{13}, m_{12}, m_6, and m_7 can be eliminated by this measure (red entries in Table 7-9). As a final step, the "best" remaining metrics (those with highest *M/N* ratios) are chosen to be implemented in the real time multipath monitor. Assuming that the monitor shall base on only two metrics, the analysis above would advise the use of m_{13} and m_{12}.

7.4.5 Metric Selection for RTMM

The computations carried out in the previous section only served as an example of how to reduce the number of available metrics in order to obtain an optimal subset of metrics which can be used for multipath monitoring. The results of the analysis presented in this section also base on the basic algorithm described in the previous section but includes all possible metrics introduced in Table 7-5. In addition, the following requirements have to be considered:

- The analysis includes all relevant correlator configurations (OEM3 and OEM4 configurations).

- The analysis has to be carried out for different multipath relative amplitudes. The objective is to determine metrics that are best suited for the detection of strong multipath signals and others that are suited for detecting weak multipath signals. Therefore, the metric selection process covers two cases:
  - Strong multipath signals, represented by attenuation factors of α=0.5, 0.4 and 0.3
  - Weak multipath signals, represented by attenuation factors of α=0.2, 0.1 and 0.05

- The analysis has to be carried out for different signal power levels, i.e. different C/N_0's have to be taken into account for the computation of the M/N ratios. The objective is to determine whether or not different metrics have to be used for different signal power conditions.

- Finally, the analysis differentiates between short-delay and long-delay multipath performance. The objective is to determine metrics that are most susceptible to short-delay multipath and others that are more suitable for detecting long-delay multipath.

The last requirement origins from the conclusions attained from Figure 7-4, where it turned out that there are obviously metrics which are sensitive to short-delay multipath while others seem to be more susceptible to long-delay multipath. The analysis carried out in section 7.4.4 based on M/N values that considered the whole multipath error envelope. However, the metric selection process for RTMM differentiates between short-delay and long-delay multipath performance. Therefore, the computation of the M/N ratios has to be carried out twice. The first computation considers only path delays between 0 and 0.5 chips and for the second one, path delays of larger than 0.5 chips are assumed. The objective is to obtain a set of 4 test metrics that are not highly correlated ($\rho<=0.8$) and best suited for the detection of any kind of multipath signal (short-delay, long-delay, weak or strong) under various signal power conditions (selection criterion: elimination of high correlations).

The main drawback of this metric selection approach is that due to the elimination of correlated metric pairs, the resulting set of test metrics may contain metrics showing rather poor M/N ratios. However, in case that maximum monitoring sensitivity is the major design driver, correlations between test metrics must remain unconsidered and only the metrics showing the highest M/N ratios have to be used. These metrics can be determined in a second metric selection process (selection criterion: maximum monitoring sensitivity). They are very sensitive to all types of multipath signals but also highly correlated in most cases. The results of both metric selection processes are summarized in the following tables:

OEM3 Standard (328 possible metrics)											
After Elimination of High Correlations						Maximum Monitoring Sensitivity					
Selected Metrics	Correlation Coefficients					Selected Metrics	Correlation Coefficients				
67,132,279,314		M_1	M_2	M_3	M_4	67,126,258,286		M_1	M_2	M_3	M_4
$M_{S1} = \frac{I_0}{I_{0.25}}$	M_1	1	0.77	0.73	0.62	$M_{S1} = \frac{I_0}{I_{0.25}}$	M_1	1	1.00	0.96	1.00
$M_{S2} = \frac{I_{0.1} - I_{0.25}}{I_0}$	M_2	0.77	1	0.12	0.28	$M_{S2} = \frac{I_0 - I_{0.25}}{I_0}$	M_2	1.00	1	0.96	1.00
$M_{S3} = \frac{I_0 - I_{0.1}}{I_{0.25}}$	M_3	0.73	0.12	1	0.67	$M_{S3} = \frac{I_{-0.05} - I_{0.25}}{I_{0.25}}$	M_3	0.96	0.96	1	0.96
$M_{S4} = \frac{I_{0.075} - I_{0.1}}{I_{0.25}}$	M_4	0.62	0.28	0.67	1	$M_{S4} = \frac{I_0 - I_{0.25}}{I_{0.25}}$	M_4	1.00	1.00	0.96	1

Table 7-10: Suitable test metrics for the OEM3 Standard configuration.

OEM4 Narrow (81 possible metrics)											
After Elimination of High Correlations						Maximum Monitoring Sensitivity					
Selected Metrics	Correlation Coefficients					Selected Metrics	Correlation Coefficients				
16,19,52,65		M_1	M_2	M_3	M_4	16,18,19,27		M_1	M_2	M_3	M_4
$M_{N1} = \frac{I_{-0.025}}{I_{0.075}}$	M_1	1	0.80	0.57	0.78	$M_{N1} = \frac{I_{-0.025}}{I_{0.075}}$	M_1	1	0.95	0.80	-0.80
$M_{N2} = \frac{I_{0.025}}{I_{0.075}}$	M_2	0.80	1	0.13	0.25	$M_{N2} = \frac{I_0}{I_{0.075}}$	M_2	0.95	1	0.94	-0.94
$M_{N3} = \frac{I_{-0.075} - I_{0.025}}{I_{0.025}}$	M_3	0.57	0.13	1	0.78	$M_{N3} = \frac{I_{0.025}}{I_{0.075}}$	M_3	0.80	0.94	1	-1
$M_{N4} = \frac{I_{-0.025} - I_{0.025}}{I_{0.075}}$	M_4	0.78	0.25	0.78	1	$M_{N4} = \frac{I_{0.075}}{I_{0.025}}$	M_4	-0.80	-0.94	-1	1

Table 7-11: Suitable test metrics for the OEM4 Narrow configuration.

OEM4 UltraNarrow (360 possible metrics)											
After Elimination of High Correlations						Maximum Monitoring Sensitivity					
Selected Metrics	Correlation Coefficients					Selected Metrics	Correlation Coefficients				
105,184,320,360		M_1	M_2	M_3	M_4	102,105,312,336		M_1	M_2	M_3	M_4
$M_{UN1} = \frac{I_{0.025}}{I_{0.1}}$	M_1	1	0.52	0.77	0.76	$M_{UN1} = \frac{I_{-0.025}}{I_{0.1}}$	M_1	1	0.85	1.00	0.85
$M_{UN2} = \frac{I_{-0.1} - I_{0.075}}{I_{0.1}}$	M_2	0.52	1	0.62	0.21	$M_{UN2} = \frac{I_{0.025}}{I_{0.1}}$	M_2	0.85	1	0.85	1.00
$M_{UN3} = \frac{I_{0.025} - I_{0.05}}{I_{0.1}}$	M_3	0.77	0.62	1	0.19	$M_{UN3} = \frac{I_{-0.025} - I_{0.1}}{I_{0.1}}$	M_3	1.00	0.85	1	0.85
$M_{UN4} = \frac{I_{0.075} - I_{0.1}}{I_{0.1}}$	M_4	0.76	0.21	0.19	1	$M_{UN4} = \frac{I_{0.025} - I_{0.1}}{I_{0.1}}$	M_4	0.85	1.00	0.85	1

Table 7-12: Suitable test metrics for the OEM4 UltraNarrow configuration.

Table 7-10 - Table 7-12 contain the equations and the correlation coefficients of the most suitable test metrics for all available correlator configurations. The left parts of the tables contain the resulting metrics after the elimination of highly correlated metric pairs. The right parts contain the results without consideration of metric correlations; these subsets can be used if maximum monitoring sensitivity is to be achieved. The tables also contain the internal metric numbers. As an example, the internal metric number of M_{UN2} in the subset of weakly to moderately correlated metrics (left column of Table 7-12) is 184. This metric can also be expressed as M_{184}.

Now that the most suitable test metrics have been determined, the next step is to provide a procedure for the computation of instant monitor thresholds based on the metrics' theoretical noise variances.

7.5 Noise Variances and Monitor Thresholds

In order to ensure real time capability, it is necessary to have instant knowledge about the monitor thresholds. As can be derived from Figure 7-5, these thresholds depend on the current influence of thermal noise, which in turn is a function of the current C/N$_0$ as reported by the receiver. In order to be able to compute the monitor thresholds at any time, the objective is to base the threshold computation on the determination of the theoretical noise variance of each test metric. Once the noise variances are known, the monitor thresholds can be easily obtained by simply applying an extension factor to these noise variances. This leads to the following computations that have to be carried out at each point in time t_k:

- Computation of current metric value (metric value at epoch t_k, according to selected metric)

- Computation of (theoretical) noise variance σ_k^2 or standard deviation σ_k at epoch t_k by use of current $C/N_{0,k}$

- Computation of monitor threshold by application of a suitable expansion factor m_{exp} ($threshold = m^* \pm m_{exp}\,\sigma_k$)

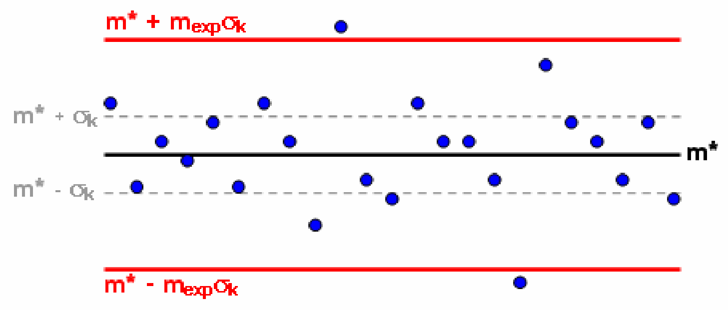

Figure 7-7: Time series of metric values (blue dots), long-term mean metric value (black solid line), theoretical noise influence (grey dashed lines) and monitor thresholds (red solid lines).

These steps assume that the long-term mean values m^* of all metrics are known in advance. As a consequence, these mean values must be determined for each visible satellite during a calibration campaign in a multipath-free environment.

As indicated by Figure 7-7, it is possible that due to the statistical nature of the observations, even in the absence of multipath the metric values exceed the selected monitor thresholds from time to time. The probability of such events depends on the selected expansion factor m_{exp} and can be interpreted as the expected false alarm rate of the monitor. All these aspects (computation and verification of theoretical noise variances as well as threshold computation) are addressed in the following sections.

7.5.1 Noise Variances for Selected Metrics

The theoretical noise influences can be computed by equation (145). The diagonal elements $\sigma_{m,i}^2$ of the matrix (143) are a by-product of the metric selection process and can be obtained during the computation of the metric correlations. Based on these computations, the theoretical noise variances for all test metrics listed in Table 7-10 - Table 7-12 can be expressed as follows:

	Elimination of High Correlations		Maximum Monitoring Sensitivity	
	Metric	Noise Variance	Metric	Noise Variance
OEM3 STANDARD	$M_{S1} = \frac{I_0}{I_{0.25}}$	$\sigma^2_{M_{S1}} = \frac{1.3355}{2SNR \cdot T}$	$M_{S1} = \frac{I_0}{I_{0.25}}$	$\sigma^2_{M_{S1}} = \frac{1.3355}{2SNR \cdot T}$
	$M_{S2} = \frac{I_{0.1} - I_{0.25}}{I_0}$	$\sigma^2_{M_{S2}} = \frac{0.2588}{2SNR \cdot T}$	$M_{S2} = \frac{I_0 - I_{0.25}}{I_0}$	$\sigma^2_{M_{S2}} = \frac{0.4316}{2SNR \cdot T}$
	$M_{S3} = \frac{I_0 - I_{0.1}}{I_{0.25}}$	$\sigma^2_{M_{S3}} = \frac{0.3998}{2SNR \cdot T}$	$M_{S3} = \frac{I_{-0.05} - I_{0.25}}{I_{0.25}}$	$\sigma^2_{M_{S3}} = \frac{1.4768}{2SNR \cdot T}$
	$M_{S4} = \frac{I_{0.075} - I_{0.1}}{I_{0.25}}$	$\sigma^2_{M_{S4}} = \frac{0.0413}{2SNR \cdot T}$	$M_{S4} = \frac{I_0 - I_{0.25}}{I_{0.25}}$	$\sigma^2_{M_{S4}} = \frac{1.3355}{2SNR \cdot T}$
OEM4 NARROW	$M_{N1} = \frac{I_{-0.025}}{I_{0.075}}$	$\sigma^2_{M_{N1}} = \frac{0.2323}{2SNR \cdot T}$	$M_{N1} = \frac{I_{-0.025}}{I_{0.075}}$	$\sigma^2_{M_{N1}} = \frac{0.2323}{2SNR \cdot T}$
	$M_{N2} = \frac{I_{0.025}}{I_{0.075}}$	$\sigma^2_{M_{N2}} = \frac{0.0976}{2SNR \cdot T}$	$M_{N2} = \frac{I_0}{I_{0.075}}$	$\sigma^2_{M_{N2}} = \frac{0.1739}{2SNR \cdot T}$
	$M_{N3} = \frac{I_{-0.075} - I_{0.025}}{I_{0.025}}$	$\sigma^2_{M_{N3}} = \frac{0.1835}{2SNR \cdot T}$	$M_{N3} = \frac{I_{0.025}}{I_{0.075}}$	$\sigma^2_{M_{N3}} = \frac{0.0976}{2SNR \cdot T}$
	$M_{N4} = \frac{I_{-0.025} - I_{0.025}}{I_{0.075}}$	$\sigma^2_{M_{N4}} = \frac{0.0880}{2SNR \cdot T}$	$M_{N4} = \frac{I_{0.075}}{I_{0.025}}$	$\sigma^2_{M_{N4}} = \frac{0.0771}{2SNR \cdot T}$
OEM4 ULTRANARROW	$M_{UN1} = \frac{I_{0.025}}{I_{0.1}}$	$\sigma^2_{M_{UN1}} = \frac{0.1902}{2SNR \cdot T}$	$M_{UN1} = \frac{I_{-0.025}}{I_{0.1}}$	$\sigma^2_{M_{UN1}} = \frac{0.3204}{2SNR \cdot T}$
	$M_{UN2} = \frac{I_{-0.1} - I_{0.075}}{I_{0.1}}$	$\sigma^2_{M_{UN2}} = \frac{0.4025}{2SNR \cdot T}$	$M_{UN2} = \frac{I_{0.025}}{I_{0.1}}$	$\sigma^2_{M_{UN2}} = \frac{0.1902}{2SNR \cdot T}$
	$M_{UN3} = \frac{I_{0.025} - I_{0.05}}{I_{0.1}}$	$\sigma^2_{M_{UN3}} = \frac{0.0306}{2SNR \cdot T}$	$M_{UN3} = \frac{I_{-0.025} - I_{0.1}}{I_{0.1}}$	$\sigma^2_{M_{UN3}} = \frac{0.3204}{2SNR \cdot T}$
	$M_{UN4} = \frac{I_{0.075} - I_{0.1}}{I_{0.1}}$	$\sigma^2_{M_{UN4}} = \frac{0.0291}{2SNR \cdot T}$	$M_{UN4} = \frac{I_{0.025} - I_{0.1}}{I_{0.1}}$	$\sigma^2_{M_{UN4}} = \frac{0.1902}{2SNR \cdot T}$

Table 7-13: Theoretical noise variances for the selected test metrics.

7.5.2 Verification of Derived Noise Variances

This section provides the results of the verification of the derived noise variances by means of data obtained from the GPS hardware simulator. Since the theoretical noise variances are a function of the C/N_0, they will vary with the changing elevation angle during the observation period. In order to avoid this behavior and allow instant comparison between the theoretical noise variances and the variances observed in real data, multi-correlator data has been obtained from the GPS hardware simulator assuming an omni-directional antenna gain pattern. This measure eliminates C/N_0 variations caused by antenna gain variations during the observation period and results in C/N_0 observations more or less independent from the elevation angle. From the obtained time series of test metrics, the standard deviations can be derived empirically. They are then compared to their theoretical values as computed by the equations listed in Table 7-13.

Figure 7-8 illustrates an example of this verification process using metric M_{184} (derived from observations of the OEM4 ULTRANARROW configuration). In this case, multi-correlator data was being collected during an entire pass of PRN5 and PRN15. The C/N_0 was ~44dB-Hz in both cases. The theoretical standard deviations are plotted as white solid lines and the actual standard deviations (derived numerically from the time series) are plotted as red dashed lines. Both time series show a sufficient good match between the theoretical and the empirically derived standard deviations.

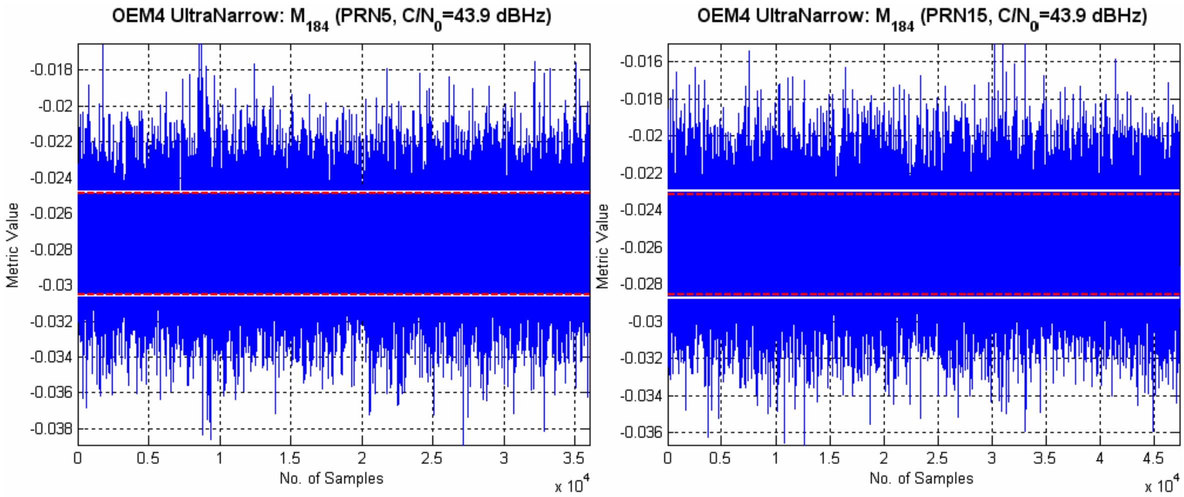

Figure 7-8: Comparison of theoretical and numerically derived standard deviations for M$_{184}$ (OEM4 ULTRANARROW) for PRN5 and PRN15. The deviations from the observed standard deviations are 3.6% for PRN5 and 7.4% for PRN15, respectively.

This verification process was carried out for all relevant test metrics, again by using data from PRN5 and PRN15 and with consideration of high and low values of C/N$_0$. The results of the verification process are summarized in the following table:

	PRN 5						PRN 15					
	C/N$_0$~48dB-Hz			C/N$_0$=~40 dB-Hz			C/N$_0$~48 dB-Hz			C/N$_0$~40 dB-Hz		
	σ_{th}	σ_{obs}	Δ [%]	σ_{th}	σ_{obs}	Δ [%]	σ_{th}	σ_{obs}	Δ [%]	σ_{th}	σ_{obs}	Δ [%]
OEM3 STANDARD												
M$_{67}$	0.0033	0.0032	3.1	0.0080	0.0081	1.2	0.0034	0.0031	9.7	0.0080	0.0075	6.7
M$_{126}$	0.0019	0.0018	5.6	0.0046	0.0046	0.0	0.0019	0.0018	5.6	0.0046	0.0045	2.2
M$_{132}$	0.0015	0.0014	7.1	0.0035	0.0036	2.8	0.0015	0.0014	7.1	0.0035	0.0035	0.0
M$_{258}$	0.0035	0.0034	2.9	0.0084	0.0085	1.2	0.0036	0.0033	9.1	0.0085	0.0080	6.3
M$_{279}$	0.0018	0.0017	5.9	0.0044	0.0045	2.2	0.0019	0.0017	11.8	0.0044	0.0042	4.8
M$_{286}$	0.0033	0.0032	3.1	0.0080	0.0081	1.2	0.0034	0.0031	9.7	0.0080	0.0075	6.7
M$_{314}$	0.0006	0.0007	14.3	0.0014	0.0020	30.0	0.0006	0.0007	14.3	0.0014	0.0019	26.3
	C/N$_0$~44dB-Hz			C/N$_0$=~34 dB-Hz			C/N$_0$~44 dB-Hz			C/N$_0$~34 dB-Hz		
OEM4 NARROW												
M$_{16}$	0.0021	0.0021	0.0	0.0057	0.0059	3.4	0.0021	0.0020	5.0	0.0057	0.0056	1.8
M$_{18}$	0.0018	0.0019	5.3	0.0050	0.0050	0.0	0.0018	0.0017	5.9	0.0049	0.0048	2.1
M$_{19}$	0.0014	0.0014	0.0	0.0037	0.0039	5.1	0.0014	0.0013	7.7	0.0037	0.0037	0.0
M$_{27}$	0.0012	0.0012	0.0	0.0033	0.0035	5.7	0.0012	0.0012	0.0	0.0033	0.0033	0.0
M$_{52}$	0.0019	0.0019	0.0	0.0051	0.0053	3.8	0.0019	0.0018	5.6	0.0051	0.0051	0.0
M$_{65}$	0.0013	0.0013	0.0	0.0035	0.0038	7.9	0.0013	0.0013	0.0	0.0035	0.0036	2.8
OEM4 ULTRANARROW												
M$_{102}$	0.0025	0.0025	0.0	0.0068	0.0066	3.0	0.0025	0.0024	4.2	0.0068	0.0064	6.2
M$_{105}$	0.0020	0.0019	5.3	0.0052	0.0052	0.0	0.0020	0.0018	11.1	0.0052	0.0050	4.0
M$_{184}$	0.0029	0.0028	3.6	0.0076	0.0072	5.6	0.0029	0.0027	7.4	0.0076	0.0071	7.0
M$_{312}$	0.0025	0.0025	0.0	0.0068	0.0066	3.0	0.0025	0.0024	4.2	0.0068	0.0064	6.2
M$_{320}$	0.0008	0.0010	20.0	0.0021	0.0028	25.0	0.0008	0.0010	20.0	0.0021	0.0027	22.2
M$_{336}$	0.0020	0.0019	5.3	0.0052	0.0052	0.0	0.0020	0.0018	11.1	0.0052	0.0050	4.0
M$_{360}$	0.0008	0.0010	20.0	0.0020	0.0028	28.6	0.0008	0.0010	20.0	0.0020	0.0027	25.9

Table 7-14: Summary of the noise variance verification process.

In addition to the pure listing of theoretical and observed standard deviations (σ_{th} and σ_{obs}), the deviation Δ [%] of the theoretical standard deviation from its observed counterpart has also been computed. The largest difference between the theoretical standard deviation and its empirical counterpart obtained by observations from the GPS hardware simulator is 30%. However, the majority of the deviations are below 10%. They are most probably due to the non-consideration of the actual PRN code and the type of band pass filter when computing the theoretical noise variances. Generally speaking, larger differences occur when incorporating correlators whose actual locations do not perfectly match with those of the modeled correlation function. Nevertheless, the match between the theoretical and observed noise variances for the majority of the test metrics is sufficient enough to serve as a basis for the computation of monitor thresholds. Suggestions for minimizing the occurring deviations are given in section 7.10.

7.5.3 Monitor Thresholds

At the beginning of this chapter, it has been proposed to compute the monitor threshold for each test metric as a multiple of the theoretical metric noise $(m_{exp}\sigma)$. If the current metric value exceeds this threshold, it is assumed that the metric is not only affected by noise but also by multipath. Due to the statistical nature of the observations, it is possible that even in the absence of multipath the metric values exceed the selected monitor threshold from time to time. The probability of such events depends on the selected expansion factor m_{exp} and can be interpreted as the expected false alarm rate of the monitor. In the following, the expected false alarm rate shall be computed for a given expansion factor m_{exp}. In order to carry out the required statistical computations, it is essential to know the nature of the underlying distribution.

The assumption is that the metric values follow a normal distribution. This can be verified by carrying out various tests. The main prerequisite for successful testing is the consideration of a sufficient large number of metric values (appropriate sample size). On the other hand, the time series must not show the influence of varying C/N_0 values because this would lead to wrong empirical values for the time series' standard deviations. This criterion restricts the considered number of metric values. The following tests base on a sample size of approximately 1000 metric observations:

1. Computation of the histogram function and computation of the corresponding density function. In case that the underlying distribution is really normal, the histogram and the density function will match.

2. The second test is the computation of the cumulative distribution function, which is scaled in such a way that if the underlying distribution is normal, the resulting function follows a linear trend. For this test, the MATLAB function `normplot` is used.

3. Computation of the Lilliefors hypothesis test for the goodness of fit to a normal distribution. For this test the MATLAB function `lillietest` is used. It performs the test on the time series of metric values and returns "1" if the hypothesis that the metric values show a normal distribution can be rejected, or "0" if the hypothesis cannot be rejected (at 5% significance level). The test compares the empirical distribution of the metric values with a normal distribution having the same mean and variance.

All three tests are carried out exemplarily for two time series of metric values. Other time series based on other metrics or PRNs would show the same general behavior. The results of test No. 1 and 2 are illustrated in the following diagrams.

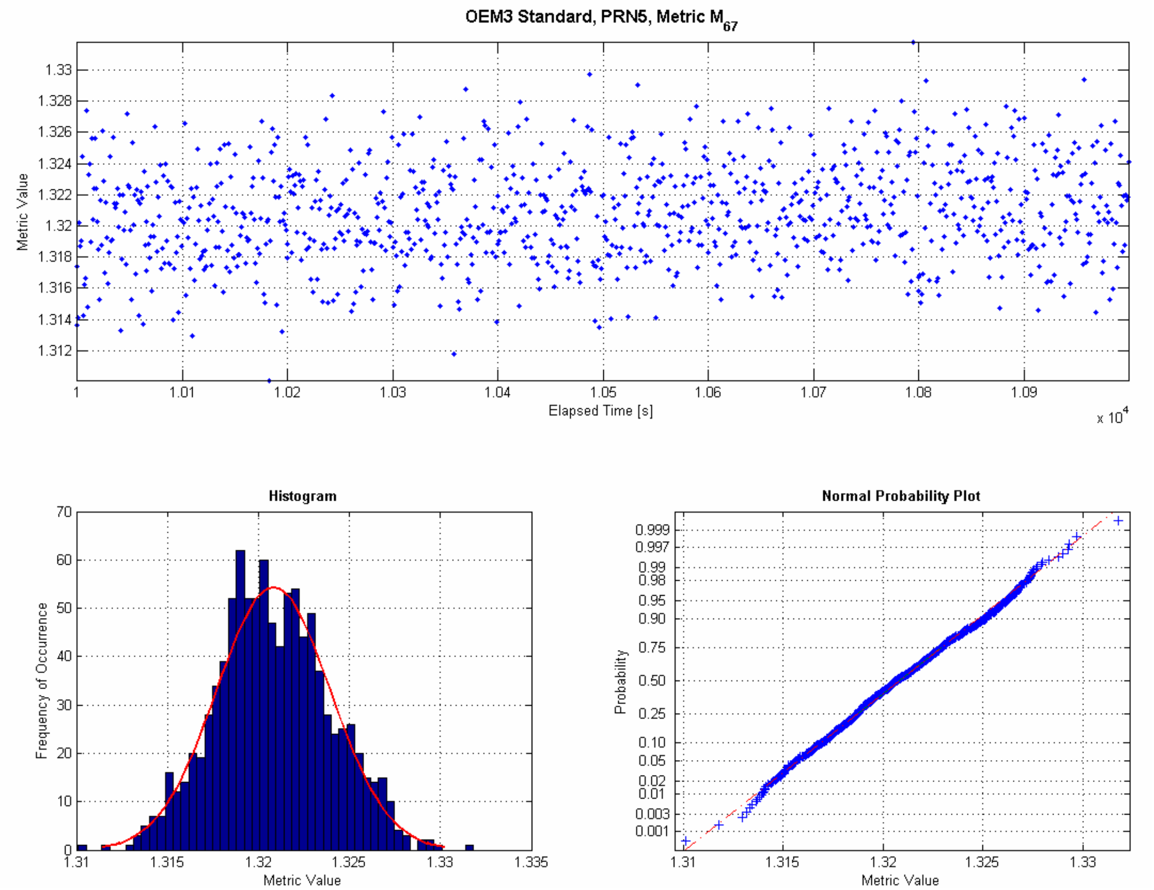

Figure 7-9: Verification of a normal distribution for OEM3 metric M_{67} (PRN5).

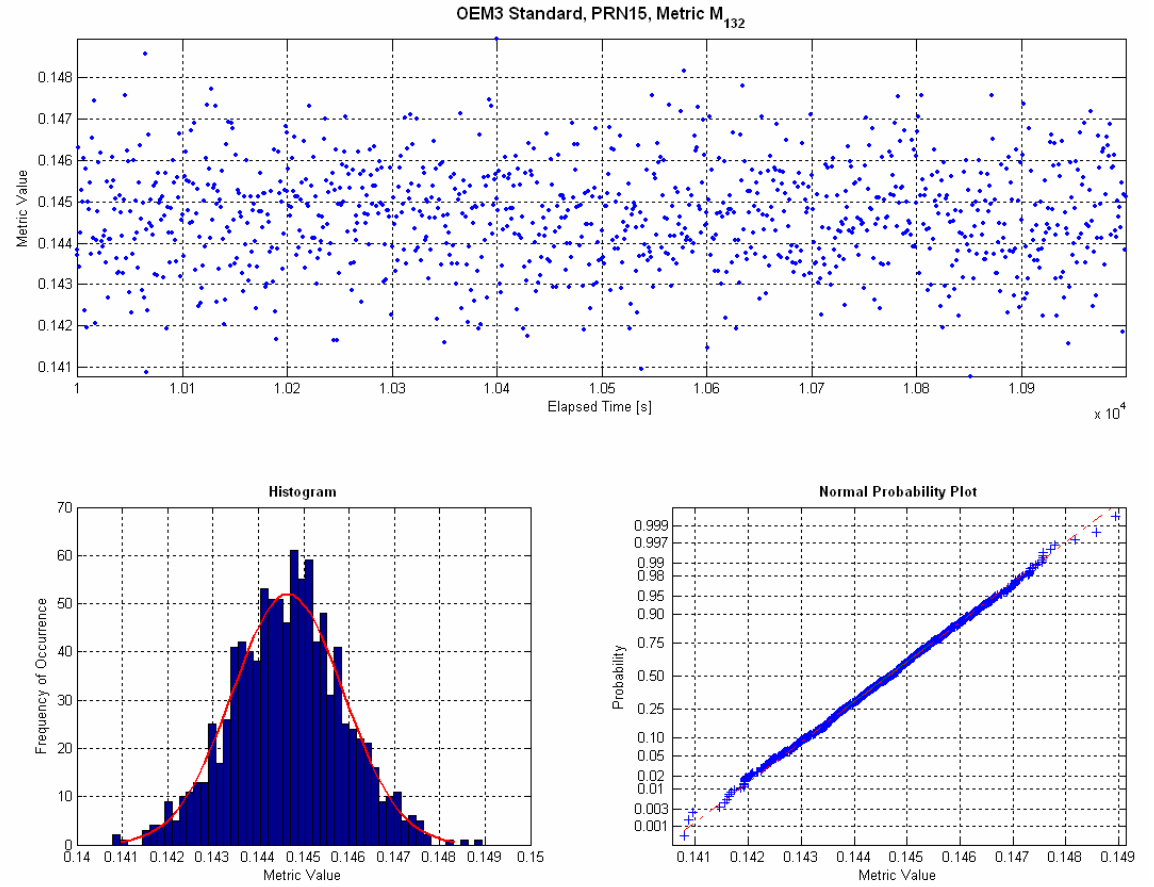

Figure 7-10: Verification of a normal distribution for OEM3 metric M_{132} (PRN15).

In both cases, the results of the first two tests indicate that the metric values are normally distributed (match between the red density function and the histogram and linear behavior of the scaled cumulative distribution function). The Lilliefors test also indicates that the underlying distribution is normal (h=0 in both cases).

Based on the fact that the metric values are normally distributed, the false alarm rate can be simply considered as the probability P that one single metric value m_i exceeds a multiple m_{exp} of its theoretical standard deviation σ (recall that $m^* \pm \sigma m_{exp}$ serves as the monitor threshold). These probabilities can be easily determined from suitable tables describing the normal distribution. Figure 7-11 exemplarily illustrates the computation of false alarm rates for two different expansion factors (m_{exp}=1 and m_{exp}=2). For this purpose, a normal distribution with a mean value of zero and unity standard deviation has been considered. The required false alarm rate is simply the area beneath the probability density function which is located outside of the blue area.

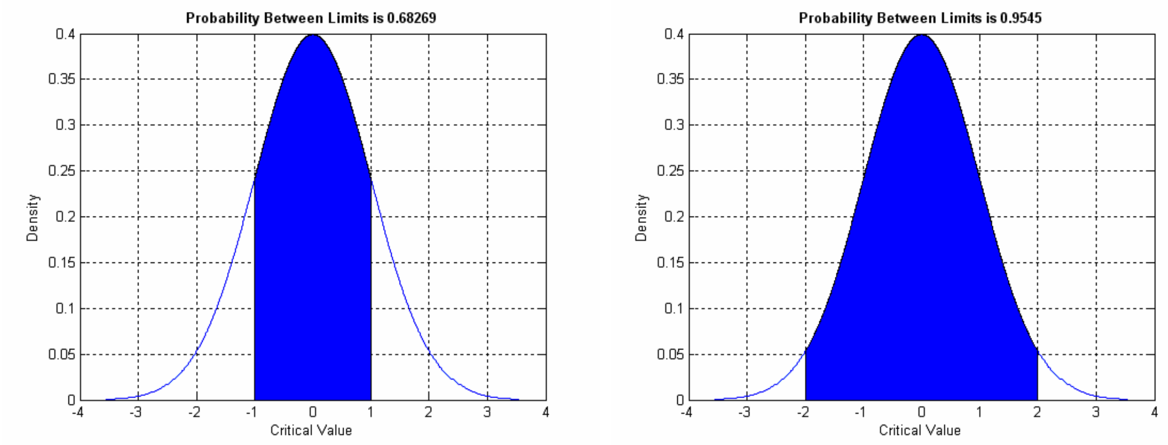

$$P(|m_i| > \sigma) = 1 - 0.6827 = 0.3173 \qquad P(|m_i| > 2\sigma) = 1 - 0.9545 = 0.0455$$

Figure 7-11: Computation of false alarm rates as the probability that a metric value exceeds a certain level.

The following table lists the expected false alarm rates for different expansion factors (m_{exp}=1…6). It also lists the theoretical amount of observations between two successive false alarm events (rounded to the nearest integer).

Expansion Factor m_{exp}	1	2	3	4	5	6
Monitor Threshold	$m^* \pm \sigma$	$m^* \pm 2\sigma$	$m^* \pm 3\sigma$	$m^* \pm 4\sigma$	$m^* \pm 5\sigma$	$m^* \pm 6\sigma$
False Alarm Rate	0.3173	0.0455	0.0027	6.33E-5	5.73E-7	1.97E-9
False Alarm every nth obs.	3	22	370	15.787	1.744.278	506.797.317

Table 7-15: Probabilities of false alarm for different monitor thresholds.

With respect to the selection of a suitable monitor threshold for multipath monitoring, a trade-off between a low false alarm rate and the ability to detect relatively weak multipath signals has to be made. For the realization of low false alarm rates, the monitor threshold must be relatively large which might prevent weak multipath signals from being detected by the monitor. On the other hand, if the multipath sensitivity of the monitor is to be increased, the thresholds have to be decreased which in turn increases the probability of false alarm. A reasonable compromise seems to be an expansion factor of 5, offering the chance to detect weak multipath signals at a low false alarm rate of 5.73E-7. This value serves as a default value for the monitoring software. However, the user can adjust the monitor threshold by either setting the expansion factor or by providing a dedicated value for the false alarm rate.

7.6 The Real Time Multipath Monitor (RTMM)

The monitoring approach described in the previous sections has been implemented in the form of a Matlab-based graphical user interface called “Real Time Multipath Monitor” (RTMM). The current version of RTMM is capable of reading NovAtel receiver data (some dedicated logs) for up to 12 channels via the serial port if a suitable multi-correlator receiver is connected to the PC (real-time mode). As an alternative, the required logs can be recorded and stored separately and then be provided as ASCII files after the observation session (post processing mode). A screenshot of the RTMM software is illustrated in Figure 7-12.

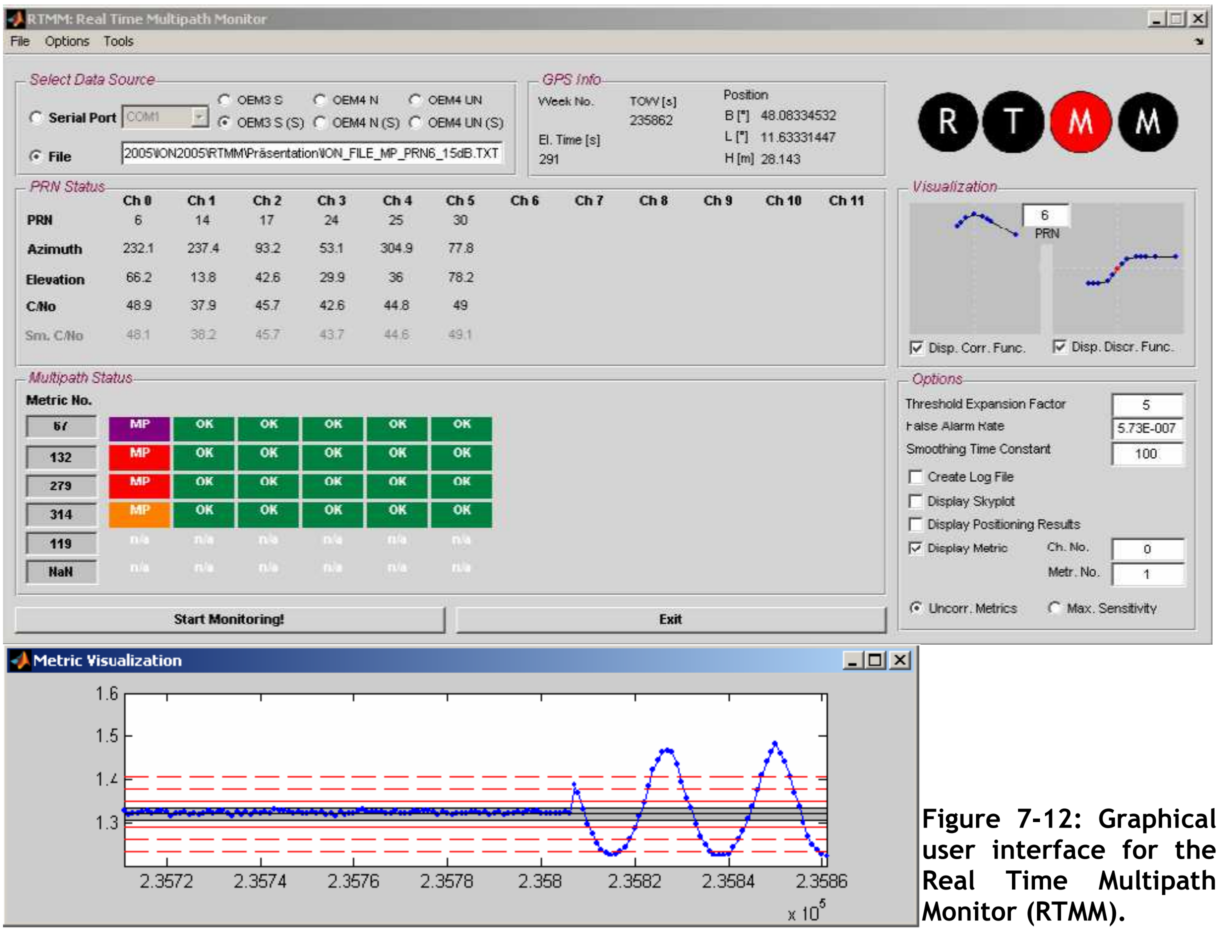

Select Data Source

○ Serial Port COM1 ○ OEM3 S ○ OEM4 N ○ OEM4 UN
● OEM3 S (S) ○ OEM4 N (S) ○ OEM4 UN (S)
● File 2005\ION2005\RTMM\Präsentation\ION_FILE_MP_PRN6_15dB.TXT

GPS Info

Week No.
TOW [s] 235862
El. Time [s] 291
Position
B [°] 48.08334532
L [°] 11.63331447
H [m] 28.143

PRN Status

	Ch 0	Ch 1	Ch 2	Ch 3	Ch 4	Ch 5	Ch 6	Ch 7	Ch 8	Ch 9	Ch 10	Ch 11
PRN	6	14	17	24	25	30						
Azimuth	232.1	237.4	93.2	53.1	304.9	77.8						
Elevation	66.2	13.8	42.6	29.9	36	78.2						
C/No	48.9	37.9	45.7	42.6	44.8	49						
Sm. C/No	48.1	38.2	45.7	43.7	44.6	49.1						

Multipath Status

Metric No.						
67	MP	OK	OK	OK	OK	OK
132	MP	OK	OK	OK	OK	OK
279	MP	OK	OK	OK	OK	OK
314	MP	OK	OK	OK	OK	OK
119	n/a	n/a	n/a	n/a	n/a	n/a
NaN	n/a	n/a	n/a	n/a	n/a	n/a

Visualization: PRN 6
☑ Disp. Corr. Func. ☑ Disp. Discr. Func.

Options

Threshold Expansion Factor: 5
False Alarm Rate: 5.73E-007
Smoothing Time Constant: 100
☐ Create Log File
☐ Display Skyplot
☐ Display Positioning Results
☑ Display Metric Ch. No. 0 Metr. No. 1
● Uncorr. Metrics ○ Max. Sensitivity

Figure 7-12: Graphical user interface for the Real Time Multipath Monitor (RTMM).

Based on the correlation peak observations and the C/N$_0$ data provided by the receiver, the software constantly computes the metric values and their theoretical noise variances for every epoch and any visible satellite. Based on the long-term mean values that have to be determined in advance during a calibration campaign, the monitor thresholds are computed and constantly compared to the current metric value. The result is illustrated in the software’s “Multipath Status” panel. Test metric values that do not exceed the monitor thresholds indicate that the signal is only affected by thermal noise; they are marked with a green rectangle. If the metric value exceeds its corresponding threshold, the color of the rectangle changes indicating the presence of a multipath signal. This allows instant knowledge whether or not a dedicated satellite signal is affected by multipath. The following table provides a brief description of the software’s most important features.

Panel Name	Description
Select Data Source	The RTMM software can process five types of OEM3 data logs (POSA, containing data of the latest position solution, SATA, containing satellite specific data like azimuth and elevation, RGEA, containing the raw data, CORA, containing the multi-correlator observations and SVDA, containing the XYZ-coordinates of each satellite in view) and the corresponding OEM4 data logs. The data can either originate from a text file containing recorded logs (post processing mode) or from real time data provided through the serial port. In either case, the data is provided in the same data format, so that RTMM makes no difference between the two data streams with respect to its internal processing algorithms. Furthermore, the user has to specify the correlator configuration (OEM3 STANDARD, OEM4 NARROW/ULTRANARROW, connected to the GPS simulator (S) or to an antenna). By doing so, RTMM loads mean values and noise variance information of the most suitable test metrics according to the selected configuration.
PRN Status	This panel provides an overview of the visible satellites and their assignment to the 12 available channels. The satellite specific data consists of PRN number, azimuth and elevation angle and the current C/N_0 of each signal. In addition, the smoothed C/N_0 which is used to determine the monitor threshold is also listed. If the channel assignment changes – mainly due to rising or setting satellites – the smoothed C/N_0 is written in red for the next *T* seconds (with *T* indicating the smoothing time constant that can be adjusted in the "Options" panel). After this initialization period, during which the smoothed C/N_0 can vary significantly due to multipath influences, the color for the smoothed C/N_0 turns to grey. The need for smoothing the C/N_0 values will be discussed in more detail in section 7.9.
Multipath Status	This panel indicates the signal health states for all available signals as indicated by the different linear test metrics. Test metric values within the monitor thresholds indicate that the signal is only affected by thermal noise; they are marked with a green rectangle. If the metric value exceeds the monitor thresholds, the color of the rectangle turns to orange, red or purple depending on how distant the current metric value is from its nominal mean value. In this case, the signal is assumed to be affected by multipath. "*n/a*" indicates that metric values are not available. It should be noted that this monitor approach is also suitable for detecting satellite signal failures. However, RTMM cannot distinguish instantly between multipath signals and other types of Evil Waveforms. Since the occurrence of these Evil Waveforms is assumed to be a rather rare event, all alarms are assumed to origin mostly from multipath signals.
GPS Info	If available, the current position derived from the POSA logs (OEM3) or from the corresponding OEM4 logs are listed in this panel. In addition, the current GPS time (GPS week and TOW, expressed in [s]) and the elapsed time (EL) (time since the "Start Monitoring!"-Button has been pushed) are listed.

Table 7-16: RTMM monitoring options and functionalities (Table 1).

Panel Name	Description
Visualization	This panel contains two diagrams that visualize the correlation function and the corresponding discriminator function. The computation of the correlation function simply bases on the current correlation peak observations provided by the receiver; the discriminator function is computed mathematically (early minus late, chip spacing d=0.1). Both functions are displayed for the PRN number appearing in the editor field between both diagrams (provided that the check boxes are activated).
Options	This panel allows the setting of some processing and visualization options: • Threshold expansion factor or false alarm rate: The threshold expansion factor is the factor by which the theoretical noise variances are to be multiplied to set up the monitor threshold. This factor can be directly related to the false alarm rate of the monitor that can be defined via the second editor field in this panel. Expansion factors are automatically converted to the corresponding false alarm rate and vice versa. Default value for the expansion factor is 5. • Smoothing time constant for the computation of smoothed C/N_0 values. Smoothing of C/N_0s is necessary because they are affected by periodic changes if multipath signals are present. Since they are used to compute the monitor thresholds, the smoothing process reduces periodic changes of the C/N_0s and the derived monitor thresholds. Default value for the smoothing constant is 100s. • Create log file: If enabled, a log file is created containing information about when and by which metric a multipath signal has been detected. • A skyplot can be displayed (refreshes every 20s). • Display positioning results: If enabled, the results of three positioning solutions will be displayed during the monitoring process. The first positioning approach uses all visible satellites, the second one excludes multipath-affected signals from the positioning solution and the third one applies a suitable weighting scheme to the observations (all satellites are used, but the observations are weighted). This allows instant comparison of the positioning performance with and without the presence of multipath signals. • Display metric values: Graphical illustration of metric values and monitor thresholds as a function of time (requires provision of metric and channel number). • Selection of metric types: Two sets of metrics are available. The first set consists of metrics that are not fully correlated ($\rho<=0.8$), the metrics of the second set are highly or fully correlated ($\rho>0.8$) but in general more sensitive to multipath than the first set.

Table 7-17: RTMM monitoring options and functionalities (Table 2).

7.7 Performance Analysis

In order to demonstrate the effectiveness of the proposed monitoring scheme, several simulations were carried out using the GPS hardware simulator. The use of a simulator allows controlled access over a variety of parameters and offers various capabilities:

- Definition of number of occurring multipath signals
- Adjustment of power of multipath signals relative to LOS component
- Assignment of multipath signal to dedicated satellites
- Definition of distance between antenna and reflector
- Definition of antenna patterns
- Simulation of static or dynamic receivers
- Direct signal component can be switched off (simulation of shadowing effects)

Basically, the STR4760 allows the simulation of two types of multipath signals:

- "Fixed-offset multipath" (constant multipath relative phase): This type of multipath is a rather rare event and normally occurs only in case that transmitter, reflector and receiver are static (e.g. when pseudolites are used). This type of multipath also allows the simulation of satellite signal failures ([JAKAB 1999]) and is defined by the geometric path delay and the multipath relative power.
- Ground multipath can be simulated by "placing" the antenna at a distinct height above the reflecting surface and by defining the relative power of the multipath signal (see Figure 3-11 for an illustration of the geometrical situation). By means of this approach, dedicated multipath delays can be realized by adjusting the antenna height.

It is also possible to construct complex multipath environments by defining the location and characteristics of reflecting surfaces and regions of partial or complete obstruction. However, these models have not been used for the verification of the monitoring scheme. Most of the following analyses base on the ground multipath model. The required mean metric values for each satellite have been determined in advance by recording undistorted multi-correlator observations during entire satellite passes.

7.7.1 Verification of Derived Mean Values

As a first step, the mean metric values derived from the long-term multipath-free multi-correlator observations are to be verified. It is also to be shown that the proposed scheme for the computation of the monitor thresholds (that are derived from the current C/N_0's) is a valid approach. For this purpose, multipath-free metric values were observed during a certain period of time. Figure 7-13 exemplarily illustrates OEM3 metric M_{67} for PRN5 as a function of time. The predicted mean metric value is plotted as a solid black line; the thresholds are indicated by the solid red lines. The observed metric values are always located around the predicted mean metric value and stay within the monitor thresholds.

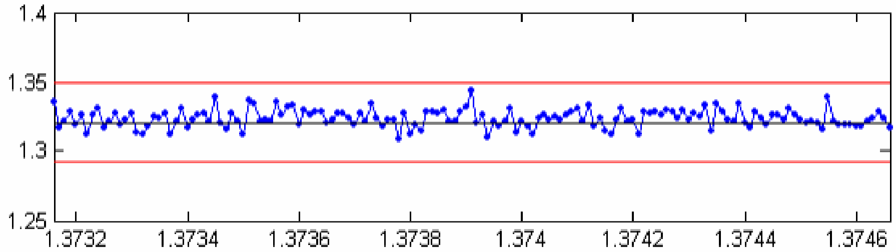

Figure 7-13: Verification of mean metric value and derived monitor thresholds for metric M_{67}.

It can be expected that multipath with path delays larger than approximately 1 chip does not significantly affect the test metrics (see e.g. Figure 7-4). Thus, even in the presence of strong long-delay multipath, the metric values should not show any periodic variations, follow the predicted mean value and stay within the monitor thresholds. In order to verify this behavior, a strong multipath signal (0dB, equal signal power than direct component) with a path delay of 391m has been simulated. The corresponding time-series of metric values is illustrated in Figure 7-14 (OEM3, M_{67}). Despite the presence of a strong multipath signal, no periodic variations are visible. Moreover, the observed metric values are well within the derived monitor thresholds.

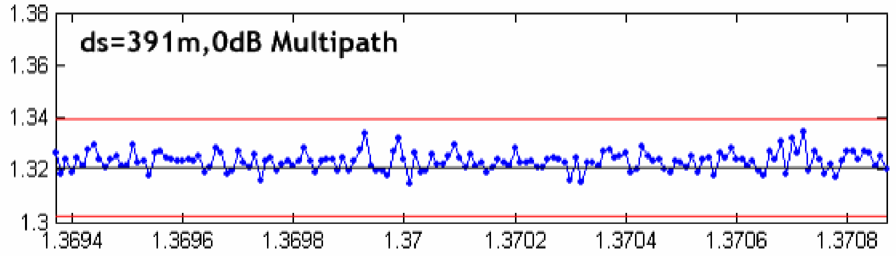

Figure 7-14: Effect of strong long-delay multipath on M_{67}.

7.7.2 Detection of Fixed-Offset Multipath

Fixed-offset multipath is characterized by a constant, non-varying multipath relative phase, i.e. the relative phase between the direct signal component and the multipath signal does not undergo periodic variations. Due to this behavior, the selected test metrics will not show such variations either. Instead of showing a periodic behavior, fixed-offset multipath is expected to produce a more or less constant offset with respect to the nominal mean metric value. This offset depends on the multipath relative power and the exact (constant) multipath relative phase.

Figure 7-15 illustrates the resulting metric values as a function of time for slightly different multipath delays *ds*. Although these path delay differences are rather small, the resulting relative phases can significantly differ (a path delay difference of 0.095m corresponds to a 180° phase shift at L1). Depending on the combination of multipath relative power and geometric path delay, it is possible that the resulting metric values do not exceed the monitor thresholds and thus remain undetected. However, as long as the metric values remain within the thresholds, it can be assumed that the negative impact on pseudorange determination and positioning performance is not severe (this statement only holds true if a compound signal is processed by the receiver; a discussion of the ability of the monitor to detect multipath signals without the presence of the LOS component is given in the following section). In order to verify this statement, residual ranging errors due to undetected multipath influences will be presented in section 7.7.7.

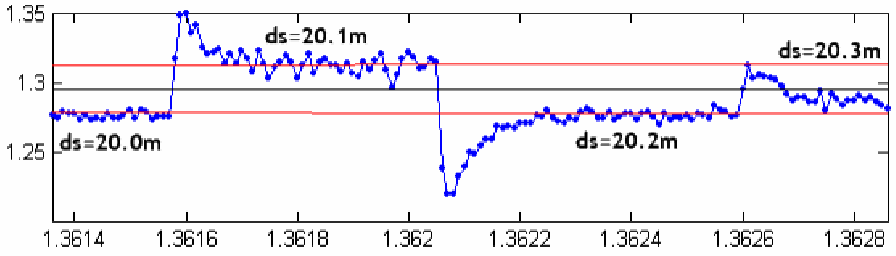

Figure 7-15: Influence of fixed-offset multipath on OEM3 metric M_{67}.

7.7.3 Absence of Direct Signal Component

Especially in urban environments, partial or complete signal obstruction has to be expected from time to time. Even in case that the LOS component is completely obstructed, the user may receive one or several multipath components. Depending on the signal power of the multipath components, these propagation conditions can have the following effects on signal tracking and multipath monitoring performance:

- The multipath signal(s) is/are relatively weak, so that they cannot be acquired and processed by the receiver. In this case, no negative impact on pseudorange determination and positioning performance has to be expected. Multipath monitoring is not affected either, as there are simply no multi-correlator observations the monitor could process in such cases.
- The multipath signal(s) is/are strong enough for being acquired by the receiver or to "force" the tracking loops to maintain lock even if the direct signal component gets lost. In this case, the multipath signal(s) is/are treated as a "normal" signal and tracked accordingly. In case that there is only one single multipath signal, there will be no periodic signal variations, because there is no varying multipath relative phase that could cause such variations. Therefore, it has to be expected that such multipath influences (one single multipath signal without LOS component) cannot be detected by means of the proposed monitoring scheme. This may result in large pseudorange errors.

Figure 7-16 illustrates the influence of one single multipath signal without the presence of the direct signal component.

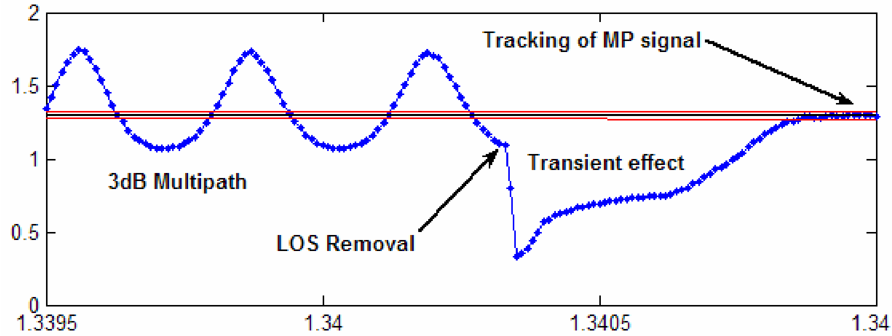

Figure 7-16: Influence of multipath without the presence of the LOS component.

At the beginning of the simulation, a strong multipath signal (-3dB with respect to the LOS component) was simulated and added to the direct signal. As expected, this results in distinct variations of the metric value that clearly exceed the monitor thresholds and allow easy detection by means of the proposed monitoring approach. At a distinct point in time (indicated by "LOS Removal" in Figure 7-16), the direct signal component was removed from the simulation so that the receiver kept on tracking the multipath signal only. After a certain period of time (indicated by "Transient Effect" in Figure 7-16), the metric values "returned" to their nominal values within the monitor thresholds without showing any periodic variations. This simulation confirms the assumption that one single multipath signal cannot be detected without the presence of the LOS signal. This is the major limitation of the proposed monitoring scheme. Further but minor limitations are discussed in section 7.9.

This behavior is expected to be limited to the case where there is only one multipath signal without LOS component. In case that there is more than one multipath component, the relative phases between these components should cause the metric values to show periodic variations again. If this compound signal is strong enough, it should be detectable by the multipath monitor. Unfortunately, this case could not be simulated with the GPS hardware simulator under controlled conditions.

7.7.4 Monitoring Sensitivity

For the determination of the monitoring sensitivity, one single ground multipath signal with different relative power levels was simulated. The antenna height was adjusted such that – depending on the satellite elevation – dedicated geometric path delays could be realized. In order to obtain results that are also valid for multipath signals with positive elevation angles, an antenna phase pattern that is symmetrical with respect to the local horizontal plane was assumed. It should be noted that due to the nature of the ground multipath model, the multipath signals are assumed to have the same elevation angle as the line-of-sight (LOS) component (see Figure 3-11). In order to determine the sensitivity of the multipath monitor, the relative signal power of the multipath signal was decreased bit by bit until the monitor was unable to detect the multipath influence (monitor threshold m*±5σ in all cases, see Figure 7-17).

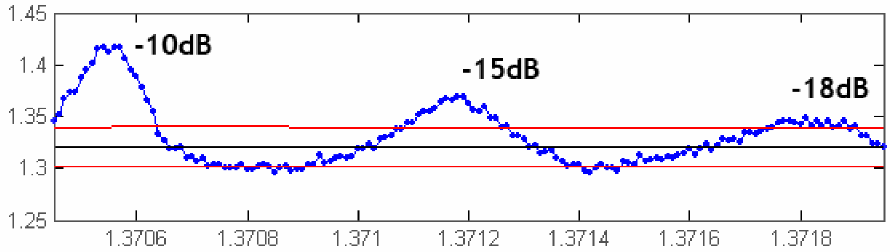

Figure 7-17: Determination of minimum multipath relative signal power required to be detected by the monitor. A geometric path of ds=25m has been simulated in this case.

The monitoring sensitivity strongly depends on the geometric path delay and the multipath relative power. In order to account for these variables, the procedure mentioned above was carried out for different geometric path delays and different C/N$_0$'s for the direct signal component (48dBHz and 40dBHz, representing elevation angles of about 45° and 20° in this case).

7.7.4.1 Monitoring Sensitivity for OEM3 and OEM4 Configurations

The monitoring sensitivity was determined for the correlator configurations OEM3 Standard and OEM4 Narrow and UltraNarrow. The results for the OEM3 Standard configuration are summarized in Figure 7-18, the results for the other two configurations are illustrated in Figure 7-19 and Figure 7-20, respectively.

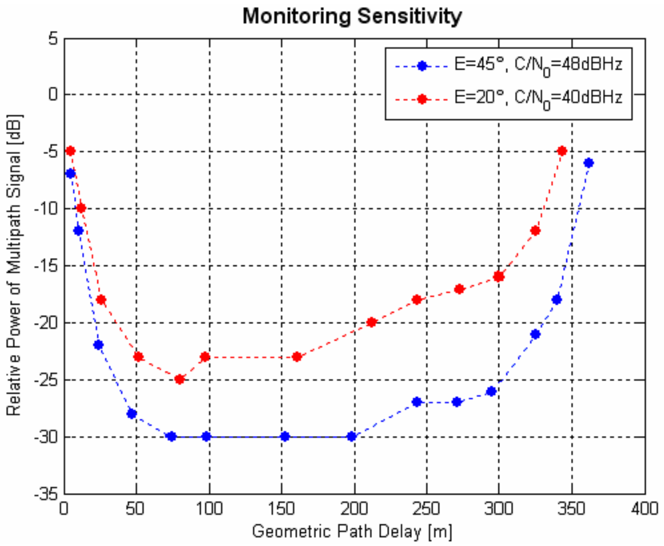

Figure 7-18: Sensitivity of the multipath monitor as a function of the geometric path delay and the direct signal's mean C/N$_0$ (valid for OEM3 metric M$_{67}$).

Between path delays of ~50m and ~300m, the performance of this monitoring implementation is much better than for small and very long path delays (the sensitivity decreases for smaller geometric path delays as well as for path delays in the order of one code chip). Due to the varying influence of thermal noise, the monitor is more sensitive to weak multipath signals at high C/N_0 than at lower signal power levels. At high C/N_0s it is possible to detect multipath signals which are ~30dB weaker than the LOS component.

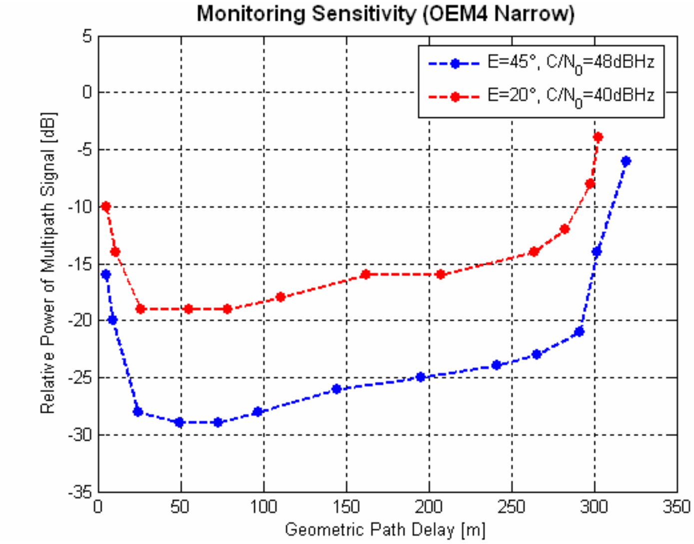

Figure 7-19: Sensitivity of the multipath monitor as a function of the geometric path delay and the direct signal's mean C/N_0 (valid for OEM4 NARROW metric M_{16}).

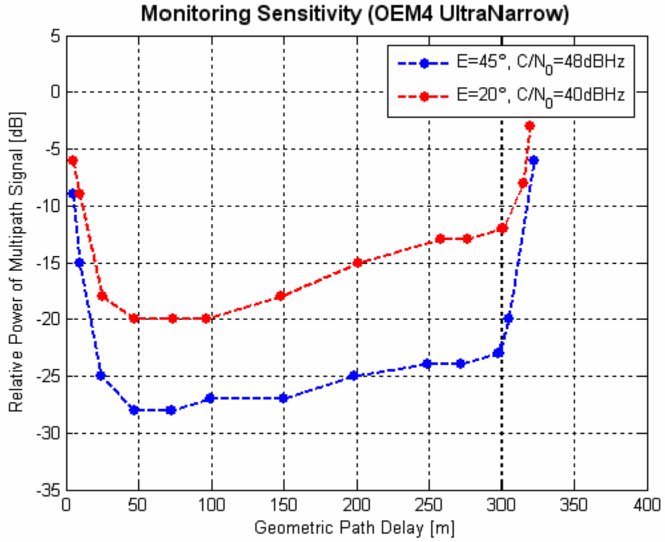

Figure 7-20: Sensitivity of the multipath monitor as a function of the geometric path delay and the direct signal's mean C/N_0 (valid for OEM4 ULTRANARROW metric M_{105}).

With respect to the maximum monitoring sensitivity, the OEM3 configuration outperforms the two OEM4 configurations. Multipath signals with relative power levels of down to -30dB can be detected - at least in the presence of a sufficient strong LOS component and in case of geometric path delays between 50m and 250m. Weak multipath signals of about -30dB relative to the LOS component can also be detected by the OEM4 NARROW configuration but only in case of path delays of about 50m-75m. However, both OEM4 configurations slightly outperform the OEM3 configuration in case of the presence of short-delay multipath (see e.g. the monitoring sensitivity at path delays of 10 or 25m). Note that in contrast to the OEM4 configurations, the OEM3 configuration is able to detect long-delay multipath with path delays of around 350m. This is due to the use of the correlator position $\tau=+0.25$ when setting up the metric M_{67}; this correlator is relatively far away from the correlation peak.

7.7.4.2 Further Sensitivity Enhancements

Although the monitoring sensitivity of all considered correlator configurations is quite impressive there is potential for further enhancement by smoothing or averaging over *N* successive I-Samples or metric values (after the metric formation process). The averaging process increases the effective *T* in equation (145), thereby reducing the influence of thermal noise and results in lower monitor thresholds and increased monitoring sensitivity. However, a major drawback of this measure is that monitoring results are available at a data rate which is by a factor of *N* lower than the original data rate.

Figure 7-21 illustrates an example of such an averaging process. In this case, multi-correlator data was obtained from the GPS hardware simulator assuming an omni-directional antenna pattern. This results in noise levels more or less constant during the entire satellite pass. The green time series is the result of averaging 5 original metric values. Since the original data output interval was 1s and the I-Samples are integrated during *T*=1s within the receiver, averaging over 5 metric values leads to an effective *T* of 5s. According to equation (145), the theoretical noise variance can be reduced by a factor of 5. Correspondingly, the standard deviation should decrease by a factor of sqrt(5)≈2.24. The actual standard deviations of the time series illustrated in Figure 7-21 are 0.001995 and 0.000907, respectively. This results in a ratio of ~2.20 between both empirically derived standard deviations and consequently confirms the theoretical prediction.

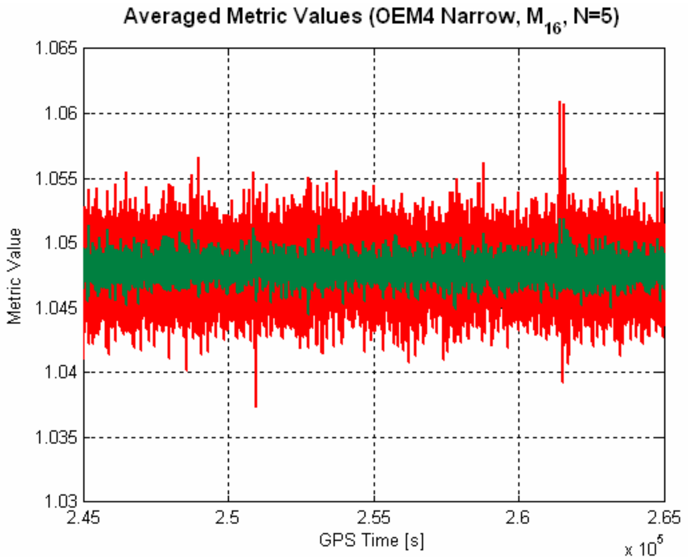

Figure 7-21: Reduction of the influence of thermal noise by averaging 5 successive metric values of M_{16} (OEM4 NARROW).

The increased monitoring sensitivity that can be achieved by this approach has to be traded off with the issue that the monitoring information is available at a lower data rate. In the case illustrated in Figure 7-21, the data rate would reduce from 1Hz to 0.2Hz.

7.7.4.3 Interrelation between Thresholds and Monitoring Sensitivity

In section 7.5, the computation of the monitor threshold based on the observation of the current C/N_0 (from which the theoretical noise influence on the implemented test metrics can be derived) has been introduced. Based on the calibrated mean metric values m^*, the monitoring thresholds are computed by multiplying the current theoretical noise influence σ_m with a threshold expansion factor m_{exp} that determines not only the false alarm rate of the multipath monitor but also affects the sensitivity of the monitor; increasing the monitor thresholds will result in a less sensitive monitoring process.

In order to quantify this loss in monitoring sensitivity, the use of one single metric *M* with two different expansion factors $m_{exp,1}$ and $m_{exp,2}$ is assumed. In this case, the two sets of instantaneous monitor thresholds can be expressed as follows:

$$\begin{gathered} \text{thres}_1 = m^* \pm m_{exp,1} \cdot \sigma_m \\ \text{and} \\ \text{thres}_2 = m^* \pm m_{exp,2} \cdot \sigma_m \end{gathered} \tag{146}$$

Assuming that the calibrated mean metric value *m** is subtracted from the observed metric value prior to the threshold computation, equation (146) simplifies to

$$\begin{gathered} \text{thres}_1 = \pm m_{exp,1} \cdot \sigma_m \\ \text{and} \\ \text{thres}_2 = \pm m_{exp,2} \cdot \sigma_m \end{gathered} \tag{147}$$

and the sensitivity loss (or gain) Δ_{Sens} [dB] with respect to $m_{exp,1}$ can be expressed as follows:

$$\Delta_{Sens} = 20 \cdot \lg\left(\frac{\pm m_{exp,1} \cdot \sigma_m}{\pm m_{exp,2} \cdot \sigma_m}\right) = 20 \cdot \lg\left(\frac{m_{exp,1}}{m_{exp,2}}\right) \text{ [dB]} \tag{148}$$

In order to assess the influence of a modified threshold expansion factor on the monitoring sensitivity, it is sufficient to analyze the ratio of two expansion factors. Note that a sensitivity loss with respect to $m_{exp,1}$ occurs for $m_{exp,1} < m_{exp,2}$, whereas a sensitivity gain with respect to $m_{exp,1}$ occurs for $m_{exp,1} > m_{exp,2}$. For the implementation of the proposed monitoring scheme, a threshold expansion factor of 5 has been suggested. Figure 7-22a illustrates the increased (or decreased) monitoring sensitivity when using expansion factors other than $m_{exp}=5$. Thus, an expansion factor of $m_{exp}=10$ would lead to a sensitivity loss of ~6dB with respect to the proposed default setting. Translated into an illustration similar to Figure 7-18 - Figure 7-20, the monitoring sensitivity for the OEM4 NARROW configuration has been plotted for different threshold expansion factors (Figure 7-22b).

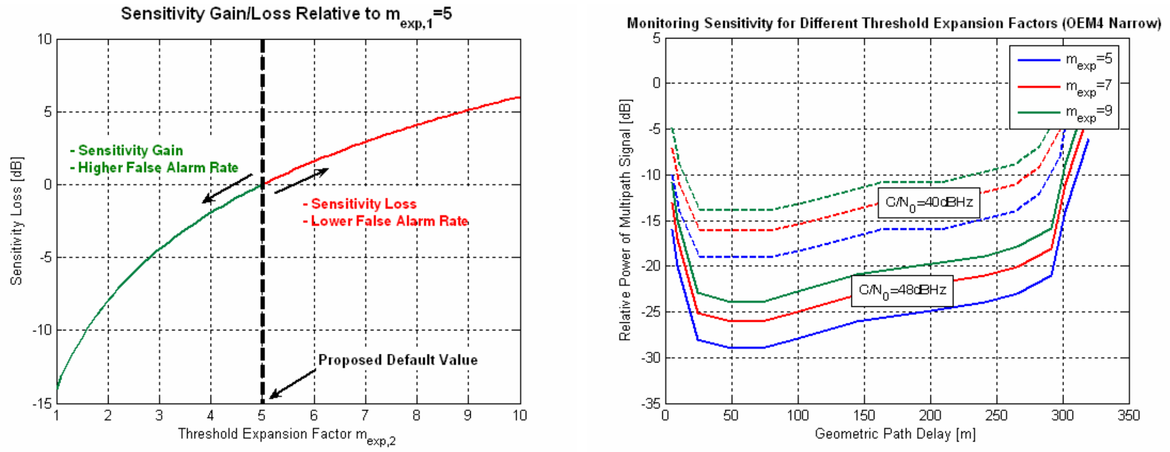

Figure 7-22: Increased/decreased monitoring sensitivity for different expansion factors relative to the proposed default value (left diagram) and monitoring sensitivity of the OEM4 NARROW configuration with consideration of different threshold expansion factors (right diagram).

7.7.5 Enhancement of Positioning Performance

Since all occurring multipath signals can be detected in real-time, information about the presence of multipath signals is instantly available. This information can be further used for navigation processing by either excluding the affected signals from the subsequent positioning algorithm or by de-weighting the affected observations. The latter approach is more suitable in critical environments where several satellites may be affected and the exclusion of these satellites would lead to an insufficient amount of remaining observations.

Figure 7-23 illustrates the potential enhancement with respect to the positioning performance. In this case, a -15dB multipath signal with a geometric path delay of about 130m was simulated for one satellite (PRN6) and the result of the positioning process was computed on the basis of an epoch-by-epoch least squares adjustment. For the computation of the upper diagram all 6 available satellites were used (also the one affected by multipath) whereas the lower left diagram illustrates the positioning performance after exclusion of the affected observations. For the computation of the positioning solution illustrated in the lower right diagram, the observations were weighted according to the distance of the current metric value from its nominal mean (the larger the metric value’s distance from its nominal mean, the smaller the weight).

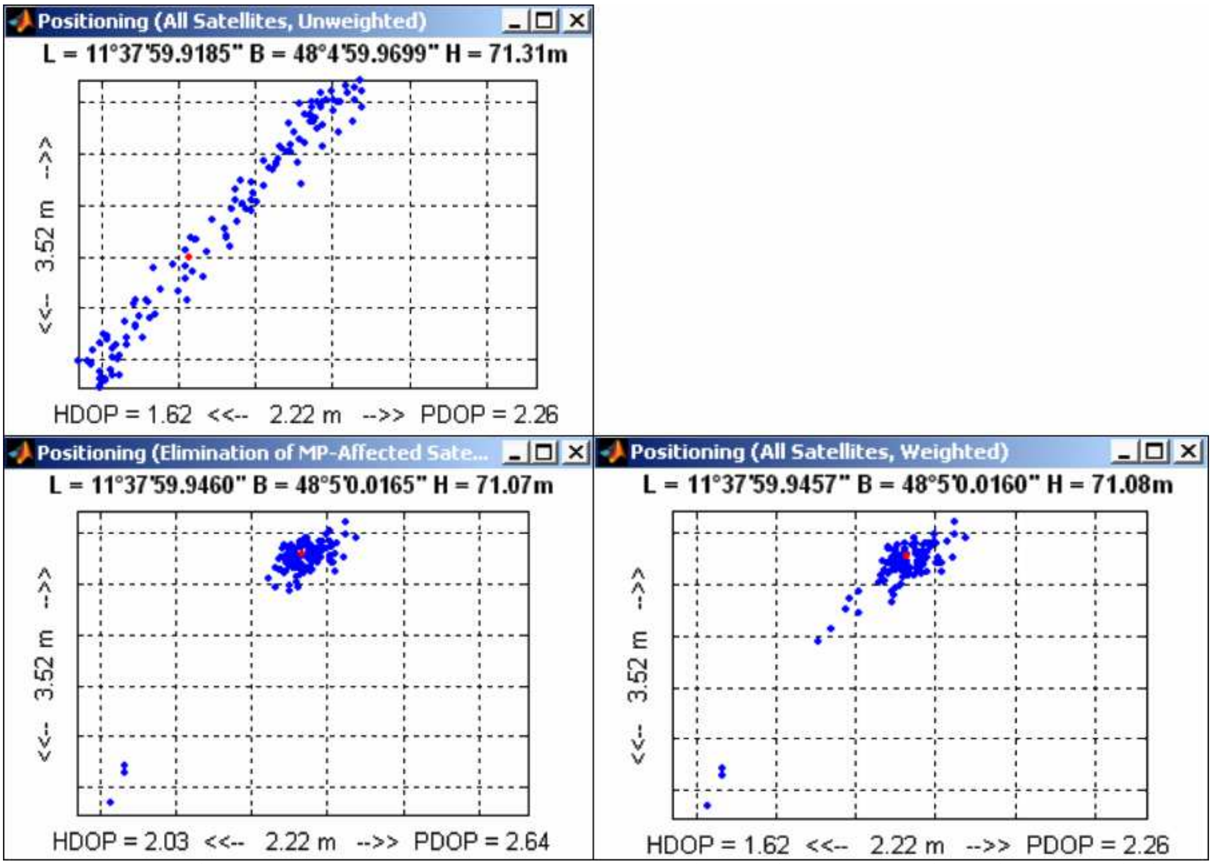

L = 11°37'59.9185" B = 48°4'59.9699" H = 71.31m

HDOP = 1.62 <<-- 2.22 m -->> PDOP = 2.26

L = 11°37'59.9460" B = 48°5'0.0165" H = 71.07m

HDOP = 2.03 <<-- 2.22 m -->> PDOP = 2.64

L = 11°37'59.9457" B = 48°5'0.0160" H = 71.08m

HDOP = 1.62 <<-- 2.22 m -->> PDOP = 2.26

Figure 7-23: Enhancement of positioning performance by exclusion of multipath-affected observations (lower left diagram) or by de-weighting affected observations (lower right diagram).

As indicated in Figure 7-23, the positioning performance can be enhanced significantly by processing information about occurring multipath influences. However, performance enhancements as illustrated in Figure 7-23 cannot be achieved in all cases. Especially in case that multipath influences remain undetected, the positioning performance is expected to degrade. Such aspects are discussed in the following section.

7.7.6 Positioning in Case of Undetected Multipath

Multipath influences which do not cause the metric values to exceed the monitor thresholds remain undetected and may lead to pseudorange errors and a degraded positioning performance. Figure 7-24 illustrates such a case. The simulations were carried out twice: during the first simulation run, only the influence of thermal noise was considered (green time series); during the second run, a weak multipath signal was added to one of the six signals resulting in variations of OEM3 metric M_{67} that are just below the limit of detection (red time series). The simulations were carried out for two different values of C/N_0, namely 45dBHz (left column) and 39.5dBHz (right column). The position scatter plots for the undistorted (green) and the degraded cases (red) are illustrated in the form of the two lower diagrams.

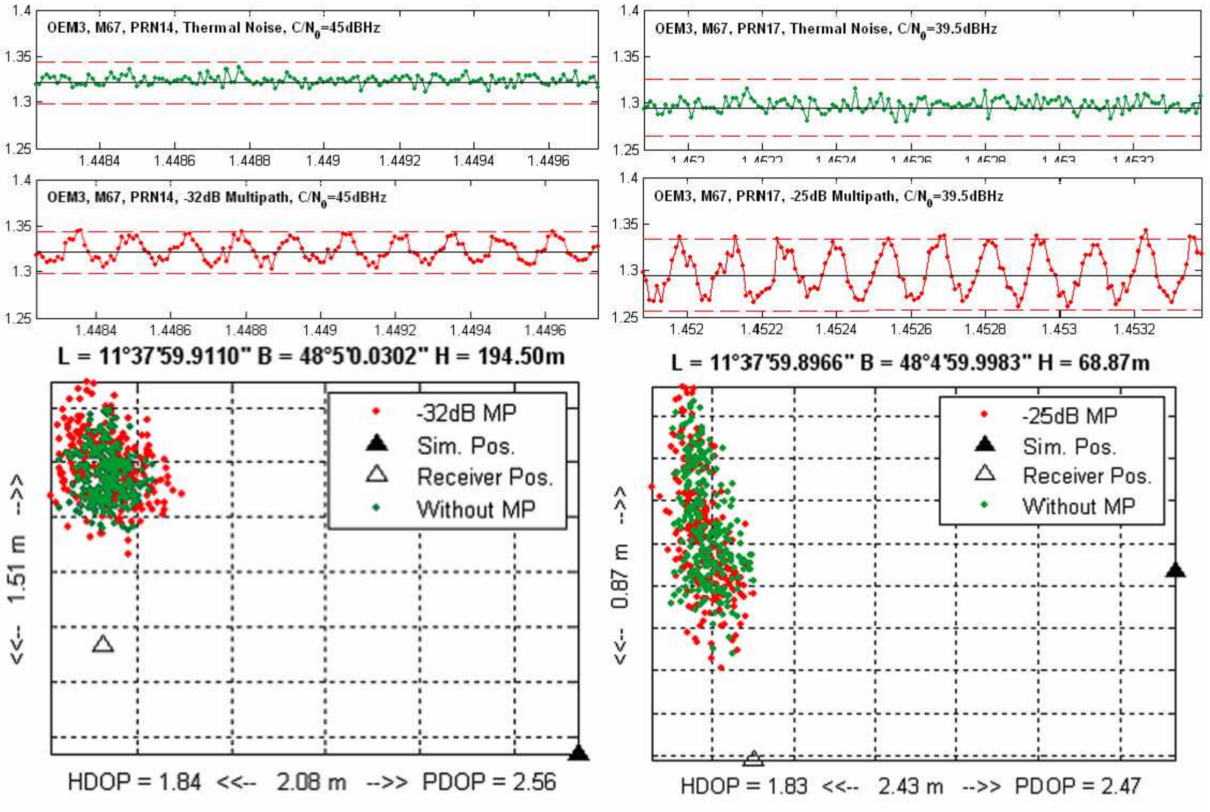

Figure 7-24: Degradation of positioning performance due to undetected multipath.

As can be derived from Figure 7-24, these weak multipath signals barely degrade the positioning performance. However, the conclusion that undetected multipath signals have only minor effects on the positioning performance does not hold true in all cases. In fact, the actual positioning performance in case of the occurrence of undetected multipath signals depends on the frequency of the occurring multipath variations. In both cases illustrated in Figure 7-24, the geometric path delays were of the order of ~150m resulting in relatively rapid, short-periodic variations. In case that short path delays are considered, the frequency of the variations decreases and the positioning performance degrades accordingly. The influence of such a slow-varying multipath signal on OEM3 metric M_{67} and on the positioning performance is shown in Figure 7-25 where the results of three consecutive simulation runs are illustrated.

During the first run, all signals were multipath-free so that only the influence of thermal noise is visible on both the multi-correlator observations and the derived positions (green data). During the second run, a -26dB multipath signal with a path delay of ~75m was added to PRN5, resulting in rapid multipath variations ($T \approx 8s$). These multipath influences have only minor effects on the positioning performance (blue data). During the last simulation run, a -6dB multipath signal with a short path delay of ~5m was added to PRN5 resulting in very slow signal variations (T≈120s). Although being below or just at the limit of detection this short-delay multipath signal significantly degrades the positioning performance (red data). The C/N_0 was ~40dBHz in all cases. As a conclusion, it can be assumed that undetected short-delay multipath causes larger pseudorange errors than undetected long-delay multipath.

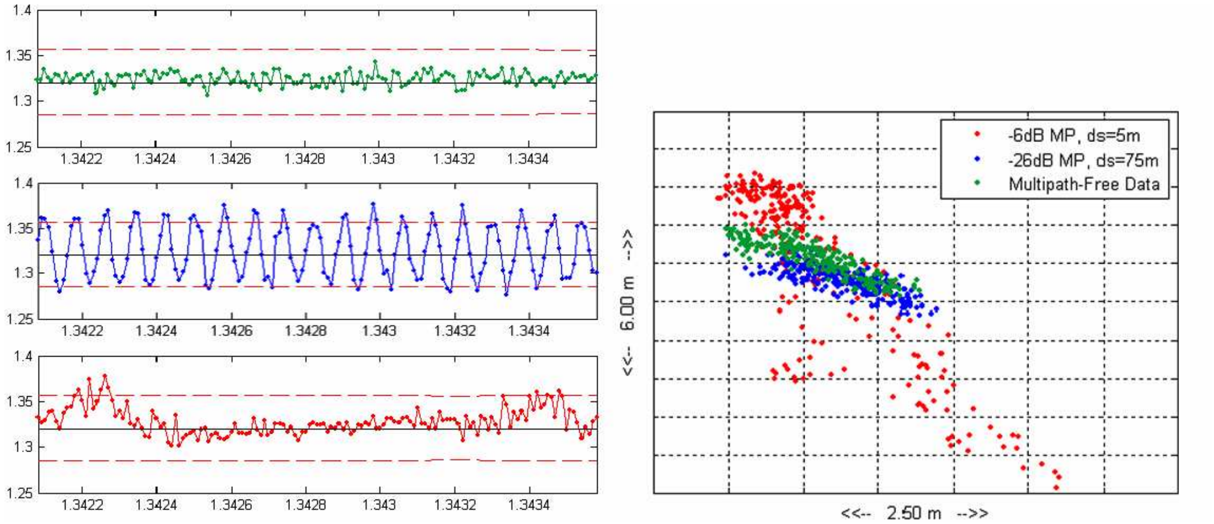

Figure 7-25: Degradation of positioning performance due to slow-varying undetected multipath.

7.7.7 Ranging Errors Due to Undetected Multipath

In order to envisage how large remaining ranging errors due to undetected multipath can become, “code minus carrier” (CMC) residuals were computed for multipath affected observations, again considering different geometric path delays and different power levels of the direct signal component. The relative power of the multipath signals was chosen such that the resulting variations are near or just below the limit of detection. Figure 7-26 illustrates the result of this analysis (valid for the OEM3 Standard configuration).

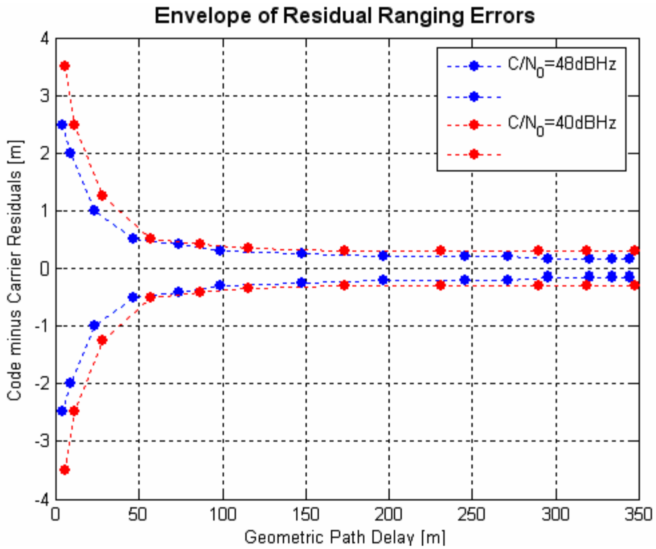

Figure 7-26: Residual ranging errors due to undetected multipath as a function of the geometric path delay and the mean C/N_0 of the direct signal (OEM3 Standard).

The ranging errors plotted in Figure 7-26 were obtained from a time series (~15min) of the CMC residuals representing the conditions at a dedicated geometric path delay and containing the multipath variations. Significant ranging errors up to a few meters only occur for undetected short-delay multipath. For longer path delays, however, the remaining errors are of the same order as the corresponding thermal noise influence, which is ~0.15m for the 48dBHz and ~0.3m for the 40dBHz case (derived from multipath-free simulator observations).

It should be noted that the envelope illustrated in Figure 7-26 does not only depend on the selected metric but also on the underlying receiver architecture. The OEM3 receiver uses a carrier-aided 1st order DLL with a loop bandwidth of 0.0125 Hz. Against this background, the rapid decrease of residual ranging errors with increasing path delays can be explained by looking at the underlying multipath relative power levels and the occurring multipath phase rates. For path delays <25m, the multipath signals are still relatively strong and the frequency of the multipath variations is below or of the same order as the code loop bandwidth (slow-fading multipath). In this region time-varying multipath errors show up clearly. For larger path delays, however, the multipath signals become weaker (see Figure 7-18), multipath phase rates become larger than the code loop bandwidth (transition to fast-fading multipath) and the loop filter more and more removes the multipath variations through averaging ([Kelly et al. 2003]). Similar analyses have been carried out for the two OEM4 configurations. The results are illustrated in the following diagrams.

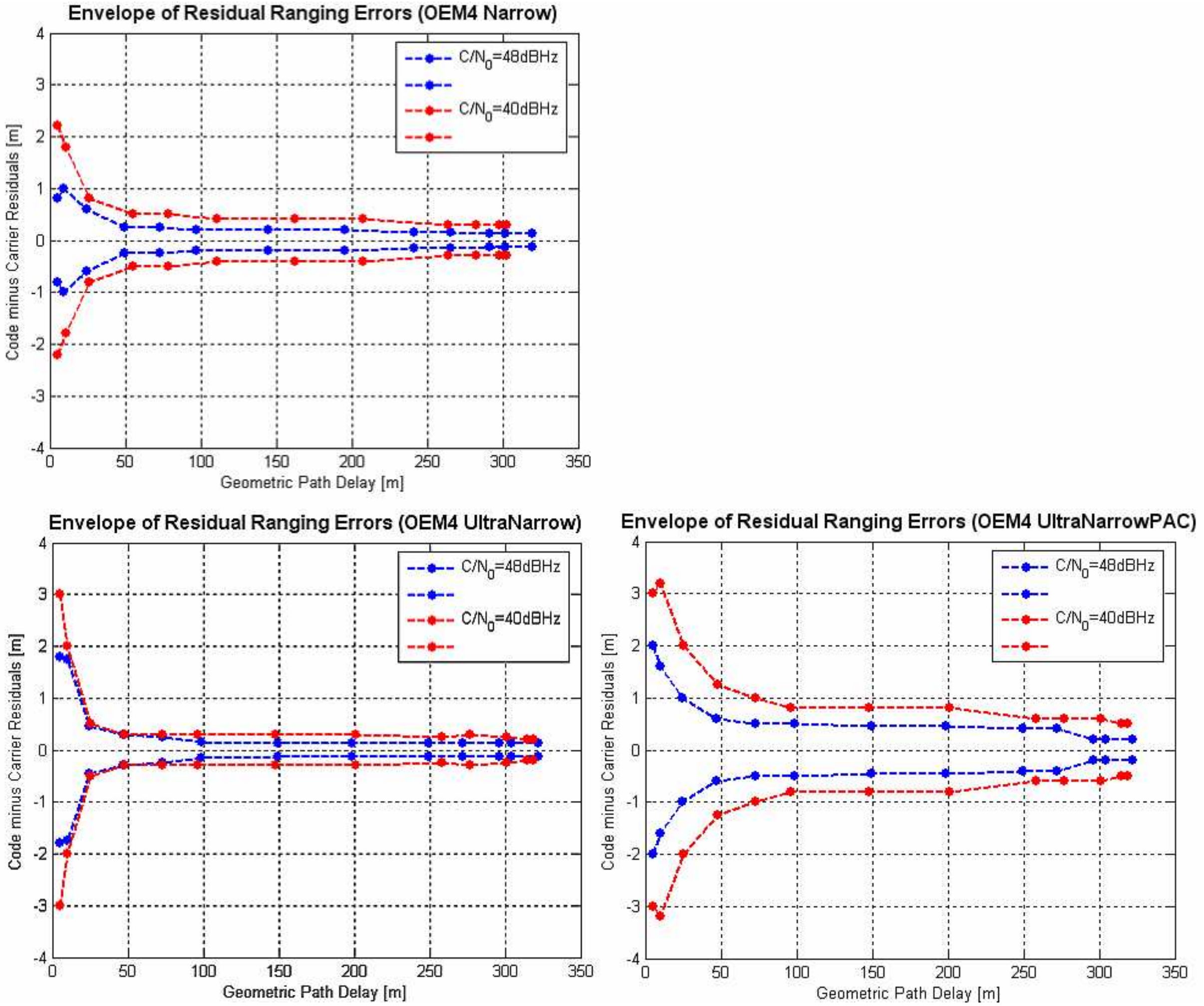

Figure 7-27: Residual ranging errors due to undetected multipath as a function of the geometric path delay and the mean C/N_0 of the direct signal. Simulation results are plotted for the OEM4 Narrow configuration (upper left diagram) as well as for the UltraNarrow and UltraNarrowPAC configuration (lower diagrams).

As expected, the OEM4 configurations show the same general behavior as the OEM3 case with residual ranging errors of up to a few meters for short path delays and decreasing errors for longer path delays. Again, for long path delays, the remaining errors are of the same order as the corresponding thermal noise influence. Compared to the OEM3 case, the OEM4 configurations NARROW and ULTRANARROW produce slightly smaller residual ranging errors for short path delays. This behavior could be expected and is in accordance with the sensitivity analysis presented in section 7.7.4. Because the multipath monitor based on the OEM4 metrics is more sensitive to weak multipath signals with short path delays than in the OEM3 case, multipath signals which cannot be detected are also weaker. This results in smaller residual ranging errors. With respect to the OEM4 receiver parameters, the same loop noise bandwidth as for the OEM3 case was used (B_L=0.0125Hz) in both cases. In contrast to the OEM3 receiver, the OEM4 receiver uses a carrier-aided 2nd order DLL.

Note that the OEM4 configurations ULTRANARROW and ULTRANARROWPAC provide the same correlator outputs (identical correlator positions) but differ with respect to the discriminator implementation. ULTRANARROWPAC uses a double-delta discriminator which is known to show a poorer noise performance than a standard early-late discriminator implementation ([MCGRAW and BRAASCH 1999]). This degraded noise performance is clearly visible in Figure 7-27 and results in larger residual ranging errors (especially for undetected medium- and long-delay multipath).

7.8 Determination of Mean Metric Values

7.8.1 Calibration Campaign

As already shown in section 7.1, the mean metric values depend on the actual shape of the signal's correlation function which in turn depends on the received PRN and several receiver parameters (pre-correlation bandwidth or filter characteristics). Since the thresholds used by the RTMM to indicate multipath signals are defined relative to the mean metric values, these mean values have to be known during the monitoring process. This is why the mean metric values have to be determined in advance during a calibration campaign.

The calibration procedure requires that all satellites that ever become visible at a certain user position are to be observed during their entire pass. To ensure that the correct mean metric values are determined, no other error sources are allowed to occur except for thermal noise, so that the calibration campaign has to be carried out in an environment free of multipath. Once the correct mean metric values have been computed, they are valid for the receiver which has been calibrated and can then be used for the purpose of multipath monitoring. Such a calibration campaign has to be carried out once for each receiver providing multi-correlator functionality.

7.8.2 Possible Influences on Mean Metric Values

In order to identify any unwanted effects that may influence the mean metric values, several analyses based on observations obtained from the GPS hardware simulator were performed. Influences that might affect the shape of the correlation function (besides the front-end characteristics) are atmospheric effects (ionospheric and tropospheric influences), the antenna pattern, the loop noise bandwidth of the tracking loop and signal dynamics. The objective was to determine whether or not these parameters influence the mean metric values and, if so, how the monitoring concept can be adjusted in order to cope with such influences.

In order to detect possible influences, the mean metric values for each metric and each satellite have to be known very precisely. For observations obtained from the GPS hardware simulator, consecutive calibration measurements under identical conditions are expected to result in identical mean metric values. However, as will be discussed in the following paragraph, this assumption is not true.

7.8.2.1 Repeatability of Mean Metric Values

In order to verify the repeatability of mean metric values, multi-correlator observations obtained from the GPS hardware simulator were processed for all selected metrics of the OEM4 NARROW configuration and for all visible satellites. During the observation period, 29 satellites and 6 metrics were considered, resulting in a total amount of 174 time series *TS* (metric values as a function of time) from which 174 mean metric values can be derived.

This calibration procedure was repeated twice using exactly the same simulation scenario so that three time series and three derived mean values (obtained from independent simulation runs) were available for every metric-satellite combination, resulting in a total amount of 522 time series *TS*. An omni-directional antenna phase pattern was assumed for each simulation run to ensure similar thermal noise influence during the entire observation period; this measure resulted in nearly identical standard deviations for the three time series.

The mean values of two time series TS_1 and TS_2 can be compared with each other by performing a significance test. For this purpose, the Matlab function `ttest2` was used (part of Matlab's Statistics Toolbox). This test compares the mean values of two normally distributed data samples by assuming unknown but equal standard deviations. The null hypothesis H_0 states that the two mean values are equal whereas the alternative hypothesis *H1* states that both means are different:

$$H_0 : \mu_{TS_1} = \mu_{TS_2} \quad H_1 : \mu_{TS_1} \neq \mu_{TS_2} \tag{149}$$

This (two-sided) test was carried out for all metric-satellite combinations and the three corresponding time series, resulting in a total amount of 522 significance tests (comparison of TS_1 with TS_2, TS_1 with TS_3 and TS_2 with TS_3 for all metric-satellite combinations). Each of the tests were carried out for two levels of significance, namely α=0.025 and α=0.005. If the difference of the independently derived mean values is statistically insignificant, only 5% of the significance tests are permitted to fail for α=0.025. For α=0.005, only 1% of the tests are permitted to fail. The actual fail rates, however, were 71.3% (α=0.005) and 66.9% (α=0.005), respectively. As a result, it must be stated that the mean metric values obtained from the simulator measurements (calibration measurements) are **not reproducible** in a statistical sense. Similar results were obtained by performing another version of this significance test that uses the actual standard deviations of the time series as an input.

As a consequence, the simple comparison of two mean values derived from two time series of the same metric is not sufficient to detect possible influences on the mean metric values. Instead of using the mean value of one single time series as a reference, several time series have to be considered to obtain a mean value that can serve as a reference. Such a mean value can be obtained by averaging the mean values of each time series and by computing a confidence interval. As long as other derived mean values lie within this confidence interval, they are not considered to be significantly different than the reference value.

7.8.2.2 Confidence Intervals for Expected Mean Metric Values

In order to provide a reference value and a corresponding confidence interval against which all possible influences can be compared, the reference observations have the following simulator- and receiver-specific characteristics:

- Atmospheric effects turned off (no ionospheric and tropospheric path delays)
- Use of an omni-directional antenna phase pattern
- Static scenario (no user dynamics)
- Loop noise bandwidth: B_L=0.0125 Hz

Based on these parameters, a total amount of eight satellites were simulated during an observation period of approximately two hours using the GPS hardware simulator. Multi-correlator data was collected using the NARROW configuration of the NovAtel OEM4 receiver. Based on one single simulation run, the mean metric values $\overline{m}_{i,1}$ and the corresponding empirical variance S_i^2 for the OEM4 NARROW metrics listed in Table 7-11 were derived. Based on *n* simulation runs, the desired reference mean metric values and their corresponding standard deviations are

$$\overline{m}_{i,ref} = \frac{1}{n}(\overline{m}_{i,1} + \overline{m}_{i,2} + \ldots + \overline{m}_{i,n}) = \frac{1}{n}\sum_{j=1}^{n}\overline{m}_{i,j} \tag{150}$$

$$S_{i,ref} = \frac{1}{n}\sqrt{(S_{i,1}^2 + S_{i,2}^2 + \ldots + S_{i,n}^2)} \approx \frac{1}{n}\sqrt{n \cdot S_i^2} = \frac{S_i}{\sqrt{n}} \tag{151}$$

as the empirical variance S^2_i of the metric m_i is approximately the same for every simulation run. The derived mean metric values $\overline{m}_{i,n}$, however, are expected to vary for every simulation run. Assuming that the reference mean metric values as defined by equation (150) are normally distributed and only empirically derived variances S_i^2 are available, the corresponding random variable follows a t-distribution with (n-1) degrees of freedom

$$\frac{\overline{m}_{i,ref} - \mu}{S}\sqrt{n} \sim t(n-1) \tag{152}$$

and the corresponding confidence interval can be expressed as

$$\left[\overline{m}_{i,ref} - t_{1-\alpha/2}(n-1)\frac{S_i}{\sqrt{n}}, \overline{m}_{i,ref} + t_{1-\alpha/2}(n-1)\frac{S_i}{\sqrt{n}}\right] \tag{153}$$

where $t_{1-\alpha/2}(n-1)$ is the $(1-\alpha/2)$ quantile of the t-distribution with (n-1) degrees of freedom and $100(1-\alpha)$% is the probability that the estimation of confidence intervals actually leads to an interval that contains $\overline{m}_{i,ref}$ ([FAHRMEIR et al. 1999]).

7.8.2.3 Evaluation of Potential Influences on Mean Metric Values

Potential influences which are to be examined are varying atmospheric conditions, different antenna patterns, different loop noise bandwidths and signal dynamics. The latter aspect is very important in order to determine whether or not the proposed monitoring scheme can also be used for dynamic applications without modifications. Depending on the number of satellites being acquired automatically by the receiver and thus being available for analysis, the reference mean values were computed on the basis of four or five independent simulation runs (n=4 or n=5). Based on the derived reference mean values, the associated 90% confidence intervals were computed.

After the determination of the reference mean values for all metric-satellite combinations, additional simulations that also considered the potential influences were carried out. The mean metric values were compared with the confidence intervals computed according to equation (153). Significant influences on the mean metric values can only be postulated in case they exceed the defined confidence interval. As already introduced above, the following influences were simulated:

Atmospheric Effects. In contrast to the calibration measurements carried out to obtain reference mean values, both tropospheric and ionospheric path delays were simulated. The STANAG model was used for modeling tropospheric delays, ionospheric influences were modeled by a standard terrestrial ionospheric model. Two simulations considering atmospheric effects were performed.

Antenna Pattern. In order to simulate more realistic antenna characteristics, the omni directional antenna pattern used for the calibration measurements was replaced by an elevation-dependent (not azimuth-dependent!) pattern. Two simulations were performed.

Loop Noise Bandwidth. For the calibration measurements, a loop noise bandwidth of B_L=0.0125 Hz was used. In order to examine possible influences of varying bandwidths, the loop bandwidth was narrowed to B_L=0.0025 Hz making the tracking loop more sensitive to signal dynamics. Two simulations were performed using this loop bandwidth.

Signal Dynamics. Two types of dynamic scenarios were simulated. The first simulation assumed a car performing various acceleration and deceleration maneuvers including a turn to simulate lateral acceleration (simulation carried out four times). The second simulation type assumed a vehicle performing a circular motion. An overall of 11 simulations were performed assuming circle radii between 100m and 5m and velocities between 1m/s and 10m/s, resulting in maximum accelerations of ~2g.

The analyses were carried out for several satellites and all 6 OEM4 NARROW test metrics. By this measure, an overall of 148 derived mean values could be compared to the 90% confidence interval for the reference mean value derived from the calibration measurements as described in the previous section. All of these 148 mean values (affected by the influences mentioned above) were within the confidence interval. As a result, it can be stated that the mean metric values are not influenced by the assumed influences.

Figure 7-28 summarizes the result of this analysis for PRN3 observed with OEM4 NARROW metric M_{16}. The green solid line represents the reference mean metric value obtained from 5 independent calibration measurements. The gray area represents the 90% confidence interval as defined in and computed according to equation (153). For this metric-satellite combination, 19 mean metric values were derived from observations affected by the influences mentioned above; they are represented by the red dots. All mean values (potentially affected by the assumed influences) are well within the confidence interval.

It should be noted, however, that the obtained results strongly depend on the receiver architecture. Especially the influence of signal dynamics depends on parameters like loop noise bandwidth, tracking loop order and implementation (aiding on/off). The used OEM4 receiver, for example, makes use of a carrier-aided second-order DLL that virtually removes most of the signal dynamics. If the carrier-aiding option could be switched off or the loop noise bandwidth is decreased and/or more signal dynamics is applied to the scenario, the mean values are expected to differ from the reference value. In this case, however, with activated carrier-aiding and accelerations of up to 2g, the mean metric values do not seem to change significantly. The OEM4 receiver seems to be suitable for multipath monitoring purposes even in highly dynamic environments.

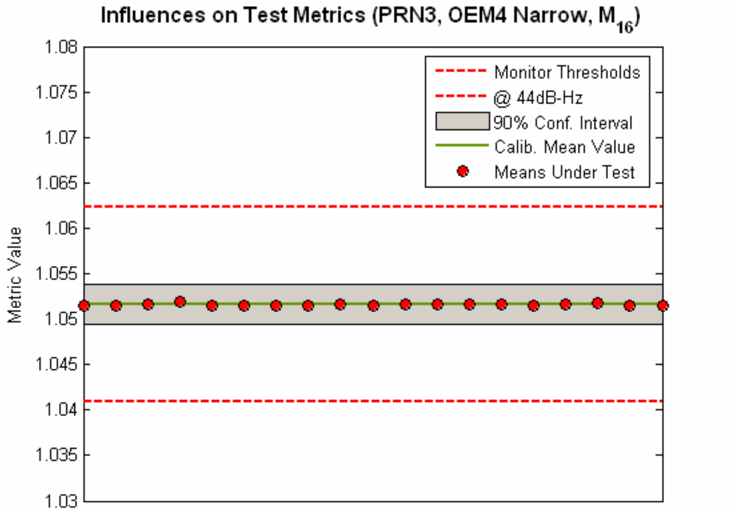

Figure 7-28: Mean metric values for PRN3 (OEM4 NARROW, metric M_{16}) as derived from measurements affected by the effects mentioned in the text. All observations were obtained at a C/N_0 of ~44dBHz; the corresponding monitor thresholds (valid for m_{exp}=5) are also plotted.

7.8.2.4 Maximum Tolerable Signal Dynamics

Since a second-order DLL is sensitive to acceleration stress, it can be expected that strong LOS accelerations deform the correlation function and can affect the mean metric values. In order to verify this statement, several simulations were carried out by means of the GPS hardware simulator:

After having stood still for 10min to ensure proper signal acquisition, the vehicle – a car in this specific case – accelerated during a period of 100s and then swiveled into a circular motion (assuming a constant radius of 100m). For each simulation run, different velocities were used for the circular motion, leading to different vehicle accelerations. After having finished the circular motion, the vehicle passed into a linear trajectory again and decelerated during a period of 100s until it came to a stop. Figure 7-29 illustrates the influence of strong LOS acceleration on the OEM4 NARROW metric M_{18} as obtained from multi-correlator observations of PRN3. In this case, LOS accelerations of up to ~93 m/s^2 (~9.5g) occurred during the circular motion of the vehicle (lower diagram). During this time, the mean metric value is significantly different from the value derived from other parts of the trajectory (upper diagram).

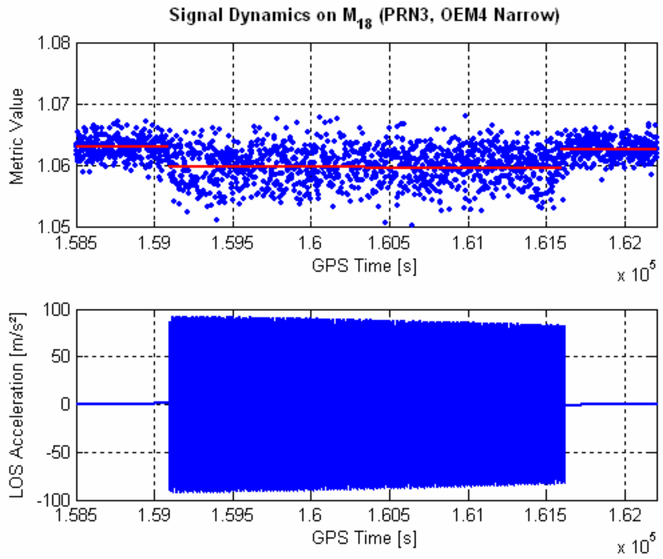

Figure 7-29: Influence of strong LOS acceleration on OEM4 NARROW metric M_{18}.

Furthermore, it seems that not only the mean metric value is affected by the LOS signal dynamics but also the noise influence. This, however, is mainly due to the geometrical conditions of the simulation. Since the satellite is not located directly overhead but rather near the horizon, the LOS acceleration constantly changes as the vehicle moves through the circle. Thus, also low LOS accelerations can occur that lead to metric values of the same order as they would appear in the undistorted case. It can also be derived from the lower diagram of Figure 7-29 that the maximum LOS acceleration slightly decreases as time proceeds. This is due the slow satellite motion in the sky.

In order to evaluate the general influences of signal dynamics on the test metrics, the mean metric values for PRN3 and all relevant OEM4 NARROW metrics were determined only for the part of the trajectory where the signal is subject to the highest LOS accelerations (the part of circular motion). Similar to Figure 7-28, the resulting mean metric values are plotted together with their calibrated mean values, the corresponding confidence intervals and monitor thresholds as a function of the mean LOS acceleration (which is different for each simulation run). The mean LOS acceleration was derived from acceleration profiles as shown in the lower diagram of Figure 7-29 by first computing the absolute values of all LOS accelerations occurring during the circular motion and then determining the median of these absolute LOS accelerations.

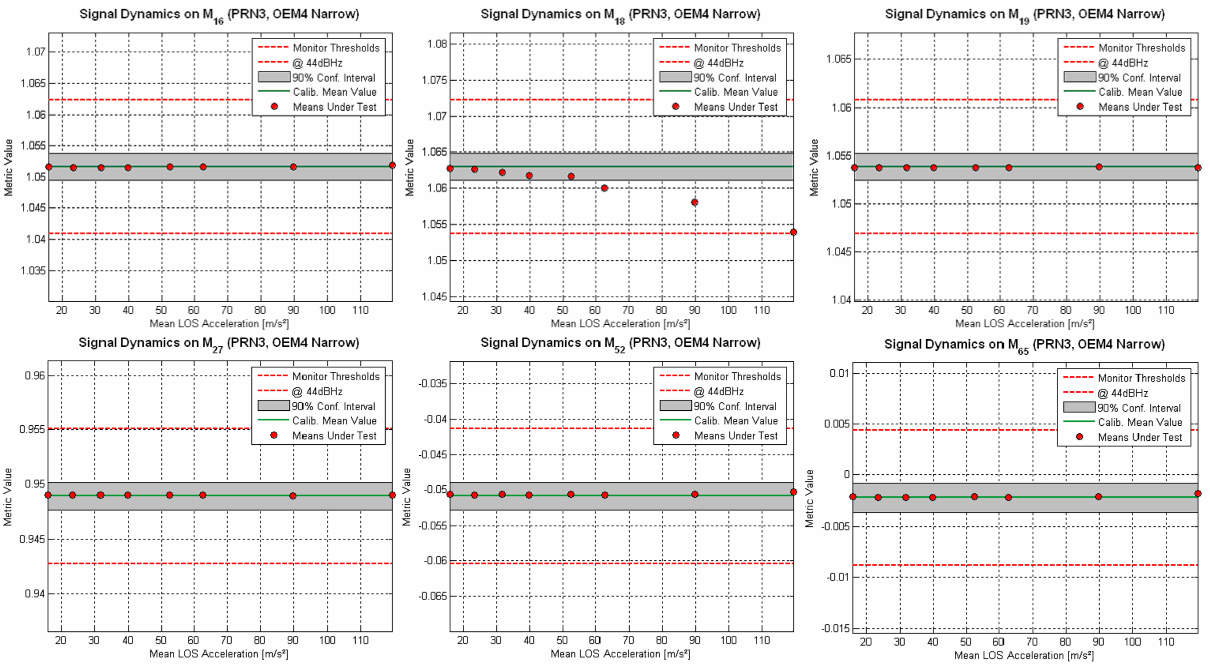
Signal Dynamics on M_{16} (PRN3, OEM4 Narrow)
Signal Dynamics on M_{18} (PRN3, OEM4 Narrow)
Signal Dynamics on M_{19} (PRN3, OEM4 Narrow)
Signal Dynamics on M_{27} (PRN3, OEM4 Narrow)
Signal Dynamics on M_{52} (PRN3, OEM4 Narrow)
Signal Dynamics on M_{65} (PRN3, OEM4 Narrow)

Figure 7-30: Mean metric values as a function of the mean LOS acceleration.

Interestingly, the mean value of only one of the 6 OEM4 NARROW test metrics (M_{18}) seems to be affected significantly by the simulated signal dynamics. The mean values of all other metrics stay within the limits of the 90% confidence interval that has been derived from the unaffected calibration measurements. Nevertheless, the maximum tolerable LOS acceleration can be derived from the behavior of M_{18}. As already defined, the mean values can be deemed to be unaffected by signal dynamics as long as they remain inside the confidence interval. In such a case, the monitoring concept can be applied without modifications and the calibrated mean metric values can be used to derive the monitor thresholds. However, with increasing signal dynamics, the observed metric values more and more approach the monitor thresholds (as can be derived from the behavior of metric M_{18}) and might exceed them even if the signal is not affected by multipath. In such a case the calibrated mean metric values cannot be used for monitoring any more.

Figure 7-31 illustrates the mean metric values of M_{18} for PRN3 and PRN6 as a function of the mean LOS acceleration. In order to be able to determine a boundary value for the maximum tolerable LOS acceleration, a second order polynomial was fitted to the individual metric means. In both cases, the affected mean metric values exceed the 90% confidence interval at a mean LOS acceleration of ~5g. This means that (mean) LOS acceleration below ~5g does not severely affect the monitoring performance and that the proposed monitoring scheme also works for dynamic applications.

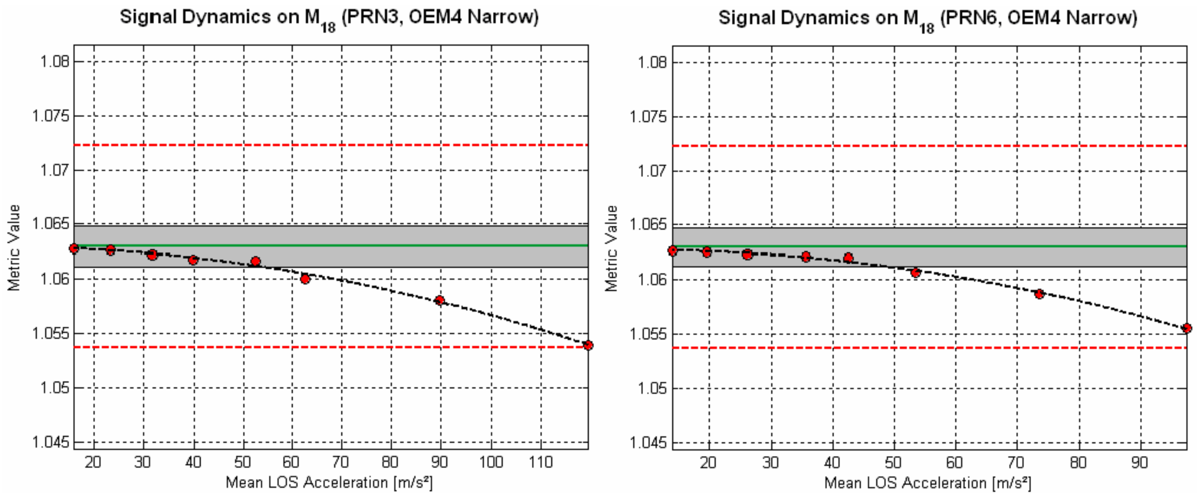

Figure 7-31: Mean metric values as a function of the mean LOS acceleration.

It should be noted, however, that the influence of signal dynamics on the monitoring performance for an arbitrary receiver strongly depends on the receiver implementation (tracking loop order, loop noise bandwidth). The results presented in this chapter are only valid for the OEM4 receiver (DLL bandwidth: B_L=0.0125 Hz).

7.9 Issues and Limitations

7.9.1 Conceptual Issues

The proposed multipath monitoring approach uses the noise variances listed in Table 7-13 as a basis for the computation of monitor thresholds. The noise variances and the corresponding thresholds are a function of the current C/N_0 (the key feature for getting instant information about the influence of multipath signals). However, multipath signals themselves may cause significant variations of the C/N_0 in turn causing the monitor thresholds to vary periodically as well. This undesired behavior can be attenuated by smoothing consecutive C/N_0 values by means of a low-pass filter.

Figure 7-32 illustrates a time series of C/N_0 values showing strong variations at low elevation angles. These signal variations are due to multipath and – if remain unconsidered – would cause the monitor threshold to vary in a similar manner. The use of a low pass filter with a time constant of 250s leads to a much smoother appearance of the C/N_0 time series (red curve).

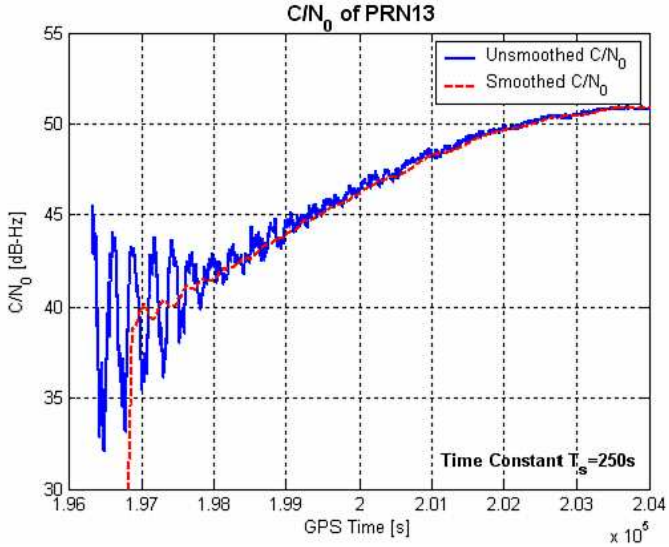

Figure 7-32: Smoothing of the C/N_0 values in order to avoid strong short-term variations of the monitor thresholds.

Another issue that has already been addressed in section 7.7.3 is that multipath influences cannot be detected in case that only one single and strong multipath component is present (absence of LOS component). This is a major drawback of the proposed monitoring approach because such undetected influences may result in large pseudorange and positioning errors.

The need for carrying out a calibration campaign to determine the long-term mean values of the selected metrics can also be considered as a limitation of the proposed monitoring approach. Since all satellites have to be observed during several passes, this procedure is a rather time-consuming process. The key issue, however, is to find a multipath-free environment to provide undistorted correlation peak observations.

A final conceptual issue is related to the exclusion of multipath-affected satellites from the navigation solution. It should be noted, however, that this issue is not related to the monitoring approach itself but on the way the monitoring information is further processed. Since information about multipath influences is available in real time, the affected satellites can remain unconsidered in the navigation solution. While this is a suitable approach in environments with only few affected satellites, it may fail in case that there are many affected satellites (i.e. if an insufficient number of healthy satellites remain, e.g. in urban canyon environments). This issue may become a minor problem with additional Galileo satellites becoming available. However, additional satellites do not necessarily mean that there will be proportionately more healthy satellites, because due to similar geometric conditions, several satellites located in a similar region of the sky tend to produce similar multipath influences. Therefore, a better approach seems to be the development of suitable weighting schemes (as indicated in section 7.7.5) or a combination of satellite exclusion and weighting. These aspects are not addressed in this thesis; they offer the potential for further examinations and developments.

Even if the exclusion of multipath-affected signals is possible, the multipath influences may be too small to be detected by the monitor. In such cases, residual ranging errors of up to several meters occur for short path delays. Undetected long-delay multipath is not an issue.

7.9.2 Practical Issues

In order to be able to identify the practical issues of the monitoring scheme, an experimental mobile multipath monitoring system was set up. For that purpose, an antenna of the same type as used for the calibration measurements was mounted on top of a vehicle (but not exactly the same as used for the calibration measurements). The GPS receiver (a NovAtel OEM3 model in this case) was connected to a laptop where the monitoring software was installed (see Figure 7-33).

Figure 7-33: Experimental mobile multipath monitoring system.

For the first trials, multi-correlator data was collected in an environment that was expected to be largely multipath-free. The objective was to verify the mean metric values that had been determined in advance by several calibration measurements for each satellite. The following diagrams show two time series obtained during the same period of time. While the first one shows a good match between the calibrated mean value and the actual metric values, an offset between the expected and the observed metric values is obvious for the second time series.

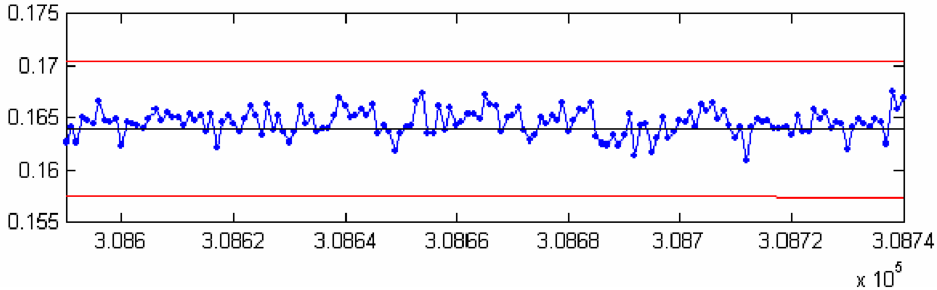

Figure 7-34: Observed metric values (blue) vs. predicted/calibrated mean metric value (black) for PRN8 processed with OEM3 metric M_{132}.

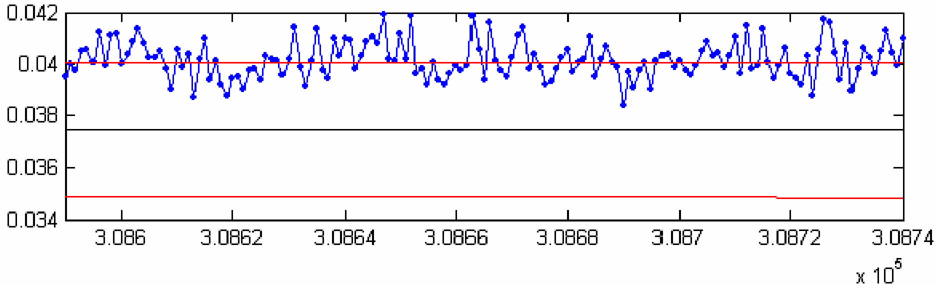

Figure 7-35: Observed metric values (blue) vs. predicted/calibrated mean metric value (black) for PRN8 processed with OEM3 metric M_{314}.

This behavior could also be observed with other satellite-metric combinations indicating systematic influences on the test metrics. It turned out that most of these discrepancies can be explained by not having used the same antenna as for the calibration measurements. For a second test campaign, the same antenna that had already been used to calibrate the mean metric values was used for monitoring. The data showed a significantly better match between the observed (mean) metric values and the predicted (calibrated) means. Figure 7-36 illustrates a comparison between an observed mean value and its calibrated counterpart (observation period: ~5min). The monitor thresholds are also shown (m_{exp}=5).

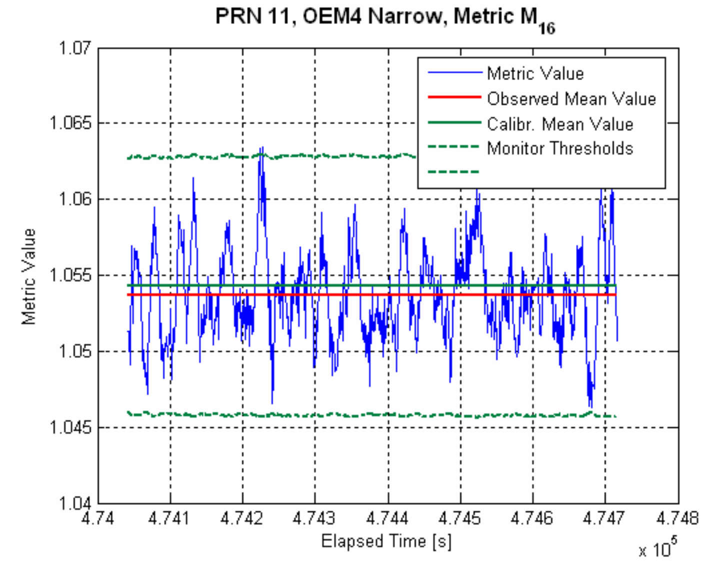

Figure 7-36: Observed metric values (blue) vs. predicted/calibrated mean metric value (green) for PRN11 processed with OEM4 NARROW metric M_{16}.

The obtained results indicate that **the same antenna that is used for the calibration measurements also has to be used for the monitoring process**. Obviously, two identically constructed antennas do not necessarily lead to identical mean metric values so that it is not sufficient to use an antenna of the same type.

But even if the same antenna is used for calibrating the mean metric values and for the monitoring process itself, there are slight remaining differences between observed and calibrated means in many cases (see Figure 7-36). Mainly two reasons can be considered for this behavior:

- **Possible temperature influences**. According to an email conversation with antenna and receiver specialists from NovAtel, it cannot be ruled out completely that the temperature in the antenna environment slightly affects the shape of the correlation function ([J. AULD, personal communication, 2005]). However, in order to verify such a statement, extensive examinations on this subject would be necessary. To the knowledge of the author and NovAtel, such analyses have not been carried out so far.
- **Varying multipath conditions**. The calibration measurements should be carried out in a largely multipath-free environment. For the calibration measurements obtained for this thesis, this requirement could not be met strictly. In the case where multipath influences cannot be excluded completely, the multipath influence strongly depends on the conditions in the antenna environment. Varying weather conditions (dry weather, rain or snow) affect the dielectric characteristics of the reflector surface resulting in varying coefficients of reflection and varying multipath influences on the observations that affect the derived mean metric values.

Figure 7-37 illustrates the different metric values (OEM3 metric M_{67}) as obtained from four passes of satellite PRN2 under different conditions (dry weather, rain and heavy snow fall). The resulting mean value (the average of the four derived mean values) that could be used for real time multipath monitoring is illustrated as a black dashed line.

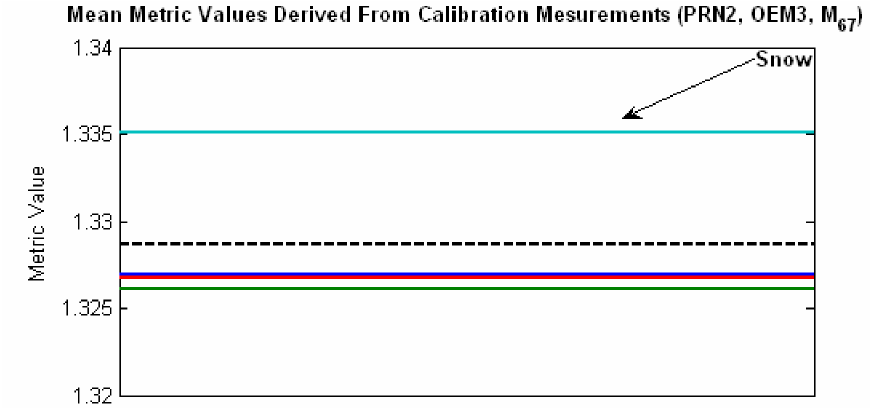

Figure 7-37: Potential effect of different environmental conditions on mean metric values.

The following chapter discusses possible approaches to consider such influences for a practical implementation of the proposed monitoring concept.

7.10 Optimizing the Monitoring Concept

Against the background of the practical issues identified in the previous section, this chapter provides some recommendations for the optimization of the proposed monitoring concept. In addition to the issue of varying mean metric values due to changing conditions during the calibration process, there is also the problem that some of the monitor thresholds are too small. This can be derived from Table 7-14 where the differences between actual and theoretically derived noise influences are listed. For metric M_{314}, the theoretical noise variance may be up to 30% too small (depending on the actual C/N_0 and the satellite being tracked). Accordingly, this deviation leads to smaller monitor thresholds. Such influences must be taken into account for a practical implementation of the monitoring scheme.

7.10.1 Problems and Solutions

The following tables summarize the main practical issues of the proposed monitoring scheme and suggest possible solutions.

Problem 1	Monitor thresholds for some metrics are too small (up to ~30%). This issue can be derived from Table 7-14, where the differences between actual and theoretically derived noise influences are listed. Typically, the actual noise influence is always larger than predicted resulting in monitor thresholds that are up to 30% too small.
Reason	For the computation of the theoretical noise influence, a modeled correlation function has been used. The difference between the modeled and the actual correlation function depends on the correlator location. For some correlators, this difference is larger than for others. This is why only few metrics are affected.

Solution(s)	**Solution 1.** Non-consideration of metrics causing large deviations. **Solution 2**. Determination of the actual shape of the correlation function (by means of long-term multi-correlator observations in a multipath-free environment) and use of the actual correlation function for the computation of the theoretical noise influence instead of using a modeled correlation function (time-consuming and labor-intensive!). **Solution 3**. Determination of differences between theoretical and observed noise influence (as listed in Table 7-14) for all satellite-metric combinations and computation of a correction term that can be added to the theoretical noise influence (look-up table).
Result	Better match between modeled and actual noise influence on the metrics and more realistic monitor thresholds.

Table 7-18: Problem of non-perfect modeling of theoretical noise influences.

Problem 2	Mean metric values are not reproducible in a statistical sense (neither for real data nor for multi-correlator data obtained from the GPS hardware simulator).
Reason	For hardware simulators: Unknown For real GPS data: Changing environmental influences during or between the calibration measurements (e.g. varying coefficients of reflections due to changing weather conditions or temperature influences).
Solution(s)	**Solution 1**. Optimization of antenna site (complete prevention of multipath influences) by means of careful antenna siting and/or use of absorbent material. **Solution 2**. Determination of mean metric values for many different environmental conditions (dry weather, rain, snow, different temperatures), determination of the statistical spread of the mean values and adaptation of monitor thresholds (time-consuming!). **Solution 3**. Examination and modeling (if possible) of temperature influences by means of measurements under controlled conditions (e.g. by using a climatic chamber).
Result	More realistic but also larger monitor thresholds that reduce the monitoring sensitivity (in case that solution 2 is considered).

Table 7-19: Problem of variability of mean metric values.

7.10.2 Optimizing RTMM

A closer look at Table 7-14 indicates that there are only a few metrics for which the actual and the predicted noise influence diverges significantly. Especially for the OEM4 Narrow metrics this aspect does not seem to be a major issue.

In order to verify this statement, the verification process carried out in section 7.5.2 has been repeated for all considered correlator configurations, all considered test metrics and all visible satellites. Again, the analysis based on observations obtained from the GPS hardware simulator (the mean C/N_0 was ~44 dBHz). The deviations Δ [%] of the metrics' theoretical standard deviations from their observed counterparts were computed for all correlator configurations and are illustrated in the form of histograms. The frequency of occurrence of the deviations is related to a 1% bin.

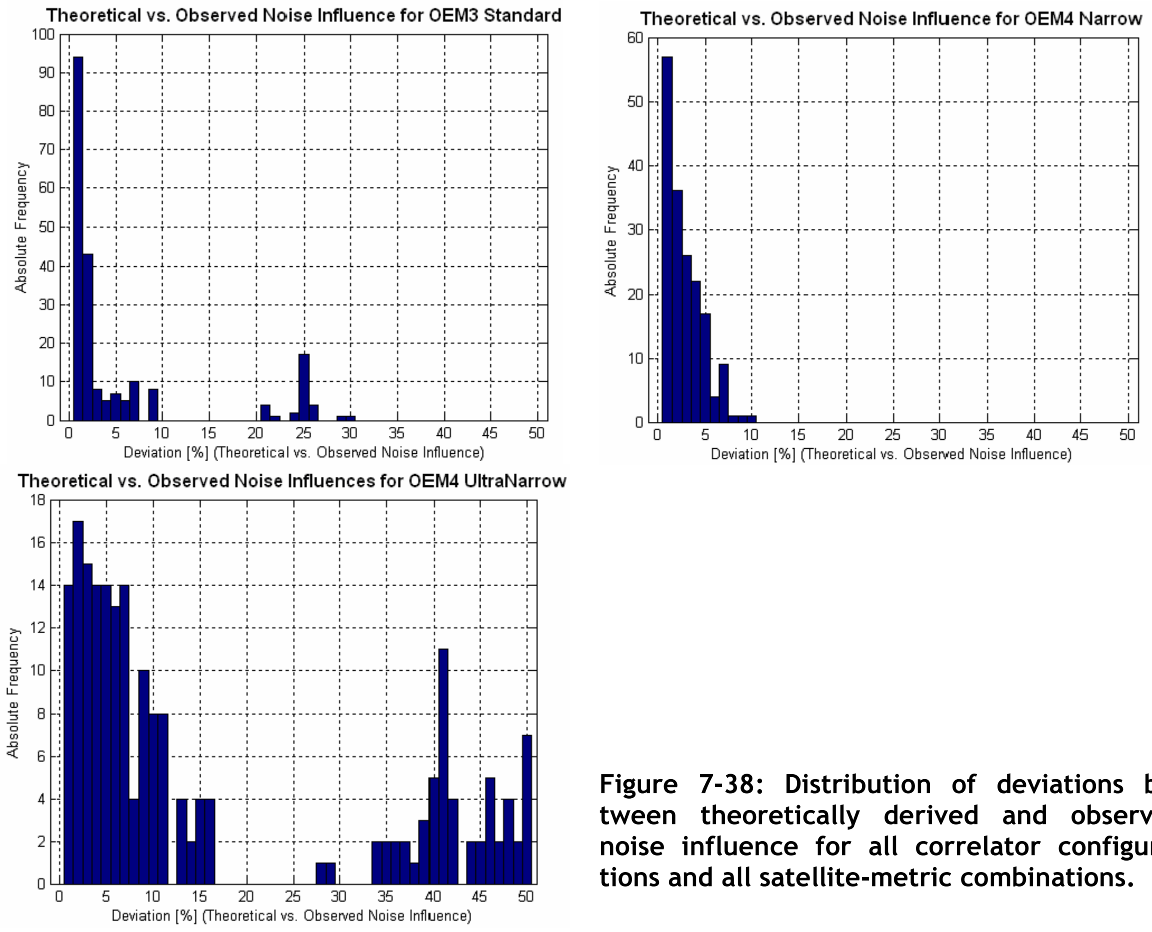

Figure 7-38: Distribution of deviations between theoretically derived and observed noise influence for all correlator configurations and all satellite-metric combinations.

As already indicated by Table 7-14, large deviations mainly occur for the OEM3 Standard and the OEM4 UltraNarrow configuration. They are caused by metrics M_{314} (OEM3), M_{320} and M_{360} (OEM4 UltraNarrow). On the other hand, the maximum deviation for an OEM4 Narrow metric is 10%. Deviations larger than 5% occur only in ~13% of all considered cases. As a consequence, the slight inaccuracies of the theoretically derived noise variances are not an issue for the OEM4 Narrow configuration and in case that this configuration is used for multipath monitoring none of the measures listed in Table 7-18 is really necessary.

In order to deal with the problem of varying mean metric values obtained from different calibration measurements (see Table 7-19), the statistical spread of the mean values for each satellite-metric combination was determined in the form of confidence intervals. Based on the general procedure introduced in section 7.8.2.2, the 90% confidence intervals were computed based on the following data basis and processing steps:

- For each satellite, 5 passes have been observed
- For each satellite pass and each test metric, the weighted mean metric values and the associated standard deviations were computed; each individual observation has been weighted according to the current C/N_0
- Computation of final mean metric values and associated standard deviations according to equation (150) and the left part of equation (151)
- Computation of 90% confidence intervals based on equation (153)

The confidence intervals are used to compute optimized (more realistic) monitor thresholds. Figure 7-39 illustrates the result of such a computation. The diagram shows the mean metric value of OEM4 Narrow metric M_{16} as obtained for PRN1, the corresponding confidence intervals and the monitoring thresholds with and without consideration of the confidence intervals boundaries (C/N_0=44dBHz, expansion factor m_{exp}=5).

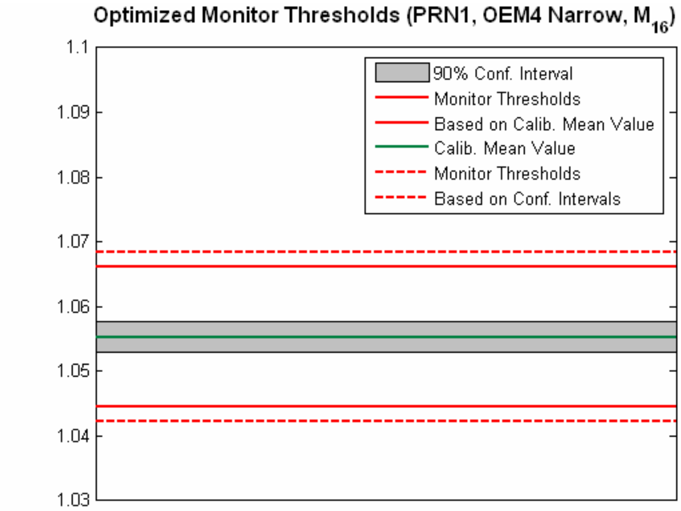

Figure 7-39: Determination of optimized monitor thresholds using confidence intervals.

Since the computation of optimized monitor thresholds does not base on the calibrated mean metric values anymore but rather on the lower and upper boundaries of the confidence intervals, the monitor thresholds increase and the monitoring sensitivity is reduced.

By means of multi-correlator observations obtained by the GPS hardware simulator, the resulting sensitivity reduction was determined for different C/N_0s. The results are illustrated in Figure 7-40. The diagram also contains the monitoring sensitivity without consideration of confidence intervals (gray curves, also illustrated in Figure 7-40).

As can be derived from Figure 7-40, significant degradation of the monitoring sensitivity only occurs for high C/N_0s. In this case, the monitoring sensitivity is degraded by 2-4dB, depending on the actual geometric path delay of the multipath signal. For low C/N_0s, no significant degradation can be observed. This behavior could be expected because the optimized monitor thresholds do not only depend on the actual C/N_0 but also on the width of the confidence interval. Based on the calibrated mean metric value, the monitor thresholds are computed as a multiple of the theoretical noise influence (which is a function of the actual C/N_0) plus half of the confidence interval. The latter contribution is constant for each satellite-metric combination and does not depend on the actual C/N_0. In case of high C/N_0s, the contribution of the confidence interval is comparatively larger than for low C/N_0s. As a result, the relative enlargement of the monitor thresholds is not equal for all C/N_0s. For low C/N_0s, the relative contribution of the confidence interval is much smaller, so that the monitoring sensitivity is not degraded significantly.

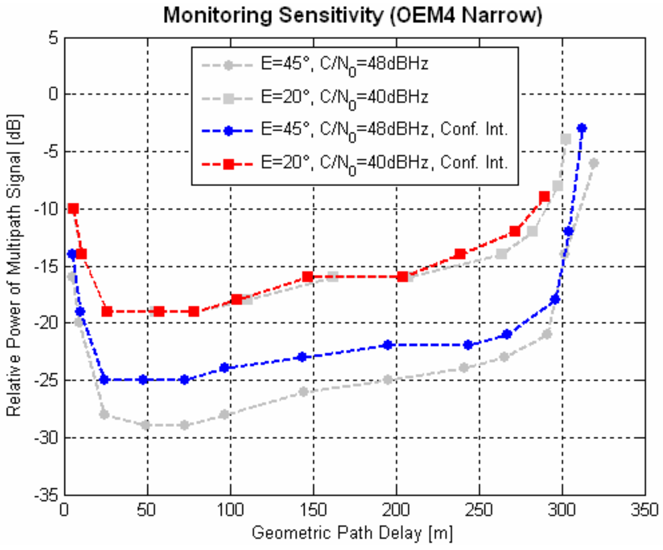

Figure 7-40: Sensitivity of the multipath monitor as a function of the geometric path delay and the mean C/N_0 of the direct signal for increased monitor thresholds due to the consideration of confidence intervals (valid for OEM4 metric M_{105}).

7.10.3 Using RTMM: Monitoring Results

In order to demonstrate RTMM's functional capabilities for multipath monitoring purposes, several long-term measurements have been carried out in different multipath environments. Since RTMM's monitoring sensitivity is rather high, it can be expected that multipath is detected very frequently. Therefore, three different multipath categories were defined:

• Weak multipath (Cat.1):	Metric value exceeds monitor threshold but is still smaller than two times the threshold
• Moderate multipath (Cat.2):	Metric value larger than two times the monitor threshold but smaller than three times the threshold
• Strong multipath (Cat.3):	Metric value exceeds three times the monitor threshold

It should be noted, however, that this classification is not related to the multipath relative power but is only a measure of how far away the actual metric value is deviated from its nominal mean. It is not a statement about how strong the multipath signal really is! Information on all detected multipath signals is stored in a log file. This file contains information about the metrics that have detected the influence, the multipath category (weak/moderate/strong) and the azimuth and elevation of the LOS component for which multipath had been detected. This information can then be used to compute azimuth/elevation diagrams as shown below. The log file containing the detected multipath signals is processed in the following manner:

- A multipath signal is only classified as such if at least two of the four implemented metrics detect the influence simultaneously.
- In case that different metrics detect different multipath categories (weak/moderate/strong multipath), the actually indicated multipath status is the worst of all occurring categories.

As a first step, multi-correlator data has been collected on two successive days during a period of ~10h. Both observations were carried out at the same sidereal time in order to show the day-to-day repeatability of multipath influences. Figure 7-41 illustrates the results of this analysis showing the azimuth and elevation of the LOS component that caused the multipath influence. Note that only Cat.3 multipath has been considered.

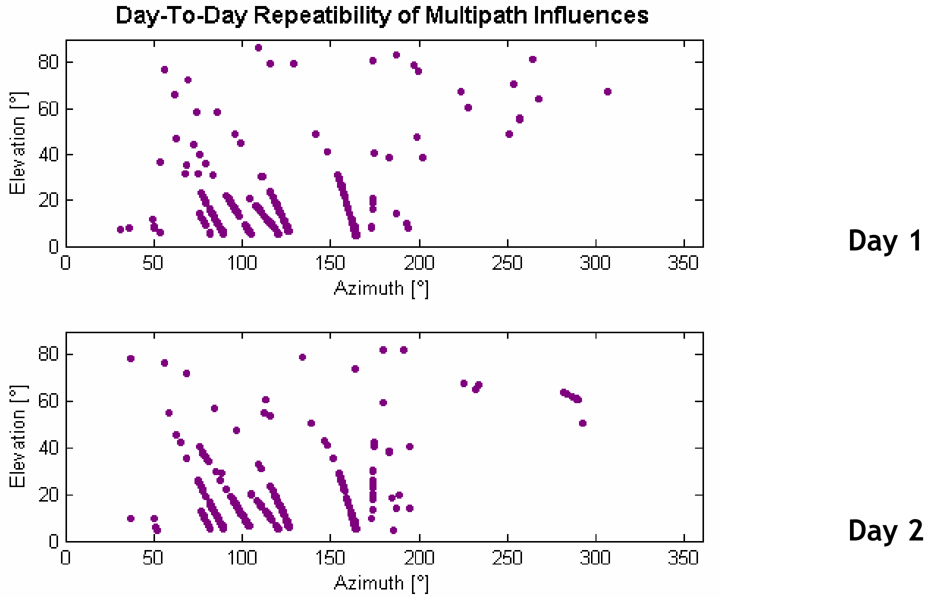

Figure 7-41: Strong multipath influences on two successive days as detected by RTMM.

A closer look at Figure 7-41 reveals that the multipath influences do not seem to show a strict day-to-day repeatability. Possible reasons are:

- Changes in the multipath environment due to passing or parking cars (measurements were carried out in the vicinity of a parking lot)
- Changes of reflector characteristics due to meteorological influences (e.g. rain, moisture)
- The way the monitoring concept is actually implemented: Whenever a satellite rises, sets or its signal gets lost temporarily, the channels are reassigned and the process of smoothing the C/N_0s is reinitialized in turn affecting the monitor thresholds. Since the multi-correlator receiver performs an automatic channel assignment, it cannot be guaranteed that during the first observation period the same satellites are acquired at the same time as during the second observation period. As a result, assuming two observations taken at the same sidereal time (identical geometry), the monitor thresholds at both epochs might be slightly different.

As a next step, multipath influences in different environments were recorded during a period of 24h and - as presented in Figure 7-41 - also visualized in the form of azimuth/elevation diagrams. In this case, only Cat.2 and Cat.3 multipath is considered. However, the percentage and temporal distribution of unaffected signals and Cat.1 – Cat.3 multipath that occurred during the 24h observation period is also presented. Note that due to the automatic channel assignment, it could not be guaranteed that each satellite has been observed during its entire pass.

7.10.3.1 Environment 1: Parking Lot of University FAF Munich

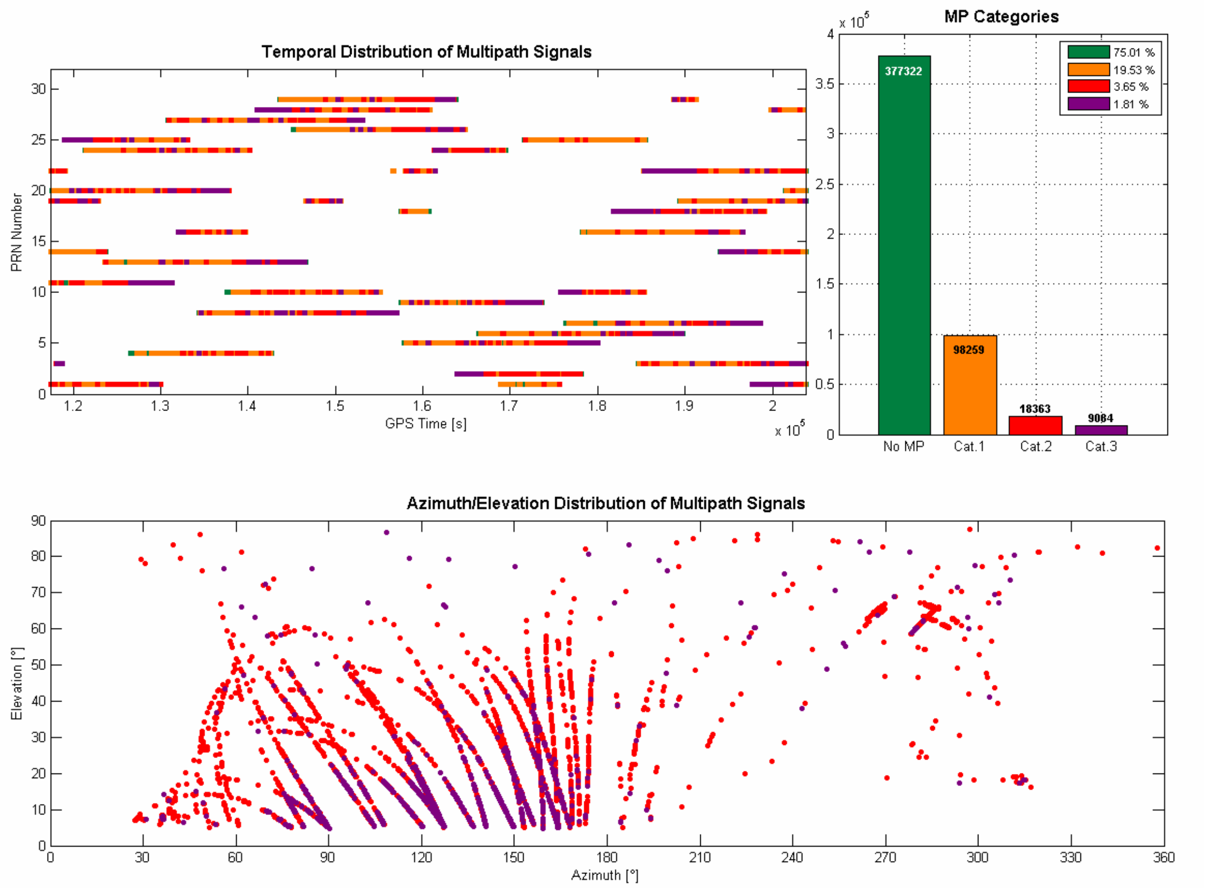

Figure 7-42: Temporal distribution, histogram of multipath categories and azimuth/elevation distribution of cat. 2 and cat. 3 multipath signals for environment 1[8].

---

[8] Source of aerial photos: Google Earth

7.10.3.2 Environment 2: Vicinity of Building 62 of University FAF Munich

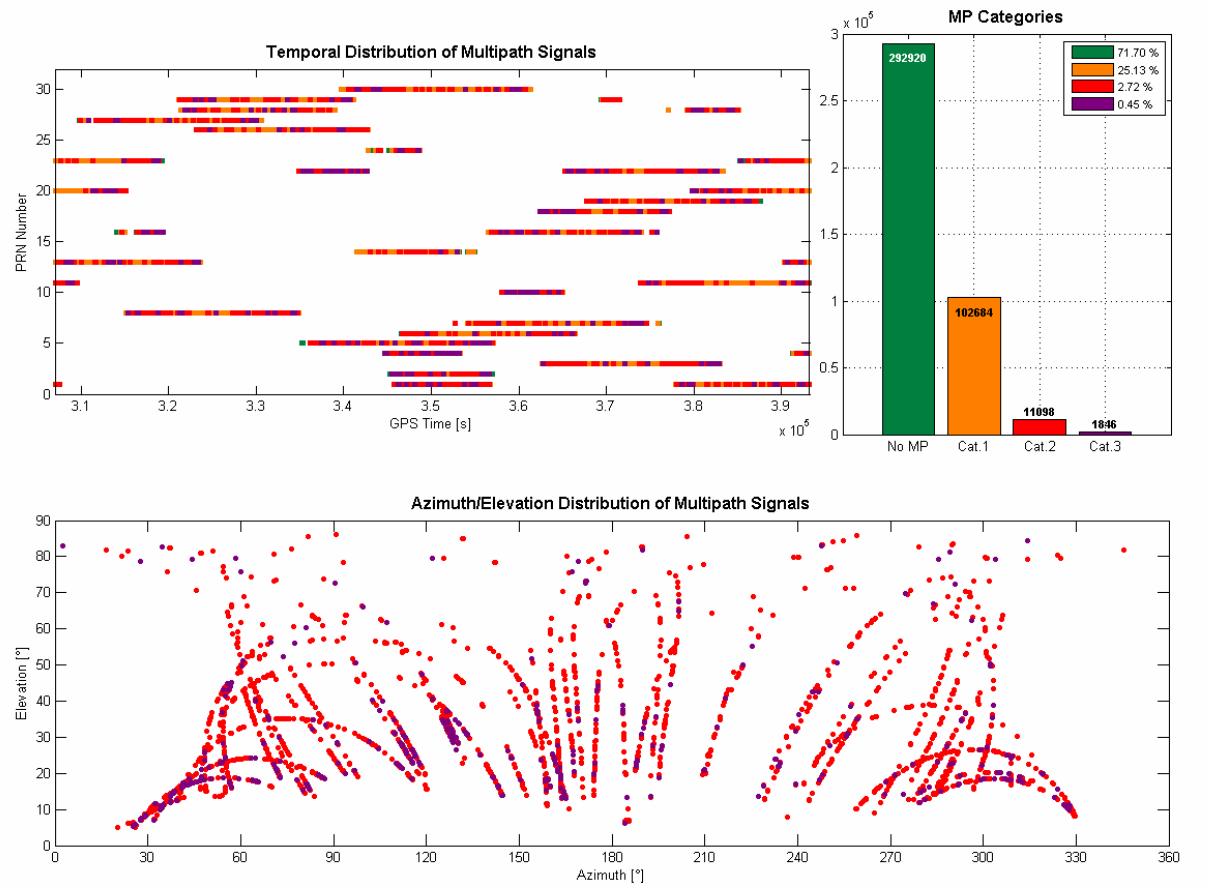

Figure 7-43: Temporal distribution, histogram of multipath categories and azimuth/elevation distribution of cat. 2 and cat. 3 multipath signals for environment 2.

7.10.3.3 Environment 3: Rooftop of Building 62 of University FAF Munich

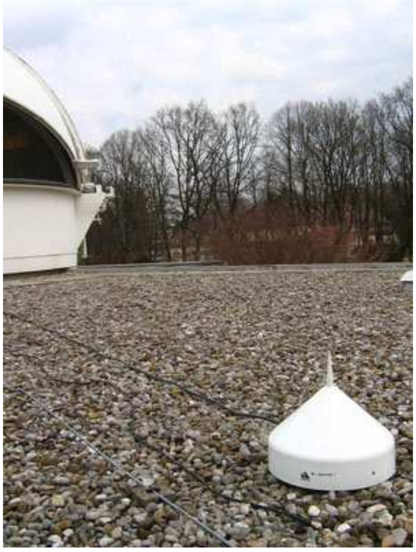

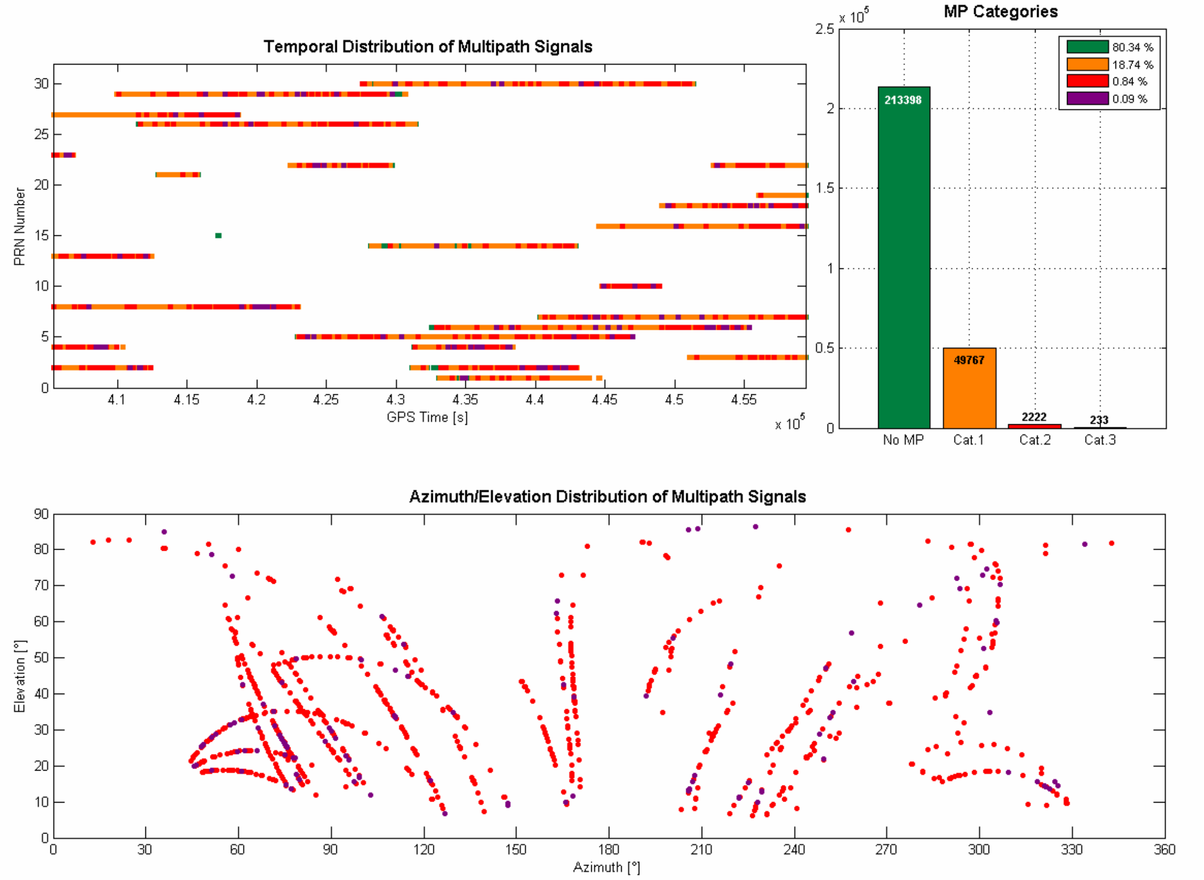

Figure 7-44: Temporal distribution, histogram of multipath categories and azimuth/elevation distribution of cat. 2 and cat. 3 multipath signals for environment 3.

7.10.3.4 Environment 4: Vicinity of Building 105 of University FAF Munich

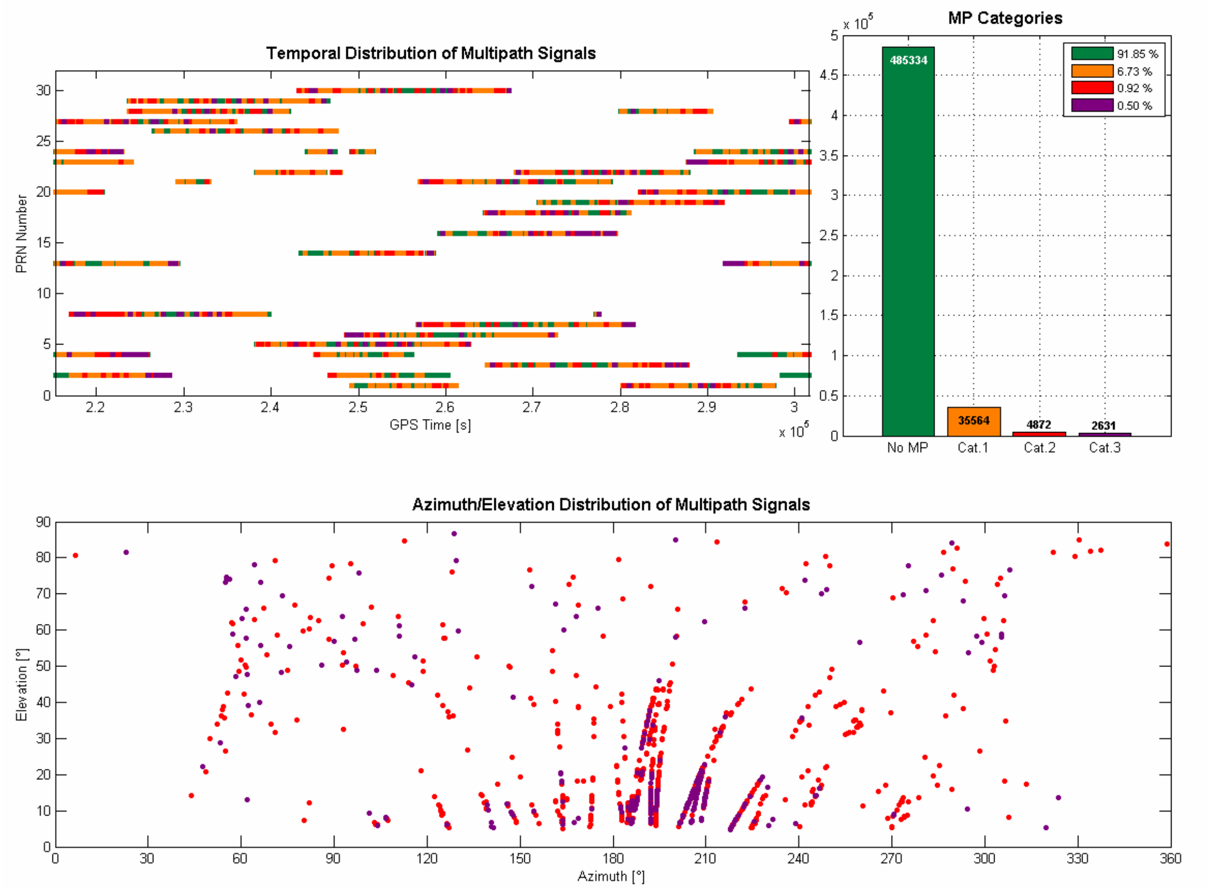

Figure 7-45: Temporal distribution, histogram of multipath categories and azimuth/elevation distribution of cat. 2 and cat. 3 multipath signals for environment 4.

7.10.3.5 Environment 5: Open Environment (Former Airport Neubiberg)

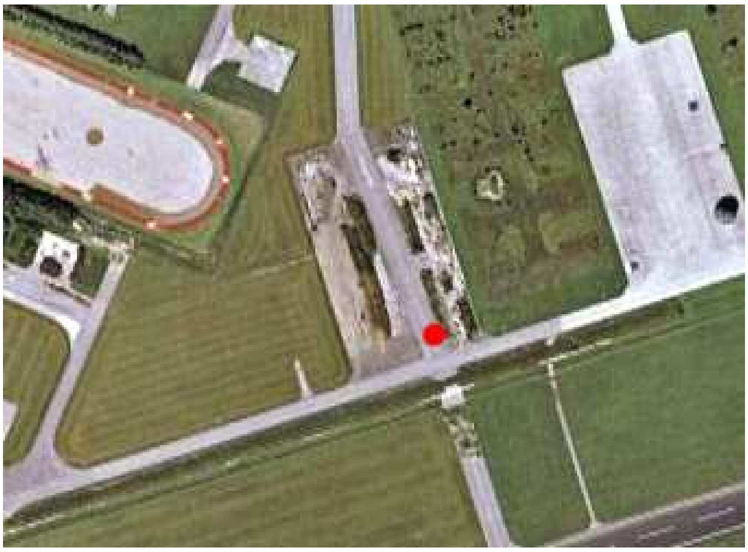

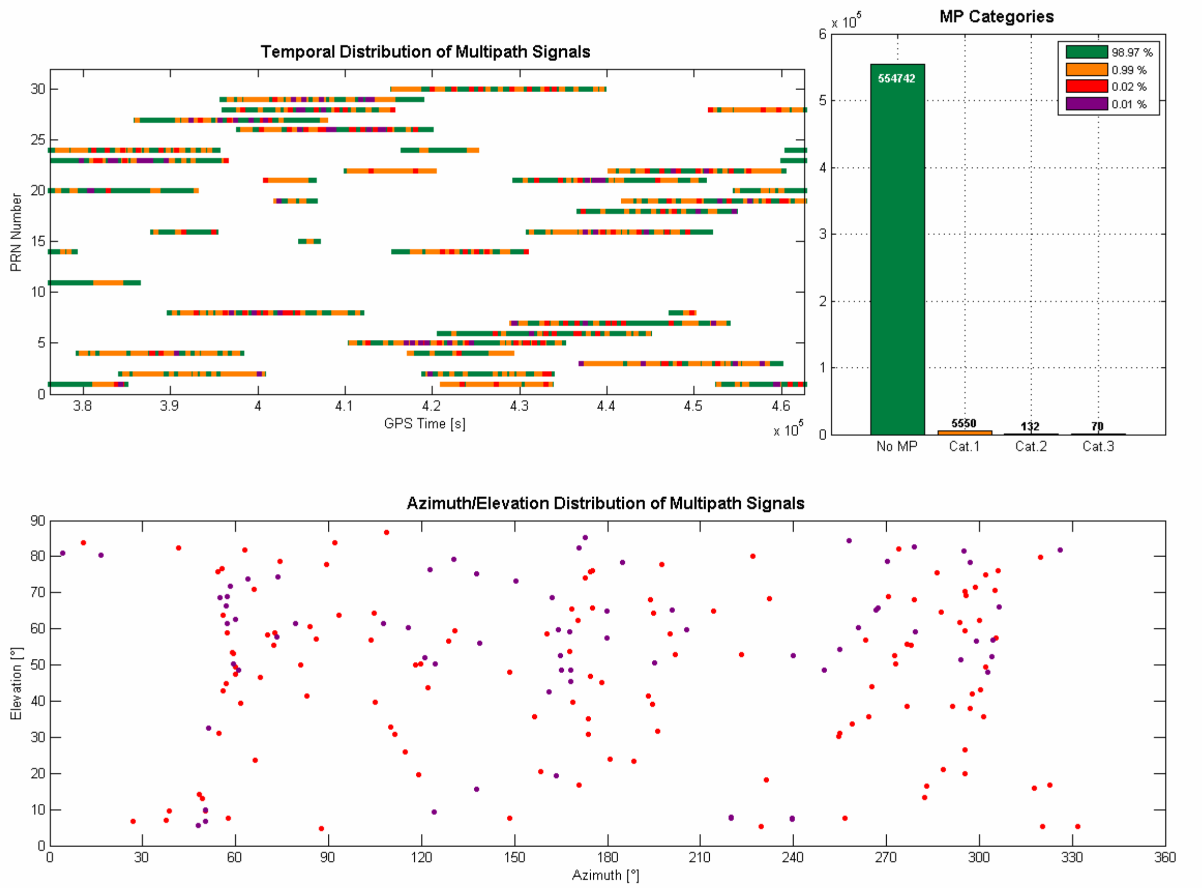

Figure 7-46: Temporal distribution, histogram of multipath categories and azimuth/elevation distribution of cat. 2 and cat. 3 multipath signals for environment 5.

7.10.3.6 Number of Simultaneously Affected PRNs

Table 7-20 illustrates the number of PRNs simultaneously affected by multipath in all five environments during the 24h observation period. Depending on the considered environment, up to 6 signals are affected by multipath simultaneously.

Environment 1

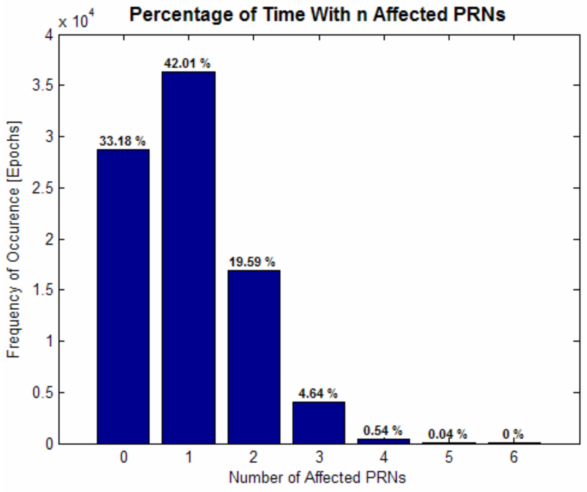

Environment 2

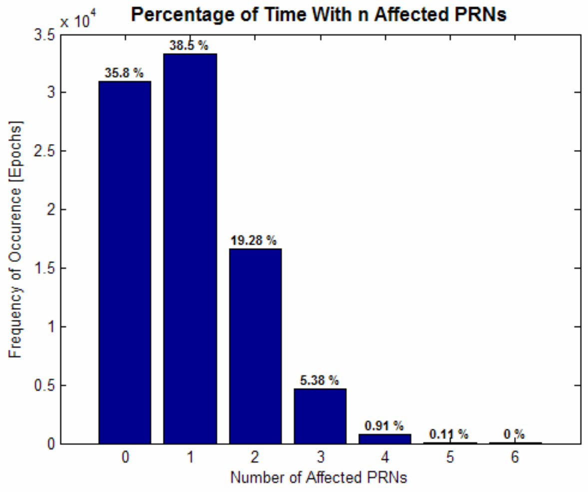

Environment 3

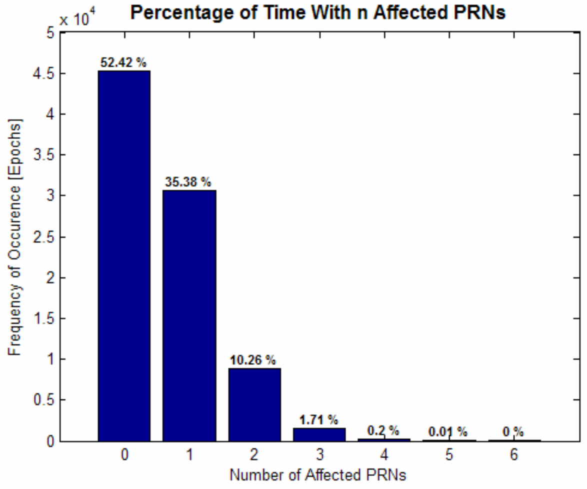

Environment 4

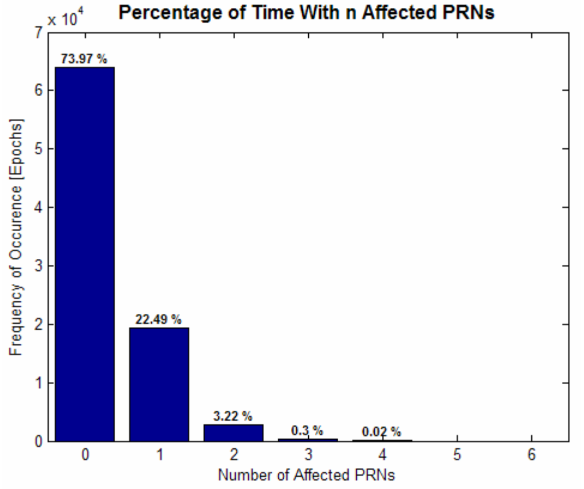

Environment 5

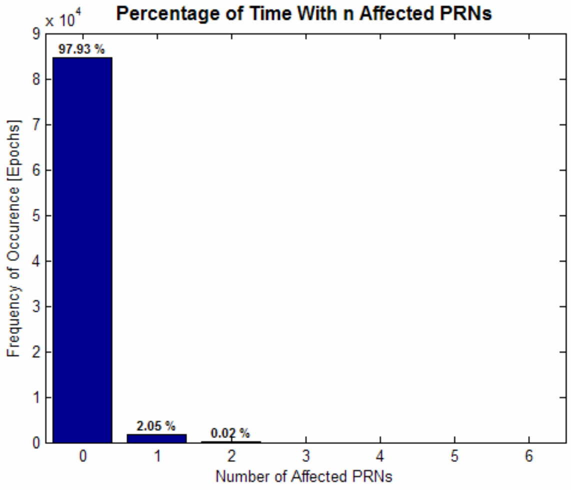

Table 7-20: Percentage of time with *n* PRNs affected by multipath.

7.11 Comparison with other Monitoring Approaches

This section provides a comparison of the RTMM implementation with other monitoring approaches with respect to the monitoring sensitivity. The first monitoring technique to which RTMM is compared is the **C/N_0 monitoring** introduced in section 6.2.2. The monitoring thresholds used for this analysis were derived from C/N_0 observations of PRN5 obtained from the GPS hardware simulator. In order to derive the monitoring sensitivity, multipath signals with different geometric path delays have been simulated and the multipath relative power has been reduced bit by bit until the C/N_0 variations have fallen just below the monitor thresholds (limit of detection). Figure 7-47 illustrates these limits of detection for path delays between 5m and 300m. The monitoring sensitivity has been determined for two different C/N_0s of the LOS component (40 dBHz and 48 dBHz). It is plotted together with the monitoring sensitivity of the RTMM approach.

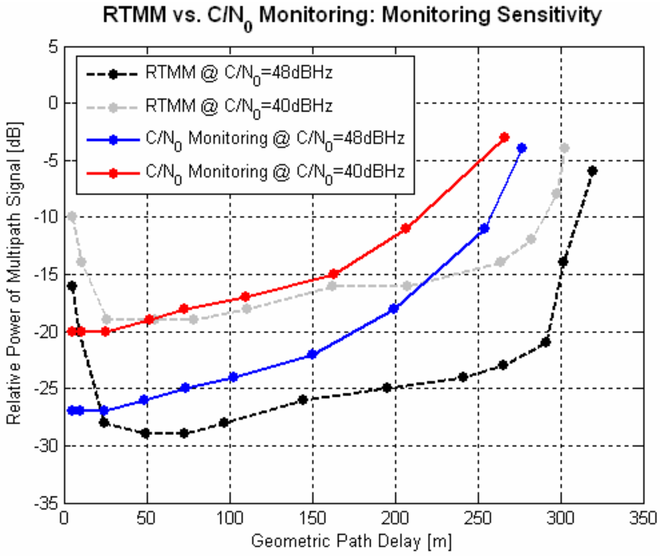

Figure 7-47: Monitoring sensitivity of RTMM (OEM4 NARROW configuration) and C/N_0 monitoring as a function of the geometric path delay.

For medium and long-delay multipath, the monitoring approach based on multi-correlator observations outperforms the C/N_0 monitoring implementation. Especially very long-delay multipath (>270m) cannot be detected by the C/N_0 monitor - whatever power it has. In this area, the RTMM implementation is much more sensitive. For short path delays (<25m), however, the C/N_0 monitor is by far more sensitive than the RTMM implementation. Since this is the area where the residual ranging errors due to undetected multipath are rather large (see Figure 7-26 and Figure 7-27), it is recommended to “augment” the RTMM implementation with a C/N_0 monitor to increase the sensitivity to short-delay multipath.

As a second step, the RTMM performance has been compared to a **CMC monitoring** implementation as described in section 6.1. The monitoring thresholds were derived from smoothed C/N_0 observations according to equations (121) and (122). In order to ensure compatibility with the other monitoring approaches discussed so far, a threshold expansion factor of 5 was used. The original CMC observations were filtered by a 6th order Butterworth filter with cutoff-frequencies of f_{min} = 0.01Hz and f_{max}=0.1Hz. The monitoring sensitivity was determined for three different C/N_0s of the LOS component (40 dBHz, 44 dBHz and 48 dBHz). It is again plotted together with the monitoring sensitivity of the RTMM approach (Figure 7-48).

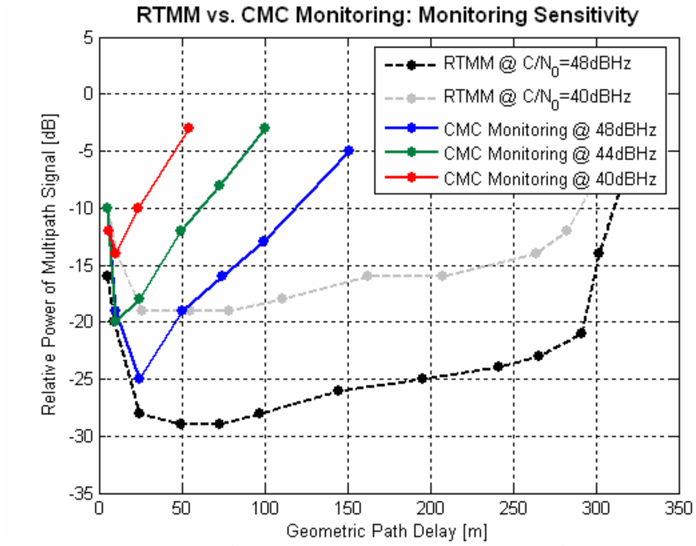

Figure 7-48: Monitoring sensitivity of RTMM (OEM4 NARROW configuration) and CMC monitoring as a function of the geometric path delay.

For short-delay multipath (up to ~25m), the sensitivity of both monitoring approaches is similar. For longer path delays, however, the sensitivity of the RTMM approach outperforms the CMC monitoring approach. Obviously, long-delay multipath cannot be detected at all by the CMC approach. It should be noted, however, that this behavior is mainly due to the characteristics of the underlying Butterworth filter that filters out all multipath variations with periods of 10s or smaller. Such high-frequency variations are caused by medium- to long-delay multipath signals. To enhance the sensitivity to long-delay multipath, the upper cutoff-frequency may be adjusted appropriately or a high-pass filter can be used instead. In any case, the actual sensitivity of a CMC monitoring approach always depends on the filter characteristics (order and cutoff-frequencies).

7.12 Test Metrics for Galileo Signals

As only GPS multi-correlator receivers are available so far, the proposed monitoring scheme has only been implemented for GPS signals. However, with the first Galileo test satellite having been launched in December 2005 and more and more Galileo (test) satellites becoming operational during the next few years, first analyses of how to adopt the monitoring scheme to Galileo signals have already been carried out. This chapter summarizes these activities.

Since commercial Galileo receivers with multi-correlator functionality are not yet available, the analyses focused on the determination of suitable test metrics for Galileo signals. The correlation functions of these signals are known (exact for some details with respect to their actual implementation) and the required computations for the metric selection process (multipath and theoretical noise influence on different test metrics) can be carried out on the basis of this knowledge.

7.12.1 Considered Galileo Signals and Correlator Locations

For the determination of suitable test metrics for Galileo signals, both Open Service (OS) signals at L1 and E5 are considered. For the BOC(1,1), the former OS baseline signal at L1 and the AltBOC(15,10) at E5, bandwidths of 24 and 51MHz are considered, respectively. In addition to the OS signals, the $BOC_{cos}(10,5)$ was also analyzed, representing the PRS signal at E6 with a bandwidth of 40MHz.

For all considered Galileo signals, a correlator configuration consisting of 15 evenly spaced correlators at dedicated correlator locations was used. For the OS signals on L1 and L5, the correlators are distributed between chip offsets of -0.1 and +0.1 resulting in a spacing of ~0.0143 chips. For the PRS signal on E6, the correlators are distributed between offsets of -0.06 and +0.06 (spacing: ~0.0086 chips). By using these 15 correlators and by forming linear test metrics according to Table 7-5, a total amount of 2205 test metrics are available that have to be tested against different multipath relative amplitudes, C/N_0s and different metric selection criteria (exclusion vs. consideration of highly correlated metrics). This results in rather time-consuming computations, the main reason why only 15 correlators have been considered. The correlator locations for all considered signals are illustrated in the following diagrams and listed in the associated tables (rounded to the fourth decimal digit).

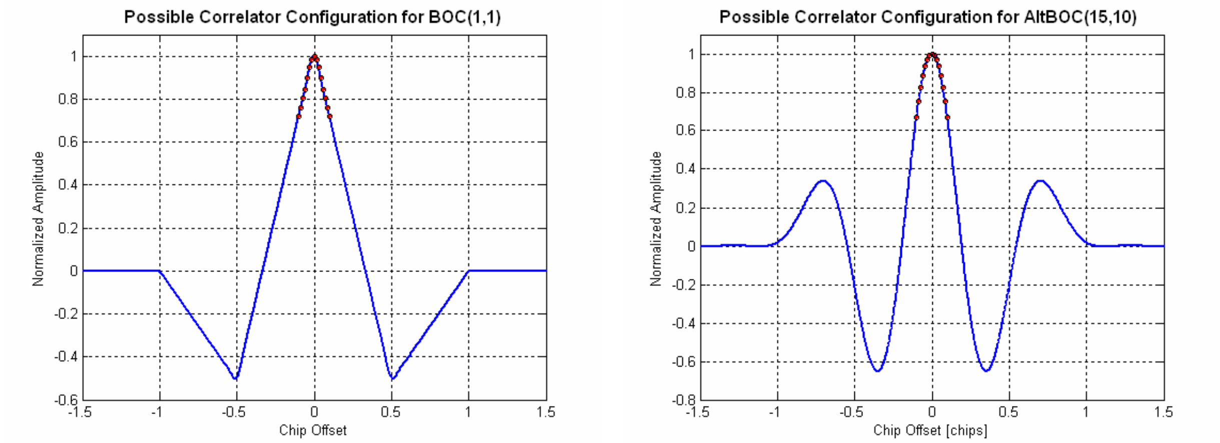

I_1	I_2	I_3	I_4	I_5	I_6	I_7	I_8	I_9	I_{10}	I_{11}	I_{12}	I_{13}	I_{14}	I_{15}
-0.1000	-0.0857	-0.0714	-0.0571	-0.0429	-0.0286	-0.0143	0.0000	0.0143	0.0286	0.0429	0.0571	0.0714	0.0857	0.1000

Figure 7-49: Selected correlator configuration for the Galileo OS signals on L1 and E5.

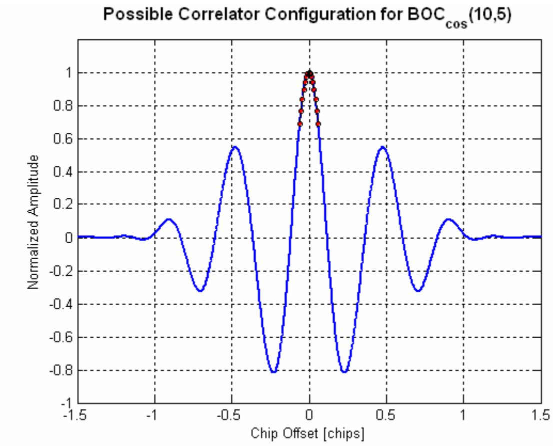

I_1	I_2	I_3	I_4	I_5	I_6	I_7	I_8	I_9	I_{10}	I_{11}	I_{12}	I_{13}	I_{14}	I_{15}
-0.0600	-0.0514	-0.0429	-0.0343	-0.0257	-0.0171	-0.0086	0.0000	0.0086	0.0171	0.0257	0.0343	0.0429	0.0514	0.0600

Figure 7-50: Selected correlator configuration for the Galileo PRS signal on E6.

7.12.2 Suitable Test Metrics

The following tables summarize the results of the metric selection process for the three Galileo signals. As it has been the case for the GPS signals and the three OEM3/OEM4 receiver configurations, the computations were carried out with and without consideration of high correlations between the test metrics. Table 7-21-Table 7-23 also list the theoretical noise variances for each metric.

	Elimination of High Correlations		Maximum Monitoring Sensitivity	
	Metric	Noise Variance	Metric	Noise Variance
Galileo OS @ L1 BOC(1,1)	$M_{273} = \frac{I_1 - I_{15} - I_4 + I_{12}}{I_{15}}$	$\sigma^2_{M_{273}} = \frac{0.7695}{2SNR \cdot T}$	$M_{497} = \frac{I_8}{I_{15}}$	$\sigma^2_{M_{497}} = \frac{1.7751}{2SNR \cdot T}$
	$M_{497} = \frac{I_8}{I_{15}}$	$\sigma^2_{M_{497}} = \frac{1.7751}{2SNR \cdot T}$	$M_{1898} = \frac{I_8 - I_{15}}{I_1}$	$\sigma^2_{M_{1898}} = \frac{0.9001}{2SNR \cdot T}$
	$M_{515} = \frac{I_{12}}{I_{15}}$	$\sigma^2_{M_{515}} = \frac{0.5266}{2SNR \cdot T}$	$M_{1899} = \frac{I_8 - I_{15}}{I_2}$	$\sigma^2_{M_{1899}} = \frac{0.8066}{2SNR \cdot T}$
	$M_{1954} = \frac{I_9 - I_{13}}{I_1}$	$\sigma^2_{M_{1954}} = \frac{0.5415}{2SNR \cdot T}$	$M_{1995} = \frac{I_9 - I_{15}}{I_{15}}$	$\sigma^2_{M_{1995}} = \frac{1.5097}{2SNR \cdot T}$

Table 7-21: Suitable test metrics and theoretical noise variances for the BOC(1,1).

	Elimination of High Correlations		Maximum Monitoring Sensitivity	
	Metric	Noise Variance	Metric	Noise Variance
Galileo OS @ E5 AltBOC(15,10)	$M_{518} = \frac{I_{14}}{I_{15}}$	$\sigma^2_{M_{518}} = \frac{0.0703}{2SNR \cdot T}$	$M_{512} = \frac{I_{11}}{I_{15}}$	$\sigma^2_{M_{512}} = \frac{1.0538}{2SNR \cdot T}$
	$M_{861} = \frac{I_1 - I_{10}}{I_{15}}$	$\sigma^2_{M_{861}} = \frac{1.0205}{2SNR \cdot T}$	$M_{518} = \frac{I_{14}}{I_{15}}$	$\sigma^2_{M_{518}} = \frac{0.0703}{2SNR \cdot T}$
	$M_{2180} = \frac{I_{13} - I_{15}}{I_3}$	$\sigma^2_{M_{2180}} = \frac{0.0195}{2SNR \cdot T}$	$M_{2138} = \frac{I_{12} - I_{14}}{I_3}$	$\sigma^2_{M_{2138}} = \frac{0.0244}{2SNR \cdot T}$
	$M_{2192} = \frac{I_{14} - I_{15}}{I_1}$	$\sigma^2_{M_{2192}} = \frac{0.0091}{2SNR \cdot T}$	$M_{2205} = \frac{I_{14} - I_{15}}{I_{15}}$	$\sigma^2_{M_{2205}} = \frac{0.0703}{2SNR \cdot T}$

Table 7-22: Suitable test metrics and theoretical noise variances for the AltBOC(15,10).

	Elimination of High Correlations		Maximum Monitoring Sensitivity	
	Metric	Noise Variance	Metric	Noise Variance
Galileo PRS @ E6 BOC_{cos}(10,5)	$M_{518} = \frac{I_{14}}{I_{15}}$	$\sigma^2_{M_{518}} = \frac{0.0610}{2SNR \cdot T}$	$M_{512} = \frac{I_{11}}{I_{15}}$	$\sigma^2_{M_{512}} = \frac{0.9111}{2SNR \cdot T}$
	$M_{833} = \frac{I_1 - I_8}{I_{15}}$	$\sigma^2_{M_{833}} = \frac{0.3961}{2SNR \cdot T}$	$M_{517} = \frac{I_{13}}{I_{15}}$	$\sigma^2_{M_{517}} = \frac{0.2385}{2SNR \cdot T}$
	$M_{2108} = \frac{I_{11} - I_{15}}{I_1}$	$\sigma^2_{M_{2108}} = \frac{0.0743}{2SNR \cdot T}$	$M_{518} = \frac{I_{14}}{I_{15}}$	$\sigma^2_{M_{518}} = \frac{0.0610}{2SNR \cdot T}$
	$M_{2192} = \frac{I_{14} - I_{15}}{I_1}$	$\sigma^2_{M_{2192}} = \frac{0.0047}{2SNR \cdot T}$	$M_{2196} = \frac{I_{14} - I_{15}}{I_5}$	$\sigma^2_{M_{2196}} = \frac{0.0044}{2SNR \cdot T}$

Table 7-23: Suitable test metrics and theoretical noise variances for the BOC_{cos}(10,5).

7.13 Summary

In this part of the thesis, it has been successfully demonstrated that multi-correlator observations can be used for multipath monitoring purposes. The formation of linear test metrics and the potential of obtaining instant monitor thresholds from the current C/N_0 has turned out to be an efficient approach to obtain information whether or not an individual signal is affected by multipath. It has also been demonstrated that the proposed monitoring approach is very sensitive even if the multipath signals are relatively weak. In general, information about the current multipath influence could be used to exclude or to de-weight affected satellites during navigation processing. If undetected, (short-delay) multipath signals lead to ranging errors of only a few meters. The following table summarizes all benefits and drawbacks of the proposed multipath monitoring scheme. It also suggests possible solutions for some of the issues related to this monitoring approach.

Benefits	Drawbacks
• Real-time capability • Works with only one receiver (no differencing of observations required) • Works with only one signal (no requirements with respect to the number of visible satellites) • Multipath influence can be unambiguously assigned to a signal • Thresholds depend on actual C/N_0 → no re-calculation of monitor thresholds for different antennas (provided that mean metric values are known) • Detection of relatively weak multipath signals (high sensitivity) • Easy to implement (low computational load) • Additional detection of satellite signal failures (Evil Waveforms) • No residual multipath errors if all multipath influences can be detected and excluded from navigation processing • Works for dynamic applications as well (statement valid for OEM4 receiver, may not apply to other receivers, depends on receiver architecture) • Only few correlators are required (in contrast to the MEDLL approach)	• C/N_0 values vary in case of multipath → monitor thresholds also vary (effect can be reduced by smoothing the C/N_0 values) • Mean metric values are required for threshold computation (requires calibration campaign in a multipath-free environment to ensure undistorted correlation peak observations) • Exclusion of satellite signal → only few healthy satellites may remain, especially in critical environments (e.g. urban canyon, may become a minor problem with use of combined GPS/Galileo and/or the application of suitable weighting schemes) • Residual ranging errors due to undetected multipath • Does not work without LOS component when only one strong multipath signal is present (mainly an issue in urban environments) • Mean metric values are subject to changing environmental conditions at the calibration site (e.g. weather conditions, influence of water or snow)

Table 7-24: Benefits and drawbacks of the proposed real-time multipath monitor.

Table 7-24 indicates that it is also possible to detect Evil Waveforms by using RTMM. However, since RTMM detects all influences that are significantly higher than the influence of thermal noise, the monitoring implementation cannot really distinguish between multipath signals and Evil Waveforms. Nevertheless, in case that the multipath influences for a specific site are recorded over a long period of time, the monitor thresholds can be adjusted such that all multipath variations are below the thresholds. Metric values that exceed these (adjusted) thresholds are most likely due to the influence of Evil Waveforms.

Provided that the signal structure and the signal's correlation function are known sufficiently well, the proposed monitoring scheme can be easily applied to other navigation signals. Suitable linear test metrics for some of the future Galileo signals have been derived along with their corresponding theoretical noise variances, providing a starting-point for the implementation of the monitoring scheme for Galileo.

Part III.

Appendices:
Test Metric Noise, Monitoring Sensitivity and Wavelet Analysis

The final part of this thesis contains further information on selected topics in the form of three major appendices. Appendix A provides the necessary formulas to determine the theoretical noise variances of different types of test metrics (simple ratio tests, symmetric ratio tests, differential ratio tests and delta tests) that are used for the implementation of the real-time multipath monitor introduced in chapter 7. Appendix B contains the derivation of an empirical function to determine the monitoring sensitivity of the proposed real-time multipath monitor for arbitrary C/N_0s, threshold expansion factors and integration times as a function of the geometric path delay. Finally, appendix C provides some basics on wavelet analysis, which can be used for multipath detection and mitigation. The remaining appendices contain lists of references, figures, tables and acronyms.

8. Appendix A: Noise Variances of Metric Types

In this section, the theoretical noise variances of different types of test metrics for multipath monitoring purposes will be derived. They will be expressed as a function of the considered correlators and the distance between certain correlator pairs. All derivations assume that the underlying correlation functions are symmetrical. Since this is an idealized assumption that does not hold true for actual receiver implementations, the derived formulas are only approximations.

The correlators that are used to set up the test metrics are denoted as I_X, I_Y and I_Z, depending on what type of metric is discussed. As already introduced in section 7.4.2, these I-samples have the following mean, variance and covariance properties:

$$\begin{aligned} I_X &= \sqrt{2 \cdot SNR \cdot T} \cdot R(d_{I_X}) = \sqrt{2 \cdot SNR \cdot T} \cdot R(X) \\ \sigma_I^2 &= 1 \\ \sigma_{I_X,I_Y} &= \sigma_{X,Y} = R(d_{I_X,I_Y}) = R(d_{X,Y}) \end{aligned} \tag{154}$$

where $d_{I,X}$ is the correlator spacing between an arbitrary I_X-sample and the punctual I-sample I_0 and $d_{IX,IY}$ is the correlator spacing between two I-samples I_X and I_Y. $R(d)$ is the normalized correlation amplitude at $\tau=d$. T is the accumulation time and SNR the signal-to-noise ratio that can be expressed as a function of the C/N_0 as reported by the receiver. The theoretical noise variances can be obtained by application of the law of error propagation. Starting point for all analyses are the metric equations that can be expressed as a function of the correlators I_X, I_Y,… used to set up the metric m_i:

$$m_i = f(I_X, I_Y, \ldots) \tag{155}$$

The Jacobian matrix A contains the partial derivatives and can be expressed as follows:

$$A = \begin{bmatrix} \dfrac{\partial m_i}{\partial I_X} & \dfrac{\partial m_i}{\partial I_Y} & \cdots \end{bmatrix} \tag{156}$$

The symmetrical covariance matrix $D(l)$ of the correlators takes on the form

$$D(l) = \begin{bmatrix} \sigma_X^2 & \sigma_{X,Y} & \cdots \\ \sigma_{Y,X} & \sigma_Y^2 & \cdots \\ \vdots & \vdots & \ddots \end{bmatrix} \tag{157}$$

and the covariance matrix $D(m)$ of the considered test metric can be computed according to the law of error propagation:

$$D(m) = A \cdot D(l) \cdot A^T \tag{158}$$

In the following, these computation will be carried out for one metric type at a time, so that the resulting matrix $D(m)$ is equal to the desired noise variance σ^2_{mi}.

8.1 Simple Ratio Tests

$$m_i = \frac{I_X}{I_Y}$$

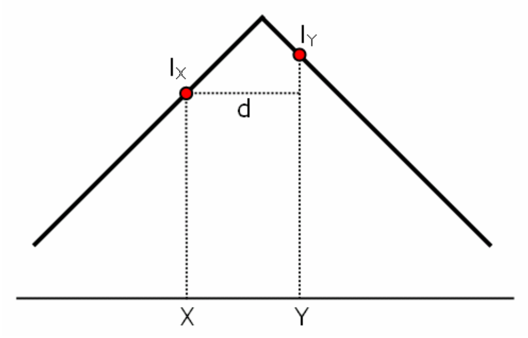

Partial derivatives and Jacobian matrix:

$$I_X = \sqrt{2 \cdot SNR \cdot T} \cdot R(X)$$
$$I_Y = \sqrt{2 \cdot SNR \cdot T} \cdot R(Y)$$

$$\frac{\partial m_i}{\partial I_X} = \frac{1}{I_Y}; \frac{\partial m_i}{\partial I_Y} = -\frac{I_X}{I_Y^2}$$

Jacobian Matrix

$$A = \frac{1}{\sqrt{2 \cdot SNR \cdot T}} \begin{bmatrix} \frac{1}{R(Y)} & -\frac{R(X)}{R^2(Y)} \end{bmatrix}$$

Covariance matrix *D(l)* for considered correlators:

$d = |X - Y| = |Y - X|$,
due to assumed symmetrical correlation function

$$D(l) = \begin{bmatrix} \sigma_X^2 & \sigma_{X,Y} \\ \sigma_{Y,X} & \sigma_Y^2 \end{bmatrix} = \begin{bmatrix} 1 & R(|X - Y|) \\ R(|Y - X|) & 1 \end{bmatrix}$$
$$= \begin{bmatrix} 1 & R(|X - Y|) \\ R(|X - Y|) & 1 \end{bmatrix} = \begin{bmatrix} 1 & R(d) \\ R(d) & 1 \end{bmatrix}$$

Variance of test metric *m_i*:

$$D(m) = \sigma_{m,i}^2 = A \cdot D(l) \cdot A^T$$

$$\sigma_{m,i}^2 = \frac{R^2(X) - 2R(d)R(X)R(Y) + R^2(Y)}{2 \cdot SNR \cdot T \cdot R^4(Y)}$$

8.2 Symmetric Ratio Tests

$$m_i = \frac{I_{-X} - I_{+X}}{I_Y}$$

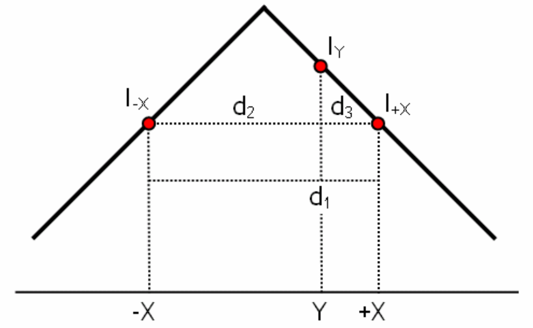

Partial derivatives and Jacobian matrix:

$$I_{-X} = \sqrt{2 \cdot SNR \cdot T} \cdot R(-X)$$
$$I_{+X} = \sqrt{2 \cdot SNR \cdot T} \cdot R(+X)$$
$$I_Y = \sqrt{2 \cdot SNR \cdot T} \cdot R(Y)$$

$$\frac{\partial m_i}{\partial I_{-X}} = \frac{1}{I_Y}; \frac{\partial m_i}{\partial I_{+X}} = -\frac{1}{I_Y}; \frac{\partial m_i}{\partial I_Y} = -\frac{I_{-X} - I_{+X}}{I_Y^2}$$

Jacobian Matrix
$R(-X) = R(+X) = R(X)$,
due to assumed symmetrical correlation function

$$A = \frac{1}{\sqrt{2 \cdot SNR \cdot T}} \begin{bmatrix} \frac{1}{R(Y)} & -\frac{1}{R(Y)} & 0 \end{bmatrix}$$

Covariance matrix *D(l)* for considered correlators:

$$d_1 = |-X - X| = 2X$$
$$d_2 = |-X - Y|$$
$$d_3 = |X - Y|$$

$$D(l) = \begin{bmatrix} \sigma_{-X}^2 & \sigma_{-X,+X} & \sigma_{-X,Y} \\ \sigma_{-X,+X} & \sigma_{+X}^2 & \sigma_{+X,Y} \\ \sigma_{-X,Y} & \sigma_{+X,Y} & \sigma_Y^2 \end{bmatrix} = \begin{bmatrix} 1 & R(d_1) & R(d_2) \\ R(d_1) & 1 & R(d_3) \\ R(d_2) & R(d_3) & 1 \end{bmatrix}$$
$$= \begin{bmatrix} 1 & R(2X) & R(d_2) \\ R(2X) & 1 & R(d_3) \\ R(d_2) & R(d_3) & 1 \end{bmatrix}$$

Variance of test metric *m_i*:

$$D(m) = \sigma_{m,i}^2 = A \cdot D(l) \cdot A^T$$

$$\sigma_{m,i}^2 = \frac{2 - 2R(2X)}{2 \cdot SNR \cdot T \cdot R^2(Y)}$$

8.3 Differential Ratio Tests

$$m_i = \frac{I_X - I_Y}{I_Z}$$

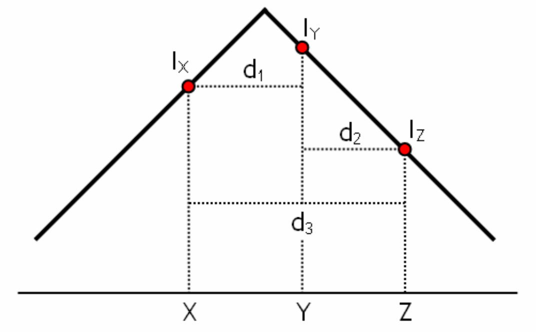

Partial derivatives and Jacobian matrix:

$$I_X = \sqrt{2 \cdot SNR \cdot T} \cdot R(X)$$
$$I_Y = \sqrt{2 \cdot SNR \cdot T} \cdot R(Y)$$
$$I_Z = \sqrt{2 \cdot SNR \cdot T} \cdot R(Z)$$

$$\frac{\partial m_i}{\partial I_X} = \frac{1}{I_Z}; \frac{\partial m_i}{\partial I_Y} = -\frac{1}{I_Z}; \frac{\partial m_i}{\partial I_Z} = -\frac{I_X - I_Y}{I_Z^2}$$

Jacobian Matrix

$$A = \frac{1}{\sqrt{2 \cdot SNR \cdot T}} \begin{bmatrix} \frac{1}{R(Z)} & -\frac{1}{R(Z)} & -\frac{R(X) - R(Y)}{R^2(Z)} \end{bmatrix}$$

Covariance matrix *D(l)* for considered correlators:

$$d_1 = |X - Y| = |Y - X|$$
$$d_2 = |Y - Z| = |Z - Y|$$
$$d_3 = |X - Z| = |Z - X|$$

$$D(l) = \begin{bmatrix} \sigma_X^2 & \sigma_{X,Y} & \sigma_{X,Z} \\ \sigma_{X,Y} & \sigma_Y^2 & \sigma_{Y,Z} \\ \sigma_{X,Z} & \sigma_{Y,Z} & \sigma_Z^2 \end{bmatrix} = \begin{bmatrix} 1 & R(d_1) & R(d_3) \\ R(d_1) & 1 & R(d_2) \\ R(d_3) & R(d_2) & 1 \end{bmatrix}$$

Variance of test metric *m_i*:

$$D(m) = \sigma_{m,i}^2 = A \cdot D(l) \cdot A^T$$

$$\sigma_{m,i}^2 = \frac{2R(Z)[1 - R(d_1)] + \left[R(X) - R(Y)\right]\left[2R(d_2) - 2R(d_3) + \frac{R(X) - R(Y)}{R(Z)}\right]}{2 \cdot SNR \cdot T \cdot R^3(Z)}$$

8.4 Delta Tests

$$m_i = \frac{(I_{-X} - I_{+X}) - (I_{-Y} - I_{+Y})}{I_Z}$$

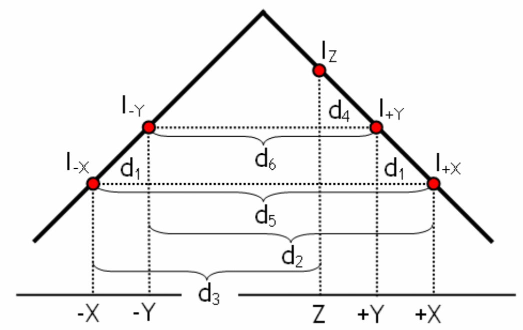

Partial derivatives and Jacobian matrix:

$$I_{-X} = \sqrt{2 \cdot SNR \cdot T} \cdot R(-X)$$
$$I_{+X} = \sqrt{2 \cdot SNR \cdot T} \cdot R(+X)$$
$$I_{-Y} = \sqrt{2 \cdot SNR \cdot T} \cdot R(-Y)$$
$$I_{+Y} = \sqrt{2 \cdot SNR \cdot T} \cdot R(+Y)$$
$$I_Z = \sqrt{2 \cdot SNR \cdot T} \cdot R(Z)$$

$$\frac{\partial m_i}{\partial I_{-X}} = \frac{1}{I_Z};\ \frac{\partial m_i}{\partial I_{+X}} = -\frac{1}{I_Z};\ \frac{\partial m_i}{\partial I_{-Y}} = -\frac{1}{I_Z};\ \frac{\partial m_i}{\partial I_{-Y}} = \frac{1}{I_Z};$$
$$\frac{\partial m_i}{\partial I_Z} = -\frac{I_{-X} - I_{+X} - I_{-Y} + I_{+Y}}{I_Z^2}$$

Jacobian Matrix
$R(-X) = R(+X) = R(X)$
$R(-Y) = R(+Y) = R(Y)$,
due to assumed symmetrical correlation function

$$A = \frac{1}{\sqrt{2 \cdot SNR \cdot T}} \begin{bmatrix} \frac{1}{R(Z)} & -\frac{1}{R(Z)} & -\frac{1}{R(Z)} & \frac{1}{R(Z)} & 0 \end{bmatrix}$$

Covariance matrix *D(l)* for considered correlators:

$$d_1 = |X - Y| = |Y - X|$$
$$d_2 = X + Y$$
$$d_3 = |Z + X|$$
$$d_4 = |Y - Z| = |Z - Y|$$
$$d_5 = 2X$$
$$d_6 = 2Y$$

$$D(l) = \begin{bmatrix} \sigma_{-X}^2 & \sigma_{-X,+X} & \sigma_{-X,-Y} & \sigma_{-X,+Y} & \sigma_{-X,Z} \\ \sigma_{-X,+X} & \sigma_{+X}^2 & \sigma_{+X,-Y} & \sigma_{+X,+Y} & \sigma_{+X,Z} \\ \sigma_{-X,-Y} & \sigma_{+X,-Y} & \sigma_{-Y}^2 & \sigma_{-Y,+Y} & \sigma_{-Y,Z} \\ \sigma_{-X,+Y} & \sigma_{+X,+Y} & \sigma_{-Y,+Y} & \sigma_{+Y}^2 & \sigma_{+Y,Z} \\ \sigma_{-X,Z} & \sigma_{+X,Z} & \sigma_{-Y,Z} & \sigma_{+Y,Z} & \sigma_Z^2 \end{bmatrix}$$
$$= \begin{bmatrix} 1 & R(d_5) & R(d_1) & R(d_2) & R(d_5 + d_3) \\ R(d_5) & 1 & R(d_2) & R(d_1) & R(d_3) \\ R(d_1) & R(d_2) & 1 & R(d_6) & R(d_6 + d_4) \\ R(d_2) & R(d_1) & R(d_6) & 1 & R(d_4) \\ R(d_5 + d_3) & R(d_3) & R(d_6 + d_4) & R(d_4) & 1 \end{bmatrix}$$

Variance of test metric *m_i*:

$$D(m) = \sigma_{m,i}^2 = A \cdot D(l) \cdot A^T$$

$$\sigma_{m,i}^2 = \frac{4 - 2R(2X) - 4R(d_1) + 4R(d_2) - 2R(2Y)}{2 \cdot SNR \cdot T \cdot R^2(Z)}$$

9. Appendix B: Monitoring Sensitivity

This chapter contains the derivation of an empirical function to determine the monitoring sensitivity of the OEM4 NARROW configuration (for which the monitoring approach has been optimized) for arbitrary C/N$_0$s, threshold expansion factors and integration times as a function of the geometric path delay (denoted as *x* in the following paragraphs).

9.1 Reference Function

The reference function is determined on the basis of the monitoring sensitivity which has been evaluated for dedicated path delays at C/N$_0$s of 40dBHz and 48dBHz (see section 7.7.4). Both sets of points can be fitted with an 8th order polynomial. The resulting functions F_{48dBHz} and F_{44dBHz} (blue and red solid curves in Figure 9-1) can now be combined to obtain the reference function F_{Ref}, which is valid for a C/N$_0$ of 44dBHz (green curve in Figure 9-1):

$$F_{Ref} = \frac{F_{48dBHz} + F_{40dBHz}}{2} \tag{159}$$

The reference function F_{Ref} is an 8th order polynomial with the following coefficients:

$$F_{Ref} = a_1x^8 + a_2x^7 + a_3x^6 + a_4x^5 + a_5x^4 + a_6x^3 + a_7x^2 + a_8x + a_9 \tag{160}$$

with

$a_1 = 12003$ $a_2 = -52697$ $a_3 = 96866$ $a_4 = -96568$ $a_5 = 56618$ $a_6 = -19844$

$a_7 = 4045.4$ $a_8 = -430.96$ $a_9 = -6.2587$

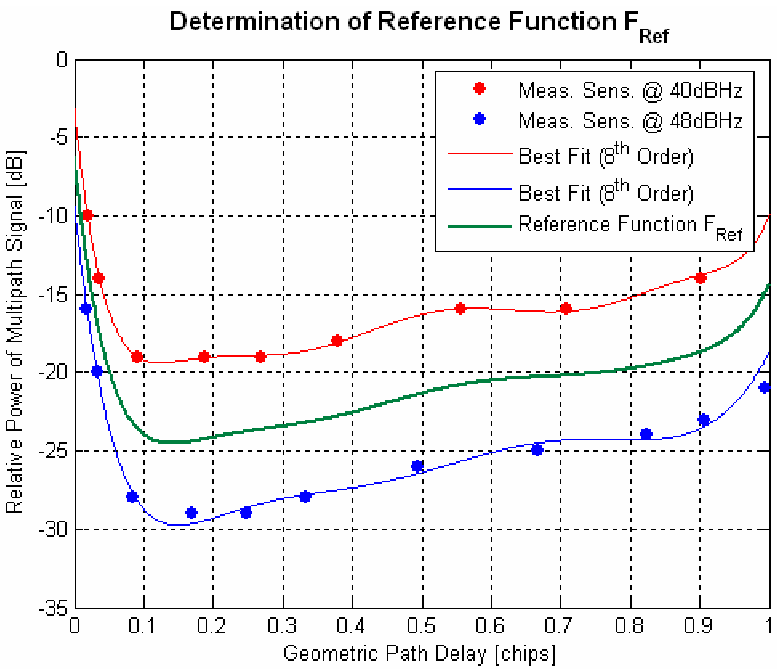

Figure 9-1: Determination of a reference function F_{Ref} for sensitivity computations.

Since the functions F_{48dBHz} and F_{44dBHz} have been determined for a threshold expansion factor of m_0=5 and an integration time of T_0=1s, the reference function F_{Ref} is only valid for this set of parameters. Based on F_{Ref}, the monitoring sensitivity for other sets of parameters can be determined by adding three terms. The first term, $\Delta F_{C/N0}$, accounts for any changes of the C/N_0 relative to the reference value of 44dBHz. The second term, ΔF_{exp}, accounts for the use of a threshold expansion factor different from m_0=5, and the third term, ΔF_T, accounts for the use of an integration time different from T_0=1s.

9.2 Delta Functions

The first Delta Function, $\Delta F_{C/N0}$, represents the sensitivity change per dBHz and can be expressed as an 8th order polynomial:

$$\Delta F_{C/N_0} = \frac{F_{48dBHz} - F_{Ref}}{4} \text{ or } \Delta F_{C/N_0} = \frac{F_{Ref} - F_{40dBHz}}{4} \text{ or } \Delta F_{C/N_0} = \frac{F_{48dBHz} - F_{40dBHz}}{8} \tag{161}$$

$$\Delta F_{C/N_0} = b_1 x^8 + b_2 x^7 + b_3 x^6 + b_4 x^5 + b_5 x^4 + b_6 x^3 + b_7 x^2 + b_8 x + b_9 \tag{162}$$

with

b_1 = -2374.1 b_2 = 9650.4 b_3 = -15882 b_4 = 13530 b_5 = -6310.9 b_6 = 1550.7
b_7 = -167.05 b_8 = 2.168 b_9 = -0.77577

$\Delta F_{C/N0}$ must be multiplied with the difference $\Delta C/N_0$ between the C/N_0 of interest and the reference value of 44dBHz and added to the reference function F_{Ref} to obtain the monitoring sensitivity, which is valid for the desired C/N_0. The second Delta Function, ΔF_{exp}, represents an offset which can be derived from equation (148)

$$\Delta F_{exp} = 20 \cdot \lg\left(\frac{m_0}{m_{exp}}\right) \tag{163}$$

and the third Delta Function, ΔF_T, can also be derived from a modified version of equation (148) by expressing the standard deviations as a function of the integration times T_0 and T (see equation (145)) and by assuming identical threshold expansion factors m_{exp}:

$$\Delta F_T = 20 \cdot \lg\left(\frac{\sigma_m(T_0)}{\sigma_m(T)}\right) = 20 \cdot \lg\left(\frac{\sqrt{\frac{\sigma_m^2}{2SNR \cdot T_0}}}{\sqrt{\frac{\sigma_m^2}{2SNR \cdot T}}}\right) = 20 \cdot \lg\left(\sqrt{\frac{T}{T_0}}\right) \tag{164}$$

The reference function and the three Delta Functions can be combined to obtain the monitoring sensitivity for a given combination of C/N_0, m_{exp} and T:

$$\begin{aligned} F_{Sens}(C/N_0, m_{exp}, T) &= F_{44dBHz, m_0=5, T_0=1s} + \Delta C/N_0 \cdot \Delta F_{C/N_0} - \Delta F_{exp} - \Delta F_T \\ &= F_{Ref} + \left(C/N_0 - C/N_{0,Ref}\right) \cdot \Delta F_{C/N_0} - 20\lg\left(\frac{m_0}{m_{exp}}\sqrt{\frac{T}{T_0}}\right) \end{aligned} \tag{165}$$

Assuming reference values of C/$N_{0,Ref}$=44dBHz, m_0=5 and T_0=1s, equation (165) simplifies to

$$F_{Sens}(C/N_0, m_{exp}, T) = F_{Ref} + \Delta F_{C/N_0}\left(C/N_0 - 44\right) - 20\lg\left(\frac{5}{m_{exp}}\sqrt{T[s]}\right) [dB]. \tag{166}$$

Note that equation (166) has been derived empirically and provides best results when operating within or near the limits of the red and blue curve illustrated in Figure 9-1.

9.3 Examples

9.3.1 Using Different Expansion Factors

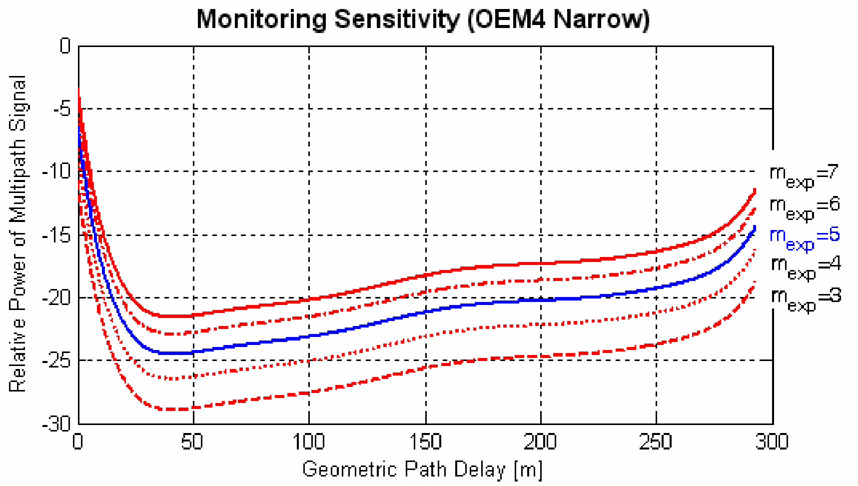

Figure 9-2: Monitoring sensitivity for different threshold expansion factors assuming an integration time of T=1000ms and a C/N_0 of 44dBHz.

9.3.2 Using Different Integration Times

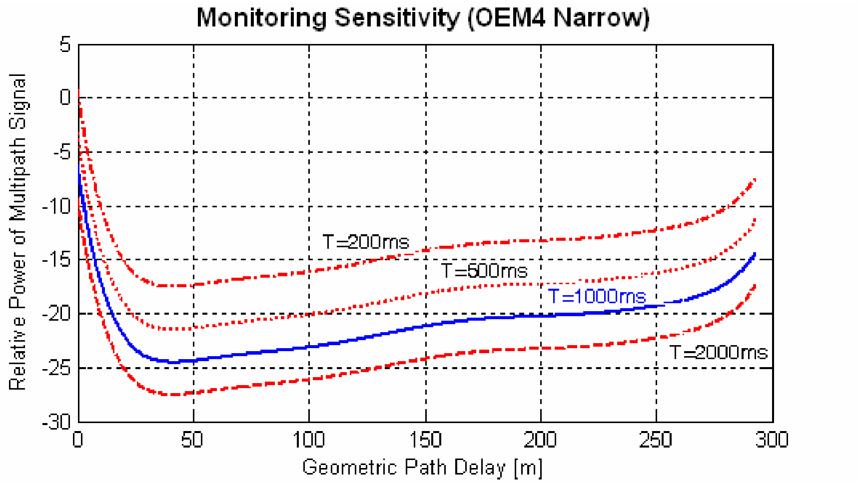

Figure 9-3: Monitoring sensitivity for different integration times (m_{exp}=5, C/N_0=44dBHz).

10. Appendix C: Wavelet Analysis

This chapter provides a brief introduction of some important aspects of wavelet analysis. The main objective is to provide the reader with the basic ideas behind this concept without focusing too much on the mathematics on which wavelets are based. After some introductory notes on the role that wavelets play in modern signal processing, the different types of wavelets and possible applications as well as the general concept behind the continuous and discrete wavelet transforms are discussed in more detail.

10.1 Wavelet Basics

10.1.1 Fourier vs. Wavelet Analysis

Wavelets are a mathematical tool to obtain a hierarchical representation of an arbitrary function. They provide the possibility to divide a function into a sum of rough approximations and finer and finer details. The basic concept is the representation of a function f as a linear combination or superimposition of a basis function Ψ_K, multiplied by the coefficients c_K ([BÄNI 2002]):

$$f = \sum_{k} c_K \Psi_K \tag{167}$$

One example for such a representation is the Fourier series by which a periodic function can be divided into a sum of harmonic waves. Assuming that the cycle duration is $T>0$ and the corresponding angular frequency is $\omega=2\pi/T$, the function $f(t)$ can be expressed by the Fourier series

$$f(t) = \frac{a_0}{2} + \sum_{k=1}^{\infty} a_k \cos(k\omega t) + b_k \sin(k\omega t)\,, \tag{168}$$

where $a_0/2$ is the constant (non-varying) signal component. The Fourier coefficients a_k and b_k can be expressed as follows:

$$\begin{aligned} a_k &= \frac{2}{T}\int_0^T f(t)\cos(k\omega t)dt \quad \text{for } k=0,1,2,\ldots \\ b_k &= \frac{2}{T}\int_0^T f(t)\sin(k\omega t)dt \quad \text{for } k=1,2,\ldots \end{aligned} \tag{169}$$

In this case, sine and cosine functions are used as basis functions Ψ_K. The basic drawback of using sine and cosine functions is that they span the entire domain of t ($t \in]-\infty;+\infty[$), i.e. they do not contain local information. Whenever it is necessary to identify or represent local characteristics (e.g. discontinuities, drifts, trends, abrupt changes, beginnings and ends of events) in an approximation according to equation (168), the use of a Fourier series is unsuitable. Furthermore, when using Fourier analysis, it is not possible to determine when a particular event took place, i.e. time information disappears.

In general, a Fourier series can also be used to compress a function. For this purpose, only a limited number of Fourier coefficients are computed and stored for later reconstruction. Omitting one single coefficient a_k or b_k, however, leads to an approximation error which occurs within the entire domain of t. To reduce this error, the number of Fourier coefficients has to be increased, resulting in poor compression rates. Both limitations (poor compression, possible quality forfeit of reconstructed function) resulted in big efforts to find other, more suitable basis functions Ψ_K, for which the following requirements can be stated ([BÄNI 2002]):

- Analysis (computation of coefficients c_k) and synthesis (reconstruction of f based on computed coefficients) are numerically stable[9] and can be computed efficiently.
- Basis functions should have a good temporal localization, i.e. they have to contain local information in the time domain ($\Psi_K \neq 0$ only within a limited interval)
- The basis functions should also have a good localization in the frequency domain
- The basis functions form an orthonormal system (to ensure unambiguous determination of coefficients c_k)

Basis functions that meet these requirements (or at least the latter one), are called "Wavelets". They are waveforms of limited duration and have an average value of zero. Starting point is a special basis function, the so-called mother wavelet $\Psi(t)$. Further wavelets $\Psi_{m,n}(t)$ (m,n $\in$ Z) can be obtained by shifting and scaling the mother wavelet:

$$\Psi_{m,n}(t) := 2^{-\frac{m}{2}}\Psi(2^{-m}t - n)\,. \tag{170}$$

Similar to the Fourier analysis, whose objective is to decompose a signal into sine and cosine waves of different frequencies, wavelet analysis breaks up a signal into shifted and scaled versions of the mother wavelet. The basic concept is illustrated in Figure 10-1.

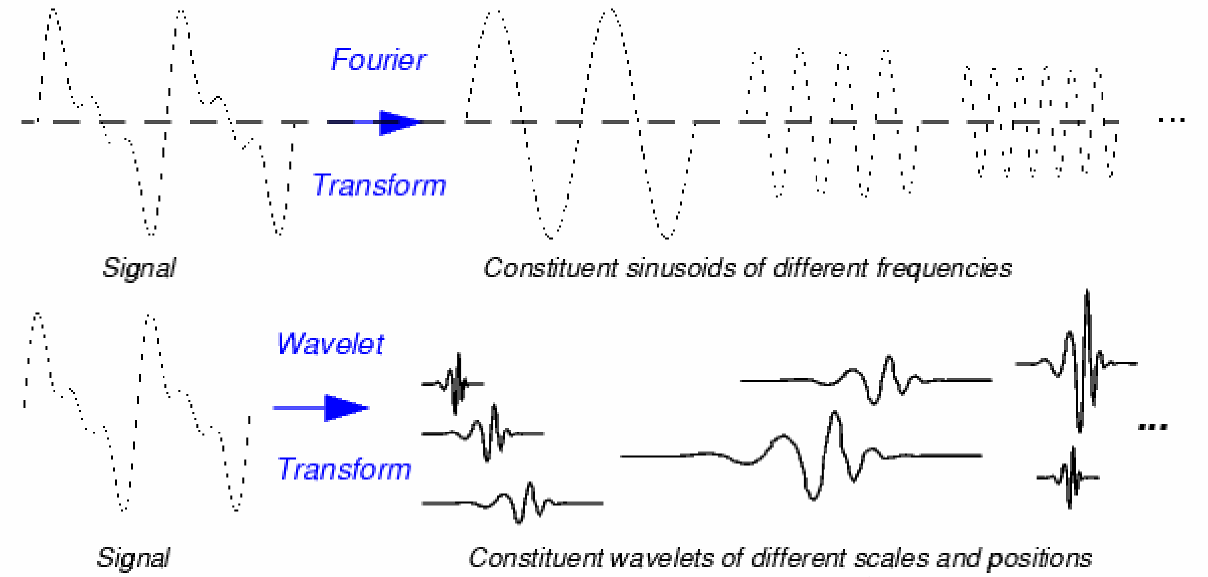

Figure 10-1: Fourier vs. wavelet analysis.[10]

10.1.2 Types of Wavelets

The result of any type of wavelet analysis depends on the mother wavelet used to process the input data. Figure 10-2 illustrates several important mother wavelets that are being used for a variety of signal processing applications.

---

[9] Small imprecision of c_k results in only small inaccuracy of the reconstructed function

[10] adopted from Matlab help files

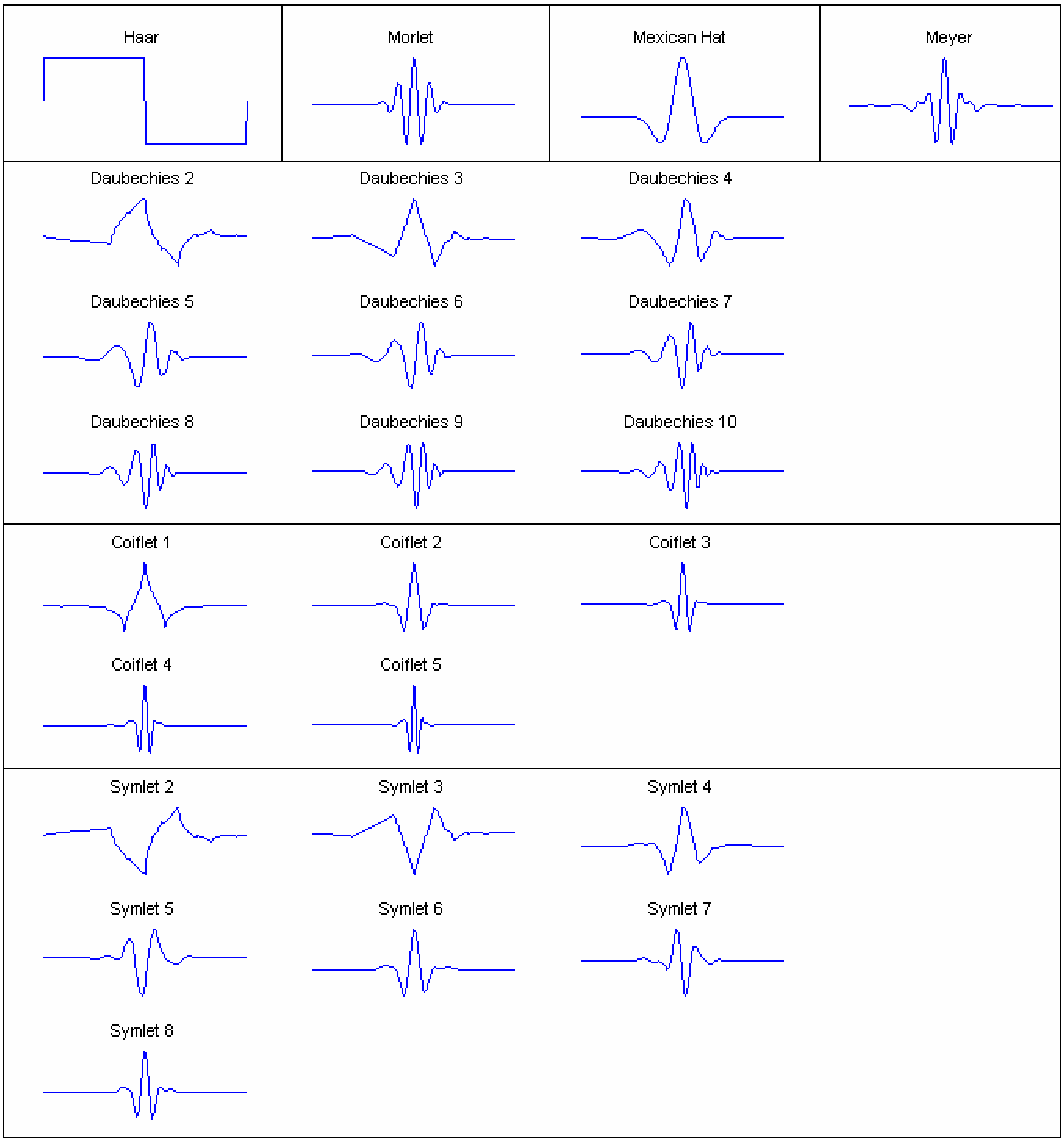

Figure 10-2: Different types of mother wavelets.

In addition to the wavelets illustrated in Figure 10-2, other wavelets such as the family of biorthogonal and reverse biorthogonal wavelets can be used as well.

10.1.3 Applications

Wavelet analysis can be used for a variety of signal processing applications. Without going into too much detail, the following list provides an overview on the most important applications:

- Detection of discontinuities (detection of the exact instant of signal changes, e.g. abrupt frequency changes)
- Detection of long-term trends (e.g. ramps that may be hidden in the noise floor and are thus not visible in the original data)
- Detection of self-similar (or fractal) signals

- Resolving a signal into sinusoids of different frequencies (in this context, wavelet analysis can perform similar tasks as Fourier analysis)
- Suppression of parts of the original signal (e.g. a polynomial trend)
- De-Noising of signals and images
- Compression of signals and images

All these applications base on the continuous and discrete wavelet transform including signal decomposition. Both approaches are the topic of the following sections.

10.2 Continuous Wavelet Transform (CWT)

Starting point for the discussion of the continuous wavelet transform is the basic concept of using shifted and scaled versions of a mother wavelet. Figure 10-3 illustrates shifted and scaled versions of the mother wavelet “Daubechies 4”.

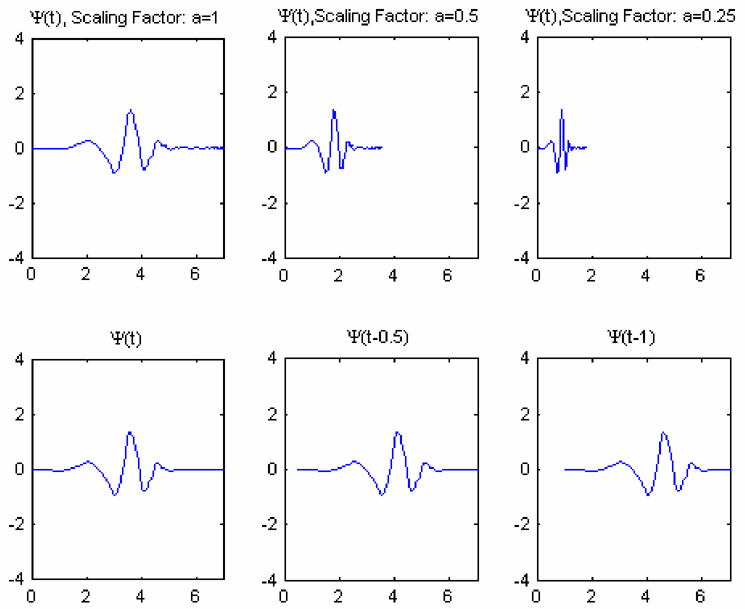

Figure 10-3: Shifted and scaled versions of the Daubechies4 mother wavelet.

These shifted and scaled versions of the mother wavelet are used to compute the CWT, which is simply the sum over the entire signal duration multiplied by scaled, shifted versions of the wavelet. This process produces wavelet coefficients that are a function of scale and position (i.e. time). In general, a basic algorithm may be expressed by the following steps:

- The original wavelet (at scale a=1) is compared to a section at the start of the original signal. For this section, a wavelet coefficient *C* is computed that indicates how closely correlated the wavelet is with this section of the signal. A higher value of *C* indicates a higher similarity between the signal section and the wavelet (in case that signal and wavelet energy are equal to one, *C* can be interpreted as a correlation coefficient).
- As a next step, the wavelet is shifted to the right and the computation of *C* is repeated for the next section of the original signal and repeated until the whole signal has been covered (see Figure 10-4 for an illustration of these steps).

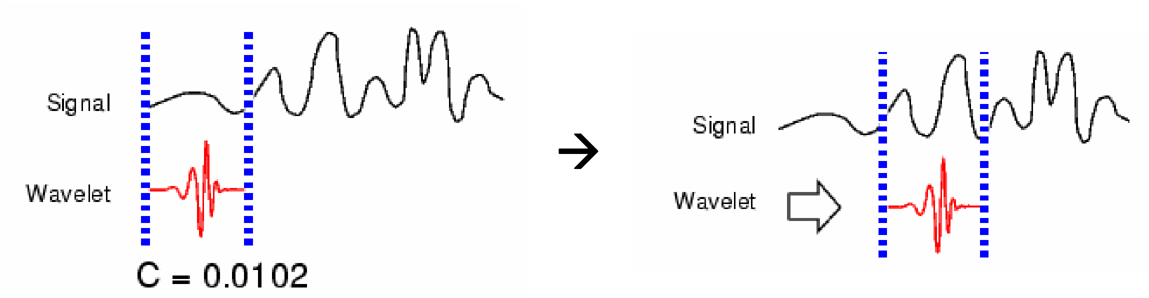

Figure 10-4: Comparison of wavelet shape and original signal for different sections.

- These two steps are now repeated with a scaled version of the wavelet (see Figure 10-5 for a graphical illustration).

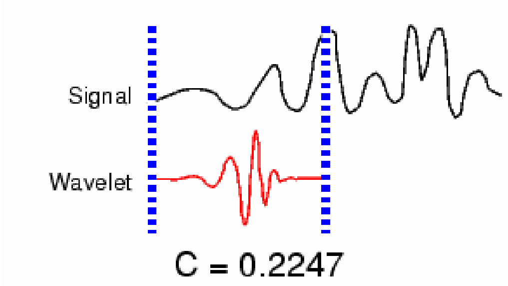

Figure 10-5: Comparison of scaled (stretched) wavelet shape and original signal.[11]

- Finally, the whole procedure is repeated for all desired scales.

The result is an array of coefficients $C_{a,t}$ for different scales a and different wavelet positions (corresponding to different points in time t). The wavelet coefficients $C_{a,t}$ at different scales can be plotted as a function of time and typically look like Figure 6-5. Higher scales correspond to the more stretched wavelets, i.e. the section of the signal to which the stretched wavelet is compared is longer as well. Thus, by using stretched wavelets, only coarse signal characteristics (the low frequency content) can be measured. On the other hand, low scales are a suitable way to measure the high frequency characteristics of a signal.

10.3 Discrete Wavelet Transform (DWT) and Signal Decomposition

As the computation of wavelet coefficients at every possible scale is a time-consuming and laborious process and since it generates a lot of data, one possible approach to reduce the amount of computations is to carry them out for only a subset of scales and positions. It can be shown that by using dyadic scales and positions (scales and positions based on powers of two), the analysis is more efficient but still accurate enough. Such an analysis is called Discrete Wavelet Transform (DWT). An efficient way to implement this scheme, which is based on the use of filters, has been proposed by [MALLAT 1989] and is roughly described in the following paragraphs.

Most signals consist of a low-frequency component (defining the global signal characteristic) and a high-frequency content (e.g. noise). If the high-frequency content is filtered out, the resulting signal is a good approximation of the original signal. In terms of wavelet analysis, an approximation is the high-scale, low-frequency component of a signal. If, on

---

[11] Figure 10-4 and Figure 10-5 adopted from Matlab help files

the other hand, the low-frequency content is filtered out, the detailed structure of the signal becomes visible. Thus, in terms of wavelet processing, the details are the low-scale, high-frequency components. This filtering process can be illustrated as follows:

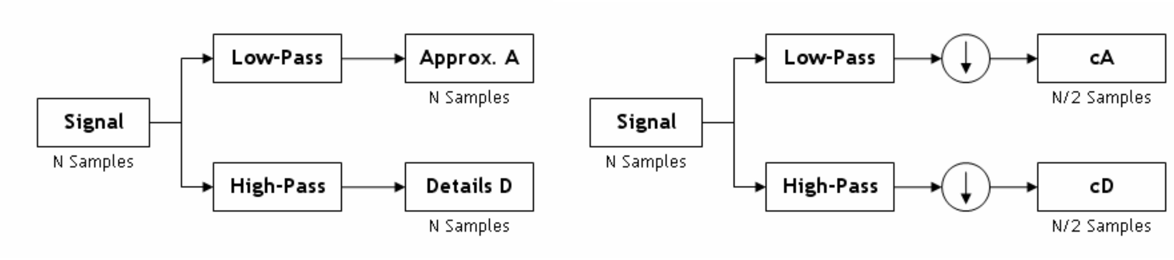

Figure 10-6: Filtering of the original signal with and without downsampling.

The original signal passes through the two filters (high- and low-pass) resulting in two filtered signals. Both filtered versions consist of the same *N* samples as the original signal (left diagram in Figure 10-6). As a result, the amount of information has doubled increasing the effort to compute wavelet coefficients. Therefore, after passing the filter, the signals are down-sampled in the sense that only every second data point is used for the subsequent computations (right diagram in Figure 10-6). The outputs are indicated by *cA* and *cD*, respectively, and represent the DWT coefficients. Figure 10-7 illustrates the obtained DWT coefficients for a sinusoidal signal (high-frequency noise added to an ideal sinusoid). The computations were performed with Matlab's wavelet processing toolbox.

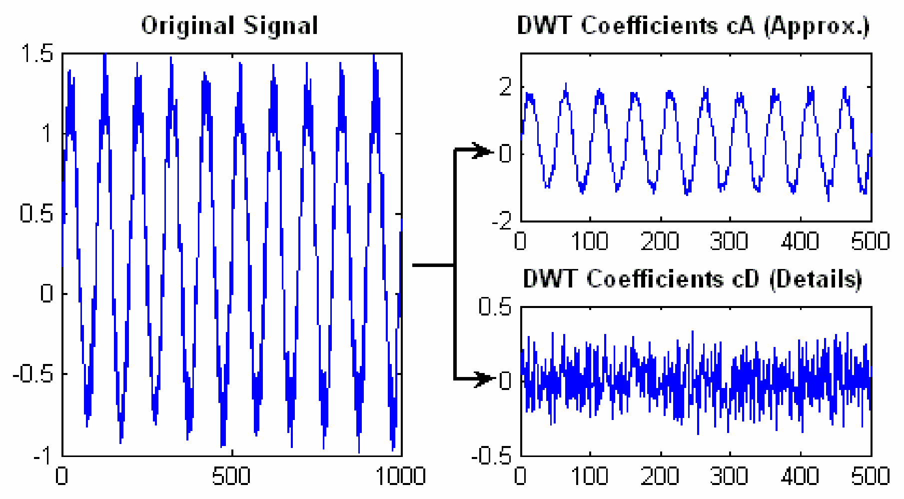

Figure 10-7: Computation of DWT coefficients for decomposition level 1.

This process can be iterated, with successive approximations being decomposed again (increase of the decomposition level), so that one signal can be broken down into many lower resolution components.

The main difference between the CWT and the DWT is the set of scales and positions at which they operate. In contrast to the DWT, the CWT can operate at every scale, from that of the original signal up to some maximum scale that only depends on the details one wishes to detect and the available computing power. For the CWT, the term “continuous” is used in the sense that the analyzing wavelet is shifted smoothly over the entire domain of the original signal.

11. Appendix D: References

AKOS, D., PHELTS, R. E., PULLEN, S., ENGE, P. (2000): *Signal Quality Monitoring: Test Results*, Proceedings of the National Technical Meeting of the Satellite Division of the Institute of Navigation, ION-NTM 2000, January 26-28, 2000, Anaheim, California

ALBAN, S., AKOS, D., ROCK, S., GEBRE-EGZIABHER, D. (2003): *Performance Analysis and Architectures for INS-Aided GPS Tracking Loops*, Proceedings of the National Technical Meeting of the Satellite Division of the Institute of Navigation, January 22-24, 2003, Anaheim, California, USA

ALOI, D, VAN GRAAS, F. (1999): *Analysis of the Effects of Earth-Surface Based Multipath Reflections on GPS Code-Phase Measurements*, Proceedings of the 55th Annual Meeting of the Satellite Division of the Institute of Navigation, ION-AM 1999, 28-30 June 1999, Cambridge, Massachusetts, 609-618

AULD, J. (jonathan.auld@novatel.ca), 13 July 2005: RE: *Multi-Correlator Observations: Technical Question*, email to M. Irsigler (markus.irsigler@unibw.de)

AUSTRALIAN GOVERNMENT (2007): MTSAT Technical Information, Bureau of Meteorology, available from: http://www.bom.gov.au/sat/MTSAT/MTSAT.shtml (accessed January 2007)

AVILA-RODRIGUEZ, J.A., HEIN, G. W., IRSIGLER, M., PANY, T. (2004): *Combined Galileo/GPS Frequency and Signal Performance Analysis*, Proceedings of the International Technical Meeting of the Satellite Division of the Institute of Navigation, ION GNSS 2004, September 21-24, 2004, Long Beach, California

AVILA-RODRIGUEZ, J.-A., HEIN, G.W., IRSIGLER, M., WALLNER, S. (2005): *Revised Combined Galileo/GPS Frequency and Signal Performance Analysis,* Proceedings of the 18th International Technical Meeting of the Satellite Division of the Institute of Navigation, ION GNSS 2005, September 13-16, 2005, Long Beach, California

AVILA-RODRIGUEZ J.A., PANY T., HEIN G.W. (2006): *Bounds on Signal Performance Regarding Multipath-Estimating Discriminators*, Proceedings of the International Technical Meeting of the Institute of Navigation, ION-GNSS 2006, 26-29 September, 2006, Fort Worth Convention Center, Fort Worth, Texas

AXELRAD, P., COMP, C. AND MACDORAN, P. (1994): *Use of Signal-To-Noise Ratio for Multipath Error Correction in GPS Differential Phase Measurements: Methodology and Experimental Results*, Proceedings of the 7th International Technical Meeting of the Satellite Division of the Institute of Navigation, ION-GPS 94, September 20-23, 1994, Salt Lake City, Utah, 655-666

BAUER, M. (1997): *Vermessung und Ortung mit Satelliten*, Wichmann-Verlag, Heidelberg

BÄNI, W. (2002): *Wavelets: Eine Einführung für Ingenieure*, Oldenbourg Wissenschafts-verlag Gmbh, München, 2002, ISBN 3-486-25427-8

BECKER, D., THIEL, K. H., HARTL, P. (1994): A Special Method of Managing Multipath Effects, Proceedings of the 7th International Technical Meeting of the Satellite Division of the Institute of Navigation, ION-GPS 94, September 20-23, 1994, Salt Lake City, Utah, 157 - 163

BECKER, D., THIEL, K-H., HARTL, PH. (1994*): A Special Method of Managing Multipath Effects*, Proceedings of the 7th International Technical Meeting of the Satellite Division of the Institute of Navigation, ION-GPS 94, September 20-23, 1994, Salt Lake City, Utah, 157-163

BECKMANN. P, SPIZZICHINO, A. (1987): The Scattering of Electromagnetic Waves From Rough Surfaces, Artec House Inc., 1987, ISBN 0-89006-238-2

BETZ, J. (2002): *Binary Offset Carrier Modulations for Radionavigation*, Navigation, Journal of the Institute of Navigation, Vol. 48, No. 4, Winter 2001-2002, 227-246

BETZ, J., GOLDSTEIN, D. (2002): *Candidate Designs for an Additional Civil Signal in GPS Spectral Bands*, Proceedings of the National Technical Meeting of the Institute of Navigation, January 28-30, 2002, San Diego, CA

BOITHIAS, L. (1987): *Radio Wave Propagation*, North Oxford Academic Publishers Ltd, London, ISBN 0-946536-06-6

BRAASCH, M. (1992): *Characterization of GPS Multipath Errors in the Final Approach Environment*, Proceedings of the 5th International Technical Meeting of the Satellite Division of the Institute of Navigation, ION-GPS 92, September 16-18, 1992, Albuquerque, New Mexico, 383-394

BRAASCH, M. (1996): *Multipath Effects*, In: GPS Positioning System Theory and Applications Vol. 1, Progress in Astronautics and Aeronautics Vol. 163. American Institute of Aeronautics and Astronautics., pp. 547-568

BRAASCH, M., VAN DIERENDONCK (1999): *GPS Receiver Architectures and Measurements*, Proceedings of the IEEE, Vol. 87, No. 1, January 1999

BRENNER, M., REUTER, R., SCHIPPER, B. (1998): GPS Landing System Multipath Evaluation Techniques and Results, Proceedings of the 11th International Technical Meeting of the Satellite Division of the Institute of Navigation, ION-GPS 98, September 1998, Nashville, Tennessee, 1025-1034

BROWN, R. G. (1992): *A Baseline GPS RAIM Scheme and a Note on the Equivalence of Three RAIM Methods*, Navigation, Journal of the Institute of Navigation, Vol. 39, No. 3, Fall 1992

CANNON, E., LACHAPELLE, G., QIU, W., FRODGE, S., REMONDI, B. (1994): *Performance Analysis of a Narrow Correlator Spacing Receiver for Precise Static GPS Positioning*, PLANS 1994, IEEE, Las Vegas, 12-15 April 1994

COMP, C., AXELRAD, P. (1996): *An Adaptive SNR-Based Carrier Phase Multipath Mitigation Technique*, Proceedings of the 9th International Technical Meeting of the Satellite Division of the Institute of Navigation, ION - GPS 96, September 17-20, 1996, Kansas City, Missouri, 683 - 697

COORDINATION SCIENTIFIC INFORMATION CENTER (2002): *Global Navigation Satellite System GLONASS: Interface Control Document (ICD) V. 5.0*, Coordination Scientific Information Center, available from: http://www.glonass-ianc.rsa.ru/i/glonass/ICD02_e.pdf (accessed January 2007)

EISSFELLER, B., WINKEL, J. (1996): *GPS Dynamic Multipath Analysis in Urban Areas*, Proceedings of the 9th International Technical Meeting of the Satellite Division of the Institute of Navigation, ION-GPS 96, September 1996, Kansas City, Missouri, 719-727

EISSFELLER, B. (1997): *Ein dynamisches Fehlermodell für GPS Autokorrelationsempfänger*, Schriftenreihe des Studiengangs Vermessungswesen, Universität der Bundeswehr München, Heft 55, Neubiberg, 1997

EUROPEAN SPACE AGENCY (ESA) (2006): *Galileo Open Service Signal In Space Interface Control Document*, draft version, May 2006

EUROPEAN SPACE AGENCY (ESA) (2007a): *Navigation: The Future - Galileo*, available from: http://www.esa.int/esaNA/galileo.html (accessed January 2007)

EUROPEAN SPACE AGENCY (ESA) (2007b): *Navigation: The Present - EGNOS*, available from: http://www.esa.int/esaNA/egnos.html (accessed January 2007)

FAHRMEIR, L., KÜNSTLER, R., PIGEOT, I., TUTZ, G. (1999): *Statistik: Der Weg zur Datenanalyse*, 2nd Edition, Springer Verlag Berlin – Heidelberg- New York, 1999

FEDERAL AVIATION ADMINISTRATION (2007): *Wide Area Augmentation System (WAAS)*, available from: http://gps.faa.gov/programs/waas/waas-text.htm (accessed January 2007)

FENTON, P., JONES, J. (2005): The Theory and Performance of NovAtel Inc.'s Vision Correlator, Proceedings of the 18th International Technical Meeting of the Satellite Division of the Institute of Navigation, ION GNSS 2005, September 13-16, 2005, Long Beach, California

FILIPPOV, V., TATARNICOV, D., ASHJAEE, J., ASTAKHOV, A., SUTIAGIN, I. (1998): *The First Dual-Frequency Choke Ring*, Proceedings of the 11th International Technical Meeting of the Satellite Division of the Institute of Navigation, ION-GPS 98, September 1998, Nashville, Tennessee, 1035-1040

FILIPPOV, V., SUTIAGIN, I., ASHJAEE, J. (1999): *Measured Characteristics of Dual Depth Dual Frequency Choke Ring for Multipath Rejection in GPS* Receivers, Proceedings of the 12th International Technical Meeting of the Satellite Division of the Institute of Navigation, September 14-17, 1999, Nashville, Tennessee

FISHER, J., SIMPSON, S., WELSH, T. (2002): *An Urban Canyon Multipath Model for Galileo*, Proceedings of the European Navigation Conference ENC-GNSS 2002, Copenhagen, Denmark, 27-30 May 2002

FLEURY, B., TSCHUDIN, M., HEDDERGOTT, R., DAHLHAUS, D., PEDERSEN, K. (1999): *Channel Parameter Estimation in Mobile Radio Environments Using the SAGE Algorithm*, IEEE Journal on Selected Areas in Communications, Vol. 17, No. 3, March 1999

FLOCK, W. L. (1979): *Electromagnetics and the Environment: Remote Sensing and Telecommunications*, Prentice-Hall, Inc., 1979, ISBN 0-13-248997-X

FLOCK, W. L. (1987): *Propagation Effects on Satellite Systems at Frequencies Below 10 GHz: A Handbook for Satellite Systems Design*, Second Edition, NASA Reference Publication 1108(02)

FORDEN, G. (2004): *The Military Capabilities and Implications of China's Indigenous Satellite-Based Navigation System*, Science and Global Security, 12, 2004, 219-250

FU, Z., HORNBOSTEL, A., HAMMESFAHR, J., KONOVALTSEV, A. (2003): *Suppression of Multipath and Jamming Signals by Digital Beamforming for GPS/Galileo Applications*, GPS Solutions, Vol. 6, No. 4, 257 - 264

GARIN, L., VAN DIGGELEN, F. and ROUSSEAU, J. (1996): *Strobe & Edge Correlator Multipath Mitigation for Code*, Proceedings of the 9th International Technical Meeting of the Satellite Division of the Institute of Navigation, ION - GPS 96, September 17-20, 1996, Kansas City, Missouri, 657-664

GARIN, L. and ROUSSEAU, J. (1997): *Enhanced Strobe Correlator Multipath Rejection for Code & Carrier*, Proceedings of the 10th International Technical Meeting of the Satellite Division of the Institute of Navigation, ION - GPS 97, September 16-19, 1997, Kansas City, Missouri, 559-568

GARIN, L. (2005): The "Shaping Correlator": Novel Multipath Mitigation Technique Applicable to GALILEO BOC(1,1) Modulation Waveforms in High Volume Markets, Proceedings of the European Navigation Conference ENC-GNSS 2005, Munich, Germany, 19-22 May 2005

GE, L., HAN, S., RIZOS, C. (2000): *Multipath Mitigation of Continuous GPS Measurements Using an Adaptive Filter*, GPS Solutions, Vol. 4, No. 2, 2000, 19 - 30

GEORGIADOU, Y., KLEUSBERG, A. (1988): On Carrier Signal Multipath Effects in Relative GPS Positioning, Manuscripta Geodaetica, 13, 1988, 172-179

GOLDHIRSCH, J., VOGEL, W. (1998): *Handbook of Propagation Effects for Vehicular and Personal Mobile Satellite Systems*, John Hopkins University & University of Texas, 1998

HAGERMAN, L. (1973): *Effects of Multipath on Coherent and Noncoherent PRN Ranging Receiver*, Aerospace Rep. TOR-0073(3020-03)-3, Development Planning Division, The Aerospace Corporation, May 15, 1973

HAMMING, R. W. (1983): *Digitale Filter*, VCH Verlagsgesellschaft, Weinheim, Germany, Deutsche Übersetzung der zweiten, überarbeiteten Auflage vom Hamming, 1987

HANNAH, B., KUBIK, K., WALKER, R. (2000): *Propagation Modeling of GPS Signals*, Quo vadis geodesia...? Festschrift for Erik W. Grafarend on the Occasion of his 60th Birthday, Part 1, Schriftenreihe der Institute des Studiengangs Geodäsie und Geoinformatik, Univ. Stuttgart, 2000, 137-150

HANNAH, B. (2001): Modeling and Simulation of GPS Multipath Propagation, Dissertation, Cooperative Research Centre for Satellite Systems, Queensland University of Technology

HARTL, PH. (1988): *Fernwirktechnik der Raumfahrt: Telemetrie, Telekommando, Bahnvermessung*, 2. Auflage, Springer-Verlag Berlin Heidelberg

HATCH, R. (1986): *Dynamic Advanced GPS at the Centimeter Level*, Proceedings of the 4th International Geodetic Symposium on Satellite Positioning , 1986, Austin, Texas, 1287

HEIN, G.W., IRSIGLER, M., AVILA-RODRIGUEZ, J.A., PANY, T. (2004): *Performance of Galileo L1 Signal Candidates*, Proceedings of the European Navigation Conference GNSS 2004, 16 - 19 May 2004, Rotterdam, The Netherlands

HEIN, G.W., AVILA-RODRIGUEZ, J.-A., RIES, L., GODET, PRATT, J. T., ISSLER, J-L. (2005): *A Candidate for the Galileo L1 OS Optimized Signal*, Proceedings of the 18th International Technical Meeting of the Satellite Division of the Institute of Navigation, ION GNSS 2005, September 13-16, 2005, Long Beach, California

HEIN, G.W., AVILA-RODRIGUEZ, J.-A., WALLNER, S., EISSFELLER, B., PANY, T., HARTL, P. (2007): *Envisioning a Future GNSS System of Systems, Part I*,Inside GNSS, January/February 2007, 58 - 67

HÖPER, M., BOELOW, T., HOFFMANN, H. (2001): Detection of Multipath Influence at DGPS Reference Stations, Proceedings of the 14th International Technical Meeting of the Satellite Division of the Institute of Navigation, ION-GPS 2001, September 11-14, 2001, Salt Lake City, Utah, 581 - 590

HWANG, P., MCGRAW, G., BADER, J. (1998): *Enhanced Differential GPS Carrier-Smoothed Code Processing Using Dual Frequency Measurements*, Proceedings of the 11th International Technical Meeting of the Satellite Division of the Institute of Navigation, ION-GPS 98, September 15-18, 1998, Nashville, Tennessee, 461-470

IRSIGLER, M. (2001): *Comparison C-Band/L-Band: Signal Propagation*, Project “Satellitennavigation im C-Band” (C-Band Satellite Navigation), Technical Note, January 2001

IRSIGLER, M., EISSFELLER, B. (2003): *Comparison of Multipath Mitigation Techniques with Consideration of Future Signal Structures*, Proceedings of the 16th International Technical Meeting of the Satellite Division of the Institute of Navigation, ION GPS/GNSS 2003, September 9-12, 2003, Portland, Oregon

IRSIGLER, M., HEIN, G.W., EISSFELLER, B. (2004): *Multipath Performance Analysis for Future GNSS Signals*, Proceedings of the National Technical Meeting of the Satellite Division of the Institute of Navigation, ION NTM 2004, January 26-28, 2004, San Diego, California

IRSIGLER, M., HEIN, G.W., EISSFELLER, B., SCHMITZ-PEIFFER, A., KAISER, M., HORNBOSTEL, A., HARTL, P.(2002): *Aspects of C-Band Satellite Navigation: Signal Propagation and Satellite Signal Tracking*, Proceedings of the European Navigation Conference ENC-GNSS 2002, Copenhagen, Denmark, 27-30 May 2002

IRSIGLER, M., AVILA-RODRIGUEZ, J.-A., HEIN, G.W. (2005): *Criteria for GNSS Multipath Performance Assessment*, Proceedings of the 18th International Technical Meeting of the Satellite Division of the Institute of Navigation, ION GNSS 2005, September 13-16, 2005, Long Beach, California

ITANI, K., HAMADA, K., HAYASHI, T. (1996): *Development of a Teal-Time Multipath Monitor and Experimental Results*, Proceedings of the 9th International Technical Meeting of the Satellite Division of the Institute of Navigation, ION - GPS 96, September 17-20, 1996, Kansas City, Missouri, 729 - 738

JAHN, A., BISCHL, H., HEIß, G. (1996): *Channel Characterization for Spread Spectrum Satellite Communications*, Proceedings of the IEEE 4th International Symposium on Spread Spectrum Techniques & Applications (ISSSTA'96), 1996, 1221-1226

JAKAB, A. (1999): *An Approach to GPS Satellite Failure Detection*, Proceedings of the 12th International Technical Meeting of the Satellite Division of the Institute of Navigation, ION-GPS 1999, September 14-17, 1999, Nashville, Tennessee, pp. 751-759

JULIEN, O., CANNON, E., LACHAPELLE, G. MONGRÉDIEN, C., MACABIAU, C. (2004): *A New Unambiguous BOC(n,n) Signal Tracking Technique*, Proceedings of the European Navigation Conference ENC-GNSS 2004, Rotterdam, The Netherlands, 16-19 May 2004

KAJIWARA, A. (2000): *Foliage Attenuation Characteristics for LMDS Radio Channel*, IEICE Trans. Commun., Vol. E83-B, No. 9, September 2000

KEITH, J. (2000): *Multipath Errors Induced by Electronic Components in Receiver Hardware*, Proceedings of the National Technical Meeting of the Satellite Division of the Institute of Navigation, ION-NTM 2000, January 26-28, 2000, Anaheim, California

KELLY, J., BRAASCH, M. (1999): *Mitigation of GPS Multipath via Exploitation of Signal Dynamics*, Proceedings of the 55th Annual Meeting of the Satellite Division of the Institute of Navigation, ION-AM 1999, 28-30 June 1999, Cambridge, Massachusetts, 619-624

KELLY, J., BRAASCH, M. (2000): *Validation of GPS Fading Multipath Effects Through Modeling and Simulation*, Proceedings of the National Technical Meeting of the Satellite Division of the Institute of Navigation, ION-NTM 2000, January 26-28, 2000, Anaheim, California, 684-690

KELLY, J., BRAASCH, M. (2001): *Validation of Theoretical GPS Multipath Bias Characteristics*, IEEE Proceedings, Aerospace Conference, 2001, 3-1317-1325

KELLY, J. M., BRAASCH, M.S., DIBENEDETTO, M.F. (2003): *Characterization of the Effects of High Multipath Phase Rates in GPS*, GPS Solutions, Vol. 7, No. 1, pp. 5-15, 2003

KIBE, S.V. (2006): *Indian Plan for Satellite-Based Navigation Systems for Civil Aviation*, Online Journal of Space Communication, No. 9, Winter 2006, available from: http://satjournal.tcom.ohiou.edu/issue9/indian_plan.html (accessed January 2006)

KLOBUCHAR, J.A. (1996): *Ionospheric Effects on GPS*, In: Parkinson, B. W., Spilker, J. J.: *Global Positioning System: Theory and Applications*, Volume I, Progress in Astronautics and Aeronautics, Volume 163, American Institute of Aeronautics and Astronautics, Inc., Washington, 1996, 485-515

KLUKAS, R., JULIEN, O., DONG, L., CANNON, E., LACHAPELLE, G. (2004): *Effects of Building Materials on UHF Ranging Signals*, GPS Solutions, Vol. 8, No. 1, April 2004, 1 - 8

KOVACH, K. (2000): *New User Equivalent Range Error (UERE) Budget for the Modernized Navstar Global Positioning System (GPS)*, ION NTM 2000, 26-28 January, Anaheim, California

KRAUS, K., SCHNEIDER, W. (1988): *Fernerkundung, Band 1: Physikalische Grundlagen und Aufnahmetechniken*, F. Dümmler Verlag Bonn

KUNYSZ, W. (2003): A Three Dimensional Choke Ring Ground Plane Antenna, Proceedings of the 16th International Technical Meeting of the Satellite Division of the Institute of Navigation, ION-GPS 2003, September 9-12, Portland, Oregon, 1883-1888

LEE, H. K., LEE, J. G., JEE, G. (2004): *GPS Multipath Detection Based on Sequence of Successive-Time Double-Differences*, IEEE Signal Processing Letters, Vol. 11, No. 3, March 2004, 316 – 319

LOGOTHETIS, A., CARLEMALM, C. (2000): *SAGE Algorithms for Multipath Detection and Parameter Estimation in Asynchronous CDMA Systems*, IEEE Transactions on Signal Processing, Vol. 48, No. 11, November 2000

LUO, M., PULLEN, S., ZHANG, J., GLEASON, S., XIE, G., YANG, J., AKOS, D., ENGE, P., PERVAN, B. (2000): *Development and Testing of the Stanford LAAS Ground Facility Prototype*, Proceedings of the National Technical Meeting of the Satellite Division of the Institute of Navigation, ION-NTM 2000, January 26-28, 2000, Anaheim, California, 210 - 219

LUTZ, E., WERNER, M., JAHN, A. (2000): *Satellite Systems for Personal and Broadband Communications*, Springer-Verlag Berlin Heidelberg, 2000, ISBN 3-540-66840-3

MACGOUGAN, G., LACHAPELLE, G., NAYAK, R., WANG, A. (2001): *Overview of GNSS Signal Degradation Phenomena*, Proceedings of the International Symposium on Kinematic Systems in Geodesy, Geomatics and Navigation, June 5-8, 2001, Banff, Canada, 87-100

MALLAT, S. (1989), A Theory for Multi-Resolution Signal Decomposition: The Wavelet Representation, IEEE Pattern Anal. and Machine Intell., Vol. 11, No. 7, pp. 674-693.

MARAL,G., BOUSQUET, M. (1998): *Satellite Communications Systems: Systems, Techniques and Technology*, Third Edition, John Wiley & Sons Ltd, Chichester, New York, 1998

MATTOS, PH. G. (1996): *Multipath Elimination for the Low-Cost Consumer GPS*, Proceedings of the 9th International Technical Meeting of the Satellite Division of the Institute of Navigation, ION - GPS 96, September 17-20, 1996, Kansas City, Missouri, 665-671

MCGRAW, G. A., BRAASCH, M.S. (1999): GNSS MULTIPATH MITIGATION USING GATED AND HIGH RESOLUTION CORRELATOR CONCEPTS, Proceedings of the National Technical Meeting of the Institute of Navigation, ION NTM 1999, January 25-27, San Diego, California, 333 - 342

MISRA, P., ENGE, P: (2001): Global Positioning System: Signals, Measurements and Performance, Ganga-Jamuna Press, Lincoln, Massachusetts

MITELMAN, A., PHELTS, R. E., AKOS, D., PULLEN, S. P., ENGE, P. K. (2000): *A Real-Time Signal Quality Monitor for GPS Augmentation Systems*, Proceedings of the 13th International Technical Meeting of the Satellite Division of the Institute of Navigation, ION-GPS 2000, September 19-22, 2000, Salt Lake City, Utah, 862 - 871

MOELKER, D.-J. (1997): *Multiple Antennas for Advanced GNSS Multipath Mitigation and Multipath Direction Finding*, Proceedings of the 10th International Technical Meeting of the Satellite Division of the Institute of Navigation, ION - GPS 97, September 16-19, 1997, Kansas City, Missouri, 541 - 550

NELSON, L., AXELRAD, P., ETTER, D. (1997): *Adaptive Detection of Code Delay and Multipath in a Simplified GPS Signal Model*, Proceedings of the 10th International Technical Meeting of the Satellite Division of the Institute of Navigation, ION - GPS 97, September 16-19, 1997, Kansas City, Missouri, 569 – 581

NORMARK, P.-L., XIE, G., AKOS, D., PULLEN, S., LUO, M., LEE, J., ENGE, P., PERVAN, B. (2001): *The Next Generation Integrity Monitor Test bed (IMT) for Ground System Development and Validation Testing*, Proceedings of the 14th International Technical Meeting of the Satellite Division of the Institute of Navigation, ION-GPS 2001, September 11-14, 2001, Salt Lake City, Utah, 1200 - 1208

NORMARK, P.-L., AKOS, D., XIE, G., PULLEN, S., LUO, M., ENGE, P. (2002): *The Integrity Monitor Test bed and Multipath Limiting Antenna Test Results*, Proceedings of the 15th International Technical Meeting of the Satellite Division of the Institute of Navigation, ION-GPS 2002, September 24-27, 2002, Portland, Oregon

NOVATEL INC. (2002): *OEM4 Family of Receivers, User Manual Vol. 1: Installation and Operation*, OM-20000046, p. 153/154

PANY, T., IRSIGLER, M., EISSFELLER, B. (2005): *S-Curve Shaping: A New Method for Optimum Discriminator Based Code Multipath Mitigation*, Proceedings of the 18th International Technical Meeting of the Satellite Division of the Institute of Navigation, ION GNSS 2005, September 13-16, 2005, Long Beach, California

PANY, T., EISSFELLER, B. (2006): *Use of a Vector Delay Lock Loop Receiver for GNSS Signal Analysis in Bad Signal Conditions*, Proceedings of the IEEE/ION PLANS 2006, San Diego, California, 25-27 April, 2006

PANY, T., WON, J.-H., HEIN, G.W. (2006): *GNSS Software Defined Radio: Real Receiver or Just a Tool for Experts?*, InsideGNSS, Vol. 1, No. 5, 2006, Gibbons Media&Research

PETROVSKI, I.G. (2003): *QZSS - Japan's New Integrated Communication and Positioning Service for Mobile Users*, GPS World 14(6), 24-29

PHELTS, R. E., AKOS, D. M., ENGE, P. (2000): *Robust Signal Quality Monitoring and Detection of Evil Waveforms*, Proceedings of the 13th International Technical Meeting of the Satellite Division of the Institute of Navigation, ION-GPS 2000, September 19-22, Salt Lake City, Utah

PHELTS, R. E., ENGE, P. (2000a): The Case for Narrowband Receivers, Proceedings of the National Technical Meeting of the Satellite Division of the Institute of Navigation, ION-NTM 2000, January 26-28, 2000, Anaheim, California, 511-520

PHELTS, R. E., ENGE, P. (2000b): *The Multipath Invariance Approach for Code Multipath Mitigation*, Proceedings of the 13th International Technical Meeting of the Satellite Division of the Institute of Navigation, ION-GPS 2000, September 19-22, 2000, Salt Lake City, Utah, 2376-2384

PHELTS, R. E. (2001): *Multi-correlator Techniques for Robust Mitigation of Threats to GPS Signal Quality*, Dissertation, Department of Mechanical Engineering, Stanford University

PHELTS, R. E., WALTER, T., ENGE, P. (2003): *Toward Real-Time SQM for WAAS: Improved Detection Techniques*, Proceedings of the 16th International Technical Meeting of the Satellite Division of the Institute of Navigation, ION-GPS 2003, September 9-12, Portland, Oregon

POLISCHUK, G. M., KOZLOV, V. I., ILITCHOV, V. V., KOZLOV, A. G., BARTENEV, V. A., KOSSENKO, V. E., ANPHIMOV, N. A., REVNIVYKH, S. G., PISAREV, S. B., TYULYAKOV, A. E., SHEBSHAEVITCH, B. V., BASEVITCH, A. B., VOROKHOVSKY, Y. L. (2002): *The Global Navigation Satellite System GLONASS: Development and Usage in the 21st Century*, Proceedings of the 34th Annual Precise Time and Time Interval (PTTI) Systems and Applications Meeting, December 3-5 2002, Reston, Virginia

MISRA, P., ENGE, P. (2001): *Global Positioning System: Signals, Measurements and Performance*, Ganga-Jamuna Press, Lincoln, Massachusetts, 2001

PULLEN, S., LUO, M., GLEASON, S., XIE, G., LEE, J., AKOS, D., ENGE, P., PERVAN, B. (2000): *GBAS Validation Methodology and Test Results from the Stanford LAAS Integrity Monitor Test Bed*, Proceedings of the 13th International Technical Meeting of the Satellite Division of the Institute of Navigation, ION-GPS 2000, September 19-22, 2000, Salt Lake City, Utah

PULLEN, S., LUO, M., XIE, G., LEE, J., PHELTS, R. E., AKOS, D., ENGE, P. (2002): *LAAS Ground Facility Design Improvements to Meet Proposed Requirements for Category II/III Operations*, Proceedings of the 15th International Technical Meeting of the Satellite Division of the Institute of Navigation, ION-GPS 2002, September 24-27, 2002, Portland, Oregon

REICHERT, A., AXELRAD, P. (1999): *GPS Carrier Phase Multipath Reduction Using SNR Measurements to Characterize an Effective Reflector*, Proceedings of the 12th International Technical Meeting of the Satellite Division of the Institute of Navigation, September 14-17, 1999, Nashville, Tennessee, 1951-1960

RAQUET, J., LACHAPELLE, G. (1996): *Determination and Reduction of GPS Reference Station Multipath Using Multiple Receivers*, Proceedings of the 9th Int. Technical Meeting of the Satellite Division of the Institute of Navigation, ION-GPS 96, September 17-20, 1996, Kansas City, Missouri, 673-681

RAY, J.K., CANNON, M.E. and FENTON, P. (1998): *Mitigation of Static Carrier Phase Multipath Effects Using Multiple Closely-Spaced Antennas*, Proceedings of the 11th International Technical Meeting of the Satellite Division of the Institute of Navigation, ION - GPS98, September 15-18, 1998, Nashville, Tennessee, 1025 - 1034

RAY, J., CANNON, E. (1999): *Characterization of GPS Carrier Phase Multipath*, Proceedings of the National Technical Meeting of the Institute of Navigation, ION NTM 1999, January 25-27, San Diego, California

RAY, J., CANNON, E., FENTON, P. (1999): *Code Range and Carrier Phase Multipath Mitigation Using SNR, Range and Phase Measurements in a Multi-Antenna System*, Proceedings of the National Technical Meeting of the Institute of Navigation, ION NTM 1999, January 25-27, San Diego, California, 713 - 725

RAY, J. (1999): *Use of Multiple Antennas to Mitigate Carrier Phase Multipath in Reference Stations*, Proceedings of the 12th International Technical Meeting of the Satellite Division of the Institute of Navigation, September 14-17, 1999, Nashville, Tennessee

REVNIVYKH, S. (2006): *GLONASS: Policy, Stautus and Modernization Plan*, Presentation held at the Munich Satellite Navigation Summit 2006, 21-23 February, 2006, Munich, Germany

RIES, L., LESTARQUIT, L., ARMENGOU-MIRET, E., LEGRAND, F., VIGNEAU, W., BOURGA, C., ERHARD, P., ISSLER, J.-L. (2002) : *A Software Simulation Tool for GNSS2 BOC Signals Analysis*, Proceedings of the 15th International Technical Meeting of the Satellite Division of the Institute of Navigation, ION-GPS 2002, September 24-27, 2002, Portland, Oregon, 2225-2239

RODGERS, C. E. (1992): *Multipath Simulation Software Developed for the Design of a Low Multipath DGPS Antenna for the U.S. Coast Guard*, Proceedings of the 5th International Technical Meeting of the Satellite Division of the Institute of Navigation, ION-GPS 1992, September 16-18, Albuquerque, New Mexico, USA

RTCA SPECIAL COMMITTEE (1993): *Minimum Aviation Performance Standards for the Local Area Augmentation System (LAAS)*, RTCA/DO-245, RTCA Special Committee 159, RTCA, Inc., Washington, D.C., 28 September 1993

SAWABE, M. (2006): *Status of QZSS Project*, Presentation, Munich Satellite Navigation Summit 2006, February 21-23, Munich, Germany

SCHMID, A., NEUBAUER, A. (2004): *Channel Estimation Technique for Positioning Accuracy Improvement in Multipath Propagation Scenarios*, Proceedings of the ION GNSS 2004, 21-24 September 2004, Long Beach, California, USA

SCHUSTER BRUCE, A., VAN DIERENDONCK, A.J., JAKAB, A., WIEBE, J., TOWNSEND, B. (2000): *Detection of GPS Satellite Signal Failures in Satellite Based Augmentation Systems (SBAS)*, Proceedings of the 13th International Technical Meeting of the Satellite Division of the Institute of Navigation, ION-GPS 2000, September 19-22, 2000, Salt Lake City, Utah, 189 - 198

SLEEWAGEN, J.-M. (1997): MULTIPATH MITIGATION: BENEFITS FROM USING THE SIGNAL-TO-NOISE RATIO, Proceedings of the 10th International Technical Meeting of the Satellite Division of the Institute of Navigation, ION - GPS 97, September 16-19, 1997, Kansas City, Missouri, 531-541

SLEEWAGEN, J.-M., BOON, F. (2001): *Mitigating Short-Delay Multipath: A Promising New Technique*, Proceedings of the 14th International Technical Meeting of the Satellite Division of the Institute of Navigation, ION GPS 2001, 11-14 September 2001, Salt Lake City, Utah

SPILKER, J.J. (1996a): *Foliage Attenuation for Land Mobile Users*, In: Parkinson, B. W., Spilker, J. J.: *Global Positioning System: Theory and Applications*, Volume I, Progress in Astronautics and Aeronautics, Volume 163, American Institute of Aeronautics and Astronautics, Inc., Washington, 1996, 569-583

SPILKER, J.J. (1996b): *Tropospheric Effects on GPS*, In: Parkinson, B. W., Spilker, J. J.: *Global Positioning System: Theory and Applications*, Volume I, Progress in Astronautics and Aeronautics, Volume 163, American Institute of Aeronautics and Astronautics, Inc., Washington, 1996, 517-546

SPILKER, J.J. (1996c): *Interference Effects and Mitigation Techniques*, In: Parkinson, B. W., Spilker, J. J.: *Global Positioning System: Theory and Applications*, Vol. I, Progress in Astronautics and Aeronautics, Vol. 163, American Institute of Aeronautics and Astronautics, Washington, 717-771

SPILKER, J.J. (1996d): *GPS Signal Structure and Theoretical Performance*, In: Parkinson, B. W., Spilker, J. J.: *Global Positioning System: Theory and Applications*, Volume I, Progress in Astronautics and Aeronautics, Volume 163, American Institute of Aeronautics and Astronautics, Inc., Washington, 1996, 57-119

STEINGAß, A., LEHNER, A. (2003): *Land Mobile Satellite Navigation – Characteristics of the Multipath Channel*, Proceedings of the ION GPS GNSS 2003, 9-12 September 2004, Portland, Oregon, USA

STEINGAß, A., LEHNER, A. (2004): *Measuring the Navigation Multipath Channel – A Statistical Analysis*, Proceedings of the ION GNSS 2004, 21-24 September 2004, Long Beach, California, USA

SUH, Y., KONISHI, Y., HAKAMATA, T., MANANDHAR, D., SHIBASAKI, R., KUBO, N. (2004): *Evaluation of Multipath Error and Signal Propagation in Complex 3D Urban Environments for GPS Multipath Identification*, Proceedings of the International Technical Meeting of the Satellite Division of the Institute of Navigation, ION GNSS 2004, September 21

THORNBERG, B., THORNBERG, D., DI BENEDETTO, M., BRAASCH, M., VAN GRAAS, F., BARTONE, C. (2003): *LAAS Integrated Multipath-Limiting Antenna*, Navigation, Journal of the Institute of Navigation, Vol. 50, No. 2, Summer 2003, 117 - 130

TORAN-MARTI, F., VENTURA-TRAVESET, J. (2005): The ESA EGNOS Project: The First Step of the European Contribution to the Global Navigation Satellite System (GNSS), Proceedings of the 18th International Technical Meeting of the Satellite Division of the Institute of Navigation, ION GNSS 2005, September 13-16, 2005, Long Beach, California

TOWNSEND, B., FENTON, P. (1994): *A Practical Approach to the Reduction of Pseudorange Multipath Errors in a L1 GPS Receiver*, Proceedings of the 7th Int. Technical Meeting of the Satellite Division of the Institute of Navigation, ION-GPS 94, September 20-23, 1994, Salt Lake City, Utah, 143-148

TOWNSEND, B., VAN NEE, R., FENTON, P., VAN DIERENDONCK, K. (1995a): *Performance Evaluation of the Multipath Estimating Delay Lock Loop*, Navigation 42, No. 3, Fall 1995, 503 - 514

TOWNSEND, B., FENTON, P., VAN DIERENDONCK, K., VAN NEE, R. (1995b): *L1 Carrier Phase Multipath Error Reduction Using MEDLL Technology*, Proceedings of the 8th International Technical Meeting of the Satellite Division of the Institute of Navigation, ION - GPS 95, September 12-15, 1995, Palm Springs, California, 1539 - 1544

VAN DIERENDONCK, A.J., FENTON, P. and FORD, T. (1992): *Theory and Performance of Narrow Correlator Spacing in a GPS Receiver*, Navigation 39, No. 3, Fall 1992, 265 - 283

VAN DIERENDONCK (1996): *GPS Receivers*, In: Parkinson, B. W., Spilker, J. J.: *Global Positioning System: Theory and Applications*, Volume I, Progress in Astronautics and Aeronautics, Volume 163, American Institute of Aeronautics and Astronautics, Inc., Washington, 1996, 329-407

VAN DIERENDONCK, A.J., BRAASCH, M.S. (1997): *Evaluation of GNSS Receiver Correlation Processing Techniques for Multipath and Noise Mitigation*, Proceedings of the National Technical Meeting of the Institute of Navigation, January 14-16, 1997, Santa Monica, California, 207 - 215

Van Dierendonck, A.J., Schumpert, M., Fenton, P. (1998): Acquisition, Tracking and Mitigating Multipath Using the Proposed Split Spectrum C/A Code at L2, Proceedings of the 11th International Technical Meeting of the Satellite Division of the Institute of Navigation, ION-GPS 98, September 1998, Nashville, Tennessee, 1895-1903

Van Dierendonck, A.J., Akos, D., Pullen, S., Phelts, E., Enge, P. (2000): *Practical Implementation Considerations in the Detection of GPS Satellite Signal Failure*, IAIN World Congress/U.S. ION Annual Meeting, Catamaran Hotel, San Diego, CA, USA, June 26-28, 2000

Van Nee, R. (1992): *Multipath Effects on GPS Code Phase Measurements*, Navigation, Journal of the Institute of Navigation, Vol. 39, No. 2, Summer 1992

Van Nee, R. (1993): *Spread-Spectrum Code and Carrier Synchronization Errors Caused by Multipath and Interference*, IEEE Transactions on Aerospace and Electronic Systems, Vol.29, No.4, Oct. 1993

Van Nee, R., Siereveld, J., Fenton, P., Townsend, B. (1994): *The Multipath Estimating Delay Lock Loop: Approaching Theoretical Accuracy Limits*, Proceedings of the IEEE Position, Location and Navigation Symposium, Las Vegas, Nevada, April 1994

Wanninger, L. (1993): *Der Einfluss ionosphärischer Störungen auf präzise GPS-Messungen in Mitteleuropa*, Zeitschrift für Vermessungswesen, 118, 25 - 36.

Wanninger, L., Wildt, S. (1997): *Identifikation von Mehrwegeeinflüssen in GPS-Referenzstationsbeobachtungen*, Allgemeine Vermessungsnachrichten (AVN 1/1997), 104, 12-15.

Wanninger, L. (2000): *Der Einfluss der Ionosphäre auf die Positionierung in Referenzstationsnetzen*, Proceedings zum 3. SAPOS-Symposium, 23./24.5.2000, München

Wanninger, L., May, M. (2001): *Carrier-Phase Multipath Calibration of GPS Reference Stations*, Navigation: Journal of the Institute of Navigation, Vol. 48, No. 2, Summer 2001

Ward, P. W. (1996): *Effects of RF Interference on GPS Satellite Signal Receiver Tracking*, In: Kaplan, E. D.: Understanding *GPS: Principles and Applications*, Artech House Publishers, 209-236

Weill, L. R. (1995): *Achieving Theoretical Accuracy Limits for Pseudoranging in the Presence of Multipath*, Proceedings of the 8th International Technical Meeting of the Satellite Division of the Institute of Navigation, ION - GPS 95, September 12-15, 1995, Palm Springs, California, 1521 - 1530

Weill, L. R. (1997a): *Conquering Multipath: The GPS Accuracy Battle*, GPS World 8 (4) (1997) 59-66

Weill, L. R. (1997b): *GPS Multipath Mitigation by Means of Correlator Reference Waveform Design*, Proceedings of the National Technical Meeting of the Institute of Navigation, January 14-16, 1997, Santa Monica, California 197-206

Weill, L. R. (2002a): *Multipath Mitigation Using Modernized GPS Signals: How Good Can It Get?*, Proceedings of the 15th International Technical Meeting of the Satellite Division of the Institute of Navigation, ION-GPS 2002, September 24-27, 2002, Portland, Oregon

Weill, L. R., Fisher, B. (2002a): *Methods for Mitigating Multipath Effects in Radio Systems*, United States Patent, Patent No. 6,370,207 B1, Date of Patent: 9 April 2002

Weill, L. R. (2003a): *Multipath Mitigation: How Good Can It Get with New Signals?*, GPS World, June 2003, 106-113

Weill, L. R. (2003b): *High-Performance Multipath Mitigation Using the Synergy of Composite GPS Signals*, Proceedings of the ION GPS GNSS 2003, 9-12 September 2004, Portland, Oregon, 829-840

WINKEL, J. (2003): *Modeling and Simulating GNSS Signal Structures and Receivers*, Dissertation, Institute of Geodesy and Navigation, University FAF Munich, Germany, 2003 (http://137.193.200.177/ediss/winkel-jon/meta.html)

ZHANG, Y., BARTONE, C. (2004): *Real-Time Multipath Mitigation with WaveSmooth^{TM} Technique Using Wavelets*, Proceedings of the International Technical Meeting of the Satellite Division of the Institute of Navigation, ION GNSS 2004, September 21-24, 2004, Long Beach, California

12. Appendix E: List of Figures

13. Appendix F: List of Tables

14. Appendix G: List of Acronyms

AAI	Airports Authority of India
A-GNSS	Assisted GNSS
AM	Amplitude Modulation
APME	A Posteriori Multipath Estimation
AS	Anti-Spoofing
ASCII	American Standard Code for Information Interchange
BCS	Binary Coded Symbols
BOC	Binary Offset Carrier
BPSK	Binary Phase Shift Keying
BW	Bandwidth
C/A	Coarse/Acquisition
CB	Citizens Band
CBCS	Composite Binary Coded Symbols
CMC	Code Minus Carrier
C/N_0	Carrier-To-Noise Ratio
CS	Commercial Service
CW	Continuous Wave
CWT	Continuous Wavelet Transformation
DGPS	Differential GPS
DLL	Delay Lock Loop
DOP	Dilution of Precision
DOT	Department of Transportation
DWT	Discrete Wavelet Transformation
EGNOS	European Geostationary Navigation Overlay Service
ELS	Early-Late-Slope
ESA	European Space Agency
FAA	Federal Aviation Administration
FAF	Federal Armed Forces
FD	Fault Detection
FDE	Fault Detection and Exclusion
FFT	Fast Fourier Transformation
FIR	Finite Impulse Response
FLL	Frequency Lock Loop
FM	Frequency Modulation
GAGAN	GPS And Geo Augmented Navigation
GBAS	Ground-Bases Augmentation System
GEO	Geostationary Earth Orbit
GLONASS	Globalnaja Nawigazionnaja Sputnikowaja Sistema
GNSS	Global Navigation Satellite System
GPS	Global Positioning System
GRS	Ground Reference Stations
GSTB	Galileo System Test Bed
GUS	Ground Uplink System

HRC	High Resolution Correlator
HZA	High-Zenith Antenna
ICD	Interface Control Document
IF	Intermediate Frequency
IGSO	Inclined Geosynchronous Orbit
IMT	Integrity Monitoring Test Bed
INS	Inertial Navigation System
IOV	In-Orbit Validation
IRNSS	Indian Radio Navigation Satellite System
ISRO	Indian Space Research Organization
ITU	International Telecommunication Union - Radiocommunication Sector
LAAS	Local Area Augmentation System
LHCP	Left-Hand Circularly Polarized
LHEP	Left-Hand Elliptically Polarized
LMS	Land Mobile Satellite Services
LNA	Low Noise Amplifier
LOS	Line-Of-Sight
MASPS	Minimum Aviation System Performance Standards
MBOC	Multiplexed Binary Offset Carrier
MEDLL	Multipath Estimating Delay Lock Loop
MEO	Medium Earth Orbit
MET	Multipath Elimination Technology
ML	Maximum Likelihood
MLA	Multipath Limiting Antenna
MMT	Multipath Mitigation Technique
MPI	Multipath Invariance
MSAS	Multifunction Transport Satellite Space-Based Augmentation System
NCO	Numerically Controlled Oscillator
NLES	Navigation Land Earth Stations
NNSS	Navy Navigation Satellite System
OS	Open Service
PAC	Pulse Aperture Correlator
PDP	Power-Delay Profile
PLL	Phase Lock Loop
PPS	Precise Positioning Service
PR	Pseudorange
PRN	Pseudo Random Noise
PRS	Public Regulated Service
PVT	Position Velocity Time
QPSK	Quadrature Phase Shift Keying
QZSS	Quasi-Zenith Satellite System
RAIM	Receiver Autonomous Integrity Monitoring
RHCP	Right-Hand Circularly Polarized
RHEP	Right-Hand Elliptically Polarized
RIMS	Ranging and Integrity Monitoring Stations

RMS	Root Mean Square
RTCA	Radio Technical Commission for Aviation Services
RTMM	Real Time Multipath Monitor
SAR	Search And Rescue
SBAS	Satellite-Based Augmentation System
SCM	Statistical Channel Model
SIS	Signal In Space
SMR	Signal-To-Multipath Ratio
SNR	Signal-To-Noise Ratio
SOL	Safety-of-Life
SPS	Standard Positioning Service
SQM	Signal Quality Monitoring
STANAG	Standardization Agreement
SV	Space Vehicle
TEC	Total Electron Content
TID	Traveling Ionospheric Disturbances
TM	Threat Model
TOW	Time of Week
TS	Time Series
UERE	User Equivalent Range Error
VSWR	Voltage Standing Wave Ratio
WAAS	Wide Area Augmentation System
WMS	Wide Area Master Station

Danksagung

Die vorliegende Arbeit wurde zum allergrößten Teil während meiner Tätigkeit als wissenschaftlicher Mitarbeiter am Institut für Erdmessung und Navigation der Universität der Bundeswehr München angefertigt. Während dieser Zeit konnte ich jederzeit auf die Unterstützung vieler Personen zählen, bei denen ich mich auf diesem Weg ausdrücklich bedanken möchte:

An erster Stelle möchte ich meiner Freundin Leminh danken. Danke für Deine Geduld und Deine Bereitschaft, auf viele Stunden unserer gemeinsamen Zeit zu verzichten, die ich stattdessen mit der Fertigstellung dieser Arbeit zugebracht habe. Danke auch fürs Korrekturlesen dieser Arbeit, die wertvollen Übersetzungshilfen sowie die Entschärfung der schlimmsten sprachlichen Unzulänglichkeiten. Du warst und bist mir immer eine große moralische Stütze und warst während der Anfertigung dieser Arbeit eine riesengroße Unterstützung!

Danken möchte ich an dieser Stelle auch meinen Eltern Maria und Kurt Irsigler, die mir auf meinem Weg stets mit Rat und Tat zur Seite standen und auf deren Unterstützung ich immer zählen konnte. Diese Arbeit ist auch ein Ergebnis Eurer langjährigen Unterstützung.

Besonderer Dank gilt auch Herrn Univ.-Prof. Dr.-Ing. Günter W. Hein für die Betreuung dieser Arbeit sowie Herrn Univ.-Prof. Dr.-Ing. Bernd Eissfeller, der ebenfalls stets für fachliche Diskussionen zur Verfügung stand. Beiden möchte ich ferner für die Begutachtung dieser Arbeit danken sowie dafür, dass sie mir durch die Tätigkeit am Institut die Möglichkeit geboten haben, in einem sehr aktuellen, hochinteressanten und internationalen wissenschaftlichen Umfeld zu arbeiten.

Danken möchte ich ferner meinen ehemaligen Kolleginnen und Kollegen am Institut für Erdmessung und Navigation für die langjährige gute Zusammenarbeit, die sehr zu einem äußerst angenehmen Arbeitsklima beigetragen hat und ohne die ich dem Institut wohl nicht so lange treu geblieben wäre. Mein besonderer Dank gilt meinem langjährigen Zimmerkollegen Thomas Pany für seine Diskussionsbereitschaft, für wertvolle Anregungen zu verschiedenen Aspekten dieser Arbeit sowie die stets sehr gute Zusammenarbeit im Rahmen von Projekten und Papern. Danken möchte ich auch José-Angel Avila-Rodriguez, zum einen im Speziellen für seine Unterstützung bei der Prozessierung der statistischen Kanalmodelle, welche den Ausgangspunkt für ein wesentliches Kapitel dieser Arbeit lieferten, und zum anderen ebenfalls für die immer sehr gute Kooperation im Rahmen einer Vielzahl von wissenschaftlichen Beiträgen. Danken möchte ich außerdem dafür, dass sich José trotz seines oftmals sehr hohen Zeit- und Termindrucks immer Zeit für Gespräche und Diskussionen (auch nicht-fachlicher Natur) genommen hat. In diesem Zusammenhang geht ein besonderer Dank auch an Roland Kaniuth und Petra Häfele, die für alle beruflichen, vor allem aber auch nicht-beruflichen Belange immer ein wertvoller Ansprechpartner und eine große Unterstützung waren. Danken möchte ich abschließend auch Penni Grigat, die für alle Belange stets ein offenes Ohr hatte. Bei meinen Besuchen in der Messkuppel ist ein Abstecher ins Sekretariat zum festen Bestandteil geworden.